REPORT SERIES IN AEROSOL SCIENCE
N:o 268 (2023)

Statistical modeling of atmospheric aerosols – long-term trends and emissions of traffic and small-scale wood combustion

VILLE LEINONEN

Department of Technical Physics
Faculty of Science, Forestry and Technology
University of Eastern Finland
Kuopio, Finland

Doctoral dissertation, to be presented for public discussion with the permission of the Faculty of Science, Forestry and Technology of the University of Eastern Finland, in Auditorium SN200, Yliopistonranta 1, on the 18th of August 2023 at 12 o'clock.

Aerosolitutkimusseura r.y.
Helsinki 2023

Author's Address: Department of Technical Physics
P.O.Box 1627
FI-70211 University of Eastern Finland
ville.j.leinonen@uef.fi

Supervisors: Docent Santtu Mikkonen, Ph.D.
Department of Technical Physics
University of Eastern Finland, Kuopio, Finland

Professor Juha Karvanen, D.Sc. (Tech.)
Department of Mathematics and Statistics
University of Jyväskylä, Jyväskylä, Finland

Associate Professor Taina Yli-Juuti, Ph.D.
Department of Technical Physics
University of Eastern Finland, Kuopio, Finland

Professor Annele Virtanen, D.Sc. (Tech.)
Department of Technical Physics
University of Eastern Finland, Kuopio, Finland

Reviewers: Professor Leena Järvi, Ph.D.
Institute for Atmospheric and Earth System Research
University of Helsinki, Helsinki, Finland

Associate Professor Mikko Äijälä, Ph.D.
School of Energy Systems
Lappeenranta-Lahti University of Technology LUT,
Lappeenranta, Finland

Opponent: Research Professor Marko Laine, Ph.D.
Meteorological Research
Finnish Meteorological Institute, Helsinki, Finland

ISBN 978-952-7507-14-8 (printed) ISBN 978-952-7507-15-5 (pdf)
ISSN 0784-3496 ISSN 2814-4236
Helsinki 2023 https://erepo.uef.fi
Unigrafia Oy

Acknowledgements

The research has been conducted in the Department of Technical Physics at the University of Eastern Finland. I thank the head of the Department Prof. Jari Kaipio, former head of the Department Prof. Kari Lehtinen, and the head of the Aerosol Physics Group Prof. Annele Virtanen for providing the working facilities. I want to thank Nessling foundation, European Union (Horizon 2020 project FORCeS), and Jane and Aatos Erkko Foundation (project AHMA) for funding the projects in which I have been able to participate. I also want to express my gratitude towards Tiina and Antti Herlin foundation for giving me an opportunity to participate in my first international conference and present my work there.

I would like to thank all my supervisors. I thank my principal supervisor Dr. Santtu Mikkonen for resources, discussions, and great supervision of my work along the way. I also want to thank you for giving me opportunities to participate in other academic duties that still are an important part of the academic working life (supervision, courses, and seminars). I thank Prof. Juha Karvanen for all the support related to statistics, both before and after I started working here in Kuopio. I'm grateful to Assoc. Prof. Taina Yli-Juuti for the interest and support towards my research and for the excellent leadership of the Modelling group. I'm thankful to Prof. Annele Virtanen for the great support and leadership of the whole research group, and for the open discussion of a variety of topics related to the research group during the coffee breaks.

I express my gratitude to my thesis pre-examiners, Prof. Leena Järvi and Assoc. Prof. Mikko Äijälä for dedicating their time to review my thesis and giving valuable comments. I thank Prof. Marko Laine for agreeing to be my opponent.

I thank all the co-authors for their invaluable contributions to this work. I would like to especially thank UEF Fine Laboratory, the people responsible for the measurement sites (mostly under ACTRIS), and climate modelers for providing data and support in interpreting the results. I especially want to thank the whole AHMA team for showing me a new kind of working/collaboration culture.

It has always been easy to get along with the UEF Aerosol research group. I want to thank all of you for the positive attitude towards everyone’s research topics, open support when I've needed help, interesting discussions related to everything, and nice cakes etc. people have brought to coffee breaks. Special thanks to all my roommates in Me346.

Lopuksi haluan kiittää äitiä, Pekkalan väkeä, ystäviä ja sukulaisia kaikesta tuesta mitä olen teiltä saanut, ja joka on johdattanut matkaani väitökseen asti.

Ville Leinonen

Tervo, June 2023

Ville Juhani Leinonen
University of Eastern Finland, 2023

Abstract

Atmospheric aerosols affect human health and Earth's climate in many ways. In terms of health, aerosols are associated with millions of premature deaths yearly. In terms of climate, aerosols affect the radiation balance by absorbing and scattering radiation and forming clouds. The total effect of aerosols on the radiation balance is negative when compared to the pre-industrial situation; that is, aerosols have cooled the climate. However, there is a large uncertainty associated with this cooling effect, although that has been decreasing over the last several years thanks to the improved representation of aerosols and their atmospheric processes in climate models.

In this work, statistical modeling was employed to study the aerosol particle number concentration trends and emissions from anthropogenic combustion processes. The long-term evolution of observed particle number-size distributions in Europe was investigated, and those results were compared to the results from climate models. Two case studies are presented concerning the development of statistical models for estimating the emissions from passenger vehicles and the evolution of emissions from residential wood combustion.

It was found that the particle number concentrations of submicron-sized aerosol particles had mostly decreased in Europe over the last two decades, especially for particles larger than 10 nm (i.e., particles in the Aitken and accumulation mode size ranges). Similarly, decreasing trends in particle number concentrations are seen with climate models. The results also showed seasonal differences between the models and measurements. For the modeling of anthropogenic emissions, new statistical methods for evaluating particle number concentrations in emissions from passenger vehicles and the evolution of residential wood combustion in an atmospheric chamber were shown to work and have potential.

The results suggest further research directions related to the representation of aerosols in climate models and to emissions modeling, in which two types of models—for estimating emission factors and the evolution of emissions.

Keywords: statistical modeling, trend analysis, particle number-size distributions, anthropogenic emissions, wood combustion, traffic, atmospheric aerosols

Contents

List of publications

This thesis consists of an introductory review, followed by four research articles. In the introductory part, the papers are cited according to their roman numerals.

I **Leinonen, V.**, Kokkola, H., Yli-Juuti, T., Mielonen, T., Kühn, T., Nieminen, T., Heikkinen, S., Miinalainen, T., Bergman, T., Carslaw, K., Decesari, S., Fiebig, M., Hussein, T., Kivekäs, N., Krejci, R., Kulmala, M., Leskinen, A., Massling, A., Mihalopoulos, N., Mulcahy, J. P., Noe, S. M., van Noije, T., O'Connor, F. M., O'Dowd, C., Olivie, D., Pernov, J. B., Petäjä, T., Seland, Ø., Schulz, M., Scott, C. E., Skov, H., Swietlicki, E., Tuch, T., Wiedensohler, A., Virtanen, A., and Mikkonen, S.: Comparison of particle number size distribution trends in ground measurements and climate models, Atmos. Chem. Phys., 22, 12873–12905, https://doi.org/10.5194/acp-22-12873-2022, 2022.

II Mikkonen, S., Németh, Z., Varga, V., Weidinger, T., **Leinonen, V.**, Yli-Juuti, T., and Salma, I.: Decennial time trends and diurnal patterns of particle number concentrations in a central European city between 2008 and 2018, Atmos. Chem. Phys., 20, 12247–12263, https://doi.org/10.5194/acp-20-12247-2020, 2020.

III **Leinonen, V.**, Olin, M., Martikainen, S., Karjalainen, P., and Mikkonen, S.: Challenges and solutions in determining dilution ratios and emission factors from chase measurements of passenger vehicles, Atmos. Meas. Tech. Discuss. [preprint], https://doi.org/10.5194/amt-2023-77, in review, 2023.

IV **Leinonen, V.**, Tiitta, P., Sippula, O., Czech, H., Leskinen, A., Isokääntä, S., Karvanen, J. and Mikkonen, S.: Modeling atmospheric aging of small-scale wood combustion emissions: distinguishing causal effects from non-causal associations, Environ. Sci. Atmos., 2, 1551 – 1567, https://doi.org/10.1039/D2EA00048B, 2022.

1 Introduction

Atmospheric aerosols are defined as a suspension of solid or liquid particles in a gas. Atmospheric aerosol particles are generally defined as measuring from a few nanometers to tens of micrometers in diameter (Seinfeld and Pandis, 2016). Aerosols, and their number and mass concentrations in the atmosphere, vary greatly with the time of year (seasonal variation), between geographical locations (latitude and longitude), and with altitude (Aalto et al., 2005; Asmi et al., 2011; Guibert et al., 2005; Ma and Yu, 2014; Rose et al., 2021).

Aerosols are formed directly by natural and anthropogenic sources. Natural emissions of dust and sea salt, for example, constitute most of the atmospheric aerosol mass globally (Seinfeld and Pandis, 2016). Examples of anthropogenic sources of aerosols include combustion aerosols from the burning of biomass (for heating and power plants) and fossil fuels (for power plants and transportation). Although the contribution of anthropogenic aerosols to the global aerosol mass is small, both the anthropogenic fraction of mass and especially number can be important in populated urban areas (e.g., Rivas et al., 2020; Rönkkö et al., 2017). The lifetime of an aerosol particle in the tropospheric atmosphere is seconds to several days, depending on the size of the particle and the prevailing depositional mechanism (Emerson et al., 2020; Textor et al., 2006; Williams et al., 2002).

In addition to direct emissions of aerosol particles from natural and anthropogenic sources, gaseous compounds in the atmosphere can take part in the formation of aerosol particles. These compounds are referred to hereafter as precursor gases. New particles and masses in existing particles that are formed via the gas-to-particle conversion processes of organic precursor gases are known as secondary organic aerosols (SOAs). It has been determined that a significant proportion of the (especially anthropogenic) aerosol mass in the atmosphere originates as SOAs (Hallquist et al., 2009).

Aerosols have both climatic and health effects. The climatic effects are those that alter the radiation balance of the atmosphere, and they can be negative (cooling) or positive (heating). The health effects involve human exposure to inhaled particles (Shiraiwa et al., 2017). The exposure to particulate matter (PM) of less than 2.5 μm (i.e., PM2.5) has been estimated as causing 4.2 million deaths per year (Cohen et al., 2017).

Among the properties that affect the radiation balance in climate models, the effects of aerosols cause the largest uncertainty (Forster et al., 2021). The effects of aerosols on radiation are usually divided into two categories—aerosol–radiation interactions that refer to the single aerosol particle effect on the radiation balance through the scattering and absorbing of solar energy (Kuniyal and Guleria, 2019), and aerosol–cloud interactions that refer to an aerosol's ability to form clouds and affect the radiation balance (Fan et al., 2016; Tao et al., 2012). Despite the very complex nature of these phenomena, the uncertainty related to the effect of aerosols on the radiative balance of Earth has been decreasing (Intergovernmental Panel on Climate Change [IPCC], 2021). However, the uncertainty is still high compared to

the uncertainties attached to individual greenhouse gases, such as carbon dioxide (CO_2) and methane (CH_4).

Both the climatic and health effects can depend on several properties of the aerosol, such as the particle number concentration, the size distribution of the particles, or/and their composition (Cassee et al., 2013; Seinfeld and Pandis, 2016). The climatic effects of the particles may depend on the altitude of the particles (e.g., Ban-Weiss et al. (2009), for black carbon). The factors causing health effects are uncertain, but the toxic effects of different aerosol components and the lung and cellular responses are important questions for research (Shiraiwa et al., 2017). Cohen et al. (2017) showed that higher PM2.5 concentrations were linked to a higher relative risk of certain diseases. Hence, in terms of their health effects, particles that are close to the ground and occur in urban regions are most important because both the concentrations of the aerosol particles and the number of exposed persons are high. The variety of effective particle properties and locations highlights the importance of understanding the sources, aging, and transportation of aerosols.

The anthropogenic aerosol emissions used in climate models are obtained from emission inventories, such as ECLIPSE (Stohl et al., 2015) and EDGAR (Janssens-Maenhout et al., 2019) which provide estimates of the total emissions of particulate and gaseous substances for a certain area (grid box). These estimates are based on the reported emissions from certain important emissions sources (Janssens-Maenhout et al., 2019), observations made using different measurement methods, including in-situ measurements (measurement sites and mobile measurements) and satellite remote sensing. In recent studies on aerosol emissions, both physical and chemical properties of aerosols have usually been measured and reported, such as by Tiitta et al. (2016) for wood combustion emissions and Karjalainen et al. (2016) for vehicle emissions. It is important that the emission factors (EFs) of aerosol sources (e.g., for the above-mentioned sources) can be accurately estimated, and hence the methods to estimate emissions should be developed and verified. When the emission sources are evolving (e.g., all modern vehicles are not producing CO_2, which have been used in EF calculations), new methods for EF calculations need to be developed.

Secondary aerosols, and the interaction of gas and particle phase of emissions have raised their role in aerosol research lately. The atmospheric aging of emissions (i.e., the evolution of the emissions in the atmosphere via physical [e.g., condensation or coagulation] and chemical [e.g., oxidation, polymerization] reactions) has also been studied and measured (e.g., Al-Abadleh, 2021; Hartikainen et al., 2023; Tiitta et al., 2016). Such studies have included both field and laboratory measurements. The field measurements are based on tracking air masses through space, such as by mobile laboratory (Simonen et al., 2019). The laboratory and mobile laboratory measurement of aging involves the use of oxidation flow reactors (OFRs) and atmospheric chambers (Lambe et al., 2015; Platt et al., 2013). Together with comprehensive measurements of from the chamber, the evolution of both gas- and particle-phase emissions and their interactions can be interpreted and modeled.

Aerosol representations in climate models have been developed based on the knowledge base provided by laboratory and field measurements. As the known reaction pathways of

compounds contain hundreds or tons of different chemical compounds (e.g., in the Master Chemical Mechanism [MCM], 2023), some processes such as nucleation may require more complex models to be modeled more accurately (Semeniuk and Dastoor, 2018), and the physical size distribution of aerosol particles has been measured quite well in detail, (and hence could be modeled in detail, such as by using the general dynamic equation of particles (Seinfeld and Pandis, 2016)), the exact replication of real-world processes is not possible to execute in climate models using current computational resources. Hence, simplifications must be made for the systems represented in the models. One option would be to build a model to represent a phenomenon (e.g., aging) by simplifying the observations into a smaller number of important parameters (variables) that could represent the phenomenon well enough. Then, the evolution of those important parameters could be explained with a statistical or physical model. The model should describe the evolution process as accurately as possible, but with small computational effort.

Ultimately, when a climate model has reached a certain stage of development, it is usually tested against observations measured from the atmosphere. These observation data sets come from measurement sites, satellites, and field campaigns that provide important information about a certain phenomenon. The models are validated and compared against these datasets to test: 1) how well the historical evolution described in the models matches the observed trends of e.g. aerosol optical properties (e.g., Mortier et al., 2020); and 2) how well the models can capture short-term observations, usually related to some studied phenomenon (e.g., Brown et al., 2021; Gliß et al., 2021). Models are also compared against each other to test (1) and (2) above, and for the prediction of future climate. These tests help researchers capture the differences in sensitivities of the models to certain changes in the atmosphere, and this can make the models better for predicting future climate. These models are used to estimate future climates for various scenarios that represent possible trends in anthropogenic emissions of greenhouse gases and aerosols, as explained in the IPCC reports (e.g., IPCC, 2021). The particle number-size distribution is a property that has not been compared much in previous studies. Even though the particle number concentration is not directly causing to the optical properties of aerosols, understanding long-term evolution of particle number size-distribution and the differences in measured and modeled size distributions of it might help to improve the aerosol description in the models. Current measurements of particle number size-distribution from measurement sites allow the investigation of long-term evolution of particle numbers in Europe, and hence also allows the climate model comparisons.

In this thesis, the aim was to gain information about the evolution of particle number-size distribution in Europe and compare the evolution to the results produced by climate model. The other aim was to study and improve the models related to the estimation and evolution of anthropogenic emissions. To achieve those aims, statistical modeling was applied to four datasets focusing mainly on particle number size distributions. More specifically the research objectives addressed by this thesis were:

1) To understand the trends in the particle number concentrations and size distributions of aerosol particles in Europe during the last 20 years (**Papers I and II**);

2) To determine whether the observed evolution of the particle number–size distributions was being captured in the climate models (**Paper I**);
3) To understand the differences in calculation methods of EFs for vehicle emissions, and to develop new methods for EF calculation (**Paper III**); and
4) To model the evolution of aerosols in an atmospheric chamber and to study the dependencies of the variables measured from the small-scale residential wood combustion emission (**Paper IV**).

2 Materials and methods

This chapter briefly presents the aerosol size distribution, aerosol datasets (measurements, climate models), and statistical methods used in **Papers I–IV**. The focus was on the statistical modeling of the datasets. Therefore, other aspects of measurements, such as the types of measurements (laboratory, field) used in **Papers I–IV**, with the importance of those measurements to research, and the measuring instruments themselves are briefly reviewed. Detailed discussions regarding, for example, the sampling of measurement and dilution can be found in the corresponding papers and references therein. Here, climate models are only briefly reviewed in terms of previous studies and comparing the measurement and model datasets.

2.1 Aerosol particles and emissions

2.1.1 Aerosol size distribution and aerosol modes

The diameters of aerosol particles are measured on the scale of nanometers to micrometers. It has been shown that, in many cases, the size distribution function, f, for aerosol number, surface area, and mass concentration as a function of particle diameter (d_p) is lognormal. The aerosol size distribution function (Seinfeld and Pandis, 2016) as a function of $\log(d_p)$ is usually presented as a sum of several lognormal distributions, which each have particle number concentration (N_i) of mode i

$$f(\log d_p) = \sum_{i=1}^{n} \frac{N_i}{\sqrt{2\pi} * log(\sigma_i)} \exp\left(-\frac{(\log d_p - \log D_{p,i})^2}{2 \log^2 \sigma_i}\right), \quad (1)$$

where $D_{p,i}$ is a geometric mean diameter, and σ_i is a geometric standard deviation of mode i, $i = 1, \ldots, n$, where n is the number of modes. The distribution function refers here to the atmospheric aerosol size distribution function defined as in Seinfeld and Pandis, (2016), formula (8.54). This means that the integral of f from formula (1) is equal to the number concentration, $\int_{-\infty}^{\infty} f(\log d_p)\, d \log d_p = \sum_{i=1}^{n} N_i$. Aerosol size distribution function is not the same than the probability distribution or probability density function g used in statistical literature, for which $\int_{-\infty}^{\infty} g(\log d_p)\, d \log d_p = 1$.

The particle number-size distribution usually consists of two to four modes. Figure 1 provides an example of a typical particle size distribution (number) consisting of four modes. The modes are characterized based on the geometric mean diameter. The mode with a diameter of less than 25 nm is called the nucleation mode, the mode with a diameter of between 25 and 100 nm is the Aitken mode, between 100 and 1,000 nm is the accumulation mode, and more than 1 µm is the coarse mode.

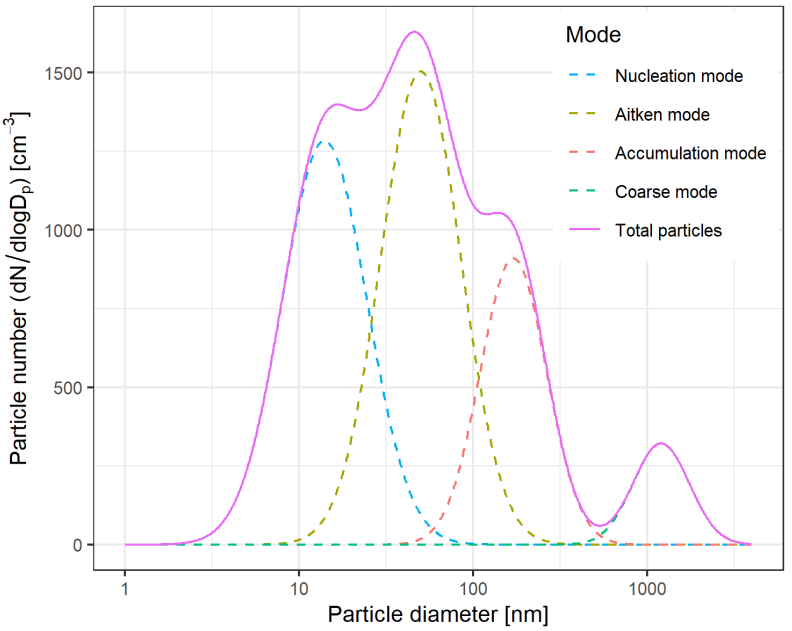

Figure 1. Illustration of the modes (nucleation, Aitken, accumulation, coarse) in an aerosol particle number-size distribution.

For describing the particle number-size distribution, algorithms have been developed that fit a mixture of log-normal size distribution functions (see illustration of log-normal modes in Figure 1, Hussein et al., 2005; Mäkelä et al., 2000; Whitby, 1978). Mode parameters (geometric mean diameter D_p, geometric standard deviation σ, and number concentration N) can help to compare number–size distribution data from measurements made either at the same location (e.g., to compare the seasonal characteristics of the modes) or between different locations (e.g., to compare the measurement sites). Hussein et al.'s (2005) algorithm was used in **Paper I** to compress a large set of particle number–size distribution data from long-term measurements from multiple measurement sites. The algorithm fits the mixture function of several lognormal distribution functions (see formula (1)) to the size distribution data by the least squares method. The algorithm iteratively searches the optimal mode parameters, and tests if the number of modes could be minimized without losing too much fit quality based on the procedure described in detail in Hussein et al. (2005). The algorithm was used to fit a maximum of three modes for each particle size–distribution measurement. After the modes were fitted, the mode parameters were used in the analysis.

2.1.2 Aerosol emissions, and their size distributions

As mentioned in the introduction, aerosol emissions consist of natural and anthropogenic emissions. On the global scale, the most common natural aerosol emissions by mass are

from oceans (sea salt) and deserts (dust). However, aerosols originating from continental areas also contain large amounts of organic compounds that come from plants and combustion processes that are both natural and anthropogenic (Jimenez et al., 2009).

In addition to direct emissions of particles, precursor gases of secondary aerosols, such as volatile organic compounds (VOCs) are important in the total aerosol mass (Guenther et al., 1995). It has been shown that these emissions increase with increasing temperature and also have a negative (cooling) effect on the radiative balance via increasing the number of cloud condensation nuclei that increase the brightness of clouds (Yli-Juuti et al., 2021). For biogenic VOC (BVOC) emissions coming from plants, seasonality is a significant factor, with most of the BVOC emissions, especially those farther from the Equator, such as in the boreal region, being produced during the growing season. Such emissions have been shown to be often exponentially correlated with temperature (Guenther et al., 1995; Hellén et al., 2018).

Anthropogenic combustion processes, including residential and vehicular, can also produce significant amounts of particulate emissions locally. Traffic emissions can have a significant effect on the air quality close to roads that have heavy traffic, such as highways, and depend on meteorological conditions, which can extend the effective area (Enroth et al., 2016; Pirjola et al., 2017). Many previous studies have focused on the aerosol mass of particles with diameter under 2.5 μm, $PM_{2.5}$. Compared to the number-size distribution, the mass-size distribution is more focused on the larger particles, as when the diameter of a spherical particle doubles, the volume is eight time the volume of the original particle.

In terms of residential combustion, the recorded fraction of $PM_{2.5}$ close to the surface of the Earth can be up to 15% to 40% in Asia, Eastern Europe, and East Africa (Butt et al., 2016). Similarly, emissions from wood combustion can contribute significantly (> 10%) to the total $PM_{2.5}$ in many parts of Europe during winter, when wood is combusted for residential heating. Note that Fountoukis et al. (2014) estimated a decrease in $PM_{2.5}$ when residential wood combustion was replaced by pellets for stoves. Both sources are therefore important for local (especially urban) air quality and human health.

Particles from primary wood combustion are mostly in the Aitken and accumulation modes for both masonry heaters and stoves (Hartikainen et al., 2020; Leskinen et al., 2014; Tiitta et al., 2016; Tissari et al., 2008), with a geometric mean diameter between 53 and 96 nm from primary emissions given in Hartikainen et al. (2020). Emissions for masonry heaters contain mostly organic species and elemental carbon, with a smaller fraction of salts, such as sodium, potassium, zinc, and iron (Kortelainen et al., 2018).

The primary emissions from passenger vehicles contain two modes, one with a D_p of around 10–30 nm and a larger mode with a diameter of around 70 nm for gasoline cars and 100 nm for diesel cars (Karjalainen et al., 2014; Wihersaari et al., 2020). In addition, a nanocluster aerosol mode (Rönkkö et al., 2017) is represented by delayed primary emissions (i.e., those that occur in the high-temperature gas-phase exhaust that immediately forms aerosol particles in the atmosphere).

2.2 Aerosol measurements and data processing

2.2.1 Atmospheric measurement sites

Atmospheric measuring sites have been established for taking long-term measurements, usually of many different gases and aerosol particle properties. “Long-term” here refers to a minimum of six years of measurements. Particle size distribution measurements have a relatively short history compared to greenhouse gas measurements (e.g., the CO_2 levels at Mauna Loa have been observed since 1958) (Keeling et al., 1976), with the longest particle number-size distribution time series used in **Paper I** having started in 1996. Hence, the number of long-term measurements of particle size distributions is still limited, even in Europe.

In addition to recording long-term trends, measuring sites can be used to observe local air quality or provide representative measurements for phenomena that occur over a wider area. A well-equipped measuring site often offers the opportunity to study observed phenomena under natural conditions, which can be supplemented by more precise laboratory measurements.

In the last few years, European measurement sites have formulated standards for measuring both greenhouse gases (ICOS - Integrated Carbon Observation System, 2023) and short-lived atmospheric constituents, including aerosol particles (ACTRIS - Aerosols, Clouds and Trace gases Research InfraStructure Network, 2023). These standards help in making sure measuring sites are appropriately equipped to record the necessary variables. In addition to actual observations, the measuring site network can include data management aspects for unifying the data produced by the individual measuring sites and ensuring its quality. This makes the job of the downstream user easier, both in terms of reading the material and trusting the data quality.

The measurement sites and data used in **Paper I** were mostly from the ACTRIS Data Centre (ACTRIS data center - an atmospheric data portal, 2023). For some of the sites that were not part of ACTRIS, the data were provided directly by the researchers managing the data from the site, while the rest came from Nieminen et al. (2018). The sites used in **Papers I and II** are listed in Table 1. The environmental classification is based on the classification used in Nieminen et al., (2018) and the classifications provided in sites’ metadata.

Table 1. List of sites used in **Papers I and II** and their environmental classification (see subsection 2.2.2 of **Paper I** for more detail). The table has been reproduced from **Paper I**, but with the addition of the Budapest site and the removal of the columns giving the locations and altitudes of the sites. The trends from the Budapest site were included in **Paper II**; all other sites were included in **Paper I**.

Sites included in both trend analysis and model comparison (Paper I)

Site name	Environment	Time period	Size range (nm)	Reference
Helsinki, Finland	Urban	2005–2018	3–1,000	Hussein et al. (2008)
Hohenpeissenberg, Germany	Rural	2008–2018	13–800	Birmili et al. (2003)
Hyytiälä, Finland	Rural	1996–2018	3–500	Hari and Kulmala (2005)
K-Puszta, Hungary	Rural	2008–2018	7–710	Salma et al. (2016b)
Puijo, Finland	Urban	2005–2015	10–500	Leskinen et al. (2012)
Mace Head, Ireland	Remote	2005–2012	21–500	O'Connor et al. (2008)
Melpitz, Germany	Rural	2008–2018	5–800	Hamed et al. (2010)
Pallas, Finland	Remote	2008–2017	7–430	Lohila et al. (2015)
San Pietro Capofiume, Italy	Rural	2002–2015	3–630	Hamed et al. (2007)
Schauinsland, Germany	High-altitude	2006–2018	10–600	Birmili et al. (2016)
Vavihill, Sweden	Rural	2001–2017	3–860	Schmale et al. (2018)
Värriö, Finland	Remote	1998–2018	8–400	Kyrö et al. (2014)
Zeppelin, Norway	Polar	2008–2018	10–800	Tunved et al. (2013)

Sites included in trend analysis only (Papers I and II)

Site name	Environment	Time period	Size range (nm)	Reference
Annaberg-Buchholz, Germany	Urban	2012–2018	10–800	Birmili et al. (2016)
Birkenes II, Norway	Rural	2010–2018	10–550	Yttri et al. (2021)
Budapest, Hungary	Urban	2008–2009, 2013–2018	6–1,000	Salma et al. (2016a)
Finokalia, Greece	Remote	2011–2018	9–760	Mihalopoulos et al. (1997)
Järvselja, Estonia	Rural	2012–2017	3–10,000	Noe et al. (2015)
Leipzig, Germany	Urban	2010–2018	10–800	Birmili et al. (2016)
Neuglobsow, Germany	Rural	2012–2018	10–800	Birmili et al. (2016)
Waldhof, Germany	Rural	2009–2018	10–800	Birmili et al. (2016)
Villum, Greenland	Polar	2010–2018	9–905	Nguyen et al. (2016)

2.2.2 Laboratory measurements

The purpose of laboratory measurements is often to study something in a more controlled way than outdoor measurements provide. In the laboratory, one can examine, for example, the primary emissions of the emissions source, a specific property of the aerosol (chemical,

physical), or aerosol aging. In many laboratories where aerosols are measured, chambers are used to monitor the transformation of the aerosol, as far as possible, under atmospheric-type conditions for several hours (e.g., Bruns et al., 2015; Robinson et al., 2007). To measure aerosols that have atmospherically relevant aging times of up to weeks or to determine the potential of aerosol samples to form SOAs, oxidation flow reactors (OFRs) can also be used (Ihalainen et al., 2019; Simonen et al., 2017). OFRs and chambers have several differences: aerosols have much shorter residence times in OFRs (minutes) than in chambers (usually at least hours), the OFRs have significantly higher oxidant concentrations (Lambe et al., 2011). OFRs are used as flow-through systems, whereas in chambers the batch of emissions is aged for several hours (Pieber et al., 2018). Information on the evolutionary process of aerosol aging is not directly obtainable from an OFR whereas in chambers, the aging of emission can be measured.

The laboratory measurements used in **Paper IV** were conducted in an ILMARI environmental chamber (Leskinen et al., 2015). The atmospheric aging chamber in the ILMARI environment has a 29-m^3 volume, is made of Teflon, and is used to study the aging of combustion aerosols. The chamber allows the study of both dark and ultraviolet (UV)-induced aging that corresponds to the typical midsummer UV irradiance in Central Finland.

Four experiments on the aging of residential wood combustion have been studied in **Paper IV**. Descriptions of the studied experiments were presented in two papers, one concentrating on the evolution of the particle emissions and SOA (Tiitta et al., 2016) and one on gas emissions, especially VOCs (Hartikainen et al., 2018). Both nighttime (Experiments 2B and 3B in Tiitta et al. (2016), and **Paper IV**) and daytime (Experiments 4B and 5B in Tiitta et al. (2016), and **Paper IV**) aging was measured in those experiments. To represent the atmospheric oxidation of the emissions, oxidants, such as ozone (O_3) in all experiments and hydroxide (OH) via nitrous acid (HONO) addition in experiments on UV-induced daytime aging, were added to the chamber before the experiment started. In the chamber experiments, the atmospherically equivalent aging time of the aerosols during the entirety of the experiments was between 7 and 18.5 h (Tiitta et al., 2016). An atmospherically relevant aging time—how long it would take an aerosol to have similar oxidant exposure in the atmosphere—was calculated from OH exposure based on Barmet et al. (2012) at typical boundary-layer OH concentrations of 10^6 cm^{-3} (Tiitta et al., 2016).

2.2.3 Mobile measurements and emission factor based on CO_2

Mobile measurements consist of measurements of aerosols that are made using a mobile laboratory setup, either by chasing an emissions source (e.g., Bukowiecki et al., 2002; Hussein et al., 2017; Pirjola et al., 2004) or situating the mobile laboratory so that an emissions source can be measured in one place. The advantages of mobile measurements include location flexibility, which enables in situ measurements of sources that are difficult or not possible to measure under laboratory conditions (e.g., ships, buses, and wildfires). A mobile laboratory is able to measure emissions from, for example, passenger vehicles as they move (chase measurements, e.g., Olin et al. (2023)). The aim is to measure the emissions of the

desired source under real-life conditions, without too much interference from other emissions sources in the measurement environment.

For **Paper III**, chase measurements of passenger vehicles were conducted under Finnish winter conditions (temperatures between -9°C and -28°C) using the Aerosol and Trace Gas Mobile Laboratory (ATMo-Lab) of Tampere University, Finland (Simonen et al., 2019).

The challenge described in **Paper III** involved determining the emission factor (EF) of aerosol particle number (N) from chase measurements. The EF describes the quantity of something (here, the number of particles) emitted by a vehicle, usually given per some unit describing the distance covered (per kilometer) or energy consumed (per liter of fuel). The usual method used to calculate the EF, which is based on CO_2 dilution, assumes that the entire emission of the measurement source is diluted equal to CO_2. For example, in Wihersaari et al. (2020), the EF was calculated as a dilution ratio (DR) of the emissions. The DR calculation used in their study assumed equal dilution by CO_2

$$DR_{N_{raw},t} = \frac{CO_{2,t}^{raw} - CO_2^{bg}}{CO_{2,t}^{meas} - CO_2^{bg}} \quad (2)$$

where $CO_{2,t}^{raw}$ is the raw concentration from the tailpipe of the vehicle at time t, CO_2^{bg} is the background CO_2 concentration (measured in **Paper III** as a median from the background concentration, and $CO_{2,t}^{meas}$ is the CO_2 concentration measured by the mobile laboratory at time t. The EF per kilometer, in the case of **Paper III** for particle number emissions, was then calculated based on the DR as an integral over time

$$EF_{N_{raw}} = \frac{\int_t [(N_t^{meas} - N^{bg}) * DR_{N_{raw},t} * Q_t] dt}{\rho_Q * \int_t v_t dt}. \quad (3)$$

Here, N_t^{meas} is the particle number concentration measured in the mobile laboratory at time t, N^{bg} is the background particle number concentration (measured as background CO_2), Q_t is the exhaust flow ratio (i.e., the volumetric exhaust flow of the vehicle), ρ_Q is the density of the exhaust, and v_t is the speed of the chased vehicle.

The method described above, and the other commonly used method, the N/CO_2 ratio (Hansen and Rosen, 1990; Zavala et al., 2006), is valid in most cases if the assumption of a constant EF in the N/CO_2 ratio is also valid. However, in all cases, the chased vehicle is not always producing CO_2. This could occur, for example, when the vehicle is going downhill, and the gas pedal is not being pressed. The modern vehicle, hybrid or electric, does not produce CO_2 when the vehicle is using electric motor only. Hence the way of determining emissions based on CO_2 is thus not always valid. For engine emissions, CO_2 can probably be used as an indicator of the emissions (i.e., when the engine is emitting, CO_2 is also being emitted), but for non-exhaust emissions (tires and brakes), the lack of CO_2 does not necessarily indicate a lack of non-exhaust emissions. With CO_2 being produced by the engine while it is working, the estimation of emissions during downhills is problematic because CO_2 is not being produced. Such emissions include particulate emissions from the brakes.

The DR of emissions from a chased vehicle observed by mobile laboratory is a function of the chasing speed, distance from the source, exhaust flow rate, and other factors, such as wind direction and wind speed. So, if the DR could be explained by a model based on those factors affecting it, then that model could be used instead of using CO_2 as a tracer for the dilution. In **Paper III**, the distance from the source (i.e., the distance between chased vehicle and mobile laboratory) was assumed to be constant. This was due to lack of distance measurements. The distance was attempted to keep as constant as possible by using same driver in the chased vehicle and mobile laboratory during the whole campaign, and also driving with relatively similar speeds in each section of the driving route.

In **Paper III**, we presented three new models for estimating the DR used to calculate the EF in one of the previous methods (N_{raw}, formula (3)). The models were based on measured variables other than CO_2.

The models in **Paper III**, (multivariate adaptive regression spline, MARS and Near-Wake dilution, NWD) were trained using the CO_2-based DR determined for the cases where observed exhaust flow rate and modeled DR were positive. The CO_2-based DR was calculated based on equation (2). See the details of the models from section 2.3 in **Paper III**. The models were then applied to the whole measurement data, including cases where the exhaust flow ratio was zero. The first model fitted was the NWD model, based on the observed dependence of DR on the ratio of exhaust flow rate and speed. The second model, MARS––which was more relevant to this work—involved using regression splines (see subsection 2.3.4 for details about splines) to estimate the DR based on observed dependences of the DR on the variables measured, such as exhaust flow rate, wind speed, vehicle speed, acceleration, and change in altitude between measurement points. Two MARS-models, one with data only from ATMo-Lab (MARS-chase) and one with variable(s) also from vehicle onboard diagnostics (OBD, variable exhaust flow rate) were formed.

2.2.4 Instruments for measuring particle number-size distribution

In this thesis, the measurements mostly concerned particle number concentrations and number-size distributions. The particle number concentrations in mobile laboratory were measured using condensation particle counters (CPCs), whereas the particle size distribution was determined using a differential mobility particle sizer (DMPS) to study the long-term trends and a scanning mobility particle sizer (SMPS) to study the long-term trends and in ILMARI chamber studying wood combustion emission.

A CPC (McMurry, 2000) measures particles based on an optical counter. For the particles to be large enough to be measured optically, they are grown using a suitable condensing liquid (e.g., butanol) under supersaturated conditions. The liquid effectively condenses on the surfaces of the existing particles in the sample air that act as condensation nuclei. Depending on the characteristics of the instrument used, a traditional CPC can measure the concentration of particles with a diameter greater than, for example, 3, 10, or 23 nm. With the addition of a particle size magnifier (Vanhanen et al., 2011), particles larger than 1 nm

can also be counted. The instrument's lower cut-off size is usually determined as the diameter at which 50% of the particles of that size can be detected.

A DMPS (Hoppel, 1978) is a combination of a differential mobility analyzer (DMA) (Knutson and Whitby, 1975) and a CPC. In the DMA, the particles are charged and certain-sized particles (hereafter referred to as a size class) are selected. The selection of particles is based on their electrical mobility (B_e). Electrical mobility, together with strength of an electric field (E) defines the electrical migration velocity of a charged particle $v_e = B_e E$ (Seinfeld and Pandis, 2016). Particles of a certain electrical migration velocity are separated, and the concentration of these selected particles is then measured using a CPC. The DMA can be subsequently used to scan multiple different size classes (by altering the voltage and hence also the electric field in the DMA), and the size distribution can be measured based on those scans. The size range of DMPS instruments used is mostly dependent on the DMA used. To achieve a broader size distribution (e.g., 3–900 nm), two DMPS systems, one with a short DMA and one with a long DMA, are used. The DMPS data were used in **Papers I and II**.

The SMPS (Wang and Flagan, 1990) has a similar setup (DMA + CPC) to the DMPS. The main difference between an SMPS and a DMPS is that the voltage used in the DMA is altered stepwise in the latter, whereas, in the SMPS, the voltage is changed continuously. The SMPS enables faster size-distribution measurements than the DMPS. The SMPS data was used in **Papers I and IV**.

2.3 Climate models and the representation of size distribution

The models that represent the state of the Earth system in general, and include the interactions of the atmosphere, cryosphere, and biosphere, are called Earth system models (Heavens et al., 2013). This is the most complex model group used in the Sixth Assessment Report (AR6) of the IPCC (IPCC, 2021).

A climate model is a model that represents Earth's climate and the various components that affect it. These include the atmosphere with clouds, greenhouse gases and aerosols, the sea, land surface, and the interaction of these in terms of radiative transfer (Chen et al., 2021).

Both Earth System models and climate models involve large systems of differential equations covering the atmosphere from the surface upward. Climate models consist of smaller models that each calculate a specific component of the whole system. Such models include general circulation models and aerosol schemes, which represent the evolution of aerosols in the models.

In **Paper I**, five climate models were used—EC-Earth3 (van Noije et al., 2021), ECHAM-M7 (Tegen et al., 2019), ECHAM-SALSA (Kokkola et al., 2018), NorESM1.2 (Kirkevåg et al., 2018), and UKESM (Sellar et al., 2019). These models used two different ways to process aerosol size distributions. The first was to represent the aerosol size distribution using lognormal modes (the EC-Earth, ECHAM-M7, NorESM, and UKESM models used

modal representation). The modal representation in models varies in terms of the number of modes and the division of the modes into water soluble and insoluble components used. Table 2 gives the number of modes used in the different models compared.

The second way was to represent the size distribution as the number of particles in predetermined size ranges (the ECHAM-SALSA). To represent a size distribution of 3 nm to 10 μm, ECHAM-SALSA used a total of 17 size bins (10 soluble and seven insoluble with different size ranges), as described in Table 2.

Table 2. Summary of the description of size distribution in the models compared in **Paper I**. Modified from Table 3 in **Paper I**.

Model name	Description of size distribution
ECHAM-M7	Seven lognormal modes—nucleation soluble, Aitken soluble, Aitken insoluble, accumulation soluble, accumulation insoluble, coarse soluble, coarse insoluble
ECHAM-SALSA	17 size sections—10 soluble bins (3 nm–10 um in diameter), seven insoluble bins (50 nm–10 um in diameter)
EC-Earth3	Seven lognormal modes—nucleation soluble, Aitken soluble, Aitken insoluble, accumulation soluble, accumulation insoluble, coarse soluble, coarse insoluble
NorESM.2	12 modes, based on mixed particles in nucleation, Aitken, accumulation, and coarse size ranges with black carbon, organic matter, sulfate, dust, and sea salt as core substrates
UKESM1	Seven lognormal modes—nucleation soluble, Aitken soluble, Aitken insoluble, accumulation soluble, accumulation insoluble, coarse soluble, coarse insoluble

2.3.1 Climate model comparisons

Climate model comparisons help the model developers to detect differences between the models and model responses to certain changes in the setup, such as aerosol radiation interactions, and to validate the model responses. Modeled experiments on future scenarios provide important knowledge on future climate and its uncertainty. Model comparisons are executed in order to assess model performance and validate the processes implemented in the models.

One of the large model comparison projects is the Coupled Model Intercomparison Project (CMIP). CMIP is part of the World Climate Research Programme (WCRP). Its aim is to "*better understand past, present and future climate changes arising from natural, unforced variability or in response to changes in radiative forcing in a multi-model context*" (WCRP Coupled Model Intercomparison Project (CMIP), 2023). The current phase of the project is CMIP6 (Eyring et al., 2016), which is focusing on: 1) Earth's response to different forcings (projections, geoengineering); 2) systematic model biases; and 3) the assessment of future climate changes given "internal climate variability, predictability, and uncertainties in scenarios" (Eyring et al., 2016, subsection 4.1).

Another large project involved in model comparison is AeroCom, which is mainly focused on aerosols and their impact (AeroCom website, 2023) and has been running for almost 20 years (Kinne et al., 2006; Penner et al., 2006). In addition to the model performance assessments provided by the CMIP projects, there are more detailed measurement comparisons related to the specific topic of measurements (e.g., aerosols in a certain area, transportation, or specific aerosol properties) in AeroCom. Control experiments for comparing climate models have also been specifically interested in some of the aerosol sources (e.g., dust or black carbon) and/or some physical properties related to aerosols (e.g., absorption, aerosol–cloud interactions, transportation, and location). Specific experiments related to changing some properties (e.g., height of biomass burning emissions and land-use change) have been conducted and planned.

2.3.2 Comparison of models with observations and the colocation of data

In **Paper I**, we compared the long-term (> 6 years, between 2000 and 2014) particle number-size distribution trends and seasonal representation of size distribution at 13 measurement sites located in Europe. **Paper I** was the first comparison of aerosol particle number-size distribution trends. Closely related studies concerning the trends and observed levels (see section 2.4.1) of aerosol optical properties (i.e., Angstrom exponent, aerosol optical depth, and aerosol light scattering and absorption) comparing climate model results to direct measurements and satellite results have been published under the umbrella of the AeroCom project (Gliß et al., 2021; Mortier et al., 2020). These studies showed that models can capture the observed, mostly decreasing, trends in aerosol optical properties relatively well in Europe and North America, where there is more observation data available (Mortier et al., 2020). The levels of aerosol optical properties have often been underestimated in the models (Gliß et al., 2021). Other model comparisons conducted that are relevant to this work include, for example, the effect of aerosol emissions harmonization to global model results (Textor et al., 2007), the global modeling of organic aerosols vs. SOAs (Tsigaridis et al., 2014), and biomass-burning aerosol absorption in measurements and climate models (Brown et al., 2021).

When comparing data from measurements and climate models, some data colocation was needed. In **Paper I**, there were three main aspects that were different between the model and the measurement data: 1) the modes (nucleation, Aitken, accumulation) were not defined similarly in all the models (see also the beginning of Subsection 2.3 and Table 2); 2) measured modes represent certain locations whereas modelled values modelling grid; and 3) time resolution was needed to be harmonized. Additionally, measurement data gaps needed to be considered.

As described above in subsection 2.3, the models in **Paper I** used two main ways to describe size distributions, modal and sectional representation. To compare the models against observations based on the same mode diameter limits, modes corresponding to both the modal and sectional model representation were calculated from the measurement datasets (see modal and sectional representation in the subsection 3.2). All the measurement bins with a

mean diameter falling into the size range of a model-based mode were summed in order to obtain the N of that mode. To calculate the representation of a mode from the measurements, at least three measurement bins were required to have a mean diameter that fell within the size range. Otherwise, the mode representation for that mode was not calculated. This was the case for the nucleation mode for some sites, which had a minimum-sized bin that measured close to the upper limits of the nucleation modal and sectional models.

For the location, the model grid box was selected to be the place containing the coordinates (latitude, longitude) of the measurement site. The height of the selected grid box was selected based on the altitude of the site. Some studies have also used the grid box with the lowest altitude, not the height of the site. For time resolution harmonization, both the measurement and model data were averaged to a monthly resolution. For the measurement data, enough data (i.e., five daily means, for which at least 12 h of data needed to be available) were required to be measured to calculate monthly mean.

2.4 Statistical methods

2.4.1 Time series data

Time series comprise a set of data points measured through time. Time series can thus describe the evolution of measured variables (e.g., a number concentration of certain-sized particles, as in **Papers I–IV**) and describe the evolution of the phenomenon in time. Measurements of such a phenomenon have usually been taken within a certain time interval (e.g., per second in **Paper III**). Measurements can also be aggregated to coarser time resolution (e.g., per month in the aggregated time series in **Paper I**).

A time series is usually denoted as y_t, where t is the index of time, which usually goes from 1 (first measurement of the time series) to T (total number of measurements).

When modeling a time series, it can consist of several components. In **Papers I–III**, time series or, in some cases (e.g., for particle number concentrations), the log-transformation of a time series, can be written in the form of

$$y_t = \mu_t + \gamma_t + \eta_t + \varepsilon_t \, , t = 1, \dots, T \quad (4)$$

where the measured time series, y_t, is described as the sum of the level, μ_t, the seasonal component, γ_t, the autoregressive (AR) component, η_t, and a random, normally distributed residual component, ε_t. When time series y_t is a log-transformation of the original time series, $\widetilde{y_t}$, then the original time series is a product of those components, $\widetilde{y_t} = \mu_t * \gamma_t * \eta_t * \varepsilon_t$.

The level component, μ_t, describes the long-term changes in the time series that are not cyclic. The seasonal component γ_t describes the cyclic component of a time series. Cyclic components can describe, for example, seasonal variations during the year (**Papers I and II**). The AR component η_t can take into account the dependency of a subsequent

observation (autocorrelation) in a time series. AR component has been used before in atmospheric time-series analysis (Mikkonen et al., 2015). The random component, ε_t, is a residual component that is usually assumed to be normally distributed with a zero mean.

Time-series analysis methods include those described in the papers forming this thesis and contain filtering and smoothing methods to handle the random variability in time series (**Papers III and IV**) and trend estimation methods (**Papers I and II**). Trend estimation is described in more detail in the following subsections.

2.4.2 Sen–Theil and regression methods

The Sen–Theil estimator is a non-parametric method for estimating linear trends in time-series data (Sen, 1968; Theil, 1950). It can estimate the trend in a time series, y_t (e.g., change per year in **Paper I**), by approximating by calculating slopes for all pairs of observations, y_{t_j} and y_{t_i}

$$\frac{y_{t_i} - y_{t_j}}{t_i - t_j} \quad (5)$$

where time points $t_i, t_j \in 1, \ldots, T, t_i \geq t_j$. The trend estimate then becomes the median of those slopes. The method is robust to outliers (i.e., single extreme-values in time series have only a minor effect on the trend estimate).

The Sen–Theil method has become popular in atmospheric sciences (e.g., Collaud Coen et al., 2020; Mortier et al., 2020). In **Paper I**, seasonality was taken into account using the TheilSen function in the *openair* package (Carslaw and Ropkins, 2012) by decomposing the time series using loess (locally estimated scatterplot smoothing, Cleveland et al. (1990)) decomposition, and then by removing the seasonal component, γ_t, before applying the Sen–Theil estimator to the time series, $y_t - \gamma_t$. The calculation of confidence intervals for the trends was based on the bootstrap method (Kunsch, 1989), implemented in the TheilSen function.

The Sen–Theil method is simple and more robust than the ordinary linear regression that has also been used in atmospheric trend studies. Ordinary regression, without any seasonal parameters, does not consider seasonality in the dataset, which can affect the trend estimate. In some studies (e.g., in **Paper II**; Asmi et al. (2013)**)**, multivariate linear regression has been used (in **Paper II** with the generalized linear mixed model, see next paragraph for description), with the predictors representing seasonal variation. Seasonality could be taken into account by having trigonometric seasonal components, based on sine and cosine functions, scaled to the seasonal cycle observed in the time series (see, e.g., Asmi et al. (2013)), using a trigonometric seasonal component with a yearly seasonal cycle, or by using dummy variables (i.e., n indicator variables for each n parts of the seasonal cycle, such as 12 months per year), or in a mixed model, as a random effect for each month that has been applied (e.g. in Mikkonen et al. (2011); **Paper II**).

A generalized linear mixed model (GLMM, McCulloch et al., 2008) was used in **Paper II**, to consider some of the factors affecting the number concentration and consider the variance-covariance structure of the variables used in the model. The model has the form

$$y = X\beta + Zu + \varepsilon, \quad (6)$$

where y is the variable of interest, X is the matrix of fixed covariates, β is a vector of estimated fixed coefficients, Z is the design matrix of random covariates u, and ε is residual term.

In **Paper II**, variables used in the model for number concentration $N_{D,t}$ of size class D at time t were the concentrations of $SO_{2,t}$, $NO_{2,t}$, $O_{3,t}$, global solar radiation $GRad_t$, relative humidity RH_t, and macro-circulation pattern class MCP_t, each measured at time t.

The model in **Paper II** was in the form

$$N_{D,t} = (\beta_0 + \beta_{setup} + u_m) + \alpha_d + (\beta_{WD} * \beta_{NPF}) * X_t + (\beta_1 + v_{1m}) * SO_{2,t} + (\beta_{2,m} + v_{2m}) * NO_{2,t} + (\beta_3 + v_{3m}) * O_{3,t} + \beta_4 * GRad_t + \beta_5 * RH_t + \beta_6 * MCP_t + \varepsilon_t, \quad (7)$$

where β_0 is the intercept, β_{setup} is the estimate for two changes in the measurement setup, u_m is the random intercept for each month m, α_d is the average trend (change/day), β_{WD} is coefficient for work days, β_{NPF} is a coefficient for new particle formation (NPF) event days, X_t is the indicator vector (2*1) for both the work day and event day at time t, $\beta_1, \ldots, \beta_5$ are the fixed coefficients for $SO_2, NO_2, O_3, GRad,$ and RH. Variables $v_{1m}, v_{2m},$ and v_{3m} are random coefficients for SO_2, NO_2, O_3 that are estimated separately for each month. Coefficient β_6 is a vector (1*13) for the estimates of the 13 different MCP classes (13*1). Variable ε_t is a residual term of the model.

2.4.3 Dynamic linear model

The dynamic linear model (DLM) belongs to a class of state-space models (Durbin and Koopman, 2012). State-space models represent measured time series as a group of observed and latent variables that are evolving with time according to certain assumptions about that evolution. The state of the variables is estimated based on assumptions about the variables' evolution and measurements from observed variables.

The DLM describes the evolution of at least one latent variable, μ, that is changing with time. The measurements (observations of y_t) provide information about the evolution of the latent variable(s), with some measurement error, ε_t, which is usually assumed to be normally distributed.

A simple model that has only a latent variable could be written in the form

$$y_t = \mu_t + \varepsilon_{obs,t}, \varepsilon_{obs,t} \sim N(0, \sigma_{obs}) \quad (8)$$

$$\mu_t = \mu_{t-1} + \varepsilon_{level,t}, \varepsilon_{level,t} \sim N(0, \sigma_{level})$$

where time $t = 1, \dots, T$, μ_t is a level, $\varepsilon_{obs,t}$ is a residual for the observations, and $\varepsilon_{level,t}$ is a residual for the level component. The DLM has already been applied in atmospheric sciences to determine trends in temperature and ozone and ion concentrations (Laine et al., 2014; Mikkonen et al., 2015; Sulo et al., 2022).

The DLM model used in **Papers I and II** contained a level with a changing trend (sometimes called a slope), a seasonal component, and an AR component

$$y_t = \mu_t + \gamma_t + \eta_t + \varepsilon_{obs,t},\ \varepsilon_{obs,t} \sim N(0, \sigma_{obs}) \quad (9)$$

$$\mu_t = \mu_{t-1} + \alpha_t + \varepsilon_{level,t},\ \varepsilon_{level,t} \sim N(0, \sigma_{level})$$

$$\alpha_t = \alpha_{t-1} + \varepsilon_{trend,t}\ \varepsilon_{trend,t} \sim N(0, \sigma_{trend})$$

$$\sum_{i=0}^{11} \gamma_{t-i} = \varepsilon_{seas,t}\ \varepsilon_{seas,t} \sim N(0, \sigma_{seas})$$

$$\eta_t = \rho \eta_{t-1} + \varepsilon_{AR,t}\ \varepsilon_{AR,t} \sim N(0, \sigma_{AR})$$

where $t = 1, \dots, T$ is time, μ_t is a level, α_t is a trend, γ_t is a seasonal component, η_t is an AR component, and $\varepsilon_{obs,t}$, $\varepsilon_{level,t}$, $\varepsilon_{trend,t}$, $\varepsilon_{seas,t}$, and $\varepsilon_{AR,t}$ are normally distributed residuals for the observations, level, trend, seasonal component, and AR-component, respectively. In **Papers I and II**, the coefficient ρ for the AR(1) component was not estimated but set to a constant value (0.4 in **Paper I**, 0.6 in **Paper II**). Otherwise, the components were estimated using the DLM MATLAB toolbox (Laine, 2020).

2.4.4 Regression splines

Regression splines (Friedman, 1991) describe a response variable as a piecewise-defined function of the predictors used in a regression model. In the case of linear splines, those functions are piecewise linear regression functions between intervals determined by the endpoints that, in the case of splines, are called knots.

In the case of linear splines, the model can be written in the form

$$y_t = \sum_{i=1}^{n} c_i B_i(x_t) + \varepsilon_t \quad (10)$$

where y_t is described as the sum of the simple basis functions, $B_i(x_t)$, of p predictor variables, x_t (p × 1), each multiplied by an estimated coefficient, c_i. The basis functions, $B_i(x_t)$, are either constant functions giving a value of 1 for each x_t, hinge functions having the form $\max(0, k_{i,j} - x_{t,j})$ for some variable of $x_j, j \in \{1, \dots, p\}$, or a product of several hinge functions that could be dependent on different variables in x (i.e. x_j and x_l, $j, l \in \{1, \dots, p\}, j \neq l$). Parameters $k_{i,j}$ are the knots (i.e., the points where the slope of the piecewise linear regression changes).

In **Paper III**, piecewise linear regression splines were used for time-series data, but without explicit information about the time-series nature of the dataset being used (i.e., all the variables used to model y_t were observed at the same time point t). Both the coefficients of the splines and the locations of the knots were estimated in the fitting process.

The modeling was performed using the *earth* package in R environment (Milborrow, 2023; R Core Team, 2022) with five-fold cross validation used as a pruning method.

2.4.5 Causal discovery and application for the evolution of the multivariate system

Causal discovery can be thought of as a problem where the researcher "wants to know something about the structure of the graph that represents causal influences and we may also want to know about the distribution of values of variables in the graph for a given population" (Spirtes et al., 2000, p. 73). For **Paper IV**, we wanted to know the (not visible) structure of measured variables that could explain the evolution of the emissions. That is, the goal was to find the structure of the variables and the causal effects of the variables on each other. The structure and effects, with knowledge of the current state (see μ_t in Subsection 2.4.1) of the environmental chamber, would explain what would happen next in the chamber (i.e., changes in the state of the chamber).

A causal structure is a structure that contains all the information about the causal connections (edges) of the variables describing a phenomenon (see Figure 2 as an example of a simple causal structure). How the variables are causally connected can be indicated based on this structure (i.e., if variable X changes, does it change the expected outcome of variable Y?). For **Paper IV**, the causal structure described the connections between different emissions components measured in a laboratory chamber. If there were changes in the current state of the chamber (e.g., if the amount of a gaseous compound in the chamber was to be increased), the structure would indicate all the variables that might have been affected by that increase.

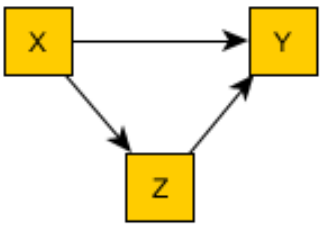

Figure 2. Example of a causal graph for three (observed) variables—X, Y, and Z. The variables are represented by yellow squares. The arrows represent the directional edges between the variables. Here, Variables X and Y are causally connected, as described by a directed edge from X to Y (X → Y). The arrow also describes the direction of causation (i.e., a change in X could also change the outcome of Y, but not vice versa).

There are several causal discovery algorithms that could be applied to search for causal structures based on the dependencies of the variables in the measured data. The PC

algorithm (Spirtes et al., 2000) was applied in **Paper IV**, based on the conditional independency tests of measured variables. In brief, the causal structure is formed by starting from a graph where, between every pair of variables, there is an undirected edge. The edges are removed from the graph based on conditional independences until this is no longer possible. After that, the edges are ordered based on predetermined rules for the ordering. The model version implemented in the R package *rcausal* (Wongchokprasitti, 2019) includes some tuning parameters (alpha and depth) that were used in the modeling in **Paper IV**. Alpha represents the significance limit used for the dependency, and depth is the upper limit for the nodes conditioned in the search (see subsection 2.2.1 in **Paper IV** for details).

Causal discovery algorithms have been previously applied in atmospheric sciences, such as in exploring causal networks in biosphere–atmosphere interactions in simulated datasets and two measured datasets (Krich et al., 2020), discovering spatial and temporal causal relationships in ocean surface pressures (Runge et al., 2015, 2019), and determining causal relationships at different spatial scales (planetary, synoptic) of atmospheric disturbances in geopotential height data (Samarasinghe et al., 2020).

In **Paper IV**, we applied PC algorithm from the R package *rcausal* (Wongchokprasitti, 2019) to search the structure between the initial state of the chamber (i.e., measured concentrations of different particle properties of the gases, such as number and masses of factors from mass spectrometers) and the observed change in the next time step, $\Delta(x) = x_t - x_{t-1}$, where x_t is the variable the evolution of which we were interested in. It and the obtained causal structure were used to estimate the dependencies between the observed change $\Delta(x)$ and the direct causes of the change in the structure using linear regression

$$\Delta(x_{j,t}) = \beta_0 + \beta_1 x_{1,t} + \beta_2 x_{2,t} + \cdots + \beta_{ik} x_{i,t} x_{k,t} + \cdots + \varepsilon_{j,t} \quad (11)$$

where $\Delta(x_j)$ is the observed change in variable j, t is time, β_i represents the regression coefficients, x_i represents the measured variables, and $x_i x_k$ are the interaction variables (i.e., product of two measured variables—see subsection 2.2 in **Paper IV**). The regression coefficients $\beta_0, \beta_1, \ldots$ are estimated separately for each variable $\Delta(x_j)$.

After estimating the dependencies, the evolution of the system was calculated using the *deSolve* package (Soetaert et al., 2010). The best model (among different tuning parameter pairs) was selected based on the calculated root-mean-square error from the evolution.

3 Results and discussion

3.1 Long-term trends of particle number-size distributions from European measurement sites

Papers I and II presented the long-term trends in particle number-size distributions from European measurement sites. In **Paper I**, trends in all the modal parameters (mean geometric diameter D_p, geometric standard deviation σ, and particle number concentration N) were studied from 21 measurement sites. In addition to the total number concentrations, the idea was to determine if the other mode parameters had changed during the long-term measurements.

It was found that the N were, on average of all sites, decreasing in all the modes. Figure 3 shows the trends calculated for the different mode parameters for the fitted nucleation, Aitken, and accumulation mode particles. For the Aitken and accumulation mode, the particle number concentrations had been decreasing at most of the measurement sites. For some of the sites, there was some decrease in diameter as well, but the absolute value of the trend (percent per year) was usually smaller than for the particle number concentration. The standard deviation had the smallest absolute values for the trends at almost all sites for all modes. For the nucleation mode particle number concentration, there were both decreasing (mostly southern sites) and increasing (mostly northern sites) trends observed. However, for most of the increasing trends, the confidence interval of the trend also included zero. Some of the particle number concentration trends in the nucleation mode were also paired with an opposite trend in diameter (i.e., the particle volume of the mode was not affected as much as the particle number concentration). Based on the results from the DLM, the trends were not monotonic, and the magnitude of the decrease or increase could change (see Figures 3, S7, and S8 in **Paper I**). Usually, the particle number concentrations and the mean diameters had short time periods when the decrease or increase was steeper. Common time periods of steep decreases or increases occurring at sites located in the same large area (e.g., a country) or at sites of the same class were not found. In **Paper I**, the reasons for the non-monotonic trends were not speculated. Some possible reasons for the non-monotonic trends are year-to-year variation in other meteorological parameters that affect the transportation of emissions to the sites and/or local emissions and momentary changes in transported and/or local emissions. However, as the changes in trends were not common in large areas such as country, the changes in meteorological parameters over a larger area or the momentary changes in transported emissions from afar are not as likely as other reasons.

In **Paper II**, the particle number concentration trends from the Budapest measurement site for different size classes were studied. The particle number concentrations of the particle size classes 6–1,000 nm ($N_{6-1,000}$), 6–100 nm (N_{6-100}), 25–100 (N_{25-100}), and 100–1,000 nm $N_{100-1,000}$ were analyzed. Figure 4 shows the estimated level, μ_t (see subsection 2.4.3 for the DLM), for particle number concentrations in different size classes in Budapest

between 2008 and 2018. The mean changes (in percentage per year), estimated by the DLM, were between -3 (for $N_{100-1,000}$) and -6 (for N_{25-100}) and by generalized linear mixed model (GLMM), the changes were between -5 (for N_{6-100}, N_{25-100}, and $N_{6-1,000}$) and -8 (for $N_{100-1,000}$).

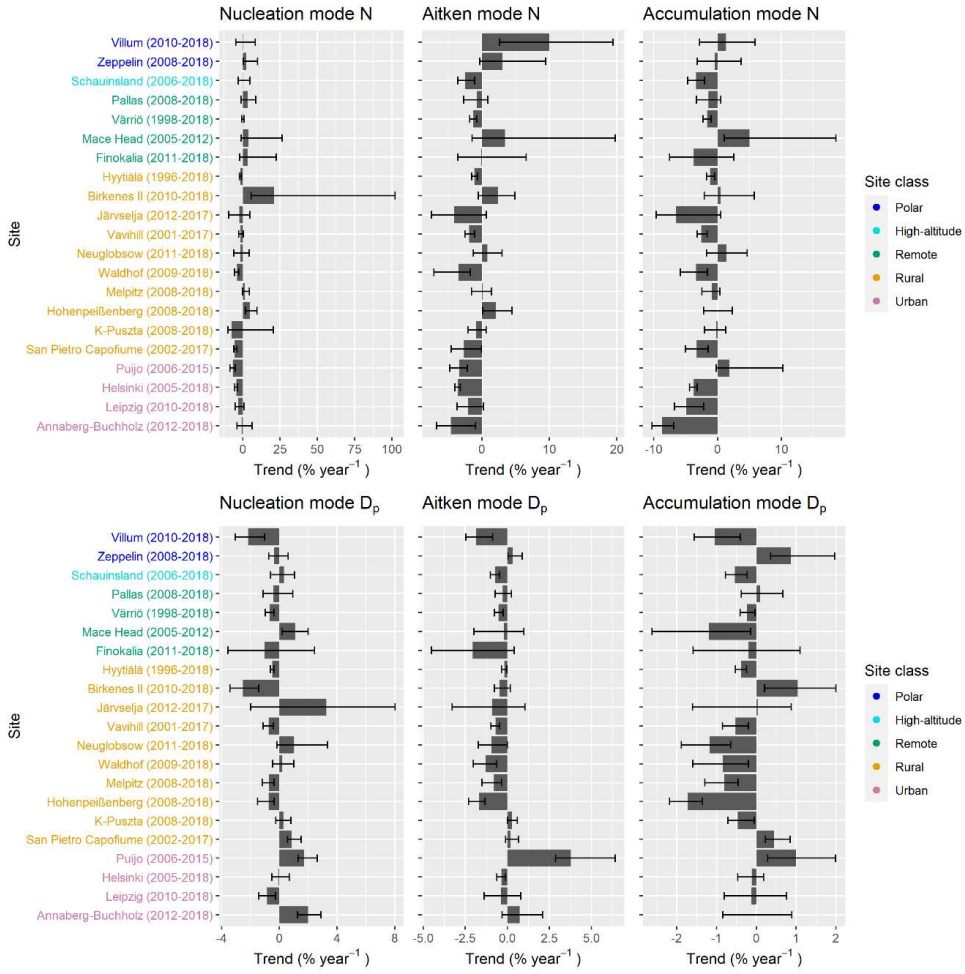

Figure 3. Long-term trend estimates for particle number concentration N and mean geometric diameter D_p, in the nucleation (NuclM), Aitken (AitM), and accumulation (AccM) modes. Confidence intervals for the trends are shown with whiskers (95% confidence level). The Sen–Theil estimator was used to calculate the trends and the trend estimates are complemented with bootstrap confidence intervals (see subsection 2.4.2 above). Figure adopted from **Paper I**.

The results of **Papers I and II** concerning the decreasing trends are in agreement with each other, even though the studied size classes were not the same. The results in **Paper II** are

somewhat comparable to those in **Paper I**, with the N_{25-100} size class being close to the Aitken mode in **Paper I** and $N_{100-1,000}$ being close to the accumulation mode in **Paper I**. For the urban sites in Central Europe (Leipzig and Annaberg-Buchholz) in **Paper I**, the trends for the Aitken mode were -2.1 and -4.6% year^{-1}, respectively, whereas for Budapest, the N_{25-100} trends were -6 (DLM) and -5 (GLMM) % year^{-1}. The accumulation mode trends for Leipzig and Annaberg-Buchholz were -4.9 and -8.7% $year^{-1}$, respectively, and for Budapest, $N_{100-1,000}$ was -3 (DLM) and -8 (GLMM) % year^{-1}.

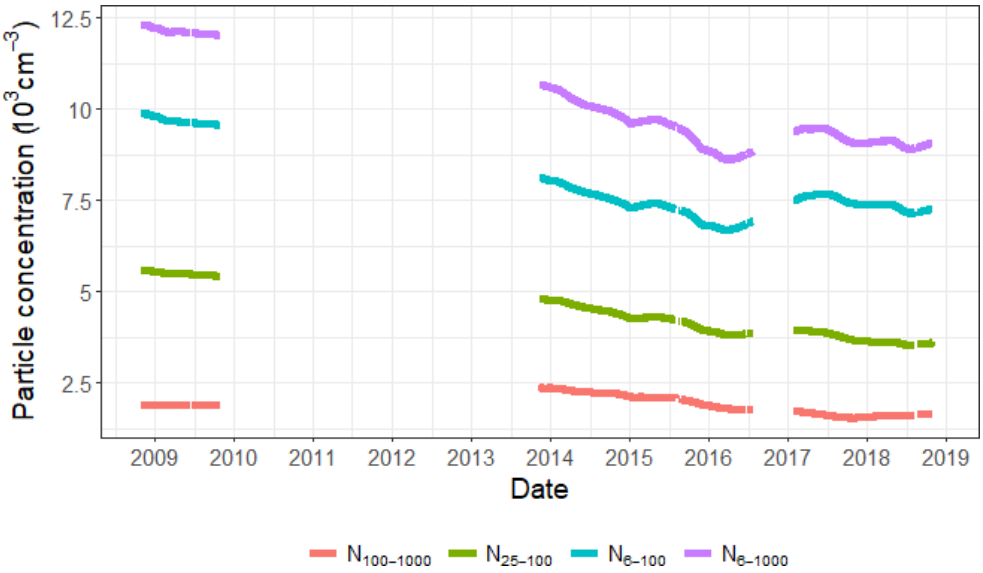

Figure 4. Trends in particle number concentration bins in the diameter ranges 6–100 nm (N_{6-100}), 25–100 nm (N_{25-100}), 100–1,000 nm ($N_{100-1,000}$), and 6–1,000 nm ($N_{6-1,000}$) for the Budapest measurement site. The trends were derived by DLM. Figure adopted from **Paper II**.

The origins of the decreasing trends in particle number concentrations in both papers were not identified. For the trends observed in **Paper II**, it was concluded that the likely reason for the observed decrease was decreased anthropogenic emissions in Budapest. The decrease was likely caused by decreasing traffic emissions, but also residential and household heating might have contributed. For **Paper I**, the reasons for the decreasing trends were not largely speculated on because the composition of the particles was not studied. It was also speculated in **Paper I** that the decreases in urban sites could be caused by decreasing anthropogenic emissions. Decrease in anthropogenic emissions in urban areas is caused by tightened air quality control. Rural and remote sites were not as dominated by anthropogenic emissions as urban sites. It was supposed that the central European rural and remote sites would on average have a larger contribution of anthropogenic emissions via transportation of emissions from the urban areas than the northern sites, due to denser incidence of large urban areas. For rural and remote sites, biogenic emissions also have significant contribution

to the total particle number concentrations. Hence the variation in factors affecting the emission factors of biogenic emissions, such as the meteorological parameters, can influence the trends. The environments of the sites, as well as the origins of the particles at the different measurement sites varied; hence, searching for the exact reasons for the decreases was outside of the scope of this model comparison study.

3.2 Climate models for estimating particle number concentration trends and seasonality

In **Paper I**, the observed trends and seasonality of the particle number concentrations were compared with climate model results. In Figure 5, the trend results are shown for the Aitken mode particles. In line with the observations, the models also showed mainly decreasing trends for the Aitken mode. The modeled trends also showed decreases for the other modes for most of the sites. The mode representations (see figures in the supplement of **Paper I**) showed that the fitted modes, modal representation calculated for the modal models, and sectional representation calculated for the sectional model produced relatively similar results to the trends. All observational trends for Aitken model in all three representations were statistically significant, except for Zeppelin, Pallas, Mace Head, and Melpitz. For modeled trends, most of the decreasing trends for rural and urban sites were also statistically significant, whereas for remote, high-altitude, and polar sites, the modeled trends were not significant.

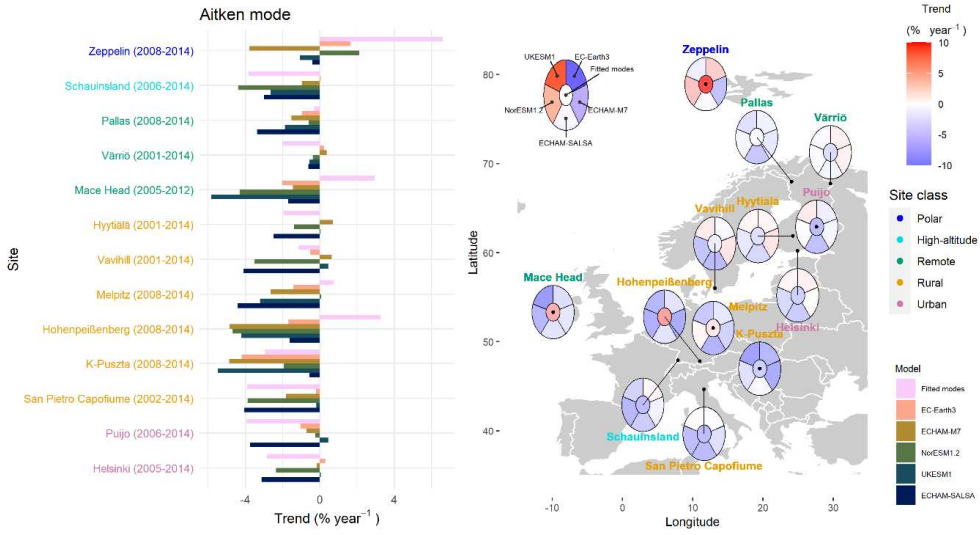

Figure 5. Long-term trend estimates for Aitken mode particle number concentrations from measurement sites and climate models. (a) Bar plot illustrating trends at different sites. The sites (*y*-axis) are arranged by site class (color–see legend on the right-hand side of the figure) and within one site class mostly from north to south. (b) Map showing estimated trends. The

trends in both figures were calculated using the Sen–Theil estimator. Figure adopted from **Paper I**.

Most of the time, the models correctly represented the sign of the particle number concentration trends. However, it was found that, on average, the absolute value of the (often decreasing) trend was underestimated in the models.

For the seasonal representation of particle size distribution, the models had more differences. Figure 6 shows the seasonal cycle for the Aitken mode represented by all models and mode representations. The Aitken mode summarizes the model representation also seen for the accumulation mode relatively well. The seasonal representation of the climate models was divided into two. For EC-Earth3 and NorESM1.2, the shape was relatively consistent for all measurement sites, although the concentration levels could vary between sites. For the other models—ECHAM-M7, ECHAM-SALSA, and UKESM1—the shape of the seasonal cycles varied between measurement sites. For the northern sites, the shape of seasonality in the Aitken mode was such that, largest modeled particle N were during spring or summer, whereas smallest N were observed than in summer, autumn, or winter. The shape of seasonal cycle was not as clear for the southern measurement sites. The shape of the measured seasonal cycles also varied between the northern and southern sites.

Other than the variability in the shape of the seasonal cycles between the northern and southern measurement sites, there were some differences observed in the shape of the single measurement sites (see Figure 6) between measurements and modes. Differences were observed in the magnitude of the seasonal cycles and the levels of particle number concentrations from single measurement sites.

In summary, the modeled trends for number concentrations of modes were close to measured in most cases. Some differences remain between measurements and climate models in terms of particle number concentrations and size distributions represented at the ground level. The exact reasons for the differences were not defined in **Paper I**. However, it was thought most likely that the differences were caused by multiple different processes in the models, and it was suggested that the differences between the individual aerosol processes (e.g., aerosol deposition, microphysics [e.g., nucleation parametrization], and transportation) in the models should be characterized in more detail in the future.

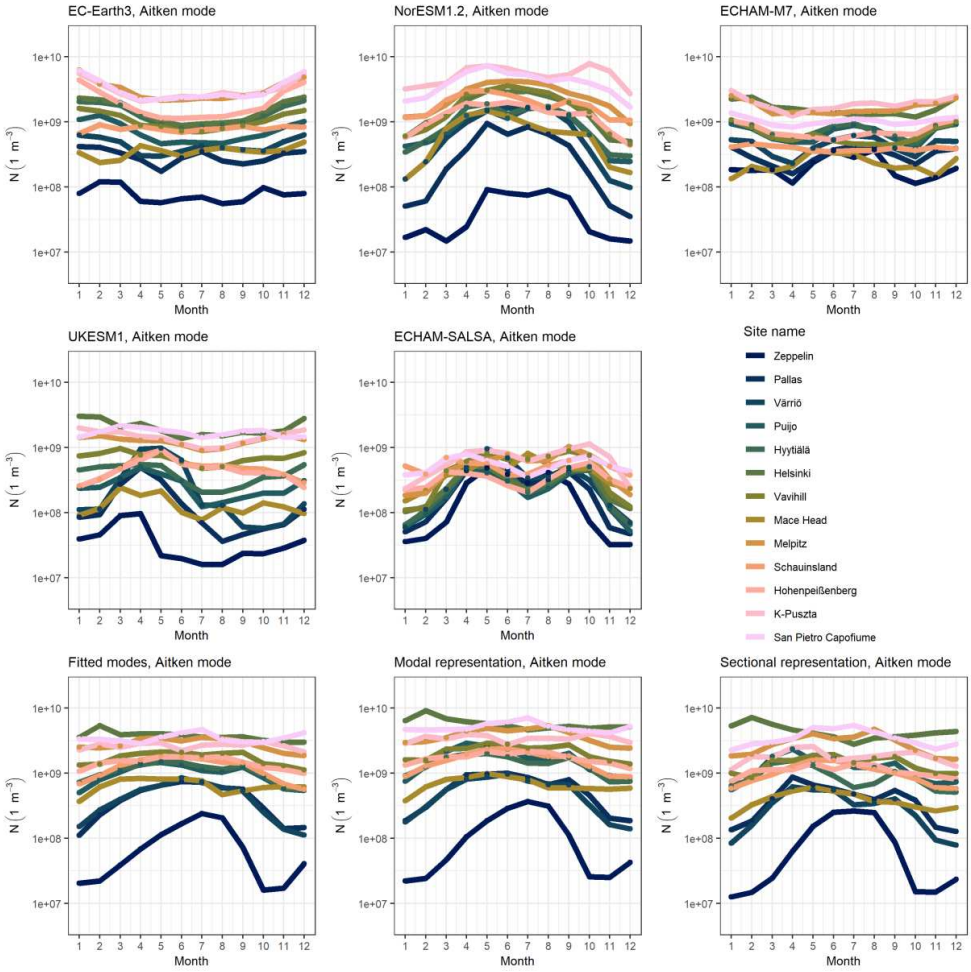

Figure 6. Aitken mode seasonal representations from measurements and climate models. The subplots represent the seasonal cycle of one model or measurement representation. The colored lines represent the medians of the monthly means for the Aitken-mode particle number concentrations for different measurement sites. The sites are arranged from most northerly to most southerly. Figure adopted from **Paper I**.

3.3 New methods for estimating the emission factors of passenger vehicles

In **Paper III**, the EFs (i.e., the total emissions per kilometer) of passenger vehicles were studied using chase measurements (see subsection 2.2.3 above for an explanation). Current methods used to estimate the EF of a vehicle from chase measurements assume that the whole emission (particles, gases) is diluted equally by CO_2.

In **Paper III**, we wanted to check whether the DR could be modeled based on other variables than CO_2 from the chase measurements. In this thesis, the results relating to the method based on multivariate adaptive regression splines (MARS) are introduced in more detail. Discussions related to other methods can be found in **Paper III**.

In **Paper III**, we modeled the DR based on CO_2 by predicting it using several other variables. Two MARS models for DR were created, one—MARS-OBD—with all the variables from chase measurements, i.e., on-board diagnostics (OBDs) of the measured passenger vehicle and variables measured in the ATMo-Lab (for ATMo-Lab, see Subsection 2.2.3 above). The other model—MARS–chase—excluded the OBD variables and used only variables measured in the ATMo-Lab. The variables used in the final model were selected based on the fit of the model. The splines for the data from all the measurement drives and vehicles are shown in Figure 7. The results show that, in the MARS–OBD model, two variables were needed to explain the DR, and in the MARS–chase model, the number of variables was three. From all the possible variables to explain the DR, exhaust flow rate (Q) was the most important in the MARS–OBD model, while lateral (with respect to the direction of travel) wind had a small effect. In the MARS–chase model, Q was replaced with speed change (i.e., acceleration), speed of the car, and altitude change, indicating whether the car was going uphill or downhill.

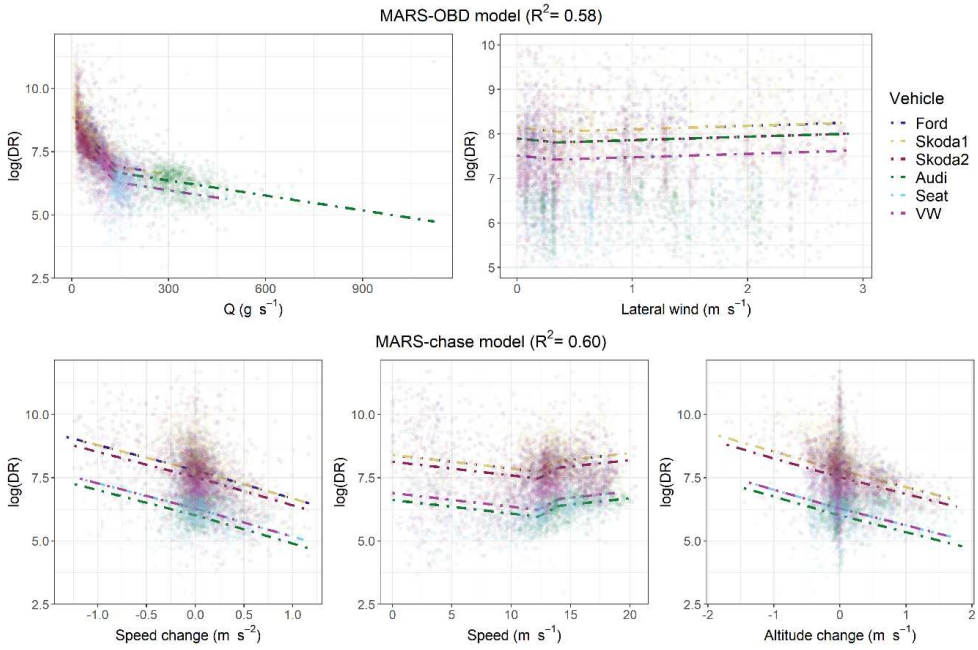

Figure 7. MARS fits for the logarithm (natural) of the DR. Variable in y-axis shows the logarithmic values. The figures show the relationships between the variables used in the model and the DR from the observed data. Upper row: variables used in the MARS–OBD model, lower row: variables used in the MARS–chase model. The colors of the measurement points and modeled dependency (lines) are based on the vehicles. Note that some of

the lines (Ford and Skoda1, Skoda2 and Audi, and Seat and VW) overlap with each other in some of the plots. Figure modified from **Paper III.**

The methods for calculating the EF were compared for the whole drive (see **Paper III**) and for the downhill section only. The downhill section was interesting because it was assumed that CO_2-based methods would work insufficiently in these sections due to smaller CO_2 emissions produced in engine braking compared to other sections. Particles could still be produced, however, from the brakes during downhill travel.

Figure 8 shows the results for the downhill section for two passenger vehicles (Seat and Skoda 2) and two drives per vehicle. For the Seat, the different methods gave relatively similar EFs. For the Skoda 2, there were more differences observed between the methods. As a conclusion, it could be said that the new methods (MARS, plus NWD, which is introduced in more detail in **Paper III**) performed relatively well in both cases, when compared to methods already in use. However, the correct EFs remain unknown, so the best method cannot be identified based on this analysis.

To summarize the results of **Paper III**, the new methods calculating EF for number of particles worked relatively similarly to other methods, such as N_{raw}. The N/CO_2 RRPA (robust regression plume analysis, see the supplement of **Paper III** for details) and N/CO_2 linear most likely give lower EF values due to uneven emissions, which then lead to uncertain linear fits of N and CO_2.

The N_{raw} method has its problems with downhill travel, with high DRs sometimes being estimated, and this resulted in high EFs for some time points. The EFs from the N/CO_2 integral and new methods (MARS–chase, MARS–OBD, and NWD) were between those of previously mentioned models. This was not a surprise because the DR used as a response variable in both MARS methods was based on the CO_2 type of DR that was used in the N_{raw} model (Wihersaari et al., 2020). The results for the newest vehicle (i.e., the model based on data from other cars used to model a vehicle) showed that more vehicle data about the dilution would be beneficial, especially for the MARS–chase model, before it can be used to estimate the EF of a random car from chase measurements, such as those measured by Olin et al. (2023).

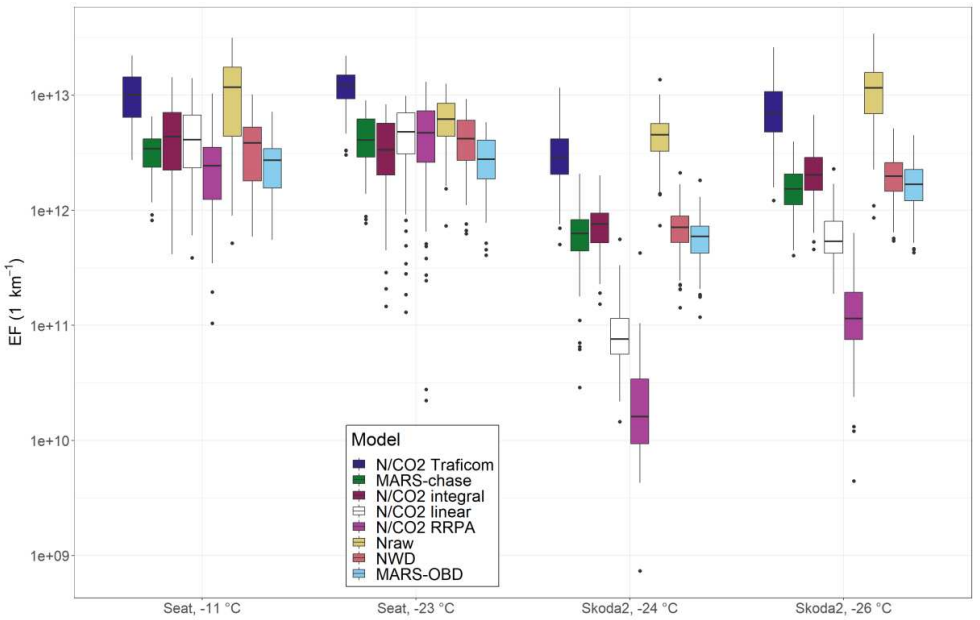

Figure 8. EFs for the > 23-nm particles from the Seat, hot-engine drives and Skoda 2, hot-engine drives except Seat –11 C that is with the subfreezing–cold start, and Skoda –26 C that is with the preheated–cold start. EFs are for downhill sections only, for 100 bootstrap samples. Note the logarithmic y-axis. MARS–OBD and MARS–chase are distinguished by the light blue and green colors, respectively. Other methods shown in the figure were previously used to estimate EFs, in addition to the NWD, which is described in **Paper III**. See subsections 2.3.1–2.3.7 in **Paper III** for a detailed description of the other methods. Figure adopted from **Paper III**.

3.4 Evolution of wood combustion emissions in the atmospheric chamber

The evolution of combustion emissions has previously been modeled using, for example, the statistical oxidation model (SOM) and MCM. The SOM (Cappa and Wilson, 2012) models the evolution of average volatility and the oxygen (O)/carbon (C) emissions ratio, and the aerosol yield. The MCM (Saunders et al., 2003) describes the evolution (they called it degradation) of the VOCs, with near-explicit presentation. In **Paper IV**, we attempted to formulate a model that would be relatively simple but would be able to describe this evolution in a laboratory chamber. Optimally model would also tell something about the dependency structure of the measured variables from the chamber, such as what measured variables would explain the evolution seen in the chamber, without using explicit information about the phenomenon. The evolution of the particle number concentrations and the chemistry parameters of the particles and gases were modeled based on data from the observed evolution of wood combustion emissions under atmospheric-like conditions and given certain

general information about the potential dependencies (see Table 1 in **Paper IV**). The information level concerned mostly classes of variables (e.g., particle size classes, particle chemical composition, and gaseous variables), such that, for the particle size class variables (nucleation, Aitken, accumulation, and coarse modes) representing the particle number concentration, the only predictors allowed were the other size class variables, although the exact predictors for each size class variable were not defined.

A relatively simple model for describing the evolution in the chamber was formulated in **Paper IV** by first searching the relevant predictors for the evolution of the change in each variable using a causal discovery algorithm (Wongchokprasitti, 2019) and information about the potential dependencies, and then modeling the effect of each predictor on the change in each variable (method described in subsection 2.4.5 above). Separate models were created for the dark and photochemical evolutions of the emissions because the oxidation chemistry differed between those. For dark aging, the oxidation is dominated by O_3 and nitrate (NO_3), whereas photochemical aging is dominated by OH radicals (Hallquist et al., 2009; Tiitta et al., 2016).

This method (see subsection 2.4.5 above) was applied to wood combustion evolution data. Figure 9 shows the modeled relations for the particle size-class number concentrations (nucleation mode [NuclM] < 25 nm, Aitken mode [AitM] 25–100 nm, accumulation mode [AccM] 100–300 nm, and coarse mode [CoarM] > 300 nm) in the case of photochemical evolution. Particle size-classes were selected as an example here because the relationships of particle size classes were known in detail beforehand. Hence it is easy to compare the modeled structure for the known dependencies. For the particle size–related variables, most of the relationships were as expected, with both the variables explaining the change in particle number concentrations in specific size classes and the sign of the effect (positive or negative). Examples of the presumably correct positive edges are those relationships where the interaction between two particle size classes is increasing the concentration of the larger particle size class (e.g., NuclM*AitM -> AccM, AitM*AccM -> AccM). As one particle from a smaller and one particle from a larger size class collide to form one particle, the resulting particle belongs to the size class of the initially larger particle, or to a size class containing even larger particles. Hence, if the number of smaller and/or larger particles increases, this results in more coagulation, and that increases the number of particles in the larger size class (at least when interactions with particles from other size classes are not considered). Similarly for negative dependencies, the relationships that decrease the number of smaller particles (e.g., AccM*CoarM -> AccM) are likely due to a decrease in the particle number concentration of smaller particles in the coagulation. However, reactions such as CoarM -> AccM (i.e., the number of coarse mode particles in the chamber should increase the change in number of accumulation-mode particles) are not obvious in a physical sense because a higher number of larger particles might cause more coagulation.

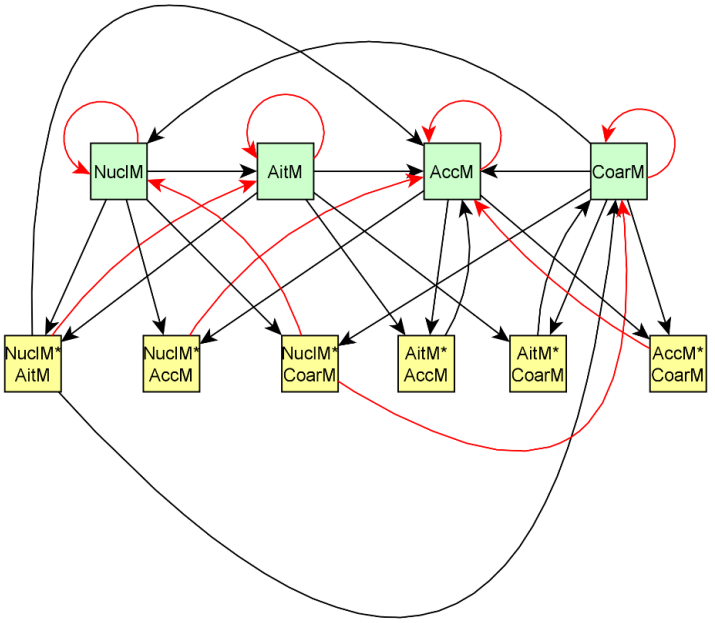

Figure 9. Particle size related part of the modeled causal graph for photochemical aging experiments. The particle size related variables (nucleation mode [NuclM], Aitken mode [AitM], accumulation mode [AccM], and coarse mode [CoarseM]), which also represent the changes in those variables (caused by the predictors), are highlighted in green. Yellow squares represent the interaction variables, which are only used as predictors for changes in variables. All variables shown in this figure were measured by SMPS. The colors of the arrows represent the sign of the effect (i.e., black arrows—positive coefficient [i.e., a larger number of predictors indicate that the change is more positive] and red arrows—negative coefficient). Figure adopted from **Paper IV**.

The model describes the evolution of different variables relatively well (also, see Figure 10 for the coarse and accumulation mode particle number concentrations from the photochemical aging experiments). However, it should be mentioned that the strengths of the dependencies were estimated from the same data (i.e., a division of data into learning and validation data was not done because the number of data points per aging type was relatively low for so many variables). Hence, validation of the performance of the model was partly done based on the simulated datasets.

The structure provided by the causal discovery algorithm was based on the dependencies obtained from the dataset. Based on the measurement data alone, and because the dependency structure of the measured variables from the wood combustion dataset was not completely known (some prior information was used, as described in subsection 2.2.1 in **Paper IV**), we could not confirm whether some dependency was causal or not. Using artificial simulated data, where all the dependencies were known, we tested whether the causal

discovery algorithm could find the correct edges. Most of the edges found by the algorithm were either correct or the predictor variable was at least highly correlated (with the mean correlations between correct and incorrect predictors being above 0.8 in most cases for the simulated data).

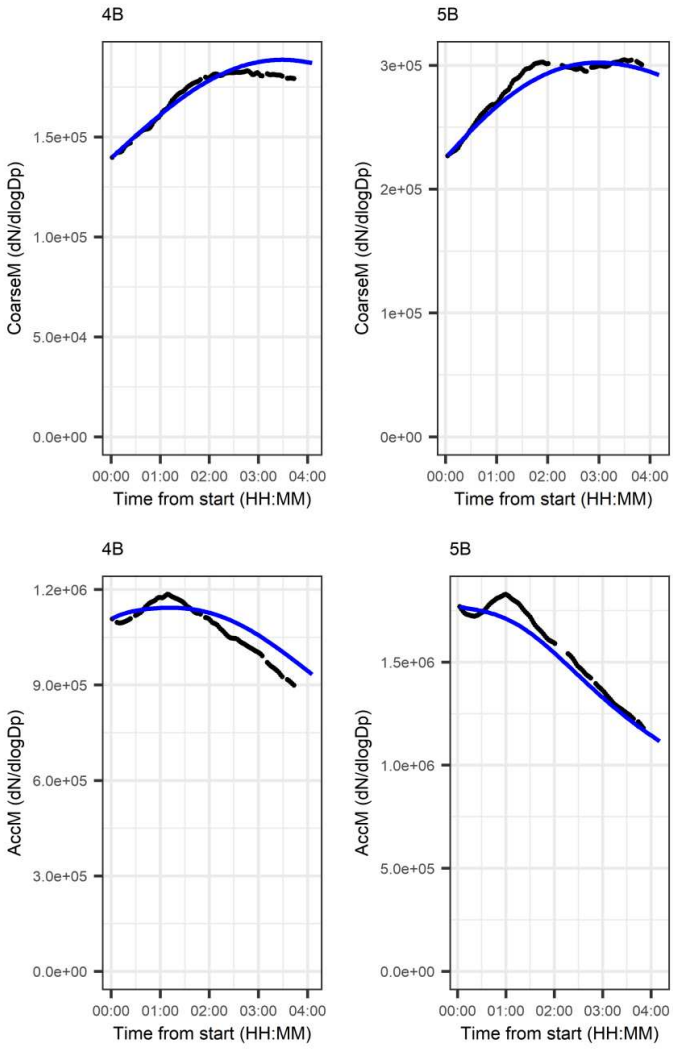

Figure 10. Evolution of the particle number concentrations of coarse (CoarseM, >300 nm, top row) and accumulation (AccM, 100–300 nm, second row) mode particles in two photochemical aging experiments (4B—left column with fast ignition, 5B—right column with slow ignition; a more detailed description of the differences in ignition type was beyond the scope of this thesis). Black points represent the filtered time series (see Subsection 2.1.2 in **Paper IV**) of the variable, and the blue line shows the modeled evolution of the same variable. Figure adopted from **Paper IV**.

To conclude, more data would be beneficial for verifying the modeled structure and the strength of the dependencies. Based on the simulation results (in the supplementary material in **Paper IV**), it was decided that some of the dependencies found by the algorithm were not the real causes of the changes in the measured variables. In this kind of case, where the dependency structure of the variables is not known beforehand, the data is also the main source of information about the dependencies.

This study works as a proof-of-concept for the application of method in this kind of dataset. Even though the exact dependencies for the studied data are not known, the results from the models can be used as a starting point for more detailed analysis of certain unknown dependencies amongst variables used in the model.

4 Review of papers and the author's contributions

Paper I reported an investigation of the long-term evolution of aerosol particle number concentrations from ground level measurement sites and the representation of the evolution in climate models. We found that the number of particles was decreasing, especially in the Aitken and accumulation modes, and that the models showed decreasing trends that were lower in terms of absolute values than the observed. I performed most of the data analysis and, with the co-authors, interpreted the results and had the leading role in writing the initial draft.

Paper II presented a study on the trends in particles and gaseous compounds, and the seasonal and diurnal cycles of the particles, in a long-term measurement dataset from Budapest. We found that the particle number concentration was decreasing, and that a statistical model was able to explain most of the variability in the particle number concentrations by using predictor variables, such as gas concentration macrocirculation patterns. I performed the trend analysis using a dynamic linear model and participated in writing up the results and commenting on the manuscript.

Paper III was a comparison of the emission factor calculation of passenger vehicles using methods from previous literature and two new methods developed and introduced in this study. We found that, in some sense, it was possible to predict the dilution ratio of the emissions without using CO_2 measurements. I participated in the measurements, performed a major part in the data analysis, including taking a leading role in developing the MARS methods, participated in interpreting the results, and had a leading role in writing the initial draft.

Paper IV studied the potential of the causal discovery algorithm and statistical modeling to model the evolution of wood combustion emissions in an atmospheric chamber. We found that the model was able to represent evolution. Based on the simulations, the dependency structure contained both correct causal dependencies and dependencies where the predictor was correlated with the correct cause. I did most of the data analysis and had a lead role in writing the initial draft. I also interpreted the results together with the co-authors.

5 Conclusions

The aim of this thesis was to apply statistical models to long-term trends of particle number concentrations and investigate how the estimation of emissions from wood combustion and passenger vehicles could be improved using statistical models. It was shown how the aerosol concentrations at the measurement sites evolved (**Papers I and II**), how the climate models were able to reproduce the long-term evolution of aerosol concentrations (**Paper I**), and how the EFs of the passenger vehicles (**Paper III**) and the evolution of residential wood combustion emissions (**Paper IV**) could be modeled. The studies were mostly focused on the aerosol size distribution; however, in **Papers II and IV**, other variables related to size distribution and emissions evolution were also considered in the models (mixed model in **Paper II**).

In this chapter, the research objectives, and how these were fulfilled, are summarized point by point, followed by a short summary of the potential future improvements that could be made in terms of the research topics addressed.

1) *To understand the trends in the particle number concentrations and size distributions of aerosol particles in Europe during the last 20 years (**Papers I and II**) (**Papers I and II**)*

The particle number concentrations were found to be decreasing at most of the studied sites and in most of the modes (i.e., nucleation, Aitken, and accumulation). The relative decrease was stronger for sites and site classes that had initially higher concentrations (i.e., sites classified to urban and rural categories). Some of the changes in mode number concentrations were connected to changes in opposite sign in mode geometric diameter. Hence, the particle volume did not always change as much as may have been indicated by the change in particle number concentration alone. The geometric standard deviation of the mode did not change much. The decreasing particle number concentration trends observed were in line with the findings of an earlier study (Asmi et al., 2013). The nucleation mode showed the greatest variation between sites in terms of the relative change in particle numbers. Based on the results from the DLM model (see Figures 3, S7, and S8 in **Paper I**), there were no clear time periods when the particle number concentrations decreased simultaneously across wide areas. Instead, these decreases were observed to happen both relatively evenly during the measurement period and more often during shorter periods than in the whole measurement period. In **Paper I**, both the Sen–Theil method and DLM suggested that some changes in the particle number concentrations were related to opposite changes in the mode geometric mean diameter (i.e., the decrease in particle number concentrations could have been compensated for by an increase in their geometric mean diameter, and vice versa).

2) *To determine whether the observed evolution of the particle number concentrations–size distributions was being captured in the climate models (**Paper I**)*

The models were mostly able to capture the sign of the change in particle number concentrations, although the absolute values of the trends—especially seasonal trends—were

sometimes underestimated. This might be related to the levels of the number concentrations, that were also underestimated some of in the models (see Figure 6). The seasonal shapes of the particle number concentrations in the models differed from the measured ones. The models also showed differences in seasonal representation. The reasons for the differences were not analyzed further in **Paper I**. As the anthropogenic emissions were the same in all the models, the differences are likely to be related to biogenic emissions, the transportation of aerosols, or the distribution of emissions in different size classes. Also, variations in the grid boxes in the models might explain part of the differences in the model results.

For objectives 1) and 2), the studies were mostly limited to descriptions of the evolutions, without characterizing the causes behind the evolutions. In **Paper II**, presenting the trends from Budapest, it was suggested that a decrease in vehicle emissions might have affected the concentrations in Budapest. However, this was not supported by studying the chemical compositions of the particles over time. In the comparison study in **Paper I**, detailed causes related to the measured trends were not identified. For the measurement–model differences, it was suggested that microphysical and depositional processes affecting the long-range transport should be considered in more detail. Differences in the single measurement–site trends, in terms of measurements and models, were not studied further. For those differences, apart from the reasons mentioned above, site-specific characteristics, such as local sources for the emissions and changes in air-mass trajectories, could have affected the results. Hence, it is suggested that, for those comparisons, a smaller number of measurement sites (e.g., from a single country or measurement network, such as the German measurement network GUAN, Birmili et al. (2016)) should be considered, and specific knowledge about the site characteristics should be collected, to be able to focus on the differences.

3) *To understand the differences in calculation methods of EFs for vehicle emissions, and to develop new methods for EF calculation (**Paper III**)*

Three new methods (MARS–chase, MARS–OBD, and NWD) were constructed to model the DR, and then provide an estimate of the EF. All new methods need training data to formulate a model. The DR is dependent on the variables, such as exhaust flow rate and speed, but also the shape of the rear.

The new methods worked relatively similarly to the methods used in the previous literature. During most of the drives, the vehicles produced CO_2. During those times, the new methods were fitted to the DR of the N_{raw} method (one of the old methods), and so the EFs for those times were close to those from the N_{raw} method. The main difference in the EF calculations came from the times when the vehicles were not producing CO_2, or the times when the modeled DR was far from the DR calculated based on CO_2.

As mentioned in **Paper III**, by increasing the number of drives and vehicles measured, the DR models could provide more accurate information for the vehicles that were not used in the model training dataset. This would enable the models to be used online (i.e., for calculating the EF quickly after the data has been collected) and, in the case of the MARS–chase model, this would not require OBD data, where there is no connection to the chased vehicle.

These methods have the potential to be extended to non-exhaust emissions. However, for these, several aspects still need to be evaluated before the method can be applied. For example, the dilution of non-exhaust emissions, such as particulate emissions from brakes and tires, has a different dilution pattern than the emissions from the tailpipe because the location of the emissions source is different (i.e., location of the tailpipe vs. the brakes or tires).

4) *To model the evolution of aerosols in an atmospheric chamber and to study the dependencies of the variables measured from the small-scale residential wood combustion emission (**Paper IV**)*

The evolution of the aging of residential wood combustion emissions was modeled using laboratory chamber measurements. The model was presented in detail in **Paper IV**. A causal discovery algorithm was used to select potential dependencies between variables, and the structure used in the model was based on those. Then, the strength of each dependence was estimated, before estimating the evolution of the whole measured system (i.e., the evolution of all the variables).

The time evolution of the variables measured using the atmospheric chamber was mostly captured by the model. Based on the simulation results, assumptions we had related to the variable relationships in the chamber dataset, some of the edges in the modeled structure were not causal. Instead, some of the predictors of the changes in the variables of interest were correlated with the correct causes. This is probably due to the nature of the predictor selection process (causal discovery algorithm + LASSO), where the potential of some variable to explain a change in the variable of interest is related to the correlation of the potential predictor to the change in the variable of interest (i.e., the causal discovery algorithm) and the dependence of the potential predictor on other potential predictors (i.e., via the limitation of the absolute sum of coefficients in LASSO).

For both emissions models (passenger vehicles, residential wood combustion) in objectives 3) and 4), increasing the number of datasets (i.e., drives with different vehicles and number of experiments in case of wood combustion) would enable better validation of the model, and would most probably increase the accuracy of the structure in residential wood combustion and in terms of the concentration/EF in both models.

References

Aalto, P., Hämeri, K., Paatero, P., Kulmala, M., Bellander, T., Berglind, N., Bouso, L., Castaño-Vinyals, G., Sunyer, J., Cattani, G., Marconi, A., Cyrys, J., von Klot, S., Peters, A., Zetzsche, K., Lanki, T., Pekkanen, J., Nyberg, F., Sjövall, B., and Forastiere, F.: Aerosol particle number concentration measurements in five european cities using tsi-3022 condensation particle counter over a three-year period during health effects of air pollution on susceptible subpopulations, J. Air Waste Manag. Assoc., 55, 1064–1076, https://doi.org/10.1080/10473289.2005.10464702, 2005.

ACTRIS data center - an atmospheric data portal: https://actris.nilu.no/, last access: 23 March 2023.

ACTRIS website: https://www.actris.eu/, last access: 23 March 2023.

AeroCom website: https://aerocom.met.no/, last access: 23 March 2023.

Al-Abadleh, H. A.: Aging of atmospheric aerosols and the role of iron in catalyzing brown carbon formation, Environ. Sci. Atmos., 1, 297–345, https://doi.org/10.1039/D1EA00038A, 2021.

Asmi, A., Wiedensohler, A., Laj, P., Fjaeraa, A. M., Sellegri, K., Birmili, W., Weingartner, E., Baltensperger, U., Zdimal, V., Zikova, N., Putaud, J. P., Marinoni, A., Tunved, P., Hansson, H. C., Fiebig, M., Kivekäs, N., Lihavainen, H., Asmi, E., Ulevicius, V., Aalto, P. P., Swietlicki, E., Kristensson, A., Mihalopoulos, N., Kalivitis, N., Kalapov, I., Kiss, G., De Leeuw, G., Henzing, B., Harrison, R. M., Beddows, D., O'Dowd, C., Jennings, S. G., Flentje, H., Weinhold, K., Meinhardt, F., Ries, L., and Kulmala, M.: Number size distributions and seasonality of submicron particles in Europe 2008-2009, Atmos. Chem. Phys., 11, 5505–5538, https://doi.org/10.5194/acp-11-5505-2011, 2011.

Asmi, A., Collaud Coen, M., Ogren, J. A., Andrews, E., Sheridan, P., Jefferson, A., Weingartner, E., Baltensperger, U., Bukowiecki, N., Lihavainen, H., Kivekäs, N., Asmi, E., Aalto, P. P., Kulmala, M., Wiedensohler, A., Birmili, W., Hamed, A., O'Dowd, C., Jennings, S. G., Weller, R., Flentje, H., Fjaeraa, A. M., Fiebig, M., Myhre, C. L., Hallar, A. G., Swietlicki, E., Kristensson, A., and Laj, P.: Aerosol decadal trends-Part 2: In-situ aerosol particle number concentrations at GAW and ACTRIS stations, Atmos. Chem. Phys., 13, 895–916, https://doi.org/10.5194/acp-13-895-2013, 2013.

Ban-Weiss, G. A., Lunden, M. M., Kirchstetter, T. W., and Harley, R. A.: Measurement of black carbon and particle number emission factors from individual heavy-duty trucks, Environ. Sci. Technol., 43, 1419–1424, https://doi.org/10.1021/es8021039, 2009.

Barmet, P., Dommen, J., DeCarlo, P. F., Tritscher, T., Praplan, A. P., Platt, S. M., Prévôt, A. S. H., Donahue, N. M., and Baltensperger, U.: OH clock determination by proton transfer reaction mass spectrometry at an environmental chamber, Atmos. Meas. Tech., 5, 647–656, https://doi.org/10.5194/amt-5-647-2012, 2012.

Birmili, W., Berresheim, H., Plass-Dülmer, C., Elste, T., Gilge, S., Wiedensohler, A., and Uhrner, U.: The Hohenpeissenberg aerosol formation experiment (HAFEX): A long-term study including size-resolved aerosol, H2SO4, OH, and monoterpenes measurements, Atmos. Chem. Phys., 3, 361–376, https://doi.org/10.5194/acp-3-361-2003, 2003.

Birmili, W., Weinhold, K., Rasch, F., Sonntag, A., Sun, J., Merkel, M., Wiedensohler, A., Bastian, S., Schladitz, A., Löschau, G., Cyrys, J., Pitz, M., Gu, J., Kusch, T., Flentje, H., Quass, U., Kaminski, H., Kuhlbusch, T. A. J., Meinhardt, F., Schwerin, A., Bath, O., Ries,

L., Wirtz, K., and Fiebig, M.: Long-term observations of tropospheric particle number size distributions and equivalent black carbon mass concentrations in the German Ultrafine Aerosol Network (GUAN), Earth Syst. Sci. Data, 8, 355–382, https://doi.org/10.5194/essd-8-355-2016, 2016.

Brown, H., Liu, X., Pokhrel, R., Murphy, S., Lu, Z., Saleh, R., Mielonen, T., Kokkola, H., Bergman, T., Myhre, G., Skeie, R. B., Watson-Paris, D., Stier, P., Johnson, B., Bellouin, N., Schulz, M., Vakkari, V., Beukes, J. P., van Zyl, P. G., Liu, S., and Chand, D.: Biomass burning aerosols in most climate models are too absorbing, Nat. Commun., 12, 277, https://doi.org/10.1038/s41467-020-20482-9, 2021.

Bruns, E. A., Krapf, M., Orasche, J., Huang, Y., Zimmermann, R., Drinovec, L., Močnik, G., El-Haddad, I., Slowik, J. G., Dommen, J., Baltensperger, U., and Prévôt, A. S. H.: Characterization of primary and secondary wood combustion products generated under different burner loads, Atmos. Chem. Phys., 15, 2825–2841, https://doi.org/10.5194/acp-15-2825-2015, 2015.

Bukowiecki, N., Dommen, J., Prévôt, A. S. H., Richter, R., Weingartner, E., and Baltensperger, U.: A mobile pollutant measurement laboratory—measuring gas phase and aerosol ambient concentrations with high spatial and temporal resolution, Atmos. Environ., 36, 5569–5579, https://doi.org/10.1016/S1352-2310(02)00694-5, 2002.

Butt, E. W., Rap, A., Schmidt, A., Scott, C. E., Pringle, K. J., Reddington, C. L., Richards, N. A. D., Woodhouse, M. T., Ramirez-Villegas, J., Yang, H., Vakkari, V., Stone, E. A., Rupakheti, M., Praveen, P. S., Van Zyl, P. G., Beukes, J. P., Josipovic, M., Mitchell, E. J. S., Sallu, S. M., Forster, P. M., and Spracklen, D. V.: The impact of residential combustion emissions on atmospheric aerosol, human health, and climate, Atmos. Chem. Phys., 16, 873–905, https://doi.org/10.5194/acp-16-873-2016, 2016.

Cappa, C. D. and Wilson, K. R.: Multi-generation gas-phase oxidation, equilibrium partitioning, and the formation and evolution of secondary organic aerosol, Atmos. Chem. Phys., 12, 9505–9528, https://doi.org/10.5194/acp-12-9505-2012, 2012.

Carslaw, D. C. and Ropkins, K.: openair --- An R package for air quality data analysis, Environ. Model. Softw., 27--28, 52–61, https://doi.org/10.1016/j.envsoft.2011.09.008, 2012.

Cassee, F. R., Héroux, M. E., Gerlofs-Nijland, M. E., and Kelly, F. J.: Particulate matter beyond mass: Recent health evidence on the role of fractions, chemical constituents and sources of emission, Inhal. Toxicol., 25, 802–812, https://doi.org/10.3109/08958378.2013.850127/SUPPL_FILE/IIHT_A_850127_SM0004.PDF, 2013.

Chen, D., Rojas, M., Samset, B. H., Cobb, K., Diongue Niang, A., Edwards, P., Emori, S., Faria, S. H., Hawkins, E., Hope, P., Huybrechts, P., Meinshausen, M., Mustafa, S. K., Plattner, G.-K., and Tréguier, A.-M.: Framing, Context, and Methods, in: Climate Change 2021: The Physical Science Basis. Contribution of Working Group I to the Sixth Assessment Report of the Intergovernmental Panel on Climate Change, edited by: Masson-Delmotte, V., Zhai, P., Pirani, A., Connors, S. L., Péan, C., Berger, S., Caud, N., Chen, Y., Goldfarb, L., Gomis, M. I., Huang, M., Leitzell, K., Lonnoy, E., Matthews, J. B. R., Maycock, T. K., Waterfield, T., Yelekçi, O., Yu, R., and Zhou, B., Cambridge University Press, Cambridge, United Kingdom and New York, NY, USA, 147–286, https://doi.org/10.1017/9781009157896.003, 2021.

Cleveland, R. B., Cleveland, W. S., McRae, J. E., and Terpenning, I.: STL: A Seasonal-Trend Decomposition Procedure Based on Loess, J. Off. Stat., 6, 3–73, 1990.

Cohen, A. J., Brauer, M., Burnett, R., Anderson, H. R., Frostad, J., Estep, K., Balakrishnan, K., Brunekreef, B., Dandona, L., Dandona, R., Feigin, V., Freedman, G., Hubbell, B., Jobling, A., Kan, H., Knibbs, L., Liu, Y., Martin, R., Morawska, L., Pope, C. A., Shin, H., Straif, K., Shaddick, G., Thomas, M., van Dingenen, R., van Donkelaar, A., Vos, T., Murray, C. J. L., and Forouzanfar, M. H.: Estimates and 25-year trends of the global burden of disease attributable to ambient air pollution: an analysis of data from the Global Burden of Diseases Study 2015, Lancet, 389, 1907–1918, https://doi.org/10.1016/S0140-6736(17)30505-6, 2017.

Collaud Coen, M., Andrews, E., Lastuey, A., Petkov Arsov, T., Backman, J., Brem, B. T., Bukowiecki, N., Couret, C., Eleftheriadis, K., Flentje, H., Fiebig, M., Gysel-Beer, M., Hand, J. L., Hoffer, A., Hooda, R., Hueglin, C., Joubert, W., Keywood, M., Eun Kim, J., Kim, S. W., Labuschagne, C., Lin, N. H., Lin, Y., Lund Myhre, C., Luoma, K., Lyamani, H., Marinoni, A., Mayol-Bracero, O. L., Mihalopoulos, N., Pandolfi, M., Prats, N., Prenni, A. J., Putaud, J. P., Ries, L., Reisen, F., Sellegri, K., Sharma, S., Sheridan, P., Patrick Sherman, J., Sun, J., Titos, G., Torres, E., Tuch, T., Weller, R., Wiedensohler, A., Zieger, P., and Laj, P.: Multidecadal trend analysis of in situ aerosol radiative properties around the world, Atmos. Chem. Phys., 20, 8867–8908, https://doi.org/10.5194/acp-20-8867-2020, 2020.

Durbin, J. and Koopman, S. J.: Time Series Analysis by State Space Methods, Oxford University Press, Oxford, 2012.

Emerson, E. W., Hodshire, A. L., DeBolt, H. M., Bilsback, K. R., Pierce, J. R., McMeeking, G. R., and Farmer, D. K.: Revisiting particle dry deposition and its role in radiative effect estimates, Proc. Natl. Acad. Sci. U. S. A., 117, 26076–26082, https://doi.org/10.1073/PNAS.2014761117/SUPPL_FILE/PNAS.2014761117.SAPP.PDF, 2020.

Enroth, J., Saarikoski, S., Niemi, J., Kousa, A., Ježek, I., Močnik, G., Carbone, S., Kuuluvainen, H., Rönkkö, T., Hillamo, R., and Pirjola, L.: Chemical and physical characterization of traffic particles in four different highway environments in the Helsinki metropolitan area, Atmos. Chem. Phys., 16, 5497–5512, https://doi.org/10.5194/acp-16-5497-2016, 2016.

Eyring, V., Bony, S., Meehl, G. A., Senior, C. A., Stevens, B., Stouffer, R. J., and Taylor, K. E.: Overview of the Coupled Model Intercomparison Project Phase 6 (CMIP6) experimental design and organization, Geosci. Model Dev., 9, 1937–1958, https://doi.org/10.5194/gmd-9-1937-2016, 2016.

Fan, J., Wang, Y., Rosenfeld, D., and Liu, X.: Review of aerosol-cloud interactions: Mechanisms, significance, and challenges, J. Atmos. Sci., 73, 4221–4252, https://doi.org/10.1175/JAS-D-16-0037.1, 2016.

Forster, P. M., Storelvmo, T., Armour, K., Collins, W., Dufresne, J. L., Frame, D., Lunt, D. J., Mauritsen, T., Palmer, M. D., Watanabe, M., Wild, M., and Zhang, H.: Chapter 7: The Earth's Energy Budget, Climate Feedbacks, and Climate Sensitivity, in: Climate Change 2021: The Physical Science Basis. Contribution of Working Group I to the Sixth Assessment Report of the Intergovernmental Panel on Climate Change, edited by: Masson-Delmotte, V., Zhai, P., Pirani, A., Connors, S. L., Péan, C., Berger, S., Caud, N., Chen, Y., Goldfarb, L., Gomis, M. I., Huang, M., Leitzell, K., Lonnoy, E., Matthews, J. B. R., Maycock, T. K., Waterfield, T., Yelekçi, O., Yu, R., and Zhou, B., Cambridge University Press., 2021.

Fountoukis, C., Butler, T., Lawrence, M. G., Denier van der Gon, H. A. C., Visschedijk, A. J. H., Charalampidis, P., Pilinis, C., and Pandis, S. N.: Impacts of controlling biomass burning emissions on wintertime carbonaceous aerosol in Europe, Atmos. Environ., 87, 175–182, https://doi.org/10.1016/j.atmosenv.2014.01.016, 2014.

Friedman, J. H.: Multivariate Adaptive Regression Splines, Ann. Stat., 19, 1–67, https://doi.org/10.1214/aos/1176347963, 1991.

Gliß, J., Mortier, A., Schulz, M., Andrews, E., Balkanski, Y., Bauer, S. E., Benedictow, A. M. K., Bian, H., Checa-Garcia, R., Chin, M., Ginoux, P., Griesfeller, J. J., Heckel, A., Kipling, Z., Kirkeväg, A., Kokkola, H., Laj, P., Le Sager, P., Tronstad Lund, M., Lund Myhre, C., Matsui, H., Myhre, G., Neubauer, D., Van Noije, T., North, P., Olivié, D. J. L., Rémy, S., Sogacheva, L., Takemura, T., Tsigaridis, K., and Tsyro, S. G.: AeroCom phase III multi-model evaluation of the aerosol life cycle and optical properties using ground- And space-based remote sensing as well as surface in situ observations, Atmos. Chem. Phys., 21, 87–128, https://doi.org/10.5194/acp-21-87-2021, 2021.

Guenther, A., Hewitt, C. N., Erickson, D., Fall, R., Geron, C., Graedel, T., Harley, P., Klinger, L., Lerdau, M., Mckay, W. A., Pierce, T., Scholes, B., Steinbrecher, R., Tallamraju, R., Taylor, J., and Zimmerman, P.: A global model of natural volatile organic compound emissions, J. Geophys. Res., 100, 8873, https://doi.org/10.1029/94JD02950, 1995.

Guibert, S., Matthias, V., Schulz, M., Bösenberg, J., Eixmann, R., Mattis, I., Pappalardo, G., Perrone, M. R., Spinelli, N., and Vaughan, G.: The vertical distribution of aerosol over Europe - Synthesis of one year of EARLINET aerosol lidar measurements and aerosol transport modeling with LMDzT-INCA, Atmos. Environ., 39, 2933–2943, https://doi.org/10.1016/j.atmosenv.2004.12.046, 2005.

Hallquist, M., Wenger, J. C., Baltensperger, U., Rudich, Y., Simpson, D., Claeys, M., Dommen, J., Donahue, N. M., George, C., Goldstein, A. H., Hamilton, J. F., Herrmann, H., Hoffmann, T., Iinuma, Y., Jang, M., Jenkin, M. E., Jimenez, J. L., Kiendler-Scharr, A., Maenhaut, W., McFiggans, G., Mentel, T. F., Monod, A., Prévôt, A. S. H., Seinfeld, J. H., Surratt, J. D., Szmigielski, R., and Wildt, J.: The formation, properties and impact of secondary organic aerosol: current and emerging issues, Atmos. Chem. Phys., 9, 5155–5236, https://doi.org/10.5194/acp-9-5155-2009, 2009.

Hamed, A., Joutsensaari, J., Mikkonen, S., Sogacheva, L., Dal Maso, M., Kulmala, M., Cavalli, F., Fuzzi, S., Facchini, M. C., Decesari, S., Mircea, M., Lehtinen, K. E. J., and Laaksonen, A.: Nucleation and growth of new particles in Po Valley, Italy, Atmos. Chem. Phys., 7, 355–376, https://doi.org/10.5194/acp-7-355-2007, 2007.

Hamed, A., Birmili, W., Joutsensaari, J., Mikkonen, S., Asmi, A., Wehner, B., Spindler, G., Jaatinen, A., Wiedensohler, A., Korhonen, H., J. Lehtinen, K. E., and Laaksonen, A.: Changes in the production rate of secondary aerosol particles in Central Europe in view of decreasing SO2 emissions between 1996 and 2006, https://doi.org/10.5194/acp-10-1071-2010, 2010.

Hansen, A. D. A. and Rosen, H.: Individual measurements of the emission factor of aerosol black carbon in automobile plumes, J. Air Waste Manag. Assoc., 40, 1654–1657, https://doi.org/10.1080/10473289.1990.10466812, 1990.

Hari, P. and Kulmala, M.: Station for Measuring Ecosystem-Atmosphere Relations (SMEAR II), Boreal Environ. Res., 10, 315–322, 2005.

Hartikainen, A., Yli-Pirilä, P., Tiitta, P., Leskinen, A., Kortelainen, M., Orasche, J.,

Schnelle-Kreis, J., Lehtinen, K. E. J., Zimmermann, R., Jokiniemi, J., and Sippula, O.: Volatile Organic Compounds from Logwood Combustion: Emissions and Transformation under Dark and Photochemical Aging Conditions in a Smog Chamber, Environ. Sci. Technol., 52, 4979–4988, https://doi.org/10.1021/acs.est.7b06269, 2018.

Hartikainen, A., Tiitta, P., Ihalainen, M., Yli-Pirilä, P., Orasche, J., Czech, H., Kortelainen, M., Lamberg, H., Suhonen, H., Koponen, H., Hao, L., Zimmermann, R., Jokiniemi, J., Tissari, J., and Sippula, O.: Photochemical transformation of residential wood combustion emissions: dependence of organic aerosol composition on OH exposure, Atmos. Chem. Phys., 20, 6357–6378, https://doi.org/10.5194/acp-20-6357-2020, 2020.

Hartikainen, A. H., Ihalainen, M., Yli-Pirilä, P., Hao, L., Kortelainen, M., Pieber, S. M., and Sippula, O.: Photochemical transformation and secondary aerosol formation potential of Euro6 gasoline and diesel passenger car exhaust emissions, J. Aerosol Sci., 171, 106159, https://doi.org/10.1016/J.JAEROSCI.2023.106159, 2023.

Heavens, N. G., Ward, D. S., and Natalie, M. M.: Studying and Projecting Climate Change with Earth System Models, Nat. Educ. Knowl., 4, 4, 2013.

Hellén, H., Praplan, A. P., Tykkä, T., Ylivinkka, I., Vakkari, V., Bäck, J., Petäjä, T., Kulmala, M., and Hakola, H.: Long-term measurements of volatile organic compounds highlight the importance of sesquiterpenes for the atmospheric chemistry of a boreal forest, Atmos. Chem. Phys., 18, 13839–13863, https://doi.org/10.5194/acp-18-13839-2018, 2018.

Hoppel, W. A.: Determination of the aerosol size distribution from the mobility distribution of the charged fraction of aerosols, J. Aerosol Sci., 9, 41–54, https://doi.org/10.1016/0021-8502(78)90062-9, 1978.

Hussein, T., Dal Maso, M., Petäjä, T., Koponen, I. K., Paatero, P., Aalto, P. P., Hämeri, K., and Kulmala, M.: Evaluation of an automatic algorithm for fitting the particle number size distributions, Boreal Environ. Res., 10, 337–355, 2005.

Hussein, T., Martikainen, J., Junninen, H., Sogacheva, L., Wagner, R., Dal Maso, M., Riipinen, I., Aalto, P. P., and Kulmala, M.: Observation of regional new particle formation in the urban atmosphere, Tellus, Ser. B Chem. Phys. Meteorol., 60, 509–521, https://doi.org/10.1111/j.1600-0889.2008.00365.x, 2008.

Hussein, T., Boor, B. E., dos Santos, V. N., Kangasluoma, J., Petäjä, T., and Lihavainen, H.: Mobile Aerosol Measurement in the Eastern Mediterranean - A Utilization of Portable Instruments, Aerosol Air Qual. Res., 17, 1875–1886, https://doi.org/10.4209/aaqr.2016.11.0479, 2017.

ICOS - Integrated Carbon Observation System: https://www.icos-cp.eu/, last access: 24 March 2023.

Ihalainen, M., Tiitta, P., Czech, H., Yli-Pirilä, P., Hartikainen, A., Kortelainen, M., Tissari, J., Stengel, B., Sklorz, M., Suhonen, H., Lamberg, H., Leskinen, A., Kiendler-Scharr, A., Harndorf, H., Zimmermann, R., Jokiniemi, J., and Sippula, O.: A novel high-volume Photochemical Emission Aging flow tube Reactor (PEAR), Aerosol Sci. Technol., 53, 276–294, https://doi.org/10.1080/02786826.2018.1559918, 2019.

IPCC: Climate Change 2021: The Physical Science Basis. Contribution of Working Group I to the Sixth Assessment Report of the Intergovernmental Panel on Climate Change, Cambridge University Press, Cambridge, United Kingdom and New York, NY, USA, https://doi.org/10.1017/9781009157896, 2021.

Janssens-Maenhout, G., Crippa, M., Guizzardi, D., Muntean, M., Schaaf, E., Dentener, F., Bergamaschi, P., Pagliari, V., Olivier, J. G. J., Peters, J. A. H. W., Van Aardenne, J. A., Monni, S., Doering, U., Roxana Petrescu, A. M., Solazzo, E., and Oreggioni, G. D.: EDGAR v4.3.2 Global Atlas of the three major greenhouse gas emissions for the period 1970-2012, Earth Syst. Sci. Data, 11, 959–1002, https://doi.org/10.5194/ESSD-11-959-2019, 2019.

Jimenez, J. L., Canagaratna, M. R., Donahue, N. M., Prevot, A. S. H., Zhang, Q., Kroll, J. H., DeCarlo, P. F., Allan, J. D., Coe, H., Ng, N. L., Aiken, A. C., Docherty, K. S., Ulbrich, I. M., Grieshop, A. P., Robinson, A. L., Duplissy, J., Smith, J. D., Wilson, K. R., Lanz, V. A., Hueglin, C., Sun, Y. L., Tian, J., Laaksonen, A., Raatikainen, T., Rautiainen, J., Vaattovaara, P., Ehn, M., Kulmala, M., Tomlinson, J. M., Collins, D. R., Cubison, M. J., Dunlea, E. J., Huffman, J. A., Onasch, T. B., Alfarra, M. R., Williams, P. I., Bower, K., Kondo, Y., Schneider, J., Drewnick, F., Borrmann, S., Weimer, S., Demerjian, K., Salcedo, D., Cottrell, L., Griffin, R., Takami, A., Miyoshi, T., Hatakeyama, S., Shimono, A., Sun, J. Y., Zhang, Y. M., Dzepina, K., Kimmel, J. R., Sueper, D., Jayne, J. T., Herndon, S. C., Trimborn, A. M., Williams, L. R., Wood, E. C., Middlebrook, A. M., Kolb, C. E., Baltensperger, U., and Worsnop, D. R.: Evolution of organic aerosols in the atmosphere, Science (80-.)., 326, 1525–1529, https://doi.org/10.1126/science.1180353, 2009.

Karjalainen, P., Pirjola, L., Heikkilä, J., Lähde, T., Tzamkiozis, T., Ntziachristos, L., Keskinen, J., and Rönkkö, T.: Exhaust particles of modern gasoline vehicles: A laboratory and an on-road study, Atmos. Environ., 97, 262–270, https://doi.org/10.1016/j.atmosenv.2014.08.025, 2014.

Karjalainen, P., Timonen, H., Saukko, E., Kuuluvainen, H., Saarikoski, S., Aakko-Saksa, P., Murtonen, T., Bloss, M., Dal Maso, M., Simonen, P., Ahlberg, E., Svenningsson, B., Brune, W. H., Hillamo, R., Keskinen, J., and Rönkkö, T.: Time-resolved characterization of primary particle emissions and secondary particle formation from a modern gasoline passenger car, Atmos. Chem. Phys., 16, 8559–8570, https://doi.org/10.5194/ACP-16-8559-2016, 2016.

Keeling, C. D., Bacastow, R. B., Bainbridge, A. E., Ekdahl, C. A., Guenther, P. R., Waterman, L. S., and Chin, J. F. S.: Atmospheric carbon dioxide variations at Mauna Loa Observatory, Hawaii, Tellus, 28, 538–551, https://doi.org/10.1111/j.2153-3490.1976.tb00701.x, 1976.

Kinne, S., Schulz, M., Textor, C., Guibert, S., Balkanski, Y., Bauer, S. E., Berntsen, T., Berglen, T. F., Boucher, O., Chin, M., Collins, W., Dentener, F., Diehl, T., Easter, R., Feichter, J., Fillmore, D., Ghan, S., Ginoux, P., Gong, S., Grini, A., Hendricks, J., Herzog, M., Horowitz, L., Isaksen, I., Iversen, T., Kirkevåg, A., Kloster, S., Koch, D., Kristjansson, J. E., Krol, M., Lauer, A., Lamarque, J. F., Lesins, G., Liu, X., Lohmann, U., Montanaro, V., Myhre, G., Penner, J. E., Pitari, G., Reddy, S., Seland, O., Stier, P., Takemura, T., and Tie, X.: An AeroCom initial assessment - Optical properties in aerosol component modules of global models, Atmos. Chem. Phys., 6, 1815–1834, https://doi.org/10.5194/acp-6-1815-2006, 2006.

Kirkevåg, A., Grini, A., Olivié, D., Seland, Ø., Alterskjær, K., Hummel, M., Karset, I. H. H., Lewinschal, A., Liu, X., Makkonen, R., Bethke, I., Griesfeller, J., Schulz, M., and Iversen, T.: A production-tagged aerosol module for earth system models, OsloAero5.3-extensions and updates for CAM5.3-Oslo, Geosci. Model Dev., 11, 3945–3982, https://doi.org/10.5194/gmd-11-3945-2018, 2018.

Knutson, E. O. and Whitby, K. T.: Aerosol classification by electric mobility: apparatus,

theory, and applications, J. Aerosol Sci., 6, 443–451, https://doi.org/10.1016/0021-8502(75)90060-9, 1975.

Kokkola, H., Kühn, T., Laakso, A., Bergman, T., Lehtinen, K. E. J., Mielonen, T., Arola, A., Stadtler, S., Korhonen, H., Ferrachat, S., Lohmann, U., Neubauer, D., Tegen, I., Siegenthaler-Le Drian, C., Schultz, M. G., Bey, I., Stier, P., Daskalakis, N., Heald, C. L., and Romakkaniemi, S.: SALSA2.0: The sectional aerosol module of the aerosol-chemistry-climate model ECHAM6.3.0-HAM2.3-MOZ1.0, Geosci. Model Dev., 11, 3833–3863, https://doi.org/10.5194/gmd-11-3833-2018, 2018.

Kortelainen, M., Jokiniemi, J., Tiitta, P., Tissari, J., Lamberg, H., Leskinen, J., Grigonyte-Lopez Rodriguez, J., Koponen, H., Antikainen, S., Nuutinen, I., Zimmermann, R., and Sippula, O.: Time-resolved chemical composition of small-scale batch combustion emissions from various wood species, Fuel, 233, 224–236, https://doi.org/10.1016/j.fuel.2018.06.056, 2018.

Krich, C., Runge, J., Miralles, D. G., Migliavacca, M., Perez-Priego, O., El-Madany, T., Carrara, A., and Mahecha, M. D.: Estimating causal networks in biosphere-atmosphere interaction with the PCMCI approach, Biogeosciences, 17, 1033–1061, https://doi.org/10.5194/bg-17-1033-2020, 2020.

Kuniyal, J. C. and Guleria, R. P.: The current state of aerosol-radiation interactions: A mini review, J. Aerosol Sci., 130, 45–54, https://doi.org/10.1016/J.JAEROSCI.2018.12.010, 2019.

Kunsch, H. R.: The Jackknife and the Bootstrap for General Stationary Observations, Ann. Stat., 17, 1217–1241, https://doi.org/10.1214/aos/1176347265, 1989.

Kyrö, E. M., Väänänen, R., Kerminen, V. M., Virkkula, A., Petäjä, T., Asmi, A., Dal Maso, M., Nieminen, T., Juhola, S., Shcherbinin, A., Riipinen, I., Lehtipalo, K., Keronen, P., Aalto, P. P., Hari, P., and Kulmala, M.: Trends in new particle formation in eastern Lapland, Finland: Effect of decreasing sulfur emissions from Kola Peninsula, Atmos. Chem. Phys., 14, 4383–4396, https://doi.org/10.5194/acp-14-4383-2014, 2014.

Laine, M.: Introduction to Dynamic Linear Models for Time Series Analysis, in: Geodetic Time Series Analysis in Earth Sciences, edited by: Montillet, Jean-Philippe. and Bos, M. S., Springer, 139–156, https://doi.org/10.1007/978-3-030-21718-1_4, 2020.

Laine, M., Latva-Pukkila, N., and Kyrölä, E.: Analysing time-varying trends in stratospheric ozone time series using the state space approach, Atmos. Chem. Phys., 14, 9707–9725, https://doi.org/10.5194/acp-14-9707-2014, 2014.

Lambe, A. T., Ahern, A. T., Williams, L. R., Slowik, J. G., Wong, J. P. S., Abbatt, J. P. D., Brune, W. H., Ng, N. L., Wright, J. P., Croasdale, D. R., Worsnop, D. R., Davidovits, P., and Onasch, T. B.: Characterization of aerosol photooxidation flow reactors: Heterogeneous oxidation, secondary organic aerosol formation and cloud condensation nuclei activity measurements, Atmos. Meas. Tech., 4, 445–461, https://doi.org/10.5194/AMT-4-445-2011, 2011.

Lambe, A. T., Chhabra, P. S., Onasch, T. B., Brune, W. H., Hunter, J. F., Kroll, J. H., Cummings, M. J., Brogan, J. F., Parmar, Y., Worsnop, D. R., Kolb, C. E., and Davidovits, P.: Effect of oxidant concentration, exposure time, and seed particles on secondary organic aerosol chemical composition and yield, Atmos. Chem. Phys., 15, 3063–3075, https://doi.org/10.5194/acp-15-3063-2015, 2015.

Leskinen, A., Arola, A., Komppula, M., Portin, H., Tiitta, P., Miettinen, P., Romakkaniemi, S., Laaksonen, A., and Lehtinen, K. E. J.: Seasonal cycle and source analyses of aerosol optical properties in a semi-urban environment at Puijo station in Eastern Finland, Atmos. Chem. Phys., 12, 5647–5659, https://doi.org/10.5194/acp-12-5647-2012, 2012.

Leskinen, A., Yli-Pirilä, P., Kuuspalo, K., Sippula, O., Jalava, P., Hirvonen, M.-R., Jokiniemi, J., Virtanen, A., Komppula, M., and Lehtinen, K. E. J.: Characterization and testing of a new environmental chamber, Atmos. Meas. Tech., 8, 2267–2278, https://doi.org/10.5194/amt-8-2267-2015, 2015.

Leskinen, J., Ihalainen, M., Torvela, T., Kortelainen, M., Lamberg, H., Tiitta, P., Jakobi, G., Grigonyte, J., Joutsensaari, J., Sippula, O., Tissari, J., Virtanen, A., Zimmermann, R., and Jokiniemi, J.: Effective density and morphology of particles emitted from small-scale combustion of various wood fuels, Environ. Sci. Technol., 48, 13298–13306, https://doi.org/10.1021/es502214a, 2014.

Lohila, A., Penttilä, T., Jortikka, S., Aalto, T., Anttila, P., Asmi, E., Aurela, M., Hatakka, J., Hellén, H., Henttonen, H., Hänninen, P., Kilkki, J., Kyllönen, K., Laurila, T., Lepistö, A., Lihavainen, H., Makkonen, U., Paatero, J., Rask, M., Sutinen, R., Tuovinen, J.-P., Vuorenmaa, J., and Viisanen, Y.: Preface to the special issue on integrated research of atmosphere, ecosystems and environment at Pallas, Boreal Environ. Res., 20(4), 431–454, 2015.

Ma, X. and Yu, F.: Seasonal variability of aerosol vertical profiles over east US and west Europe: GEOS-Chem/APM simulation and comparison with CALIPSO observations, Atmos. Res., 140–141, 28–37, https://doi.org/10.1016/j.atmosres.2014.01.001, 2014.

Mäkelä, J. M., Koponen, I. K., Aalto, P., and Kulmala, M.: One-year Data of Submicron Size Modes of Tropospheric Background Aerosol in Southern Finland, J. Aerosol Sci, 595–611 pp., 2000.

McCulloch, C. E., Searle, S. R., and Neuhaus, J. M.: Generalized, linear, and mixed models, Second., Wiley, New York, 2008.

MCM Website: http://mcm.york.ac.uk/, last access: 19 April 2023.

McMurry, P. H.: The History of Condensation Nucleus Counters, Aerosol Sci. Technol., 33, 297–322, https://doi.org/10.1080/02786820050121512, 2000.

Mihalopoulos, N., Stephanou, E., Kanakidou, M., Pilitsidis, S., and Bousquet, P.: Tropospheric aerosol ionic composition in the Eastern Mediterranean region, Tellus, Ser. B Chem. Phys. Meteorol., 49, 314–326, https://doi.org/10.3402/tellusb.v49i3.15970, 1997.

Mikkonen, S., Korhonen, H., Romakkaniemi, S., Smith, J. N., Joutsensaari, J., Lehtinen, K. E. J., Hamed, A., Breider, T. J., Birmili, W., Spindler, G., Plass-Duelmer, C., Facchini, M. C., and Laaksonen, A.: Meteorological and trace gas factors affecting the number concentration of atmospheric Aitken (DP Combining double low line 50 nm) particles in the continental boundary layer: Parameterization using a multivariate mixed effects model, Geosci. Model Dev., 4, 1–13, https://doi.org/10.5194/gmd-4-1-2011, 2011.

Mikkonen, S., Laine, M., Mäkelä, H. M., Gregow, H., Tuomenvirta, H., Lahtinen, M., and Laaksonen, A.: Trends in the average temperature in Finland, 1847–2013, Stoch. Environ. Res. Risk Assess., 29, 1521–1529, https://doi.org/10.1007/s00477-014-0992-2, 2015.

Milborrow, S.: earth: Multivariate Adaptive Regression Splines, https://cran.r-project.org/package=earth, 2023.

Mortier, A., Gliß, J., Schulz, M., Aas, W., Andrews, E., Bian, H., Chin, M., Ginoux, P., Hand, J., Holben, B., Zhang, H., Kipling, Z., Kirkevåg, A., Laj, P., Lurton, T., Myhre, G., Neubauer, D., Olivié, D., von Salzen, K., Skeie, R. B., Takemura, T., and Tilmes, S.: Evaluation of climate model aerosol trends with ground-based observations over the last 2 decades - an AeroCom and CMIP6 analysis, Atmos. Chem. Phys., 20, 13355–13378, https://doi.org/10.5194/acp-20-13355-2020, 2020.

Nguyen, Q. T., Glasius, M., Sørensen, L. L., Jensen, B., Skov, H., Birmili, W., Wiedensohler, A., Kristensson, A., Nøjgaard, J. K., and Massling, A.: Seasonal variation of atmospheric particle number concentrations, new particle formation and atmospheric oxidation capacity at the high Arctic site Villum Research Station, Station Nord, Atmos. Chem. Phys., 16, 11319–11336, https://doi.org/10.5194/acp-16-11319-2016, 2016.

Nieminen, T., Kerminen, V.-M., Petäjä, T., Aalto, P. P., Arshinov, M., Asmi, E., Baltensperger, U., Beddows, D. C. S., Beukes, J. P., Collins, D., Ding, A., Harrison, R. M., Henzing, B., Hooda, R., Hu, M., Hõrrak, U., Kivekäs, N., Komsaare, K., Krejci, R., Kristensson, A., Laakso, L., Laaksonen, A., Leaitch, W. R., Lihavainen, H., Mihalopoulos, N., Németh, Z., Nie, W., O'Dowd, C., Salma, I., Sellegri, K., Svenningsson, B., Swietlicki, E., Tunved, P., Ulevicius, V., Vakkari, V., Vana, M., Wiedensohler, A., Wu, Z., Virtanen, A., and Kulmala, M.: Global analysis of continental boundary layer new particle formation based on long-term measurements, Atmos. Chem. Phys., 18, 14737–14756, https://doi.org/10.5194/acp-18-14737-2018, 2018.

Noe, S. M., Niinemets, Ü., Krasnova, A., Krasnov, D., Motallebi, A., Kängsepp, V., Jõgiste, K., Hõrrak, U., Komsaare, K., Mirme, S., Vana, M., Tammet, H., Bäck, J., Vesala, T., Kulmala, M., Petäjä, T., and Kangur, A.: {SMEAR} Estonia: Perspectives of a large-scale forest ecosystem {\textendash} atmosphere research infrastructure, For. Stud., 63, 56–84, https://doi.org/10.1515/fsmu-2015-0009, 2015.

van Noije, T., Bergman, T., Le Sager, P., O'Donnell, D., Makkonen, R., Gonçalves-Ageitos, M., Döscher, R., Fladrich, U., Von Hardenberg, J., Keskinen, J. P., Korhonen, H., Laakso, A., Myriokefalitakis, S., Ollinaho, P., Pérez Garciá-Pando, C., Reerink, T., Schrödner, R., Wyser, K., and Yang, S.: EC-Earth3-AerChem: A global climate model with interactive aerosols and atmospheric chemistry participating in CMIP6, Geosci. Model Dev., 14, 5637–5668, https://doi.org/10.5194/gmd-14-5637-2021, 2021.

O'Connor, T. C., Jennings, S. G., and O'Dowd, C. D.: Highlights of fifty years of atmospheric aerosol research at Mace Head, Atmos. Res., 90, 338–355, https://doi.org/10.1016/j.atmosres.2008.08.014, 2008.

Olin, M., Oikarinen, H., Marjanen, P., Mikkonen, S., and Karjalainen, P.: High Particle Number Emissions Determined with Robust Regression Plume Analysis (RRPA) from Hundreds of Vehicle Chases, Environ. Sci. Technol., https://doi.org/10.1021/ACS.EST.2C08198, 2023.

Penner, J. E., Quaas, J., Storelvmo, T., Takemura, T., Boucher, O., Guo, H., Kirkevåg, A., Kristjánsson, J. E., and Seland: Model intercomparison of indirect aerosol effects, Atmos. Chem. Phys., 6, 3391–3405, https://doi.org/10.5194/acp-6-3391-2006, 2006.

Pieber, S. M., Kumar, N. K., Klein, F., Comte, P., Bhattu, D., Dommen, J., Bruns, E. A., Kiluic, D., El Haddad, I., Keller, A., Czerwinski, J., Heeb, N., Baltensperger, U., Slowik, J. G., and Prévôt, A. S. H.: Gas-phase composition and secondary organic aerosol formation from standard and particle filter-retrofitted gasoline direct injection vehicles investigated in a batch and flow reactor, Atmos. Chem. Phys., 18, 9929–9954,

https://doi.org/10.5194/ACP-18-9929-2018, 2018.

Pirjola, L., Parviainen, H., Hussein, T., Valli, A., Hämeri, K., Aaalto, P., Virtanen, A., Keskinen, J., Pakkanen, T. A., Mäkelä, T., and Hillamo, R. E.: "Sniffer"—a novel tool for chasing vehicles and measuring traffic pollutants, Atmos. Environ., 38, 3625–3635, https://doi.org/10.1016/J.ATMOSENV.2004.03.047, 2004.

Pirjola, L., Niemi, J. V., Saarikoski, S., Aurela, M., Enroth, J., Carbone, S., Saarnio, K., Kuuluvainen, H., Kousa, A., Rönkkö, T., and Hillamo, R.: Physical and chemical characterization of urban winter-time aerosols by mobile measurements in Helsinki, Finland, Atmos. Environ., 158, 60–75, https://doi.org/10.1016/j.atmosenv.2017.03.028, 2017.

Platt, S. M., El Haddad, I., Zardini, A. A., Clairotte, M., Astorga, C., Wolf, R., Slowik, J. G., Temime-Roussel, B., Marchand, N., Ježek, I., Drinovec, L., Močnik, G., Möhler, O., Richter, R., Barmet, P., Bianchi, F., Baltensperger, U., and Prévôt, A. S. H.: Secondary organic aerosol formation from gasoline vehicle emissions in a new mobile environmental reaction chamber, Atmos. Chem. Phys., 13, 9141–9158, https://doi.org/10.5194/acp-13-9141-2013, 2013.

R Core Team: R: A Language and Environment for Statistical Computing, https://www.r-project.org/, 2022.

Rivas, I., Beddows, D. C. S., Amato, F., Green, D. C., Järvi, L., Hueglin, C., Reche, C., Timonen, H., Fuller, G. W., Niemi, J. V., Pérez, N., Aurela, M., Hopke, P. K., Alastuey, A., Kulmala, M., Harrison, R. M., Querol, X., and Kelly, F. J.: Source apportionment of particle number size distribution in urban background and traffic stations in four European cities, Environ. Int., 135, 105345, https://doi.org/10.1016/j.envint.2019.105345, 2020.

Robinson, A. L., Donahue, N. M., Shrivastava, M. K., Weitkamp, E. A., Sage, A. M., Grieshop, A. P., Lane, T. E., Pierce, J. R., and Pandis, S. N.: Rethinking Organic Aerosols: Semivolatile Emissions and Photochemical Aging, Science (80-.)., 315, 1259–1262, https://doi.org/10.1126/science.1133061, 2007.

Rönkkö, T., Kuuluvainen, H., Karjalainen, P., Keskinen, J., Hillamo, R., Niemi, J. V., Pirjola, L., Timonen, H. J., Saarikoski, S., Saukko, E., Järvinen, A., Silvennoinen, H., Rostedt, A., Olin, M., Yli-Ojanperä, J., Nousiainen, P., Kousa, A., and Dal Maso, M.: Traffic is a major source of atmospheric nanocluster aerosol, Proc. Natl. Acad. Sci. U. S. A., 114, 7549–7554, https://doi.org/10.1073/pnas.1700830114, 2017.

Rose, C., Collaud Coen, M., Andrews, E., Lin, Y., Bossert, I., Lund Myhre, C., Tuch, T., Wiedensohler, A., Fiebig, M., Aalto, P., Alastuey, A., Alonso-Blanco, E., Andrade, M., Artíñano, B., Arsov, T., Baltensperger, U., Bastian, S., Bath, O., Beukes, J. P., Brem, B. T., Bukowiecki, N., Casquero-Vera, J. A., Conil, S., Eleftheriadis, K., Favez, O., Flentje, H., Gini, M. I., Gómez-Moreno, F. J., Gysel-Beer, M., Hallar, A. G., Kalapov, I., Kalivitis, N., Kasper-Giebl, A., Keywood, M., Kim, J. E., Kim, S.-W., Kristensson, A., Kulmala, M., Lihavainen, H., Lin, N.-H., Lyamani, H., Marinoni, A., Martins Dos Santos, S., Mayol-Bracero, O. L., Meinhardt, F., Merkel, M., Metzger, J.-M., Mihalopoulos, N., Ondracek, J., Pandolfi, M., Pérez, N., Petäjä, T., Petit, J.-E., Picard, D., Pichon, J.-M., Pont, V., Putaud, J.-P., Reisen, F., Sellegri, K., Sharma, S., Schauer, G., Sheridan, P., Sherman, J. P., Schwerin, A., Sohmer, R., Sorribas, M., Sun, J., Tulet, P., Vakkari, V., van Zyl, P. G., Velarde, F., Villani, P., Vratolis, S., Wagner, Z., Wang, S.-H., Weinhold, K., Weller, R., Yela, M., Zdimal, V., and Laj, P.: Seasonality of the particle number concentration and size distribution: a global analysis retrieved from the network of Global Atmosphere Watch

(GAW) near-surface observatories, Atmos. Chem. Phys., 21, 17185–17223, https://doi.org/10.5194/acp-21-17185-2021, 2021.

Runge, J., Petoukhov, V., Donges, J. F., Hlinka, J., Jajcay, N., Vejmelka, M., Hartman, D., Marwan, N., Paluš, M., and Kurths, J.: Identifying causal gateways and mediators in complex spatio-temporal systems, Nat. Commun., 6, 8502, https://doi.org/10.1038/ncomms9502, 2015.

Runge, J., Nowack, P., Kretschmer, M., Flaxman, S., and Sejdinovic, D.: Detecting and quantifying causal associations in large nonlinear time series datasets, Sci. Adv., 5, https://doi.org/10.1126/sciadv.aau4996, 2019.

Salma, I., Németh, Z., Weidinger, T., Kovács, B., and Kristóf, G.: Measurement, growth types and shrinkage of newly formed aerosol particles at an urban research platform, Atmos. Chem. Phys., 16, 7837–7851, https://doi.org/10.5194/acp-16-7837-2016, 2016a.

Salma, I., Németh, Z., Kerminen, V. M., Aalto, P., Nieminen, T., Weidinger, T., Molnár, Á., Imre, K., and Kulmala, M.: Regional effect on urban atmospheric nucleation, Atmos. Chem. Phys., 16, 8715–8728, https://doi.org/10.5194/acp-16-8715-2016, 2016b.

Samarasinghe, S. M., Deng, Y., and Ebert-Uphoff, I.: A causality-based view of the interaction between synoptic- And planetary-scale atmospheric disturbances, J. Atmos. Sci., 77, 925–941, https://doi.org/10.1175/JAS-D-18-0163.1, 2020.

Saunders, S. M., Jenkin, M. E., Derwent, R. G., and Pilling, M. J.: Protocol for the development of the Master Chemical Mechanism, MCM v3 (Part A): tropospheric degradation of non-aromatic volatile organic compounds, Atmos. Chem. Phys., 3, 161–180, https://doi.org/10.5194/acp-3-161-2003, 2003.

Schmale, J., Henning, S., Decesari, S., Henzing, B., Keskinen, H., Sellegri, K., Ovadnevaite, J., Pöhlker, M., Brito, J., Bougiatioti, A., Kristensson, A., Kalivitis, N., Stavroulas, I., Carbone, S., Jefferson, A., Park, M., Schlag, P., Iwamoto, Y., Aalto, P., Äijälä, M., Bukowiecki, N., Ehn, M., Fröhlich, R., Frumau, A., Herrmann, E., Herrmann, H., Holzinger, R., Kos, G., Kulmala, M., Mihalopoulos, N., Nenes, A., O'Dowd, C., Petäjä, T., Picard, D., Pöhlker, C., Pöschl, U., Poulain, L., Swietlicki, E., Andreae, M., Artaxo, P., Wiedensohler, A., Ogren, J., Matsuki, A., Soo Yum, S., Stratmann, F., Baltensperger, U., and Gysel, M.: Long-term cloud condensation nuclei number concentration, particle number size distribution and chemical composition measurements at regionally representative observatories, Atmos. Chem. Phys., 18, 2853–2881, https://doi.org/10.5194/acp-18-2853-2018, 2018.

Seinfeld, J. H. and Pandis, S. N.: Atmospheric chemistry and physics : from air pollution to climate change, 3rd edition, Wiley, 2016.

Sellar, A. A., Jones, C. G., Mulcahy, J. P., Tang, Y., Yool, A., Wiltshire, A., O'Connor, F. M., Stringer, M., Hill, R., Palmieri, J., Woodward, S., de Mora, L., Kuhlbrodt, T., Rumbold, S. T., Kelley, D. I., Ellis, R., Johnson, C. E., Walton, J., Abraham, N. L., Andrews, M. B., Andrews, T., Archibald, A. T., Berthou, S., Burke, E., Blockley, E., Carslaw, K., Dalvi, M., Edwards, J., Folberth, G. A., Gedney, N., Griffiths, P. T., Harper, A. B., Hendry, M. A., Hewitt, A. J., Johnson, B., Jones, A., Jones, C. D., Keeble, J., Liddicoat, S., Morgenstern, O., Parker, R. J., Predoi, V., Robertson, E., Siahaan, A., Smith, R. S., Swaminathan, R., Woodhouse, M. T., Zeng, G., and Zerroukat, M.: UKESM1: Description and Evaluation of the U.K. Earth System Model, J. Adv. Model. Earth Syst., 11, 4513–4558, https://doi.org/10.1029/2019MS001739, 2019.

Semeniuk, K. and Dastoor, A.: Current state of aerosol nucleation parameterizations for air-quality and climate modeling, Atmos. Environ., 179, 77–106, https://doi.org/10.1016/J.ATMOSENV.2018.01.039, 2018.

Sen, P. K.: Estimates of the Regression Coefficient Based on Kendall's Tau, J. Am. Stat. Assoc., 63, 1379–1389, https://doi.org/10.1080/01621459.1968.10480934, 1968.

Shiraiwa, M., Ueda, K., Pozzer, A., Lammel, G., Kampf, C. J., Fushimi, A., Enami, S., Arangio, A. M., Fröhlich-Nowoisky, J., Fujitani, Y., Furuyama, A., Lakey, P. S. J., Lelieveld, J., Lucas, K., Morino, Y., Pöschl, U., Takahama, S., Takami, A., Tong, H., Weber, B., Yoshino, A., and Sato, K.: Aerosol Health Effects from Molecular to Global Scales, Environ. Sci. Technol., 51, 13545–13567, https://doi.org/10.1021/acs.est.7b04417, 2017.

Simonen, P., Saukko, E., Karjalainen, P., Timonen, H., Bloss, M., Aakko-Saksa, P., Rönkkö, T., Keskinen, J., and Dal Maso, M.: A new oxidation flow reactor for measuring secondary aerosol formation of rapidly changing emission sources, Atmos. Meas. Tech., 10, 1519–1537, https://doi.org/10.5194/amt-10-1519-2017, 2017.

Simonen, P., Kalliokoski, J., Karjalainen, P., Rönkkö, T., Timonen, H., Saarikoski, S., Aurela, M., Bloss, M., Triantafyllopoulos, G., Kontses, A., Amanatidis, S., Dimaratos, A., Samaras, Z., Keskinen, J., Dal Maso, M., and Ntziachristos, L.: Characterization of laboratory and real driving emissions of individual Euro 6 light-duty vehicles – Fresh particles and secondary aerosol formation, Environ. Pollut., 255, 113175, https://doi.org/10.1016/j.envpol.2019.113175, 2019.

Soetaert, K., Petzoldt, T., and Setzer, R. W.: Solving Differential Equations in R: Package deSolve, J. Stat. Softw., 33, 1–25, https://doi.org/10.18637/jss.v033.i09, 2010.

Spirtes, P., Glymour, C. N., and Scheines, R.: Causation, prediction, and search., MIT Press, 543 pp., 2000.

Stohl, A., Aamaas, B., Amann, M., Baker, L. H., Bellouin, N., Berntsen, T. K., Boucher, O., Cherian, R., Collins, W., Daskalakis, N., Dusinska, M., Eckhardt, S., Fuglestvedt, J. S., Harju, M., Heyes, C., Hodnebrog, Hao, J., Im, U., Kanakidou, M., Klimont, Z., Kupiainen, K., Law, K. S., Lund, M. T., Maas, R., MacIntosh, C. R., Myhre, G., Myriokefalitakis, S., Olivié, D., Quaas, J., Quennehen, B., Raut, J. C., Rumbold, S. T., Samset, B. H., Schulz, M., Seland, Shine, K. P., Skeie, R. B., Wang, S., Yttri, K. E., and Zhu, T.: Evaluating the climate and air quality impacts of short-lived pollutants, Atmos. Chem. Phys., 15, 10529–10566, https://doi.org/10.5194/ACP-15-10529-2015, 2015.

Sulo, J., Lampilahti, J., Chen, X., Kontkanen, J., Nieminen, T., Kerminen, V. M., Petaja, T., Kulmala, M., and Lehtipalo, K.: Measurement report: Increasing trend of atmospheric ion concentrations in the boreal forest, Atmos. Chem. Phys., 22, 15223–15242, https://doi.org/10.5194/acp-22-15223-2022, 2022.

Tao, W. K., Chen, J. P., Li, Z., Wang, C., and Zhang, C.: Impact of aerosols on convective clouds and precipitation, Rev. Geophys., 50, https://doi.org/10.1029/2011RG000369, 2012.

Tegen, I., Neubauer, D., Ferrachat, S., Drian, C. S. Le, Bey, I., Schutgens, N., Stier, P., Watson-Parris, D., Stanelle, T., Schmidt, H., Rast, S., Kokkola, H., Schultz, M., Schroeder, S., Daskalakis, N., Barthel, S., Heinold, B., and Lohmann, U.: The global aerosol-climate model echam6.3-ham2.3 -Part 1: Aerosol evaluation, Geosci. Model Dev., 12, 1643–1677, https://doi.org/10.5194/gmd-12-1643-2019, 2019.

Textor, C., Schulz, M., Guibert, S., Kinne, S., Balkanski, Y., Bauer, S., Berntsen, T., Berglen, T., Boucher, O., Chin, M., Dentener, F., Diehl, T., Easter, R., Feichter, H., Fillmore, D., Ghan, S., Ginoux, P., Gong, S., Grini, A., Hendricks, J., Horowitz, L., Huang, P., Isaksen, I., Iversen, T., Kloster, S., Koch, D., Kirkevåg, A., Kristjansson, J. E., Krol, M., Lauer, A., Lamarque, J. F., Liu, X., Montanaro, V., Myhre, G., Penner, J., Pitari, G., Reddy, S., Seland, Stier, P., Takemura, T., and Tie, X.: Analysis and quantification of the diversities of aerosol life cycles within AeroCom, Atmos. Chem. Phys., 6, 1777–1813, https://doi.org/10.5194/ACP-6-1777-2006, 2006.

Textor, C., Schulz, M., Guibert, S., Kinne, S., Balkanski, Y., Bauer, S., Berntsen, T., Berglen, T., Boucher, O., Chin, M., Dentener, F., Diehl, T., Feichter, J., Fillmore, D., Ginoux, P., Gong, S., Grini, A., Hendricks, J., Horowitz, L., Huang, P., Isaksen, I. S. A., Iversen, T., Kloster, S., Koch, D., Kirkevåg, A., Kristjansson, J. E., Krol, M., Lauer, A., Lamarque, J. F., Liu, X., Montanaro, V., Myhre, G., Penner, J. E., Pitari, G., Reddy, M. S., Seland, Stier, P., Takemura, T., and Tie, X.: The effect of harmonized emissions on aerosol properties in global models - An AeroCom experiment, Atmos. Chem. Phys., 7, 4489–4501, https://doi.org/10.5194/acp-7-4489-2007, 2007.

Theil, H.: A Rank-Invariant Method of Linear and Polynomial Regression Analysis, I-III, Proc. van K. Ned. Akad. van Wet., 53, 386-392,521-525,1397-1412, 1950.

Tiitta, P., Leskinen, A., Hao, L., Yli-Pirilä, P., Kortelainen, M., Grigonyte, J., Tissari, J., Lamberg, H., Hartikainen, A., Kuuspalo, K., Kortelainen, A.-M., Virtanen, A., Lehtinen, K. E. J., Komppula, M., Pieber, S., Prévôt, A. S. H., Onasch, T. B., Worsnop, D. R., Czech, H., Zimmermann, R., Jokiniemi, J., and Sippula, O.: Transformation of logwood combustion emissions in a smog chamber: formation of secondary organic aerosol and changes in the primary organic aerosol upon daytime and nighttime aging, Atmos. Chem. Phys., 16, 13251–13269, https://doi.org/10.5194/acp-16-13251-2016, 2016.

Tissari, J., Lyyränen, J., Hytönen, K., Sippula, O., Tapper, U., Frey, A., Saarnio, K., Pennanen, A. S., Hillamo, R., Salonen, R. O., Hirvonen, M. R., and Jokiniemi, J.: Fine particle and gaseous emissions from normal and smouldering wood combustion in a conventional masonry heater, Atmos. Environ., 42, 7862–7873, https://doi.org/10.1016/j.atmosenv.2008.07.019, 2008.

Tsigaridis, K., Daskalakis, N., Kanakidou, M., Adams, P. J., Artaxo, P., Bahadur, R., Balkanski, Y., Bauer, S. E., Bellouin, N., Benedetti, A., Bergman, T., Berntsen, T. K., Beukes, J. P., Bian, H., Carslaw, K. S., Chin, M., Curci, G., Diehl, T., Easter, R. C., Ghan, S. J., Gong, S. L., Hodzic, A., Hoyle, C. R., Iversen, T., Jathar, S., Jimenez, J. L., Kaiser, J. W., Kirkeväg, A., Koch, D., Kokkola, H., H Lee, Y., Lin, G., Liu, X., Luo, G., Ma, X., Mann, G. W., Mihalopoulos, N., Morcrette, J. J., Müller, J. F., Myhre, G., Myriokefalitakis, S., Ng, N. L., O'donnell, D., Penner, J. E., Pozzoli, L., Pringle, K. J., Russell, L. M., Schulz, M., Sciare, J., Seland, Shindell, D. T., Sillman, S., Skeie, R. B., Spracklen, D., Stavrakou, T., Steenrod, S. D., Takemura, T., Tiitta, P., Tilmes, S., Tost, H., Van Noije, T., Van Zyl, P. G., Von Salzen, K., Yu, F., Wang, Z., Wang, Z., Zaveri, R. A., Zhang, H., Zhang, K., Zhang, Q., and Zhang, X.: The AeroCom evaluation and intercomparison of organic aerosol in global models, Atmos. Chem. Phys., 14, 10845–10895, https://doi.org/10.5194/acp-14-10845-2014, 2014.

Tunved, P., Ström, J., and Krejci, R.: Arctic aerosol life cycle: Linking aerosol size distributions observed between 2000 and 2010 with air mass transport and precipitation at Zeppelin station, Ny-Ålesund, Svalbard, Atmos. Chem. Phys., 13, 3643–3660,

https://doi.org/10.5194/acp-13-3643-2013, 2013.

Vanhanen, J., Mikkilä, J., Lehtipalo, K., Sipilä, M., Manninen, H. E., Siivola, E., Petäjä, T., and Kulmala, M.: Particle Size Magnifier for Nano-CN Detection, Aerosol Sci. Technol., 45, 533–542, https://doi.org/10.1080/02786826.2010.547889, 2011.

Wang, S. C. and Flagan, R. C.: Scanning electrical mobility spectrometer, Aerosol Sci. Technol., 13, 230–240, https://doi.org/10.1080/02786829008959441, 1990.

WCRP Coupled Model Intercomparison Project (CMIP): https://www.wcrp-climate.org/wgcm-cmip, last access: 23 March 2023.

Whitby, K. T.: The physical characteristics of sulfur aerosols, Atmos. Environ., 12, 135–159, https://doi.org/10.1016/0004-6981(78)90196-8, 1978.

Wihersaari, H., Pirjola, L., Karjalainen, P., Saukko, E., Kuuluvainen, H., Kulmala, K., Keskinen, J., and Rönkkö, T.: Particulate emissions of a modern diesel passenger car under laboratory and real-world transient driving conditions, Environ. Pollut., 265, 114948, https://doi.org/10.1016/j.envpol.2020.114948, 2020.

Williams, J., De Reus, M., Krejci, R., Fischer, H., and Ström, J.: Application of the variability-size relationship to atmospheric aerosol studies: Estimating aerosol lifetimes and ages, Atmos. Chem. Phys., 2, 133–145, https://doi.org/10.5194/ACP-2-133-2002, 2002.

Wongchokprasitti, C.: rcausal: R-Causal Library, https://rdrr.io/github/bd2kccd/r-causal/man/rcausal.html, 2019.

Yli-Juuti, T., Mielonen, T., Heikkinen, L., Arola, A., Ehn, M., Isokääntä, S., Keskinen, H.-M., Kulmala, M., Laakso, A., Lipponen, A., Luoma, K., Mikkonen, S., Nieminen, T., Paasonen, P., Petäjä, T., Romakkaniemi, S., Tonttila, J., Kokkola, H., and Virtanen, A.: Significance of the organic aerosol driven climate feedback in the boreal area, Nat. Commun., 12, 5637, https://doi.org/10.1038/s41467-021-25850-7, 2021.

Yttri, K. E., Canonaco, F., Eckhardt, S., Evangeliou, N., Fiebig, M., Gundersen, H., Hjellbrekke, A. G., Lund Myhre, C., Matthew Platt, S., Prevot, A. S. H., Simpson, D., Solberg, S., Surratt, J., Tørseth, K., Uggerud, H., Vadset, M., Wan, X., and Aas, W.: Trends, composition, and sources of carbonaceous aerosol at the Birkenes Observatory, northern Europe, 2001-2018, Atmos. Chem. Phys., 21, 7149–7170, https://doi.org/10.5194/acp-21-7149-2021, 2021.

Zavala, M., Herndon, S. C., Slott, R. S., Dunlea, E. J., Marr, L. C., Shorter, J. H., Zahniser, M., Knighton, W. B., Rogers, T. M., Kolb, C. E., Molina, L. T., and Molina, M. J.: Characterization of on-road vehicle emissions in the Mexico City Metropolitan Area using a mobile laboratory in chase and fleet average measurement modes during the MCMA-2003 field campaign, Atmos. Chem. Phys., 6, 5129–5142, https://doi.org/10.5194/acp-6-5129-2006, 2006.

Paper I

Atmos. Chem. Phys., 22, 12873–12905, 2022
https://doi.org/10.5194/acp-22-12873-2022

Atmospheric Chemistry and Physics
Open Access
EGU

Comparison of particle number size distribution trends in ground measurements and climate models

Ville Leinonen[1], Harri Kokkola[2], Taina Yli-Juuti[1], Tero Mielonen[2], Thomas Kühn[1,2,a], Tuomo Nieminen[3,4], Simo Heikkinen[1], Tuuli Miinalainen[1], Tommi Bergman[5,6], Ken Carslaw[7], Stefano Decesari[8], Markus Fiebig[9], Tareq Hussein[3,10], Niku Kivekäs[5], Radovan Krejci[11], Markku Kulmala[3], Ari Leskinen[2,1], Andreas Massling[12], Nikos Mihalopoulos[13], Jane P. Mulcahy[14], Steffen M. Noe[15], Twan van Noije[6], Fiona M. O'Connor[14], Colin O'Dowd[16], Dirk Olivie[17], Jakob B. Pernov[12,b], Tuukka Petäjä[3], Øyvind Seland[17], Michael Schulz[17], Catherine E. Scott[7], Henrik Skov[12], Erik Swietlicki[18], Thomas Tuch[19], Alfred Wiedensohler[19], Annele Virtanen[1], and Santtu Mikkonen[1,20]

[1]Department of Applied Physics, University of Eastern Finland, Kuopio, Finland
[2]Finnish Meteorological Institute, Kuopio, Finland
[3]Institute for Atmospheric and Earth System Research (INAR/Physics), Faculty of Science, University of Helsinki, Helsinki, Finland
[4]Institute for Atmospheric and Earth System Research (INAR/Forest Sciences), Faculty of Agriculture and Forestry, University of Helsinki, Helsinki, Finland
[5]Finnish Meteorological Institute, Helsinki, Finland
[6]Royal Netherlands Meteorological Institute, De Bilt, the Netherlands
[7]Institute for Climate and Atmospheric Science, School of Earth and Environment, University of Leeds, Leeds, UK
[8]Institute of Atmospheric and Climate Sciences (ISAC) of the National Research Council of Italy (CNR), Bologna, Italy
[9]Department of Atmospheric and Climate Research, NILU – Norwegian Institute for Air Research, Kjeller, Norway
[10]Laboratory of Environmental and Atmospheric Research (EARL), Department of Physics, the University of Jordan, Amman 11942, Jordan
[11]Department of Environmental Science, Bolin Centre for Climate Research, Stockholm University, Stockholm, Sweden
[12]Department of Environmental Science, iClimate, Aarhus University, Aarhus, Denmark
[13]Environmental Chemical Processes Laboratory (ECPL), Chemistry Department, University of Crete, Heraklion, Crete, Greece
[14]Met Office Hadley Centre, Exeter, United Kingdom
[15]Institute of Forestry and Engineering, Estonian University of Life Sciences, Tartu, Estonia
[16]School of Natural Sciences, Centre for Climate and Air Pollution Studies, Ryan Institute, National University of Ireland Galway, Galway, Ireland
[17]Norwegian Meteorological Institute, Oslo, Norway
[18]Division of Nuclear Physics, Physics Department, Lund University, Lund, Sweden
[19]Leibniz Institute for Tropospheric Research, Leipzig, Germany
[20]Department of Environmental and Biological Sciences, University of Eastern Finland, Kuopio, Finland
[a]now at: Finnish Meteorological Institute, Helsinki, Finland
[b]now at: Extreme Environments Research Laboratory, École Polytechnique fédérale de Lausanne, 1951 Sion, Switzerland

Correspondence: Annele Virtanen (annele.virtanen@uef.fi) and Ville Leinonen (ville.j.leinonen@uef.fi)

Received: 22 March 2022 – Discussion started: 24 March 2022
Revised: 26 August 2022 – Accepted: 26 August 2022 – Published: 6 October 2022

Published by Copernicus Publications on behalf of the European Geosciences Union.

Abstract. Despite a large number of studies, out of all drivers of radiative forcing, the effect of aerosols has the largest uncertainty in global climate model radiative forcing estimates. There have been studies of aerosol optical properties in climate models, but the effects of particle number size distribution need a more thorough inspection. We investigated the trends and seasonality of particle number concentrations in nucleation, Aitken, and accumulation modes at 21 measurement sites in Europe and the Arctic. For 13 of those sites, with longer measurement time series, we compared the field observations with the results from five climate models, namely EC-Earth3, ECHAM-M7, ECHAM-SALSA, NorESM1.2, and UKESM1. This is the first extensive comparison of detailed aerosol size distribution trends between in situ observations from Europe and five earth system models (ESMs). We found that the trends of particle number concentrations were mostly consistent and decreasing in both measurements and models. However, for many sites, climate models showed weaker decreasing trends than the measurements. Seasonal variability in measured number concentrations, quantified by the ratio between maximum and minimum monthly number concentration, was typically stronger at northern measurement sites compared to other locations. Models had large differences in their seasonal representation, and they can be roughly divided into two categories: for EC-Earth and NorESM, the seasonal cycle was relatively similar for all sites, and for other models the pattern of seasonality varied between northern and southern sites. In addition, the variability in concentrations across sites varied between models, some having relatively similar concentrations for all sites, whereas others showed clear differences in concentrations between remote and urban sites. To conclude, although all of the model simulations had identical input data to describe anthropogenic mass emissions, trends in differently sized particles vary among the models due to assumptions in emission sizes and differences in how models treat size-dependent aerosol processes. The inter-model variability was largest in the accumulation mode, i.e. sizes which have implications for aerosol–cloud interactions. Our analysis also indicates that between models there is a large variation in efficiency of long-range transportation of aerosols to remote locations. The differences in model results are most likely due to the more complex effect of different processes instead of one specific feature (e.g. the representation of aerosol or emission size distributions). Hence, a more detailed characterization of microphysical processes and deposition processes affecting the long-range transport is needed to understand the model variability.

1 Introduction

Atmospheric aerosols form one of the most important components that cool the climate, counteracting heating by increased greenhouse gas concentrations (Forster et al., 2021). Aerosol–radiation interactions (ARIs) and aerosol–cloud interactions (ACIs) greatly depend on particle concentration, size distribution, and chemical properties and altogether their ability to activate to cloud droplets. On the other hand, the ability of large-scale climate models to predict the aerosol direct and indirect radiative forcing depends mainly on their ability to describe the spatial and temporal distribution and characteristics of the atmospheric aerosol population. Especially the strength of cooling due to ACI depends on the number concentration of particles large enough to activate to cloud droplets (Dusek et al., 2006). The ability of global-scale models to reproduce the trends of these particles is important for reproducing the changes in aerosol radiative forcing, and further on, diagnosing the radiative forcing from anthropogenic emissions. Improvement of aerosol radiative forcing estimates, which are still the most uncertain part of total radiative forcing estimates (Forster et al., 2021), would improve the estimate of total radiative forcing, the climate sensitivity, and future climate change (Myhre et al., 2013).

It is likely that there will be changes in trends of aerosol concentrations in future. It has been proposed that both air pollution and climate change mitigation measures will lead to decreased emissions of anthropogenic aerosols (Smith and Bond, 2014). In addition, a global-warming-driven temperature increase affects the emissions of biogenic volatile organic compounds (BVOCs) and formation of secondary organic aerosol and through that concentrations and size distribution characteristics of atmospheric aerosols (Arneth et al., 2010; Hellén et al., 2018; Mielonen et al., 2012; Paasonen et al., 2013; Peñuelas and Staudt, 2010; Yli-Juuti et al., 2021). Atmospheric aerosols have already undergone significant changes caused by tightened air pollution control measures. For example, Hamed et al. (2010) showed a clear reduction in aerosol concentrations in Melpitz, Germany, between 1996 and 2006, which was associated with sulfur dioxide (SO_2) emission reductions in Europe. Several other studies have reported significant changes in the atmospheric aerosol population showing clear negative trends in particle concentrations in different size ranges (Mikkonen et al., 2020; Sun et al., 2020) as well as for total number concentration and mass (Asmi et al., 2013; Collaud Coen et al., 2013). The change in aerosol optical properties has been consistent with these observations, with aerosol optical depth showing a decreasing trend over Europe and the Arctic (Brei-

der et al., 2017; Collaud Coen et al., 2013, 2020; Schmale et al., 2022).

To decrease the uncertainty in climate models related to ARI and ACI, model constraints and comparisons of observations and models are needed. Observations of particle number concentrations and their optical properties, as well as radiation measurements, help to constrain how well climate models simulate the climate effects of aerosols. Storelvmo et al. (2018) showed that models from the 5th Coupled Model Intercomparison Project (CMIP5) do not reproduce the observed trends in incoming surface solar radiation (SSR). Moseid et al. (2020) showed that the same holds also for the CMIP6 models. Since SSR is affected by aerosol extinction and cloud cover, the analysis of Moseid et al. (2020) indicated that the discrepancy between models and observations was related, at least partly, to erroneous aerosol and aerosol precursor emission inventories. Mortier et al. (2020) studied the trends of particle optical properties and found that the trends were mostly decreasing for measured optical parameters, and climate models mainly showed relatively similar trends. However, models usually underestimate aerosol optical parameters such as optical thickness and scattering (Gliß et al., 2021). These findings indicate a need for further analysis comparing observed trends of the aerosol population with trends from global models.

Interpretation and analysis of comparison of in situ aerosol observations with global model outputs is not straightforward due to differing temporal and spatial scales represented. In situ measurements represent one point, while a global-scale model simulates average aerosol properties within a grid box, which can be on the order of 100 km in horizontal resolution and on the order of a few tens of metres in the vertical at the level of the observations. The differences in scale make one-to-one comparison of models and observations at a specific time incoherent, unless the in situ observations represent the mean value of the model grid box area well. On the other hand, the proximity of the observation site to emission sources, changes in local wind speed and direction, and the dynamics of the boundary layer can cause large fluctuations at the measurement site. This local variation cannot be captured with the coarse resolution of global models and may not be representative of a larger area. However, using long time series and a large number of observational sites allows for bridging the gap between the scales (Schutgens et al., 2017). In addition, co-locating the observations and model data in time allows for a closer comparison of the two (Schutgens et al., 2016).

In this study, we perform an aerosol number size distribution trend analysis for observations from 21 European and Arctic sites, analyse the trends of particle mode properties (number concentration, geometric mean diameter, and geometric standard deviation), and compare 13 sites with simulations from five climate models over the period of 2001–2014. In addition, we compare the seasonal cycle representation of the models to the measured seasonal cycles in different regions of Europe.

2 Data and methods

We investigated the characteristics of particle number size distributions by separating the size distribution into log-normal modes (nucleation, Aitken, and accumulation mode). We analysed the number concentration, geometric mean diameter, and geometric standard deviation and their trends for sites representing polar (Villum, Zeppelin), Arctic remote (Pallas, Värriö), rural (Birkenes II, Hohenpeißenberg, Hyytiälä, Järvselja, Melpitz, San Pietro Capofiume), rural regional background (K-Puszta, Neuglobsow, Waldhof, Vavihill), urban (Annaberg-Buchholz, Helsinki, Leipzig, Puijo), coastal remote (Mace Head, Finokalia), and high-altitude (Schauinsland) environments. Finally, to evaluate how well current climate models can reproduce the observed aerosol physical trends and seasonal variability, we compared observations from 13 selected sites with results from 5 different climate models. The selection criterion for measurement–climate model comparison was for the measurement sites to provide at least 7 years of observational data between 2001 and 2014. See Sect. 2.1 and especially 2.1.1 for more details about measurement data and Sect. 2.1.4 and 2.2 for model comparison.

Measurement data sets differ in the reported aerosol size range and time resolution. Furthermore, the climate modelling data used (see Sect. 2.2) are averages over the grid boxes containing the coordinates of the respective measurement sites. It is therefore not straightforward to compare measurement data of different locations or to compare measured and modelled data. In order to make such comparisons meaningful, the data must be adjusted and modified in a consistent manner. In Sect. 2.1, we go through the data modification process used and explain and verify the chosen approaches and methods.

Daily and monthly averages of number size distribution parameters are used in the trend analysis (see Sect. 2.3). We are using the dynamic linear model (DLM) (Petris et al., 2009) to evaluate short-term changes in trends (based on the data of daily averages) and Sen–Theil estimators for long-term trend estimation (monthly averages) and comparing with the modelled trends of climate models (monthly averages). Seasonality of observed and climate model output number concentrations of each aerosol distribution mode is compared with seasonality metrics introduced in Rose et al. (2021) using monthly data.

2.1 Data from measurement sites

2.1.1 Measurement sites

Data sets used in this study are partly the same as in the study of Nieminen et al. (2018) and are supplemented by newer

data from the Aerosol, Clouds and Trace Gases Research Infrastructure (ACTRIS) sites (https://www.actris.eu/, last access: 9 October 2019) and SmartSmear (https://smear.avaa.csc.fi/, last access: 31 July 2019). From ACTRIS sites, we have also included new sites that were not included in Nieminen et al. (2018) (Annaberg-Buchholz, Birkenes II, Leipzig, Neuglobsow, Puijo, Schauinsland, and Waldhof) and expanded the data length by including recent years that were missing in Nieminen et al. (2018). In addition, data from Villum Research Station at Station Nord (Villum) and some recent years' data from Puijo and San Pietro Capofiume were received directly from the research groups operating the sites.

In this study, we have used only long-term observations (minimum of 6 years of measurement data) of particle number size distributions. The length of the data sets (6–22 years) and corresponding data coverage (59.6 %–98.4 % of the days of the measurement period) varies between the sites (see Fig. S1 in the Supplement). The measurement sites used in this study are listed in Table 1. For model comparison, in turn, we have included only those sites that have at least 7 years of a common time period with the model simulations (2001–2014) and sufficient data coverage (i.e. coverage $> 50\,\%$ of days). In Table 1, the sites are presented in two separate lists: the first list shows the sites that are used in both trend analysis and comparisons of observational and model trends, and the second list shows sites that were used only in trend analysis.

In this study we use commonly used site classes (polar, high-altitude, remote, rural, and urban) following Nieminen et al. (2018). Site environment classification of each site is adapted from Nieminen et al. (2018) for those sites that were included in their study. For other sites, we have used classifications from the literature (Sun et al., 2020, for German sites; Yttri et al., 2021, for Birkenes II; Leskinen et al., 2012, for Puijo; Schmale et al., 2018, for Vavihill; and Nguyen et al., 2016, for Villum) for environment classification and adjusted their classification according to Nieminen et al. (2018). A detailed description of each site, including the facility and environment descriptions, can be found in the literature (see Table 1).

It should be noted that there is a significant variation in the detected size ranges of the measurement instruments between the sites and within one site over the analysed time period (see Table 1). For those sites where the size range has varied over the investigated time period, we have limited the analysis only to the size range that has been measured over the whole analysis period. This size range is site-specific to maximize the number of data at each site. We have interpolated the data to site-specific, common size resolution; i.e. the size bins of size distribution data were the same for the whole time period. Measurement data size bins were interpolated because otherwise, the size bins can vary during time series, and hence, for example, the calculated modal and sectional representations (see definitions from Sect. 2.1.4) would be calculated from the different size bins.

When the in situ observations and large-scale models are compared, it is important to consider how representative the stations are for the larger areas surrounding them. The polar and remote sites (Zeppelin, Pallas, and Värriö) as well as rural site Hyytiälä can be considered to be representative of a larger regional fingerprint (Hari and Kulmala, 2005; Kyrö et al., 2014; Lohila et al., 2015; Tunved et al., 2013), and no large cities are located close to these sites. It should be noted that the Värriö site can be impacted by pollution transported from the Kola Peninsula mining and industrial areas (200–300 km north-east from the station) at times (Kyrö et al., 2014). Mace Head represents marine environment excellently when the air masses arrive from the Atlantic but on the other hand can be affected by the continental outflow as well (O'Connor et al., 2008). The urban sites Helsinki and Puijo (as urban sites in general) are affected by strong, local sources such as traffic or local industrial activity, and the diurnal variation in the representativeness to the larger areas might be significant (Hussein et al., 2008; Leskinen et al., 2012). The rural (Hohenpeißenberg, K-Puszta, Melpitz, San Pietro Capofiume, Vavihill) sites represent European background well, but their representativeness for the model grid box depends on the placement of the grid box and on how large the fraction of the grid box covered by large cities is. It should be noted that Hohenpeißenberg is located at high altitude (988 m) and is classified as a mountain site in some of the earlier studies (e.g. Rose et al., 2021), while Nieminen et al. (2018) classified it as a rural site.

2.1.2 Fitting of log-normal modes to particle number size distributions

Multimodal log-normal size distributions were fitted to the measured data, and the trend analysis was performed on the mode parameters. We fitted three log-normal modes (nucleation, Aitken, and accumulation) to the measured data. Before fitting the modes, we first performed a visual examination of the size distribution time series to detect clear errors in the data that could affect the results of the fitting process, e.g. the absence of some modes in the fit due to problems in the data. For example, if a substantial fraction (over 20 % of the size bins) of the number size distribution was not measured during a specific size distribution measurement, the whole distribution was removed. In addition, measurement sites have performed the quality checks routinely on the data before transferring data to the database or server.

Modes were fitted for each particle size distribution using an automatic mode-fitting algorithm (Hussein et al., 2005). Briefly, the algorithm fits a combination of one to three log-normal distributions to the particle number size distribution data separately for each time step at each location. The algorithm assumes three log-normal modes as a starting point and automatically reduces the number of modes if any of the overlapping conditions for modes is true (for more details, see Hussein et al., 2005). For each mode, the algorithm re-

Table 1. Information of measurement sites used in this study. Site name, site environment type, coordinates, altitude in metres above sea level, time period, and size range (rounded to the nearest nanometre for minimum size and nearest 10 nm for maximum size) covered.

Sites in both trend analysis and model comparison						
Site name	Environment	Location	Altitude (m)	Time period	Size range (nm)	Reference
Helsinki, Finland	Urban	60°12′ N 24°58′ E	26	2005–2018	3–1000	Hussein et al. (2008)
Hohenpeissenberg, Germany	Rural	47°48′ N 11°1′ E	988	2008–2018	13–800	Birmili et al. (2003)
Hyytiälä, Finland	Rural	61°51′ N 24°17′ E	181	1996–2018	3–500	Hari and Kulmala (2005)
K-Puszta, Hungary	Rural	46°58′ N 19°33′ E	125	2008–2018	7–710	Salma et al. (2016)
Puijo, Finland	Urban	62°55′ N 27°40′ E	306	2005–2015	10–500	Leskinen et al. (2012)
Mace Head, Ireland	Remote	53°12′ N 9°48′ W	10	2005–2012	21–500	O'Connor et al. (2008)
Melpitz, Germany	Rural	51°32′ N 12°54′ E	87	2008–2018	5–800	Hamed et al. (2010)
Pallas, Finland	Remote	67°58′ N 24°7′ E	565	2008–2017	7–430	Lohila et al. (2015)
San Pietro Capofiume, Italy	Rural	44°39′ N 11°37′ E	11	2002–2015	3–630	Hamed et al. (2007)
Schauinsland, Germany	High-altitude	47°55′ N 7°55′ E	1205	2006–2018	10–600	Birmili et al. (2016)
Vavihill, Sweden	Rural	56°1′ N 13°9′ E	172	2001–2017	3–860	Schmale et al. (2018)
Värriö, Finland	Remote	67°45′ N 29°36′ E	390	1998–2018	8–400	Kyrö et al. (2014)
Zeppelin, Norway	Polar	78°56′ N 11°53′ E	474	2008–2018	10–800	Tunved et al. (2013)
Sites in trend analysis						
Site name	Environment	Location	Altitude (m)	Time period	Size range (nm)	Reference
Annaberg-Buchholz, Germany	Urban	50°34′ N 12°59′ E	545	2012–2018	10–800	Birmili et al. (2016)
Birkenes II, Norway	Rural	58°23′ N 8°15′ E	219	2010–2018	10–550	Yttri et al. (2021)
Finokalia, Greece	Remote	35°23′ N 25°40′ E	235	2011–2018	9–760	Mihalopoulos et al. (1997)
Järvselja, Estonia	Rural	58°16′ N 27°16′ E	36	2012–2017	3–10 000	Noe et al. (2015)
Leipzig, Germany	Urban	51°21′ N 12°26′ E	118	2010–2018	10–800	Birmili et al. (2016)
Neuglobsow, Germany	Rural	53°8′ N 13°2′ E	70	2012–2018	10–800	Birmili et al. (2016)
Waldhof, Germany	Rural	52°48′ N 10°45′ E	75	2009–2018	10–800	Birmili et al. (2016)
Villum, Greenland	Polar	81°36′ N 16°40′ W	30	2010–2018	9–905	Nguyen et al. (2016)

turns three parameters: geometric mean diameter, D_p; geometric variance, σ_p^2; and mode number concentration, N.

For each fit, a quality check was performed. Firstly, we checked that the number concentrations of the fitted modes were reasonable. We used measured size bin diameters as a limit and omitted those cases where the geometric mean diameter of the mode was smaller than the smallest size bin or larger than the largest size bin from the analysis. To avoid possible overestimation of the number concentration of the modes, we assigned the number concentration of the missing or removed modes to be zero, with missing geometric diameter and geometric standard deviation.

We noticed that in cases where the smallest size bin of the measured size distribution had a high number concentration, the mode-fitting algorithm did not perform well and, instead, fitted a nucleation mode that had an unreasonably high number concentration and often also a geometric mean diameter outside of the measured size range. The reason for this was that the geometric mean diameter of the nucleation mode was smaller than the smallest detected size of the instrument, especially in cases where the smallest detected size was relatively large. For the nucleation mode, this limitation removed a median of 17.8 % of the fitted nucleation modes amongst all sites, ranging from 0 % to 41.1 % (Mace Head) between sites. For the accumulation mode, a similar phenomenon was observed, resulting in high number concentrations for large diameters near the largest detected size, although this was less likely (< 0.1 % of the fitted accumulation modes).

The fitted modes were sorted into three categories – nucleation, Aitken, and accumulation mode – based on their geometric mean diameter. In the case of three fitted modes, the modes were arranged based on geometric mean diameters, with one mode always being assigned to each category. In cases with one or two fitted modes, the assignment was primarily based on the mean diameter of the mode. Here a cut-off of 20 nm was used for the fitted geometric mean diameter to distinguish between nucleation and Aitken modes, and a cut-off of 100 nm was used to distinguish between Aitken and accumulation modes. Sometimes two fitted modes both fell within the same category. In such cases, the mode was assigned to categories based on the diameter. If both modes had diameters between 20 and 100 nm (1.7 % of the cases), the mode with a diameter farther from those cut-off points was assigned to be Aitken mode, and the other mode, depending on its diameter, was assigned to be nucleation or accumulation mode. If both modes had diameters larger than

100 nm (0.4 % of the cases), the mode with the larger diameter was assigned to accumulation mode and the mode with the smaller diameter to Aitken mode. There were no cases where both modes had diameters below 20 nm.

The time resolution of the measured size distributions, and consequently the fitted modes, varied between sites and ranged from 3 to 60 min. For further analysis, we calculated daily means for each fitted mode parameter (i.e. N, D_p, and σ). For the mean to be calculated, there had to be at least 50 % of measurements available for a day (i.e. 12 h of data).

We further studied when a fraction of the different modes was missing at each site. The absence of a fitted mode at certain time points was dependent on the mode (nucleation, Aitken, or accumulation) and site. The absence was most probably caused by low concentrations of particles within the mode size range. The Aitken mode was most often present, and the nucleation mode was most often missing. Daily percentages of mode occurrence, i.e. in which fraction of measurements a certain mode was fitted for each day, for each measurement site are presented in Table 2 and Figs. S2 and S3. For Aitken and accumulation modes, the mode occurrence was more than 80 % for most of the days at all sites and was close to 100 % (i.e. mode was fitted for every observation) at most of the sites. For the nucleation mode, the mean mode occurrence was around 80 %; however, there are sites where the occurrence was much lower. This can be due to limitations of size distribution measurements for nucleation mode particles (size range starting from > 10 nm) or lack of nucleation mode particles, e.g. due to meteorological or emission-related reasons. The latter is suggested by observations of nucleation occurrence in Fig. S2: urban sites had a reasonably high coverage also in the nucleation mode, whereas remote sites had days during which the nucleation mode was fitted for only a few or even zero measurement points per day. More detailed information about coverage as a function of month and hour of day is presented in Fig. S3. There were differences in nucleation mode coverage during a day and during a year, nucleation mode most often being fitted after midday. However, the patterns were not uniform for all the sites, and especially for Mace Head, the lower limit of the detected particle size most probably affected the results.

To conclude, the absence of modes did not drastically affect the daily mean of observed modes in Aitken and accumulation modes. As the fraction of fitted nucleation modes is smaller than for Aitken and accumulation modes, results for nucleation mode number concentrations are more uncertain compared to results for the other modes, which should be kept in mind when interpreting the results.

For comparison between climate models and observations, we also computed monthly means (for trend analysis) and seasonal medians (for SeasC – ratio of maximum and minimum of seasonal median values – calculation; see Supplement) of the fitted log-normal modes to the observational data described above. As global model results were monthly means, the same time resolution was also applied for the mode data. Monthly means of the measured data were calculated using the daily averaged data, with the limitation that at least five daily mean values per month were required. This limitation removed only 2 months from the entire data set, in addition to the months that were completely missing from the observational data. Seasonal means and seasonal medians were computed using monthly means with at least two monthly means per season being required.

2.1.3 Remapping measurement data sets for comparison with climate models

As shown later in the results section, the mean diameters of the fitted modes are larger than the corresponding diameters or bins used in climate models. This might affect the model–observation comparison results, especially for the nucleation mode, where the relative difference between the diameters of fitted modes and model modes is largest. Therefore, we calculated separate representations of the measurement data, which are more directly comparable to the model results: for the modal and sectional aerosol schemes, the measurement data were re-binned using the model limits. For comparison, with the Sectional Aerosol module for Large Scale Applications (SALSA), the measured size bins with a mean geometrical diameter of 3 to 7.7 nm were assigned to the nucleation mode. This size range corresponds to the limits of the smallest size bin in a SALSA (Kokkola et al., 2018). Measured size bins from 7.7 to 50 nm (corresponding to the second- and third-smallest size bins in SALSA) were assigned to the Aitken mode and from 50 to 700 nm (fourth- to sixth-smallest size bins in SALSA) to the accumulation mode. In the modal representation for comparison with the modal models, the corresponding size limits were 3 to 10 nm for nucleation, 10 to 100 nm for Aitken, and 100 to 1000 nm for accumulation mode. As can be seen from Table 1, the corresponding diameter range of each mode category from the models is not fully captured by the measurements at every site. If measurements were covering only a part of the model's diameter range, that part has been used as a representative mode from measurements if there are at least three size bins of measurement data available. This limitation was used because the number concentrations from one or two bins have a large variance, resulting in very uncertain trends. If there were fewer bins or no measurement data available, the corresponding nucleation mode is not represented in the results section. For Aitken and accumulation modes, there were always enough data to calculate representative modes, even though the accumulation mode is not always measured up to the diameter of 1000 nm.

2.2 Data from climate models

We used climate model data from EC-Earth3-AerChem (van Noije et al., 2021), the Norwegian Earth System Model NorESM1.2 (Kirkevåg et al., 2018), and the UK's Earth Sys-

Table 2. Daily median and mean coverage and the standard deviation of the coverage of the fitted nucleation, Aitken, and accumulation modes at measurement sites during the whole measurement time series.

Site	Nucleation modes fitted			Aitken modes fitted			Accumulation modes fitted		
	(Percent of observations per day)								
	Median	Mean	SD	Median	Mean	SD	Median	Mean	SD
Annaberg-Buchholz	70.8	63.6	26.4	100.0	99.3	2.2	100.0	95.4	7.3
Birkenes II	29.2	31.1	22.7	100.0	99.3	3.4	100.0	93.2	10.6
Finokalia	45.8	47.1	23.7	100.0	99.6	2.2	100.0	98.6	4.8
Helsinki	91.6	88.1	11.4	100.0	98.6	3.1	93.1	89.0	11.7
Hohenpeißenberg	54.2	55.1	22.1	100.0	99.4	2.8	100.0	95.9	8.4
Hyytiälä	72.9	70.5	18.9	100.0	98.8	3.8	99.3	95.7	7.5
Järvselja	46.0	47.7	19.2	99.0	96.8	5.4	96.8	90.5	13.6
K-Puszta	60.0	59.5	20.9	100.0	99.3	2.3	100.0	97.8	5.0
Leipzig	69.6	66.7	19.0	100.0	99.0	2.7	100.0	95.7	7.3
Mace Head	20.8	28.5	28.1	100.0	100.0	0.2	100.0	98.6	4.4
Melpitz	78.3	74.7	18.3	100.0	98.7	3.3	100.0	96.7	6.9
Neuglobsow	41.7	43.0	21.6	100.0	99.5	2.3	100.0	97.0	6.6
Pallas	52.9	51.6	23.5	100.0	96.5	8.7	100.0	94.6	8.6
Puijo	55.0	54.5	16.8	100.0	98.1	3.6	97.5	93.1	9.7
San Pietro Capofiume	78.5	76.5	15.9	99.3	97.9	3.4	97.2	93.8	8.5
Schauinsland	58.3	57.6	22.1	100.0	99.3	2.9	100.0	95.9	8.1
Värriö	36.1	37.5	21.0	100.0	97.9	5.8	100.0	97.3	5.8
Vavihill	82.6	77.7	18.7	100.0	99.0	4.0	100.0	95.1	11.2
Villum	33.7	36.4	22.1	100.0	97.4	7.5	100.0	96.6	9.3
Waldhof	66.7	65.9	21.1	100.0	99.2	2.9	100.0	96.6	7.0
Zeppelin	40.0	41.7	25.5	100.0	97.0	7.4	100.0	94.1	11.9

tem Model UKESM1 (Sellar et al., 2019), which participated in model simulations carried out within the European-Union-funded project CRESCENDO (Coordinated Research in Earth Systems and Climate: Experiments, Knowledge, Dissemination and Outreach). CRESCENDO simulations ran from the year 2000 to 2014, except for NorESM1.2, which ran from 2001 to 2014. All the models were run in atmosphere-only configuration with sea surface temperatures and sea ice concentrations prescribed as in the Atmospheric Model Intercomparison Project (AMIP) simulation of the Coupled Model Intercomparison Project Phase 6 (CMIP6). The climate models provided monthly values for the aerosol number size distribution, making the data useful for comparison against observations. In addition, we ran two configurations of the global aerosol–chemistry–climate model ECHAM6.3-HAMMOZ2.3-MOZ1.0, one with the M7 modal aerosol model (Tegen et al., 2019) and one with the sectional aerosol model SALSA (Kokkola et al., 2018). Specific features and the aerosol representation of each model are described in the following sections and summarized in Table 3.

From the global model calculations, we selected results for grid boxes containing the coordinates of the respective measurement sites and calculated the number concentrations of nucleation, Aitken, and accumulation mode particles. If both soluble and insoluble particle concentrations were provided for the mode, the sum of those has been used as the total number concentration of that mode.

2.2.1 EC-Earth3

The atmospheric component of the global climate model EC-Earth3-AerChem (van Noije et al., 2021) consists of a modified version of the general circulation model used in the Integrated Forecasting System (IFS) cycle 36r4 from the European Centre for Medium-Range Weather Forecasts (ECMWF) and the aerosol and chemistry model TM5. The IFS model version applied in EC-Earth3-AerChem has a horizontal resolution of TL255 (i.e. a spectral truncation at wavenumber 255 with a linear N128 reduced Gaussian grid, corresponding to a spacing of about 80 km) and uses 91 hybrid sigma-pressure levels in the vertical direction with a model top at 0.01 hPa. TM5 uses an atmospheric grid with a reduced resolution of $2^\circ \times 3^\circ$ (latitude $\times$ longitude) and 34 vertical layers extending to ~ 0.1 hPa. The data exchange between the two model components is governed by the OASIS coupler.

The aerosol scheme of TM5 is based on the modal aerosol microphysical scheme M7 from Vignati et al. (2004), which includes sulfate, black carbon, organic aerosols, sea salt, and mineral dust. In TM5, the formation of secondary organic aerosols is described as in Bergman et al. (2022).

Table 3. Summary of model set-up, emissions, and aerosol microphysics in five climate models used in this study.

Model set-up				
Model name	Description of size distribution	Horizontal resolution	Vertical resolution	Nudging
ECHAM-M7	Seven log-normal modes: nucleation soluble, Aitken soluble, Aitken insoluble, accumulation soluble, accumulation insoluble, coarse soluble, coarse insoluble	T63 ($\sim 1.9° \times 1.9°$)	L47, top at 0.01 hPa	ERA-Interim
ECHAM-SALSA	17 size sections in total: 10 soluble bins (3 nm–10 µm in diameter), 7 insoluble bins (50 nm–10 µm in diameter)	T63 ($\sim 1.9° \times 1.9°$)	L47, top at 0.01 hPa	ERA-Interim
EC-Earth3	Seven log-normal modes: nucleation soluble, Aitken soluble, Aitken insoluble, accumulation soluble, accumulation insoluble, coarse soluble, coarse insoluble	IFS: TL255 (i.e. a spectral truncation at wavenumber 255 with a linear N128 reduced Gaussian grid, corresponding to a spacing of about 80 km); TM5: $2° \times 3°$ (latitude × longitude)	IFS: L91, top at 0.01 hPa; TM5: L34, top at 0.1 hPa	
NorESM.2	12 modes, based on mixed particles in nucleation, Aitken, accumulation, and coarse size range with BC, OM, sulfate, dust, and sea salt as core substrate	$0.9° \times 1.25°$ (latitude × longitude)	L30, top at approx 3 hPa	ERA-Interim
UKESM1	Five log-normal modes: nucleation soluble, Aitken soluble, Aitken insoluble, accumulation soluble, coarse soluble	$1.25° \times 1.88°$ (latitude × longitude)	L85, top at approx 85 km	ERA-Interim
Emissions				
Model name	Sea salt	Dust	SO_x	NO_3
ECHAM-M7	Calculated online based on Guelle et al. (2001)	Calculated online based on Tegen et al. (2002) with modifications described in Cheng et al. (2008) and Heinold et al. (2016)	Volcanic emissions: Carn 2017 (AeroCom Phase III; explosive and degassing emissions for the year 2010); anthropogenic and biomass: CMIP6	NA
ECHAM-SALSA	Same as ECHAM-M7	Same as ECHAM-M7	Same as ECHAM-M7	NA
EC-Earth3	Calculated online based on Gong (2003) and Salter et al. (2015)	Calculated online based on Tegen et al. (2002)	Anthropogenic and biomass burning emissions of SO_x from CMIP6, effusive volcanic emissions of SO_x from Andres and Kasgnoc (1998)	NA
NorESM1.2	Salter et al. (2015)	Calculated online in the land model, based on Zender et al. (2003)	Anthropogenic and biomass: CMIP6; effusive volcanic: Dentener et al. (2006)	NA
UKESM1	Gong (2003)	Updated version of Woodward (2001) – see Mulcahy et al. (2020) for details	Anthropogenic (no SO_2 from biomass burning in UKESM1): CMIP6 (Hoesly et al., 2018); effusive volcanic: Dentener et al. (2006)	NA

Table 3. Continued.

Emissions				
Model name	Organic aerosol (OA)	Black carbon (BC)	Dimethyl sulfide (DMS)	NH_3
ECHAM-M7	Secondary OA (SOA) is 15 % of prescribed natural terpene emissions at the surface (Dentener et al., 2006); Anthropogenic and biomass: CMIP6	Anthropogenic and biomass: CMIP6	Calculated online using sea water concentrations from Lana et al. (2011), parameterization with air–sea exchange from Nightingale et al. (2000)	NA
ECHAM-SALSA	Same as ECHAM-M7	Same as ECHAM-M7	Same as ECHAM-M7	NA
EC-Earth3	Anthropogenic and biomass burning emissions from CMIP6, biogenic emissions from MEGANv2.1 (Sindelarova et al., 2014) for the year 2000; marine organic emissions are not included	Anthropogenic and biomass burning emissions from CMIP6, biogenic emissions from MEGANv2.1 (Sindelarova et al., 2014) for the year 2000	Oceanic DMS emissions were calculated online based on Lana et al. (2011) and Wanninkhof (2014), terrestrial DMS emissions from soils and vegetation are prescribed following Spiro et al. (1992)	Anthropogenic and biomass burning emissions of NH_3 from CMIP6, biogenic emissions of NH_3 from soils under natural vegetation and oceanic emissions of NH_3 from Bouwman et al. (1997)
NorESM1.2	Natural emissions of particulate organic matter (POM) volatile organic compounds for SOA as in Kirkevåg et al. (2018); anthropogenic and biomass: CMIP6	Anthropogenic and biomass: CMIP6	Calculated online using sea water concentrations from Lana et al. (2011), parameterization with air–sea exchange from Nightingale et al. (2000)	NA
UKESM1	Natural marine emissions of POM follow Gantt et al. (2011, 2012); UKESM1 has an interactive BVOC scheme which uses Pacifico et al. (2011) for isoprene and Guenther et al. (1995) for monoterpene; note only monoterpene sources currently feed into SOA formation, and isoprene source not used in aerosol scheme – see Mulcahy et al. (2020); anthropogenic and biomass burning organic carbon (OC) CMIP6 (Hoesly et al., 2018; van Marle et al., 2017)	Anthropogenic and biomass burning: CMIP6	Oceanic DMS emissions calculated online based on seawater DMS concentrations produced by the MEDUSA ocean biogeochemistry model (Yool et al., 2013); this uses a modified version of Anderson et al. (2001) – see Mulcahy et al. (2020); air sea emission flux is calculated using Liss and Merlivat (1986)	NA
Aerosol microphysics				
Model name	Nucleation mechanism	SOA formation		
ECHAM-M7	Ion-induced nucleation (Kazil et al., 2010)	SOA is assumed to condense immediately on existing aerosol particles and to have identical properties to primary organic aerosols		
ECHAM-SALSA	Activation-type nucleation (Sihto et al., 2006)	Same as ECHAM-M7		
EC-Earth3	Riccobono et al. (2014) + binary nucleation (Vehkamäki, 2002)	Bergman et al. (2022)		
NorESM1.2	Makkonen et al. (2014), Kirkevåg et al. (2018)	Kirkevåg et al. (2018)		
UKESM1	Binary homogeneous nucleation follows Vehkamäki (2002); there is currently no representation of boundary layer nucleation of new particles	Simple oxidation of monoterpene produces a condensable secondary organic species which can condense onto pre-existing particles		

NA: not available.

The concentrations of ammonium, nitrate, and the aerosol water associated with (ammonium) nitrate are calculated assuming equilibrium gas–particle partitioning. In the current model version, this equilibrium is calculated from the Equilibrium Simplified Aerosol Model (EQSAM; Metzger et al., 2002). The chemistry scheme of TM5 accounts for gas-phase, aqueous-phase, and heterogeneous chemistry (van Noije et al., 2021). The sources of mineral dust and sea salt, the oceanic source of DMS, and the production of nitrogen oxides by lightning are calculated online. Emissions from anthropogenic activities and open biomass burning are prescribed using data sets provided by CMIP6. All other emissions are prescribed as documented in van Noije et al. (2021).

2.2.2 ECHAM-HAMMOZ

ECHAM-HAMMOZ (echam6.3-hammoz2.3-moz1.0) is a global aerosol–chemistry–climate model which consists of the atmospheric circulation model ECHAM (Stevens et al., 2013), the aerosol model HAM (Kokkola et al., 2018; Tegen et al., 2019), and the chemistry model MOZ (Schultz et al., 2018) not used in this study. The model solves atmospheric circulation in three dimensions with spectral truncation of T63, which corresponds to approximately $1.9^\circ \times 1.9^\circ$ horizontal resolution and uses 47 vertical layers extending to 0.01 hPa. The model includes the sectional aerosol model SALSA, which describes size distributions using 10 size bins between 3 nm and 10 µm in diameter, with externally mixed parallel size bins between 50 nm and 10 µm for treatment of particles consisting of insoluble material when they are emitted. The ECHAM-HAMMOZ also includes an option of using the modal aerosol model M7, which describes the aerosol size distribution with a superposition of seven log-normal modes. Details of how aerosol processes are calculated in SALSA are described by Kokkola et al. (2018). The same details for M7 are described by Tegen et al. (2019).

Both model configurations (i.e. SALSA and M7) were set up according to the AeroCom (Aerosol Comparisons between Observations and Models) initiative phase III experiment set-up. Anthropogenic aerosol emissions were according to the Community Emissions Data System (CEDS; Hoesly et al., 2018); for biomass burning, we used Biomass Burning Emissions for CMIP6 (BB4CMIP; van Marle et al., 2017). Dust, sea salt, and maritime DMS emissions are calculated online as a function of 10 m wind speed (see Tegen et al., 2019, and references therein). Atmospheric circulation (vorticity, divergence, and surface pressure) was nudged towards ERA-Interim reanalysis data (Berrisford et al., 2011), but temperature was allowed to evolve freely.

2.2.3 NorESM1.2

NorESM1.2 (Kirkevåg et al., 2018) is an earth system model which consists of the atmospheric model CAM5.3-Oslo, the sea ice model CICE4, the land model CLM4.5, and an updated version of the MICOM ocean model used in NorESM1 (Bentsen et al., 2013). CAM5.3-Oslo is based on CAM5.3 (Liu et al., 2016; Neale et al., 2012) but contains a different aerosol scheme (OsloAero5.3), along with other small modifications. In this study, the model is run with a horizontal resolution of $0.9^\circ \times 1.25^\circ$ and 30 layers in the vertical (model top at around 3 hPa).

The aerosol scheme in NorESM1.2 describes aerosols using 12 separate modes, which can consist of sulfate, BC, OM (including SOA), sea salt, or dust (see Kirkevåg et al., 2018, for a detailed description), and their interaction with radiation and clouds. Emission strength of natural aerosol precursors and aerosols such as dust, sea salt, primary marine organic matter, marine DMS, isoprene, and monoterpenes is calculated interactively (Kirkevåg et al., 2018). The nucleation scheme for new particle formation used in NorESM1.2 is described in Makkonen et al. (2014). We have used the anthropogenic emissions from Hoesly et al. (2018) and biomass burning emissions from van Marle et al. (2017). We prescribed sea-surface temperatures and sea ice concentrations based on observations, and in the atmosphere, the horizontal wind (the zonal wind speed U and the meridional wind speed V) and surface pressures were nudged to 6-hourly ERA-Interim reanalysis data.

2.2.4 UKESM1

The United Kingdom Earth System Model (UKESM1) is described in detail by Sellar et al. (2019) and is built around the Global Coupled 3.1 (GC3.1) configuration of the HadGEM3 (Hadley Centre Global Environment Model) physical climate model (Kuhlbrodt et al., 2018; Williams et al., 2018). UKESM1 additionally includes ocean and land biogeochemical processes and a stratospheric–tropospheric chemistry scheme (Archibald et al., 2020) implemented as part of the United Kingdom Chemistry and Aerosol (UKCA) model. In the simulations performed for the CRESCENDO project, UKESM1 was set to operate at a horizontal resolution of $1.25^\circ \times 1.88^\circ$ (latitude × longitude), with 85 vertical levels.

The representation of aerosols within UKESM1 is described and evaluated by Mulcahy et al. (2020); UKESM1 employs the modal version of the Global Model of Aerosol Processes (GLOMAP) two-moment aerosol microphysics scheme (Mann et al., 2010). The aerosol number size distribution is represented by soluble nucleation, Aitken, accumulation, and coarse (diameter > 1000 nm) modes and an additional insoluble Aitken mode. The above modes are used to carry information about sulfate, black carbon, particulate organic matter, and sea salt, whilst mineral dust is treated using the separate sectional scheme of Woodward (2001). In UKESM1, there is no parameterized new particle formation scheme applied in the boundary layer.

Anthropogenic emissions of aerosols are prescribed from the CMIP6 inventories: SO_2 and anthropogenic BC and OC are taken from the Community Emissions Data System

(CEDS; Hoesly et al., 2018), and biomass burning emissions are from van Marle et al. (2017). UKESM1 interactively simulates emissions of marine DMS, biogenic volatile organic compounds (BVOCs), and primary marine organic aerosol (Sellar et al., 2019).

2.3 Data analysis methods

2.3.1 Observational short-term trends: dynamic linear model (DLM)

We used the dynamic linear model (DLM) for determining the short-term variation in trends, i.e. transient changes in the (long-term) trend in timescales of some months to some years, of different measured mode parameters in the daily data set (Durbin and Koopman, 2012; Laine, 2020; Petris et al., 2009). The main advantage of DLM compared to many other non-parametric and parametric trend estimation methods is that DLM can also detect a non-monotonic trend, and the seasonality of the time series can be estimated simultaneously with the trend.

DLM explains the measured variability in the time series y_t of the mode parameter (N, D_p, or σ) with three components: firstly, the level component μ_t that is locally linear, but the trend α_t can change during the measured period; secondly, a seasonality component γ_t that captures the seasonal pattern of the time series; thirdly, a residual component η_t that uses an autoregressive model (AR(1), ρ) and accounts for autoregression of the time series, i.e. dependence of the daily measurement on that from its previous day; and finally normally distributed random noise components ε_t, $\varepsilon_{\mathrm{level},t}$, $\varepsilon_{\mathrm{trend},t}$, $\varepsilon_{\mathrm{seas},t}$, and $\varepsilon_{\mathrm{AR},t}$, which are related to uncertainties in each component. For each observation y_t at time t the DLM model used in this study is given by

$$y_t = \mu_t + \gamma_t + \eta_t + \varepsilon_t, t = 1, \ldots, T\,,$$

$$\mu_t = \mu_{t-1} + \alpha_t + \varepsilon_{\mathrm{level},t}\,,$$

$$\alpha_t = \alpha_{t-1} + \varepsilon_{\mathrm{trend},t}\,,$$

$$\sum_{i=0}^{11} \gamma_{t-i} = \varepsilon_{\mathrm{seas},t}\,,$$

$$\eta_t = \rho\eta_{t-1} + \varepsilon_{\mathrm{AR},t}\,,$$

where $\varepsilon_t \sim N(0, \sigma_t)$, $\varepsilon_{\mathrm{level},t} \sim N(0, \sigma^2_{\mathrm{level}})$, $\varepsilon_{\mathrm{trend}} \sim N(0, \sigma^2_{\mathrm{trend}})$, $\varepsilon_{\mathrm{seas}} \sim N(0, \sigma^2_{\mathrm{seas}})$, and $\varepsilon^2_{\mathrm{AR}} \sim N(0, \sigma^2_{\mathrm{AR}})$. We have used $\rho = 0.4$ as a value for AR(1) coefficient in all model fittings. The initial value of the level has been set to be the yearly mean of the first year. Calculation of the DLM model has been done in the MATLAB environment (MATLAB, 2019) using the DLM MATLAB Toolbox (Laine et al., 2014).

As the applied DLM formulation assumes normally distributed data, we used log10 transformation for mode number concentrations. If number concentration was zero (i.e. no fitted modes were available for that day), we used a value of one as a number concentration for that day to avoid problems with log10 transformation. For mode diameter and geometric standard deviation, no transformations were applied. We investigated the residuals ε_t after the model fitting, and in most cases, the assumptions of the model are sufficiently fulfilled, with the distribution of the residuals being close to a normal distribution. Before interpreting the level and the trend of the number concentration of each mode, we have transformed the level μ_t and trend α_t back to the original scale by using the exponential back-transformation.

2.3.2 Long-term linear trends: Sen–Theil estimator

Long-term trends of measured mode parameters in the data set were estimated using the Sen–Theil estimator (Sen, 1968; Theil, 1950). The Sen–Theil estimator is a non-parametric method to estimate a linear trend. The advantages of the Sen–Theil estimator compared to more common linear regression methods are that it does not assume normality of the data, and it is more robust to outliers. Compared to the more complex DLM model, the Sen–Theil estimator also works with a lower number of data points, which is one reason we used it in the model comparison.

Trend estimation was performed using the *TheilSen* function from *openair* package in the R environment (Carslaw and Ropkins, 2012; R Core Team, 2021). The calculation of 95 % confidence intervals is based on the bootstrap method (Kunsch, 1989). Trend estimation was done for whole-year data (monthly averages) and seasonal data (monthly averages of a specific season). Before trend estimation for the whole-year data set, the time series was de-seasonalized with seasonal trend decomposition using loess, and autocorrelation for consecutive months was taken into account when calculating the uncertainty in the trend estimates. Seasons have been defined to be 3 months each, winter consisting of December–February, spring March–May, summer June–August, and autumn September–November. In the trend estimation for observational data sets (Sect. 3.1), we have used all months available from each site. In all comparisons of observations and models (Sect. 3.2), we used only those months that were available from the measurement sites.

We have used relative change (% yr^{-1}) as the main parameter for comparing results. Relative change has been calculated for the Sen–Theil estimator and confidence intervals by using the option slope-percent. The function uses the fitted value of a first observation as a reference for calculating relative change (Carslaw and Ropkins, 2012).

2.3.3 Magnitude and pattern of seasonality

The seasonality of particle number concentration and its magnitude is highly varying between different measurement sites, depending on, for example, latitude and environment type of site (Asmi et al., 2013; Rose et al., 2021) and the mode studied. Similarly, parameters such as cloud conden-

sation nuclei (CCN) number concentrations and new particle formation (NPF) frequency have a seasonal cycle (Asmi et al., 2011; Nieminen et al., 2018). Seasonality of the optical properties in models has been studied (Gliß et al., 2021), but for particle number concentrations we are not aware of studies that compare measurements and models based on long-term data sets.

We compared the seasonality of number concentrations in models and measurements by studying modes separately. We used two variables, the normalized interquartile range (NIQR) and SeasC (Rose et al., 2021), to compare seasonality between models and measurements. When calculating these seasonal parameters from measurements and model results, we included only those months for which the measurement and model data were available. We calculated NIQR and SeasC separately for each year to also assess the distribution of values in the studied period.

NIQR, defined as $\mathrm{NIQR} = \frac{\text{3rd quartile} - \text{1st quartile}}{\text{Median}}$, describes the interquartile range of observations for 1 year. NIQR was calculated using monthly averages of concentrations, with at least 10 monthly averages needed to be available. The calculation of NIQR is slightly different from Rose et al. (2021), who used daily values calculating NIQR. As we had only monthly averages from model data, daily values could not be used. Based on the measurement data, we checked whether the time resolution would change the NIQR values, by comparing NIQR values calculated from daily and monthly averages. We found that the NIQR values calculated from daily averages were usually higher, sometimes as much as twice the one calculated from monthly averages. Therefore, NIQR values presented in this study are not comparable to values presented in Rose et al. (2021) but only between the different data sets in this study or others calculated from monthly averages.

SeasC is the ratio of maximum and minimum of seasonal median values, calculated separately for each year and mode in each data set. It was calculated by first taking the seasonal averages for each season. For calculating the seasonal median, at least two monthly means from the season were required. Then, if we were able to calculate all the seasonal medians for the year, SeasC was calculated as the ratio of the maximum and minimum of those seasonal medians.

In general, both SeasC and NIQR describe the distribution of number concentrations within 1 year. SeasC focusses more on utmost values, minimum and maximum of seasonal medians, whereas NIQR focusses on values closer to the yearly median. Neither SeasC nor NIQR considers when the maximum and minimum in number concentrations are achieved. Though the seasonal cycle of the measured and modelled number concentrations might be opposite to each other, the difference in SeasC or NIQR values can be small when comparing measurements and model data.

To assess whether the seasonal maximums and minimums have similarities between measurements and models, we have calculated the seasonal averages, selected the seasons that have most often had seasonal maximum and minimum during the measured time period, and evaluated how modelled results correspond to the measurements.

3 Results

3.1 Observational number size distribution characteristics and trends in daily in situ measurement data sets

We investigated the mode characteristics (number concentration N, geometric mean diameter D_p, and geometric standard deviation σ) for nucleation, Aitken, and accumulation modes for 21 European and Arctic sites representing Polar (Villum, Zeppelin), arctic remote (Pallas, Värriö), rural (Birkenes II, Hohenpeißenberg, Hyytiälä, Järvselja, Melpitz, San Pietro Capofiume), rural regional background (K-Puszta, Neuglobsow, Waldhof, Vavihill), urban (Annaberg-Buchholz, Helsinki, Leipzig, Puijo), coastal remote (Mace Head, Finokalia), and high-altitude (Schauinsland) environments. Median values and interquartile ranges for different mode parameters for the sites over the analysis period are shown in Fig. 1 (and for different seasons in Figs. S4–S6). Figure 1 shows a large variation in N's between the sites. As expected, the Arctic and other remote sites had the lowest concentrations overall (median concentrations 10–150 cm^{-3} for nucleation and 40–1400 cm^{-3} for Aitken mode), while urban sites and central European sites had the highest concentrations, especially for the nucleation and Aitken modes (400–2000 cm^{-3} for nucleation and 800–3600 cm^{-3} for Aitken mode). Generally, N values were higher for southern compared to northern sites. Partially the differences between southern and northern sites could be explained by the relation between population density and station location: more polluted site types were typically found in the south. However, the concentrations for southern sites were higher also within site classes. For the accumulation mode, the highest N values were found at more polluted rural sites in central Europe, K-Puszta and San Pietro Capofiume. These results are in line with previous results for number concentrations, such as those found by Rose et al. (2021).

For modal D_p and σ, results were not as distinctive for different environments. Standard deviations σ were highest for nucleation modes and lowest for accumulation modes without clear differences between site environmental types. This was kind of expected based on the earlier results showing the relationship between aerosol variability and size (Williams et al., 2002).

Coastal sites Finokalia and Mace Head showed the largest modal D_p in Aitken and accumulation modes, while Birkenes II (rural) and Mace Head showed the largest modal D_p in nucleation mode. Järvselja (rural) had the lowest modal D_p in all modes. One aspect that could explain some of the differences in modal D_p between sites is the lower limit of the detected size range in the measurements. The lower value

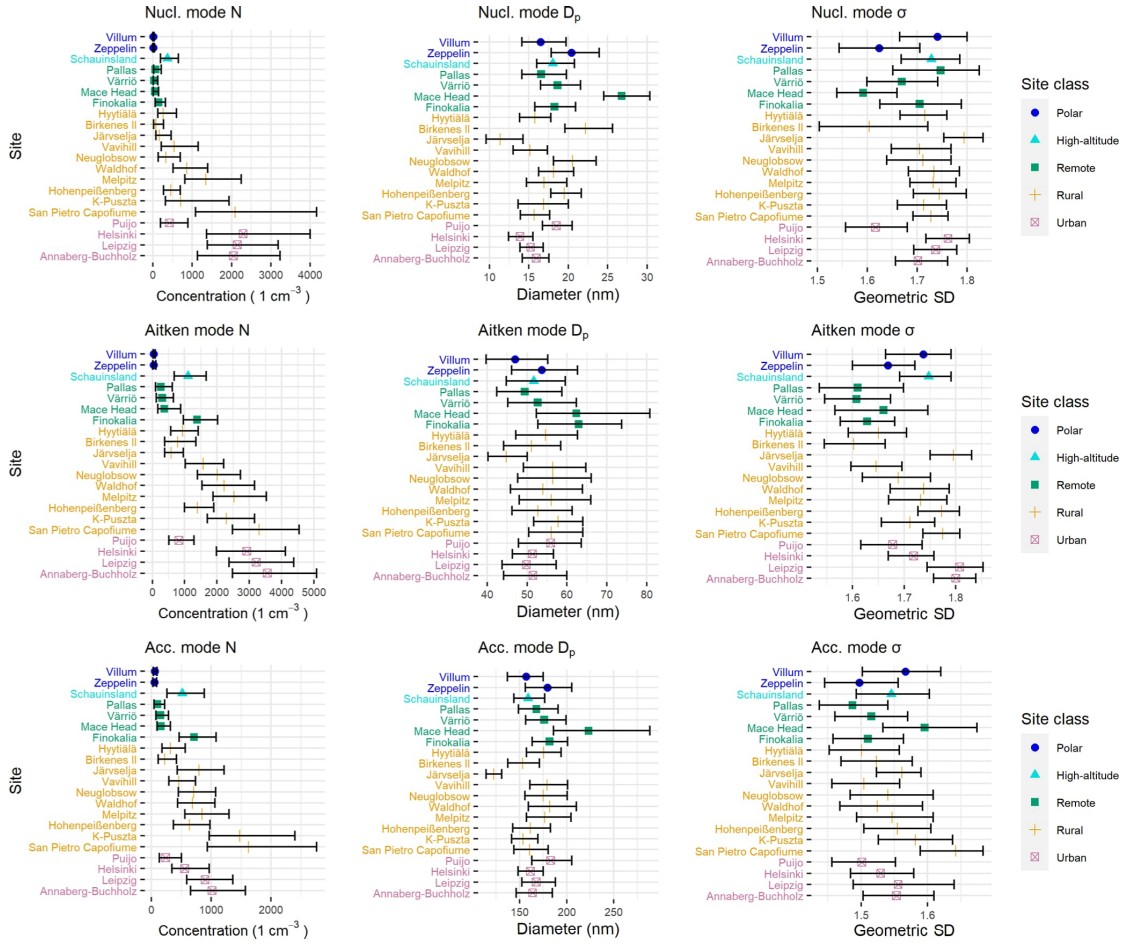

Figure 1. Summary of mode parameters (number concentration N, geometric mean diameter D_p, and geometric standard deviation σ) for the measurement sites. The median values are marked with dots and interquartile ranges (25 % and 75 %) with whiskers for different mode parameters in fitted modes.

of the smallest detectable size might increase the probability that the modal D_p of fitted nucleation mode is smaller. For example, for the Mace Head site the lowest measured size bin is around 21 nm, affecting the modal D_p of the fitted nucleation mode. The lowest detected size may also affect the fitted Aitken mode diameter. However, for Finokalia and Järvselja, the measured size range could not completely explain observed high and low modal D_p of the nucleation, respectively. This was tested by using a minimum size of ~ 10 nm for those sites that have measured < 10 nm particles and calculating the mode parameters as in Fig. 1. For this test, modal D_p was calculated using ~ 10 nm, as the lowest size in Finokalia was close to diameters using the original lowest size in Fig. 1. Geometric mean diameters in Järvselja increased by some nanometres but were still lowest among all sites, except in nucleation mode, where Villum then had the lowest modal D_p.

To investigate the effect of measurement size range on mode fitting, we studied the dependence of modal D_p and minimum size bin measured amongst all sites. Spearman's rank correlation between modal D_p and the lowest size bin amongst sites was positive, 0.67 for nucleation, 0.03 for Aitken, and 0.26 for accumulation mode, indicating the strongest dependence for nucleation modes and only a minor dependence for accumulation modes. Thus, especially for nucleation modes, the lowest detectable size is related to the lower modal D_p in Fig. 1.

Results for modal D_p are somewhat different compared to what has been observed in Rose et al. (2021). Rose et al. (2021) used a slightly different site classification than that employed in this study. Unlike the classification used in our study, they classified the stations based on both geographic area (e.g. mountain and continental site classes) and footprint (e.g. urban and rural site classes). In their study, one site could have belonged to more than one site class. Hence, even if there are the same sites used in Rose et al. (2021) and our study, the classification was different. With their classification, they reported that mode diameters for Aitken and accumulation modes were smallest for urban sites (32 ± 11 and 122 ± 37 nm; Leipzig in our study), followed by mountain (39 ± 9 and 142 ± 25; Hohenpeißenberg), polar (42 ± 14 and 149 ± 37; Pallas, Värriö, and Zeppelin), and continental (51 ± 13 and 174 ± 29; Annaberg-Buchholz, Birkenes II, Hyytiälä, K-Puszta, Leipzig, Melpitz, Neuglobsow, Schauinsland, Vavihill, and Waldhof) sites. (The sites used in both studies are mentioned in the brackets.) In our results, most urban sites had a smaller Aitken mode modal D_p compared to most of the rural continental sites, with the most notable exceptions from this tendency being Puijo and Järvselja. Otherwise, the differences between site types reported by Rose et al. (2021) were not observed in our study. In general, the modal D_p values were smaller in our study; however, the rural sites in our study and continental sites in Rose et al. (2021) have accumulation mode diameters close to each other. Rose et al. (2021) studied only particles ranging from 20 to 500 nm and the year 2016 or 2017, depending on the site. They also had a larger number of sites considered. In our analysis, the analysed particle size range has in particular affected the mean diameters since at least part of the 20–30 nm particles were fitted into nucleation mode, whereas in Rose et al. (2021), those were included in the Aitken mode. As a result, the fitted Aitken modes in our study had slightly larger modal D_p compared to fitting only Aitken and accumulation mode.

It is worth noting that the fitted modes and their diameters were mostly larger than what is usually assumed in climate models. Fitted nucleation modes had mean diameters from above 10 nm (Järvselja) to around 20 nm (Mace Head), while the upper limit of the nucleation mode in sectional (7 nm) and modal (10 nm) model representations is below all the medians of fitted mean diameters to the observational data. Higher nucleation mode mean diameter detected in the measurements may be due to the fact that the lowest detectable diameter is usually around the upper limit of model representations. As the measurements do not capture the smallest nucleated particles and only detect them after some growth, the average nucleation mode diameters determined from measurements may be an overestimation.

To investigate the short-term trends at different measurement sites over the analysed time periods, we used DLM analysis as described in Sect. 2.3.1. To demonstrate the characteristics of a DLM trend fit, Aitken mode N's and their estimated level for the Mace Head site are shown in Fig. 2. Aitken mode N's at Mace Head were selected as an example because there is a substantially large increase in number concentration during the measured period, which is also seen in Fig. 3, showing the estimated trend in Aitken mode for all sites. The trend at Mace Head given by DLM (red line in Fig. 2) was temporarily over 10 % yr^{-1}. It must be noted that the concentrations at Mace Head were quite low compared to many other sites, and the variation in average N in Aitken modes between days was relatively large, ranging from 50 to 3000 particles cm^{-3}. The number of high-concentration days (here denoted as > 500 particles cm^{-3} on average) increased towards the year 2010 and has been decreasing since then. In the year 2010, the frequency of high-concentration days was about 68 % of the days observed, while in 2005–2008 it was about 46 %. In the year 2012, the frequency of high-concentration days was increased to 51 %. For Mace Head, the Aitken mode D_p had an opposite but a much weaker trend: there was an increasing trend in diameter before the year 2008 and a decreasing trend from 2008 to 2010, and after that, the trend was increasing again. Based on this data set, we cannot derive the exact reasons for the changing N.

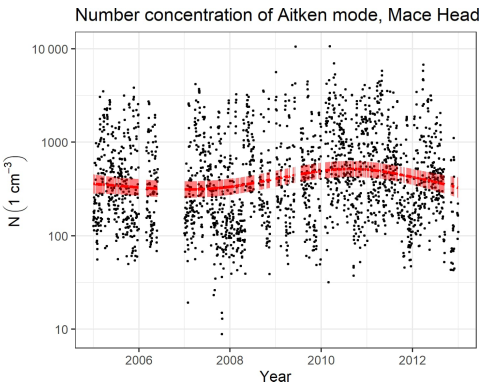

Figure 2. DLM fit for Mace Head Aitken mode number concentration. Black dots represent daily averages of Aitken mode number concentrations at Mace Head. The solid red line represents the estimated level, and the red ribbon represents the 95 % confidence interval for the level.

In Fig. 3. we present the coefficients for the DLM trend for Aitken mode D_p and N. Mode parameters D_p and N were selected because those parameters show the strongest trends. Results for nucleation and accumulation modes are shown in Figs. S7 and S8. The trend derived using the DLM showed the transient changes in the level of the time series. The trend from the DLM was constantly changing during the time series, achieving the best fit to the data as can be seen in Fig. 3. For Fig. 3, the unit of the change was scaled to be comparable with the long-term trends presented later. To get a DLM trend for 1 year, the 1 d trend given by the model was

multiplied by the number of days in a year (365 used for all years) and divided by the mean of the variable over the first observed year.

The most important result of the DLM analysis was that the trends are usually not monotonic during the measured period. Therefore, long-term trends should be only thought of as an approximation of the average change during the time period. It is also good to note that the mode parameters are connected; i.e. for some of the short-term trends observed in mode number concentration, there was an opposite trend in mode mean diameter. This can also be seen later in the long-term trends (Sen–Theil results) for some of the modes and sites.

The long-term trends were investigated using Sen–Theil estimators (Fig. 4). Exact numbers for trends and confidence intervals are shown in Fig. S9. Number concentration N of the modes showed the largest changes over the investigated time periods, modal D_p has the second-largest changes, and σ showed only minor variations compared to the other two parameters. This was similar for both the Sen–Theil estimator and DLM results.

Amongst all variables and sites considered, accumulation mode N showed the largest decrease, followed by Aitken and nucleation mode N when long-term trends are considered (Fig. 4). Only urban sites showed consistent decreases in number concentration for almost all modes and sites. The only exception here is semi-urban Puijo, which showed an increasing trend in accumulation mode N. Urban sites are dominated by anthropogenic emissions (e.g. traffic and industrial activities), which are affected by recent air quality control measures in Europe. This naturally explains the decreasing trends at urban sites, as discussed in previous studies (Mikkonen et al., 2020; Sun et al., 2020). For rural and remote sites, there was more site-to-site variation in trends, and some of these sites showed trends of increasing N in all three modes. The rural and remote sites are less directly affected by anthropogenic sources, but more by biogenic or other natural sources compared to urban sites. The strength of the anthropogenic contribution varies between the rural and remote sites depending on the strength of the natural sources and transportation efficiency of air masses from more polluted environments. For example, the central and southern European rural sites are likely more affected by anthropogenic sources than northern European rural or remote sites due to denser incidence of large urban areas in central and southern Europe. The biogenic emissions depend greatly on environmental factors, which can vary significantly on a year-to-year basis and between sites. In case of accumulation mode there can also be differences in removal efficiency linked to differences in cloud cover and precipitation at different sites. These factors may partly explain the large variation in trends between the different rural or remote sites. The difference in trends of N in the three modes at the same site may be related to different sources and their temporal changes. Furthermore, nucleation and Aitken mode particles are likely to be emitted or formed close to the measurement site, while accumulation mode particles are often transported to the location over longer distances. In particular, nucleation mode N values are dependent on the formation of particles and their growth to larger sizes, which in turn are dependent on not only the precursor gas emissions but also meteorological conditions and background particle concentrations (Nieminen et al., 2018). Thus, a decreasing trend in the concentration of larger particles could even strengthen new particle formation.

Mace Head showed distinctly different behaviour compared to other sites as the number concentration of all three modes had increasing annual (Fig. 4) and seasonal trends (Fig. 5). It should be noted here that the investigated period of the Mace Head data set differs considerably from other investigated data sets: for Mace Head, the investigated period ends in the year 2012, while for other sites the time period ends in 2017 or 2018.

Accumulation mode correlation between the estimated trend coefficients for modal D_p and N was -0.27. So, the decrease in number concentration was somewhat concurrent with increased particle size in accumulation mode (see also Fig. S10). For the σ parameter, the trend was almost zero for most of the sites.

For the Aitken mode and especially the nucleation modes, there were some sites that show an increase in N. For the Aitken mode, the Spearman correlation between trend estimates of modal D_p and N was -0.25, and for nucleation mode, the spearman correlation was -0.47. Thus, especially in nucleation mode, some of the increases and decreases in number concentration were partially connected with a decrease or increase in modal D_p (see also Fig. S10). Additionally, in nucleation and Aitken modes, the σ parameter showed only minor changes during the measured period.

We also investigated if the trends have a seasonal behaviour. For seasonal trends in general, a decrease in N was strongest for winter and weakest for summer (Fig. 5, exact numbers in Figs. S11 and S12). In winter, there were relatively consistent decreasing trends all over Europe. In autumn (Figs. 5 and S11), the trends were also mostly decreasing. In summer and spring (Figs. 5, S11, and S12), there were clear differences in trends between sites. Again, the most consistent trends were at urban sites, showing a decrease for accumulation and Aitken mode N. Nucleation mode N for urban sites also mostly decreased. Other site classes did not show consistent decreases, possibly due to different contributions of anthropogenic and biogenic emissions between sites, as previously discussed in this section. Large, sporadic, increasing trends in nucleation mode might have resulted from a large portion of missing nucleation modes fitted and small concentrations, which might cause large trends even for small absolute changes. During the winter season (Figs. 5 and S11), this results in a stronger, decreasing trend in wintertime concentrations compared to summertime trends. This was most evident for accumulation and Aitken mode particles. Interestingly, especially during

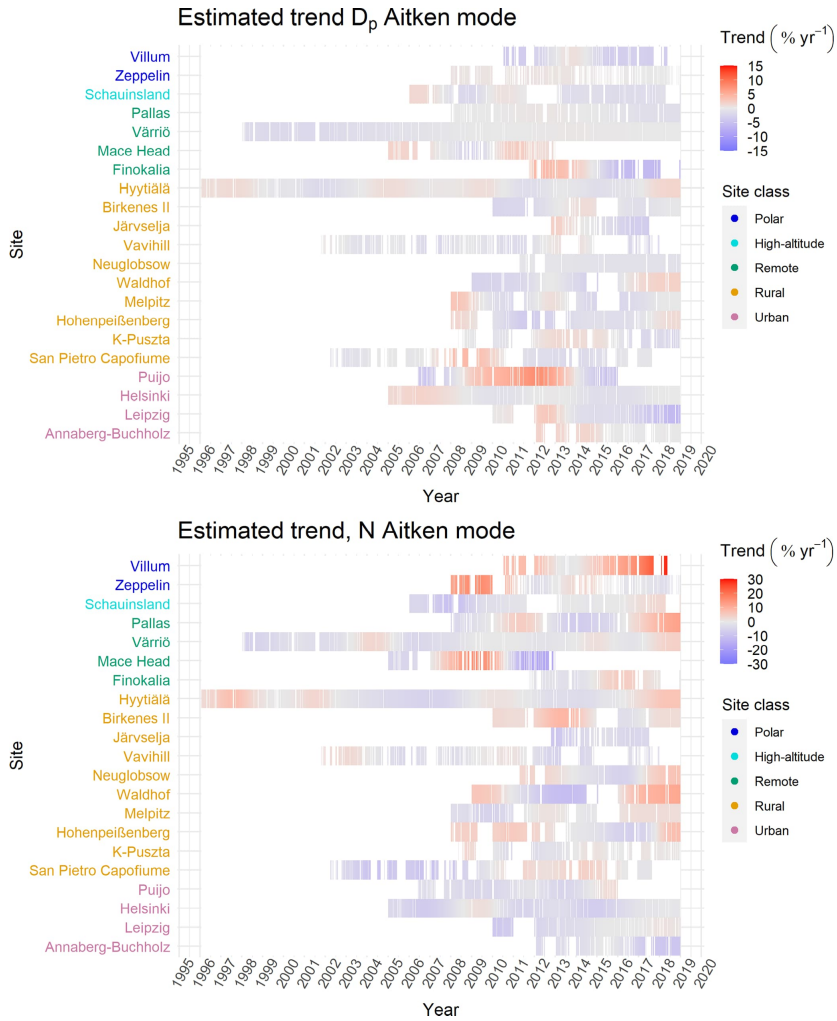

Figure 3. Estimated trends for Aitken mode D_p and N at measurement sites. Trend has been calculated by DLM; see Sect. 2.3.1 for details. The overall trend presented in the figure is comparable with the long-term trend estimates given in Sect. 3.1. To get a DLM trend for 1 year, the 1 d trend given by the model was multiplied by the number of days in a year (365 used for all years) and divided by the mean of the variable over the first observed year. For example, if the trend shows an increase of 10 % yr^{-1} it means that if the short-term increase would continue for a year, the concentration would be increased by 10 % during the year compared to the first-year mean.

winter seasons, the nucleation mode exhibits an opposite observed trend to the accumulation and Aitken mode concentrations (Figs. 5 and S11). As noted earlier, different trends in nucleation mode number concentrations than for larger particles might be related to different sources and the effect of background particles on new particle formation acting as a condensation sink.

3.2 Comparison of observed particle mode concentrations and climate model results

In this section, we compare the observational trends of N of each mode to the trends of the climate model simulation data. These results are not fully comparable to the results presented in Sect. 3.1 since the investigated time period in this section is different from the time period in Sect. 3.1. For comparison of simulations and observations, at least 7 years of data were required. Because model data were only avail-

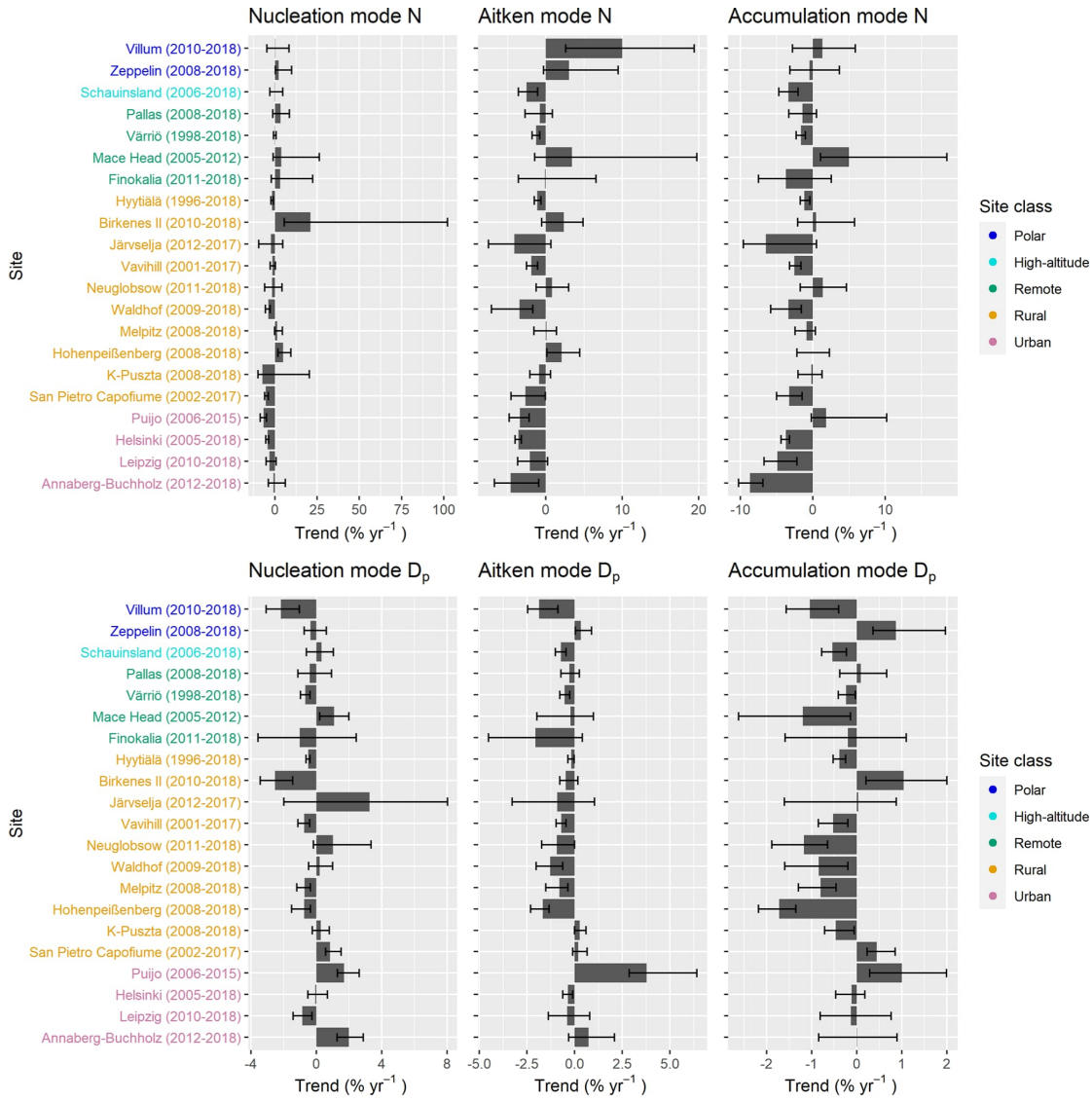

Figure 4. Long-term trend estimators for measured trends of all mode parameters (mean geometric diameter D_p, geometric standard deviation σ, and number concentration N) in nucleation (NuclM), Aitken (AitM), and accumulation mode (AccM). Confidence intervals (95 % confidence level) are shown with whiskers. Trends have been calculated using the Sen–Theil estimator and complemented with bootstrap confidence intervals (see Sect. 2.3.2).

able for the years 2001 through 2014, this limited the number of sites available for the comparison. Figures 6–8 display the 13 sites that had sufficient data coverage for this time period. In the cases where measurement data were missing for a site for a certain month, model data for the corresponding month were omitted as well. As explained in Sect. 2.1.4, log-normal modes that were fitted to the measurement data were not directly comparable to the data provided by the climate models. We therefore additionally remapped the size distributions for specific size intervals (see Sect. 2.1.4) which were used in the models from the measurement data to correspond to the sectional (ECHAM-SALSA) and modal (EC-Earth3,

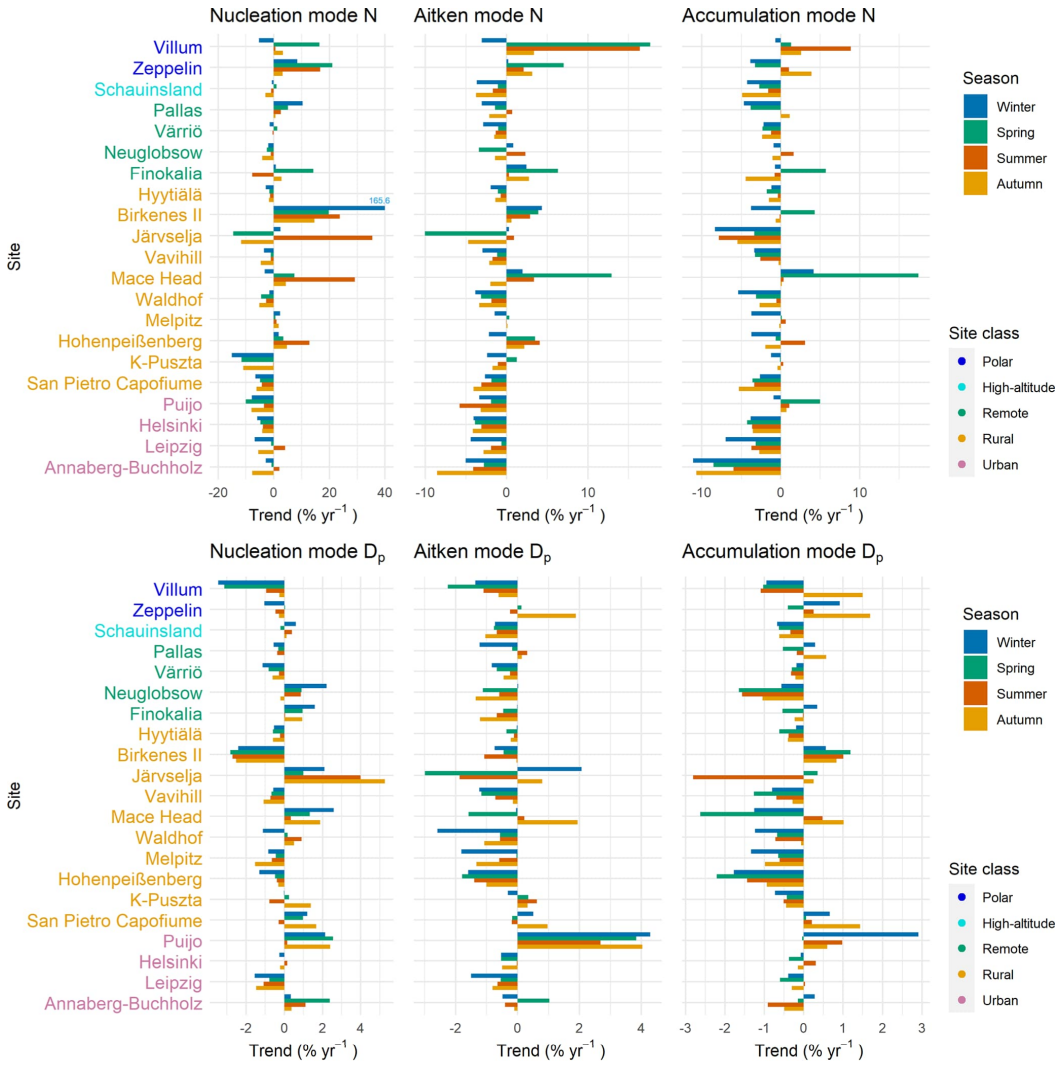

Figure 5. Seasonal long-term trend estimates for all mode parameters: mean geometric diameter D_p, geometric standard deviation σ, and number concentration N in nucleation (NuclM), Aitken (AitM), and accumulation mode (AccM) during autumn (September, October, and November), winter (January, February, and December), spring (March, April, and May), and summer (June, July, and August). Trends have been calculated using the Sen–Theil estimator and complemented with bootstrap confidence intervals (see Sect. 2.3.2). Correct number for nucleation mode N trend for Birkenes II is shown next to the bar.

ECHAM-M7, NorESM1.2, and UKESM1) representations of nucleation, Aitken, and accumulation mode as used in the models. To this end, we used the model-internal parameters to separate the respective modes (see Sect. 2.1.4 for details). In the following, we thus analyse three representations of the same measurement data, which we refer to as "fitted modes" (Sect. 2.1.3) and "sectional" and "modal representation of the measurement data" (Sect. 2.1.4). While these three representations were not directly comparable to each other (because the size ranges for different modes varied between the different representations), it was still instructive to visualize them side by side. It should also be noted that the trends for the fitted modes in Figs. 6–8 were not the same as in Fig. 4 because the time intervals of the trend analyses were not the same.

3.2.1 Comparison of yearly trends

Figure 6 shows the trends in nucleation mode N; exact numbers for trends are shown in Fig. S13. Unfortunately, at many measurement sites, the minimum detected particle diameter was too large to compute meaningful results for nucleation-mode-sized particles that were comparable to the models. Hence only five of the measurement sites (Hyytiälä, Helsinki, Vavihill, Melpitz, San Pietro Capofiume) could be compared to all models, and three additional sites (K-Puszta, Pallas, Värriö) could be compared to models with modal aerosol representation. Of these sites, Hyytiälä, Helsinki, Vavihill, and San Pietro Capofiume showed comparable trends for all three representations of the measurement data, which were all decreasing and statistically significant. At all four of these measurement sites, the models showed decreasing trends as well, but in many cases, the negative trends were weaker, and sometimes no significant trend was found. Observations at Pallas showed a strong increasing trend for both fitted mode and modal representation of the data, while all models showed slightly decreasing trends, of which one result was statistically significant.

When inter-comparing model results, we found that for most sites all models showed slight to medium decreasing trends (about 0 % to $-5\,\%\,\mathrm{yr}^{-1}$) for nucleation mode N (Figs. 6 and S13). This was also expected, as all models used the same anthropogenic emission inventory, which exhibits a steadily decreasing trend in sulfur dioxide emissions over Europe for the modelled period (Hoesly et al., 2018). This directly affects nucleation rates and condensation rates of sulfuric acid in the models. There were only two measurement sites that deviate from this general model trend. At K-Puszta, EC-Earth3 and ECHAM-SALSA showed increasing trends for the nucleation mode concentration. The other exception was a very strong decreasing trend in nucleation mode particle concentration for K-Puszta and Hohenpeißenberg in NorESM1.2. For both sites, however, the accumulation mode showed a positive trend in NorESM1.2, which was not present for the other models. A growing number of accumulation mode particles probably led to a larger condensation sink and therefore to suppression of new particle formation in the model.

Figure 7 shows the yearly trends in Aitken mode N; exact numbers for trends are shown in Fig. S13. When the three representations of observations were investigated it can be concluded that the three different representations of the measurement data qualitatively agreed at most sites. The only exceptions were Pallas, where trends varied between $-0.7\,\%$ (fitted mode) and $+3.1\,\%\,\mathrm{yr}^{-1}$ (sectional representation), and for Zeppelin, where the positive trend was stronger in the sectional representation compared to the other two representations (Fig. S13). Furthermore, except for Zeppelin, Pallas, Mace Head, and Melpitz, all observational trends for all three representations were statistically significant. Of all statistically significant trends, only Hohenpeißenberg showed a positive trend in Aitken mode N for all three observational representations. Mace Head and Zeppelin were quite different, as here the calculated trends for measurements were quite large and positive, but still not statistically significant. This is very likely explained by both sites' close vicinity to the ocean (O'Connor et al., 2008; Tunved et al., 2013).

Most model trends for Aitken mode at sites in northern Europe were not statistically significant, while for the rest of the European sites, most trends were significant (Figs. 7 and S13). Interestingly, the sectional model ECHAM-SALSA showed a significantly decreasing trend at most of the northern sites. This might be due to the different size limits used in the modal and sectional models. At most sites where both measurement and model trends were significant, the models agreed quite well with the measurements in both strength and direction of the trend. However, Hohenpeißenberg was an exception where measurements showed a strong increasing trend, while the modelled trends were negative. The reasons for these differences are not clear.

Figure 8 shows the yearly trends in accumulation mode N; exact numbers for trends are shown in Fig. S13. Again, for most measurement sites, the different representations of the measurement data showed statistically significant trends of equal direction and similar strength. Exceptions were Melpitz and Hohenpeißenberg, which showed fairly weak, insignificant trends altogether; Zeppelin, which showed strong, opposite but, due to high variance, not statistically significant trends; and Puijo, which showed strong positive (but only partly significant) trends for all representations.

Concerning the model data, we did not find trends at any of the measurement sites that were statistically significant in the models. A general but weak tendency was that occurrence of statistical significance increased with decreasing latitude of the site. However, this tendency was not systematic in terms of which model produced significance at which site. Additionally, accumulation mode N depends on wildfire, sea salt, and mineral dust emissions (and atmospheric processes such as cloud processing) and hence on the means of how these emissions are calculated and inserted into the model atmosphere. Considering these factors in combination with the relatively short period analysed here, a strong model internal and inter-model variability is to be expected.

There were only two sites, Helsinki and Vavihill, where all models and measurement representations agreed on the direction of the trend (negative in both cases) in accumulation mode N (Figs. 8 and S13). Some sites stood out because the different models found strong trends in opposite directions there. Hohenpeißenberg and K-Puszta stood out, as here the model trends were mainly negative except for NorESM1.2, which showed positive (albeit not significant) trends for both sites, as was also already discussed in connection with the nucleation mode trends.

In general, the agreement between models and observations in trends of N for all modes varied a lot within the site

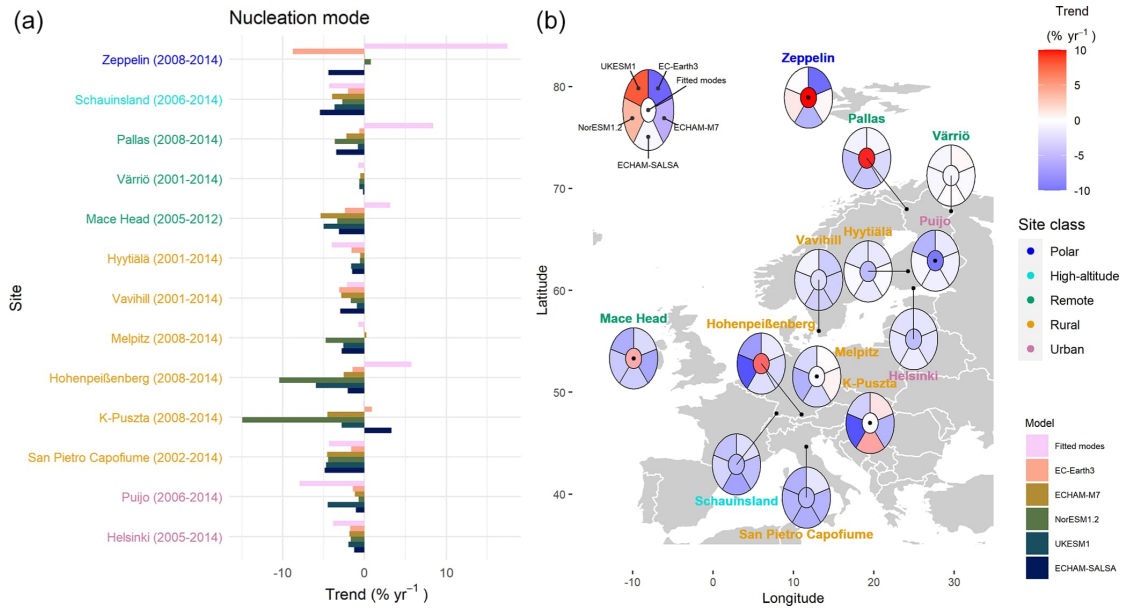

Figure 6. Long-term trend estimates for measured and modelled nucleation mode number concentration. **(a)** Bar plot of trends for different sites. The sites (y axis) are arranged by site class and within site class most northerly to most southerly. **(b)** Estimated trends presented on the map. The colour of the central part follows the trend of the fitted modes. Trends have been calculated using the Sen–Theil estimator and complemented with bootstrap confidence intervals (see Sect. 2.3.2).

classes, and no specific factor explaining the variation was found (see Figs. S14–S16).

3.2.2 Comparison of seasonal trends

Figures 9 and 10 show the seasonal trends for Aitken and accumulation mode N, respectively, at all measurement sites analysed in Sect. 3.2.1. Results for nucleation mode are shown in Fig. S17. Seasonal trends of N included more uncertainty than yearly average trends due to fewer data points. Particularly the modelling results rarely showed statistically significant trends, even though the actual magnitudes of the calculated trends were often quite large. In general, the trends derived for the measurement data did not depend strongly on the representation used. The few exceptions to this were Aitken mode trends at Zeppelin, Pallas, and Melpitz and accumulation mode trends at Zeppelin and Hohenpeißenberg. Seasonal model trends varied quite a lot between models, depending on the season, mode, and measurement site. We found that the differences between the models and observations and between models were largest for the sites where the observations show a strong positive trend (Zeppelin, Mace Head, and Hohenpeißenberg). For such stations, models exhibited either negative trends or lower trends than what was observed.

Apart from a few exceptions, the measurements showed decreasing seasonal trends of the Aitken mode N, which were also significant for some sites (Fig. 9). The exceptions were Zeppelin, Hohenpeißenberg, and Mace Head. Additionally, the measurements at K-Puszta showed increasing trends in the autumn. In general, most of the significant model trends were negative and were found during spring and summer. Neither observed nor simulated data showed significant trends in opposite directions for any of the two seasons; i.e. the significant seasonal trends were either decreasing or increasing for the one site and one measurement or model. Insignificant trends for the same site and measurement or model were sometimes decreasing for some seasons and increasing for some other seasons. The clearest difference between trends in modelled and measured data could be seen for the sites located in Finland, especially during winter and autumn, where the measurements showed a decreasing trend, while the models mostly showed an increasing trend. Those differences observed during winter and autumn could affect the differences in yearly trends observed in Fig. 7.

There was no general agreement between different models concerning accumulation mode N trends (Fig. 10). The trends in the measurements for accumulation mode were mostly fairly similar to the Aitken mode trends. For many sites, these trends from measurements were significant only during spring. Aitken mode trends from models were mostly

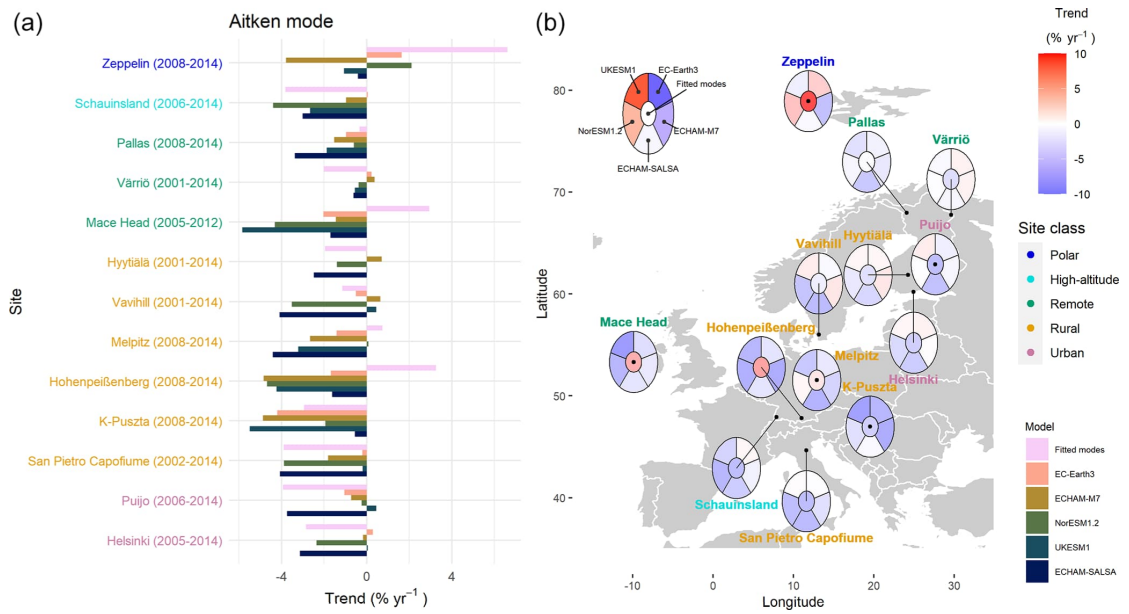

Figure 7. Long-term trend estimates for measured and modelled Aitken mode number concentration. **(a)** Bar plot of trends at different sites. Sites (y axis) are arranged by site class and within site class most northerly to most southerly. **(b)** Estimated trends presented on the map. The colour of the central part follows the trend of the fitted modes. Trends have been calculated using the Sen–Theil estimator and complemented with bootstrap confidence intervals (see Sect. 2.3.2).

insignificant. As can be expected from the yearly trends, the models reproduced measurement trends rather poorly, with no model performing much better or worse than any other model.

3.2.3 Comparison of seasonality and its pattern

In this section, we describe the seasonality and its pattern for nucleation (Fig. S24), Aitken (Fig. 11), and accumulation (Fig. 12) modes. More quantitative investigation based on SeasC and NIQR described in Sect. 2.3.3 can be found in Sect. S1 in the Supplement.

For pattern of seasonality in modelled data, two models, NorESM1.2 and EC-Earth3, had relatively consistent patterns for all sites, whereas for the other three models the seasonal cycle changed between north and south (Fig. 11 for Aitken mode and Fig. 12 for accumulation mode). NorESM1.2 and EC-Earth3 had relatively constant patterns of seasonality throughout Europe, even though the seasonal maximum variation between the sites varied. For NorESM1.2, nucleation mode had its maximum N in winter (see Fig. S24), whereas Aitken and accumulation mode had their maximum N in summer. EC-Earth3 had also consistent modes among all sites: nucleation mode had its maximum in summer; Aitken and accumulation mode had their maximum in winter or early spring.

The other three models – ECHAM-M7, ECHAM-SALSA, and UKESM1 – showed more clear changes in the patterns of seasonality between sites, typically showing stronger seasonality at northern sites. For Aitken mode (Fig. 11), ECHAM-SALSA showed two maxima in the seasonality in Aitken mode; however the seasonality is weaker at southern sites. ECHAM-SALSA also showed two maxima for nucleation mode (Fig. S24). ECHAM-M7 showed the summer maximum for northern sites (Fig. 11), whereas for southern sites the seasonal curve was constant throughout the year or has the maximum in winter. Looking at the measurement-based representations (modal and sectional representation), the differences in seasonal patterns between the two ECHAM models were not only due to differences in Aitken mode diameter ranges. One likely contributor to the differences between M7 and SALSA was that they use different nucleation parameterizations. M7 uses the parameterization by Kazil et al. (2010), and SALSA uses the activation nucleation parameterizations by Sihto et al. (2006). In addition, it has been shown that solving simultaneously occurring nucleation and condensation within microphysical models will have implications for simulated new particle formation and growth of particles (Kokkola et al., 2009; Wan et al., 2013). Thus, the differences between M7 and SALSA are also related to differences in their numerical methods used for solving nucleation and

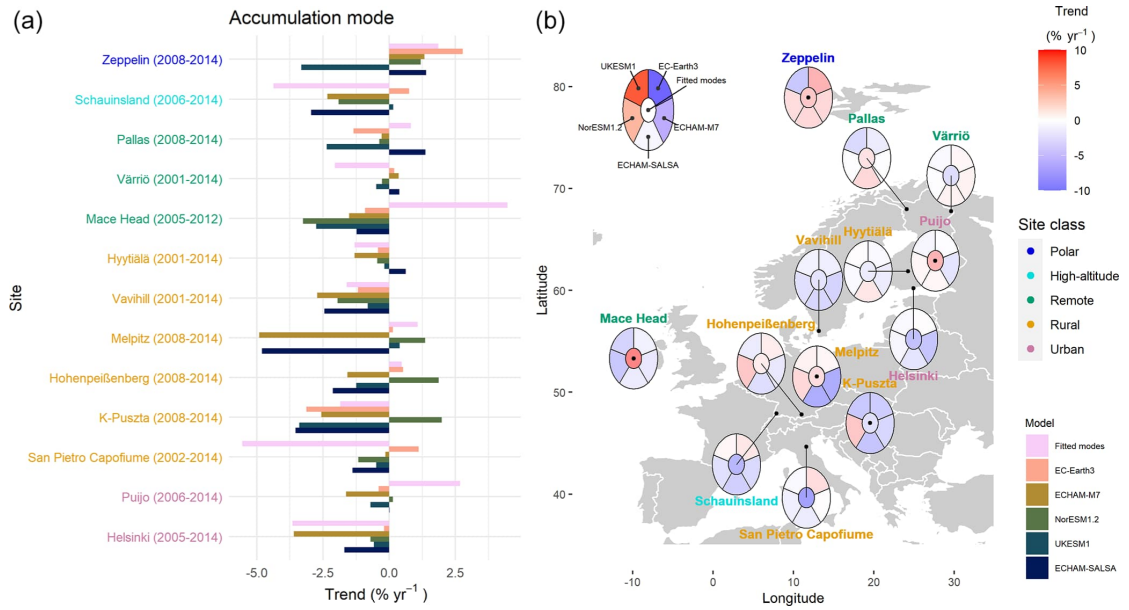

Figure 8. Long-term trend estimates for measured and modelled accumulation mode number concentration. **(a)** Bar plot of trends at different sites. Sites (y axis) are arranged by site class and within each site class from north to south. **(b)** Estimated trends presented on the map. The colour of the central part follows the trend of the fitted modes. Trends have been calculated using the Sen–Theil estimator and complemented with bootstrap confidence intervals (see Sect. 2.3.2).

condensation (see Kokkola et al., 2008, 2009). For the accumulation mode (Fig. 12), these three models show a summer maximum at northern sites. For southern sites, ECHAM-SALSA shows a summer maximum with a weaker seasonal effect, and UKESM1 and ECHAM-M7 show consistent seasonal curves or winter N maxima with weak seasonal effects. For nucleation mode, ECHAM-SALSA and ECHAM-M7 have two maxima in spring and autumn, whereas UKESM1 has typically only one maximum in winter or early spring (Fig. S24).

Additionally, modelled N's for different sites and the ratio between the highest- and lowest-concentration sites varied significantly between the models. Differences in Aitken mode N's between models can be due to differences in model microphysics (see Table 3), and especially in accumulation mode these differences can be due to varying deposition rates that affect the efficiency of long-range transportation of particles or the way emissions are divided into different size ranges. Differences were large, especially in Aitken mode, when we compared how N's were distributed between the sites in models and measurements. Furthermore, there were large variations in measured concentrations between the sites for all three investigated modes. The ratio for Aitken mode yearly median concentrations between the highest- and lowest-concentration sites was between 65 and 90 for different measurement-based representations (fitted modes, modal and sectional representation) and between 4 and 180 for models (see also Fig. 11). For Aitken mode, ECHAM models had the least variation in concentrations between sites, followed by EC-Earth3, UKESM1, and NorESM1.2. For accumulation mode, ratios were smaller, between 34 and 40 for measurement-based representations and between 11 and 111 for models. For accumulation mode, the ratios were between 11 and 15 for UKESM1, EC-Earth3, and ECHAM-M7; 58 for ECHAM-SALSA; and 111 for NorESM1.2. A large difference between ECHAM models might be due to differences in accumulation mode diameters and low concentration of accumulation mode particles at the Zeppelin site in ECHAM-SALSA. The concentrations in sectional model representation (particle diameter 50–700 nm) were higher than for modal representation (100–1000 nm) for both ECHAM models and measurement-based representations.

4 Summary and conclusions

In this study, we had two aims: (1) to study the trends of particle modes, namely nucleation, Aitken, and accumulation, and their properties (N, D_p, σ) in Europe and the Arctic and (2) to provide the first extensive comparison for climate model aerosol number concentration trends and seasonality with measured ones. In addition to providing a data set

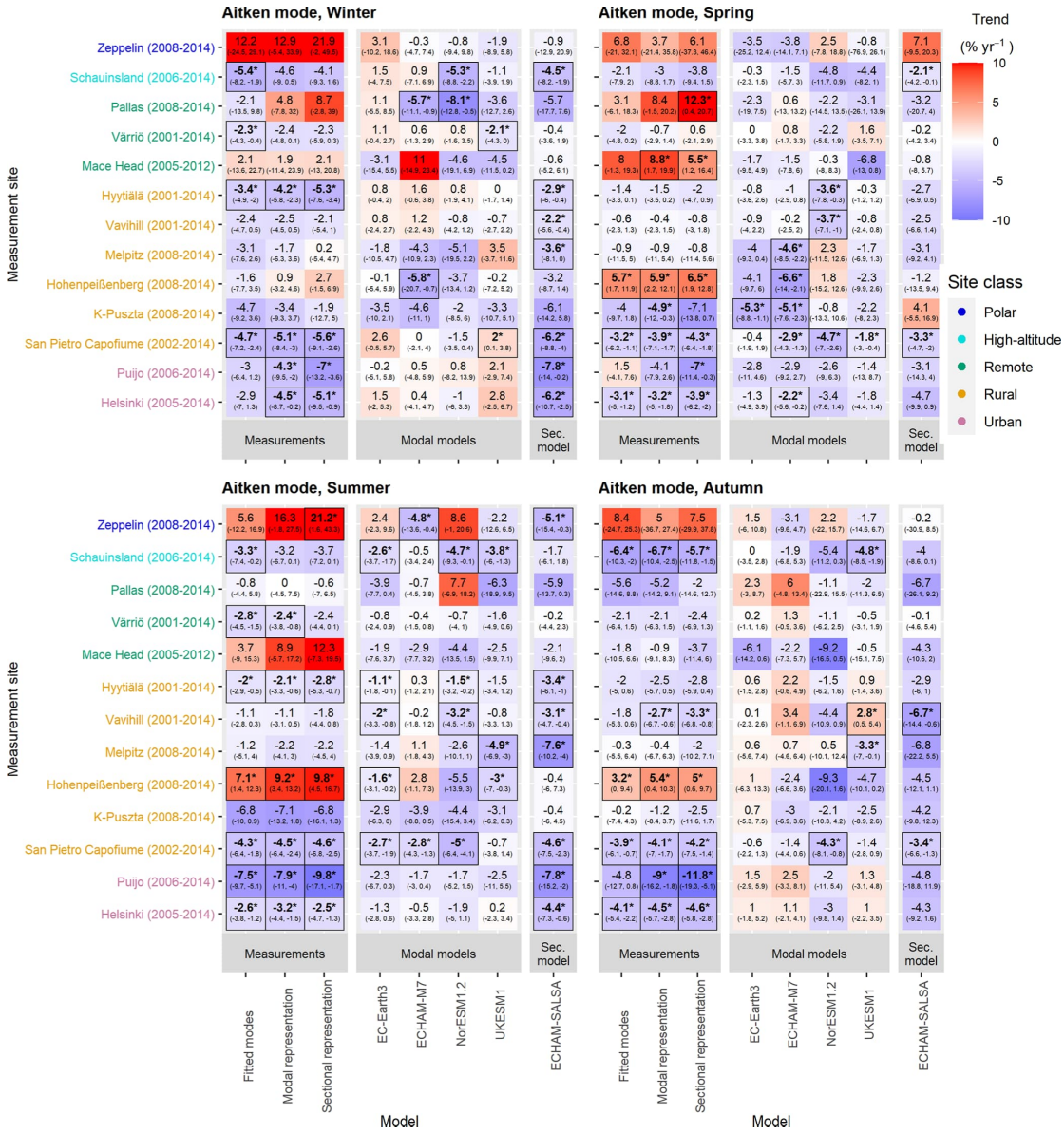

Figure 9. Seasonal trend estimates for Aitken mode number concentration for four seasons: winter (January, February, December), spring (March, April, May), summer (June, July, August), and autumn (September, October, November). Sites are ordered by site class and within site class most northerly to most southerly. Bold numbers, asterisks, and line borders around the estimate indicate that the trend is statistically significant (95 % confidence level). Trends have been calculated using the Sen–Theil estimator and complemented with bootstrap confidence intervals (see Sect. 2.3.2).

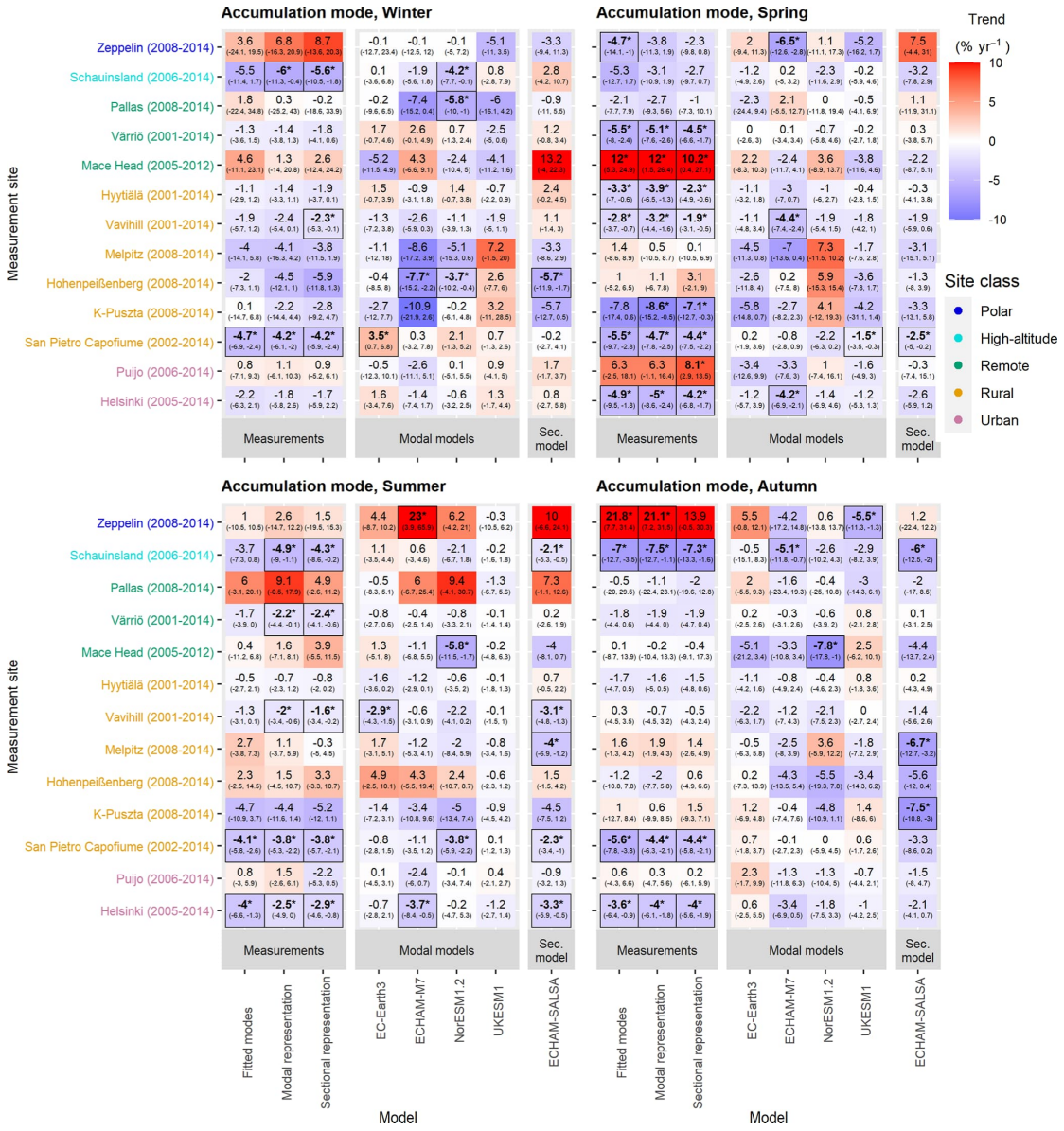

Figure 10. Seasonal trend estimates for accumulation mode number concentration for four seasons: winter (January, February, December), spring (March, April, May), summer (June, July, August), and autumn (September, October, November). Sites are ordered by site class and within site class from most northerly to most southerly. Bold numbers, asterisks, and line borders around the estimate indicate that the trend is statistically significant (95 % confidence level). Trends have been calculated using the Sen–Theil estimator and complemented with bootstrap confidence intervals (see Sect. 2.3.2).

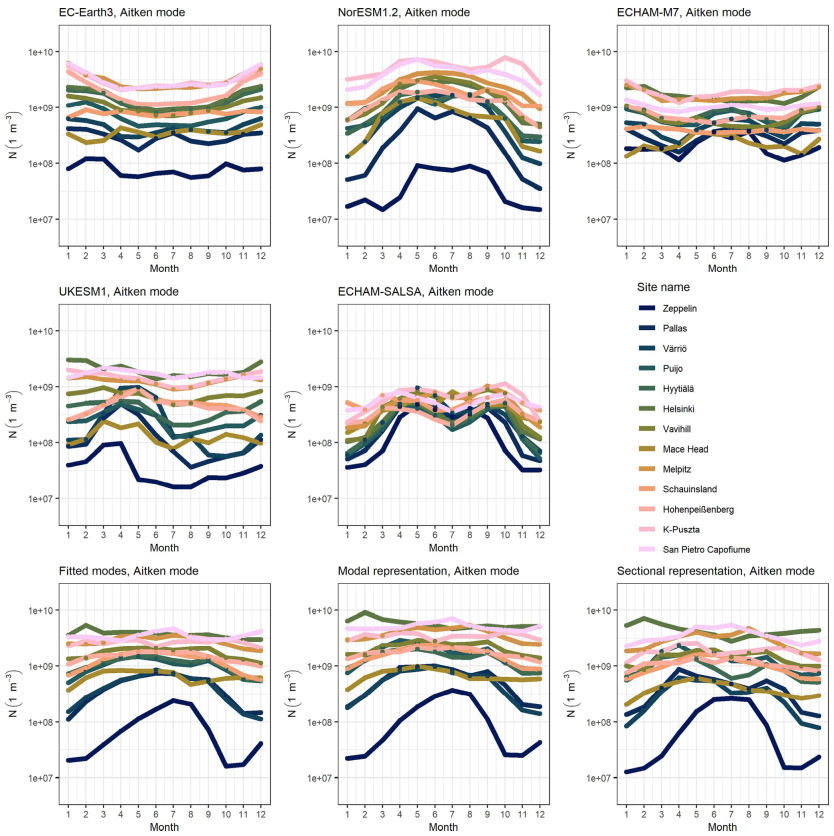

Figure 11. Seasonal cycle of Aitken mode number concentration in measurements and climate models for measurement sites. A subplot represents the seasonal cycle in one model or measurement. Coloured lines represent the median of the monthly means for Aitken mode number concentrations. Sites are ordered from most northerly to most southerly.

for model evaluation, the observational data compiled in this study could also facilitate studies on how the aerosol size distributions have evolved during previous years and how they have changed, e.g. the cloud activation capability of aerosol.

The results for measured data sets were in line with previous studies, showing that the number concentrations of particles were usually higher at urban sites and southern and central Europe than at rural sites in northern Europe. Additionally, our results from measurements showed a decreasing trend for most of the mode number concentrations and sites, which supports earlier findings. Our investigation for mode fittings revealed that mode diameter and number concentrations are dependent: increasing number concentration was sometimes related to a decrease in mode mean diameter. This dependency was stronger for particles of smaller diameters.

We also found that the trends in measured number concentrations differ between seasons and that the sign and the magnitude of the trend were not constant during the time period. The dynamic linear model (DLM) model was applied to characterize the changes in trends. DLM results supported our finding of dependence of diameter and number concentration in mode-fitting data. In addition, we found that the changes in parameters are site-specific; i.e. time periods of decrease and at the same time increase among other sites of the same area were found. On the other hand, sites are considered to be point measurements, which means that if decreases in the particle properties would have been observed at the same time in a certain area, it should have resulted from uniform changes in the particle properties at a regional level.

We compared measured and modelled trends for aerosol number concentrations. The measured trends were made comparable with global model results by calculating corresponding sectional and modal representations also from the measured data. It was seen that the factors affecting the fitted modes, namely larger diameters in fitted modes and correla-

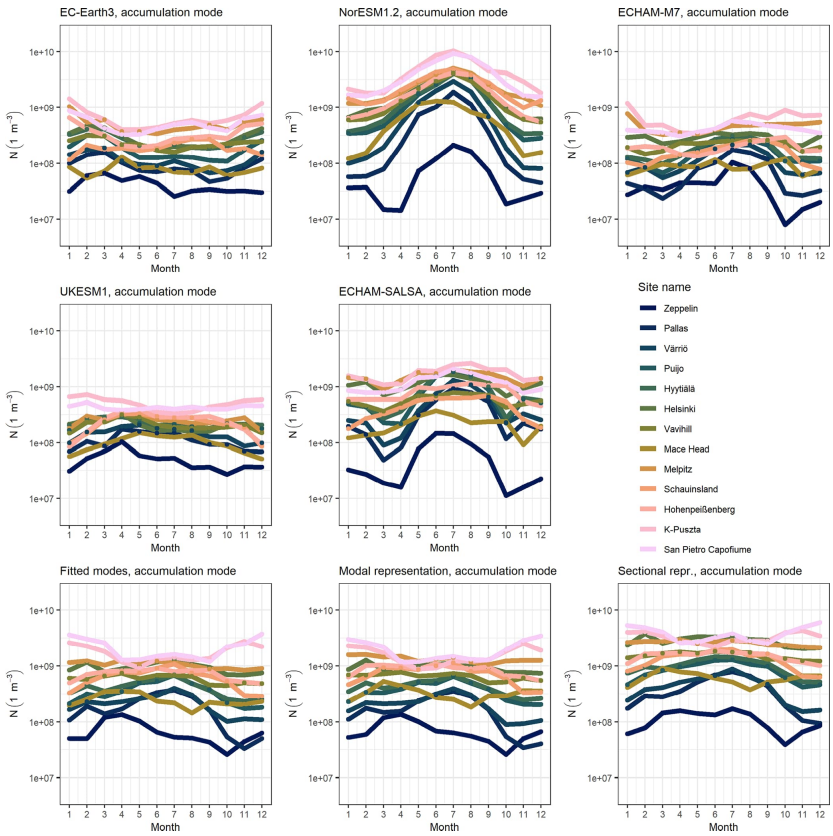

Figure 12. The seasonal cycle of accumulation mode number concentration in measurements and climate models for measurement sites. A subplot represents the seasonal cycle in one model or measurement. Coloured lines represent the median of the monthly means for accumulation mode number concentrations. Sites are ordered from most northerly to most southerly.

tions between the mean diameter and number concentration, did not have a large role in the estimated trends from the measured data. Trend estimates for mode-fitting data and corresponding sectional and modal representations were close to each other. For some sites, long-term measurements of small (< 10 nm) particles were not available; thus, conclusions about the nucleation mode trends for those sites were uncertain.

We found that models were mostly able to reproduce long-term decreasing trends in Aitken and accumulation modes. Modelled trends of yearly data were usually smaller in absolute value but had the same direction as measured trends for most of the sites. We found that the differences between the models and observations were largest for the sites where the observations show a strong positive trend (Zeppelin, Mace Head, and Hohenpeißenberg). We assume that those sites may represent more local conditions than the area captured by the climate model grid box. For seasonal trends in general, the differences were larger. However, the number of data points in seasonal trend estimation is relatively small. In general, the agreement between the models and observations varied a lot within the site classes, and no specific factor explaining the variation was found.

For seasonality representation, we found models with differences in their representation despite the anthropogenic mass emissions used in models being the same. There were differences in the seasonal pattern, its magnitude, and when the maxima of number concentrations are achieved. Furthermore, for some models, the seasonal pattern was relatively uniform for all the sites, whereas for other models, the seasonal pattern varied between sites: for ECHAM-M7, ECHAM-SALSA, and UKESM1, the seasonal pattern varied between sites, while for EC-Earth3 and NorESM1.2, the pattern was consistent for all sites. Also, the modelled number concentrations for different models had large differences. In general, we found that the seasonality analysed from models

and its differences between the sites did not depend solely on emissions used in the models or, for example, on aerosol size distribution representation (sectional or modal), but it is likely that the seasonality behaviour is driven by representation of different physical processes and their interplay. Also, the differences in modelled N of Aitken and accumulation particles suggest that the modelled microphysics, e.g. particle deposition rates and long-range transportation, could explain some of the differences in the Aitken and accumulation mode N, and this effect should be studied separately. Our results indicate that the availability and nature of the observations we have limit our ability to understand whether the models accurately represent trends in particle concentrations and how this, in turn, affects ACI. In addition to consistent long-term data, good characterization of the measurement sites and the surrounding areas that they present is important for a thorough comparison between models and observations. We suggest that a more detailed characterization of processes causing model differences should be conducted in the future. It would be important to study the effect of other individual aerosol processes of the models on the modelled aerosol number concentrations to extract the most important reasons for the differences.

Code and data availability. Most of the particle number size distribution measurement data sets are already available from ACTRIS (https://actris.nilu.no/, last access: 31 July 2019; NILU, 2019) and SmartSmear (https://smear.avaa.csc.fi/, last access: 9 October 2019; Ministry of Education and Culture of Finland and CSC, 2019) databases. Data from Nieminen et al. (2018; https://doi.org/10.5194/acp-18-14737-2018), missing measurement sites (Järvselja, San Pietro Capofiume, Villum), and model data as well as the codes are available upon request from the authors.

Supplement. The supplement related to this article is available online at: https://doi.org/10.5194/acp-22-12873-2022-supplement.

Author contributions. HK, TYJ, TK, TN, AV, and SM planned the analysis; HK, TeM, TK, TB, KC, SD, MF, TH, NK, RK, MK, AL, AM, NM, JPM, SMN, TvN, FMO, CO, DO, JBP, TP, ØS, MS, CS, HS, ES, TT, and AW participated in data collection; VL, SH, and TuM wrote the code for data analysis; VL, HK, TYJ, TeM, TK, TN, AV, and SM performed data analysis, analysed the results, and contributed to the writing of the original draft, with comments from all co-authors.

Competing interests. At least one of the (co-)authors is a member of the editorial board of *Atmospheric Chemistry and Physics*. The peer-review process was guided by an independent editor, and the authors also have no other competing interests to declare.

Disclaimer. Publisher's note: Copernicus Publications remains neutral with regard to jurisdictional claims in published maps and institutional affiliations.

Acknowledgements. The Villum Foundation is gratefully acknowledged for financing the establishment of Villum Research. Thanks to the Royal Danish Air Force and the Arctic Command for providing logistic support to the project. Christel Christoffersen, Bjarne Jensen, and Keld Mortensen are gratefully acknowledged for their technical support.

Financial support. This research has been supported by the European Union's Horizon 2020 research and innovation programme under grant agreement nos. 821205 (FORCeS) and 641816 (CRESCENDO), Academy of Finland Flagship funding (grant nos. 337550, 337552, and 337549), and the Academy of Finland competitive funding to strengthen university research profiles (PROFI) for the University of Eastern Finland (grant no. 325022). The research leading to these results has received funding from the European Union's Horizon 2020 research and innovation programme under grant agreement nos. 262254 (ACTRIS), 654109 (ACTRIS-2), 739530 (ACTRIS-PPP), 871115 (ACTRIS-IMP), and 689443 (ERA-PLANET). Tero Mielonen's and Harri Kokkola's work was supported by the Academy of Finland (grant nos. 308292 and 317390). Steffen M. Noe was supported by the Estonian Ministry of Sciences projects (grant nos. P180021, P180274, and P200196) and by the Estonian Research Infrastructures Roadmap Project "Estonian Environmental Observatory" (3.2.0304.11-0395). Fiona M. O'Connor was supported by the BEIS and DEFRA Met Office Hadley Centre Climate Programme (GA01101). Catherine E. Scott received funding from the UK's Natural Environment Research Council under NE/S015396/1. Erik Swietlicki was supported by the Swedish Research Council (Vetenskapsrådet) for ACTRIS Sweden under contract 2021-00177. This research has been partly financially supported by the Danish Environmental Protection Agency and the Danish Energy Agency with means from MIKA/DANCEA funds for environmental support to the Arctic region (project nos. Danish EPA: MST-113-00-140; Ministry of Climate, Energy, and Utilities: 2018-3767) and ERA-PLANET (the European network for observing our changing Planet) projects; iGOSP and iCUPE; and finally the Graduate School of Science and Technology, Aarhus University.

Review statement. This paper was edited by Lynn M. Russell and reviewed by two anonymous referees.

References

Anderson, T. R., Spall, S. A., Yool, A., Cipollini, P., Challenor, P. G., and Fasham, M. J. R.: Global fields of sea surface dimethylsulfide predicted from chlorophyll, nutrients and light, J. Marine Syst., 30, 1–20, https://doi.org/10.1016/S0924-7963(01)00028-8, 2001.

Andres, R. J. and Kasgnoc, A. D.: A time-averaged inventory of subaerial volcanic sulfur emissions, J. Geophys. Res.-Atmos., 103, 25251–25261, https://doi.org/10.1029/98JD02091, 1998.

Archibald, A. T., O'Connor, F. M., Abraham, N. L., Archer-Nicholls, S., Chipperfield, M. P., Dalvi, M., Folberth, G. A., Dennison, F., Dhomse, S. S., Griffiths, P. T., Hardacre, C., Hewitt, A. J., Hill, R. S., Johnson, C. E., Keeble, J., Köhler, M. O., Morgenstern, O., Mulcahy, J. P., Ordóñez, C., Pope, R. J., Rumbold, S. T., Russo, M. R., Savage, N. H., Sellar, A., Stringer, M., Turnock, S. T., Wild, O., and Zeng, G.: Description and evaluation of the UKCA stratosphere–troposphere chemistry scheme (StratTrop vn 1.0) implemented in UKESM1, Geosci. Model Dev., 13, 1223–1266, https://doi.org/10.5194/gmd-13-1223-2020, 2020.

Arneth, A., Harrison, S. P., Zaehle, S., Tsigaridis, K., Menon, S., Bartlein, P. J., Feichter, J., Korhola, A., Kulmala, M., O'Donnell, D., Schurgers, G., Sorvari, S., and Vesala, T.: Terrestrial biogeochemical feedbacks in the climate system, Nat. Geosci., 3, 525–532, https://doi.org/10.1038/ngeo905, 2010.

Asmi, A., Wiedensohler, A., Laj, P., Fjaeraa, A.-M., Sellegri, K., Birmili, W., Weingartner, E., Baltensperger, U., Zdimal, V., Zikova, N., Putaud, J.-P., Marinoni, A., Tunved, P., Hansson, H.-C., Fiebig, M., Kivekäs, N., Lihavainen, H., Asmi, E., Ulevicius, V., Aalto, P. P., Swietlicki, E., Kristensson, A., Mihalopoulos, N., Kalivitis, N., Kalapov, I., Kiss, G., de Leeuw, G., Henzing, B., Harrison, R. M., Beddows, D., O'Dowd, C., Jennings, S. G., Flentje, H., Weinhold, K., Meinhardt, F., Ries, L., and Kulmala, M.: Number size distributions and seasonality of submicron particles in Europe 2008–2009, Atmos. Chem. Phys., 11, 5505–5538, https://doi.org/10.5194/acp-11-5505-2011, 2011.

Asmi, A., Collaud Coen, M., Ogren, J. A., Andrews, E., Sheridan, P., Jefferson, A., Weingartner, E., Baltensperger, U., Bukowiecki, N., Lihavainen, H., Kivekäs, N., Asmi, E., Aalto, P. P., Kulmala, M., Wiedensohler, A., Birmili, W., Hamed, A., O'Dowd, C., G Jennings, S., Weller, R., Flentje, H., Fjaeraa, A. M., Fiebig, M., Myhre, C. L., Hallar, A. G., Swietlicki, E., Kristensson, A., and Laj, P.: Aerosol decadal trends – Part 2: In-situ aerosol particle number concentrations at GAW and ACTRIS stations, Atmos. Chem. Phys., 13, 895–916, https://doi.org/10.5194/acp-13-895-2013, 2013.

Bentsen, M., Bethke, I., Debernard, J. B., Iversen, T., Kirkevåg, A., Seland, Ø., Drange, H., Roelandt, C., Seierstad, I. A., Hoose, C., and Kristjánsson, J. E.: The Norwegian Earth System Model, NorESM1-M – Part 1: Description and basic evaluation of the physical climate, Geosci. Model Dev., 6, 687–720, https://doi.org/10.5194/gmd-6-687-2013, 2013.

Bergman, T., Makkonen, R., Schrödner, R., Swietlicki, E., Phillips, V. T. J., Le Sager, P., and van Noije, T.: Description and evaluation of a secondary organic aerosol and new particle formation scheme within TM5-MP v1.2, Geosci. Model Dev., 15, 683–713, https://doi.org/10.5194/gmd-15-683-2022, 2022.

Berrisford, P., Kållberg, P., Kobayashi, S., Dee, D., Uppala, S., Simmons, A. J., Poli, P., and Sato, H.: Atmospheric conservation properties in ERA-Interim, Q. J. Roy. Meteor. Soc., 137, 1381–1399, https://doi.org/10.1002/qj.864, 2011.

Birmili, W., Berresheim, H., Plass-Dülmer, C., Elste, T., Gilge, S., Wiedensohler, A., and Uhrner, U.: The Hohenpeissenberg aerosol formation experiment (HAFEX): a long-term study including size-resolved aerosol, H_2SO_4, OH, and monoterpenes measurements, Atmos. Chem. Phys., 3, 361–376, https://doi.org/10.5194/acp-3-361-2003, 2003.

Birmili, W., Weinhold, K., Rasch, F., Sonntag, A., Sun, J., Merkel, M., Wiedensohler, A., Bastian, S., Schladitz, A., Löschau, G., Cyrys, J., Pitz, M., Gu, J., Kusch, T., Flentje, H., Quass, U., Kaminski, H., Kuhlbusch, T. A. J., Meinhardt, F., Schwerin, A., Bath, O., Ries, L., Gerwig, H., Wirtz, K., and Fiebig, M.: Long-term observations of tropospheric particle number size distributions and equivalent black carbon mass concentrations in the German Ultrafine Aerosol Network (GUAN), Earth Syst. Sci. Data, 8, 355–382, https://doi.org/10.5194/essd-8-355-2016, 2016.

Bouwman, A. F., Lee, D. S., Asman, W. A. H., Dentener, F. J., Van Der Hoek, K. W., and Olivier, J. G. J.: A global high-resolution emission inventory for ammonia, Global Biogeochem. Cy., 11, 561–587, https://doi.org/10.1029/97GB02266, 1997.

Breider, T. J., Mickley, L. J., Jacob, D. J., Ge, C., Wang, J., Sulprizio, M. P., Croft, B., Ridley, D. A., McConnell, J. R., Sharma, S., Husain, L., Dutkiewicz, V. A., Eleftheriadis, K., Skov, H., and Hopke, P. K.: Multidecadal trends in aerosol radiative forcing over the Arctic: Contribution of changes in anthropogenic aerosol to Arctic warming since 1980, J. Geophys. Res., 122, 3573–3594, https://doi.org/10.1002/2016JD025321, 2017.

Carslaw, D. C. and Ropkins, K.: *openair* — An R package for air quality data analysis, Environ. Modell. Softw., 27–28, 52–61, https://doi.org/10.1016/j.envsoft.2011.09.008, 2012.

Cheng, T., Peng, Y., Feichter, J., and Tegen, I.: An improvement on the dust emission scheme in the global aerosol-climate model ECHAM5-HAM, Atmos. Chem. Phys., 8, 1105–1117, https://doi.org/10.5194/acp-8-1105-2008, 2008.

Collaud Coen, M., Andrews, E., Asmi, A., Baltensperger, U., Bukowiecki, N., Day, D., Fiebig, M., Fjaeraa, A. M., Flentje, H., Hyvärinen, A., Jefferson, A., Jennings, S. G., Kouvarakis, G., Lihavainen, H., Lund Myhre, C., Malm, W. C., Mihapopoulos, N., Molenar, J. V., O'Dowd, C., Ogren, J. A., Schichtel, B. A., Sheridan, P., Virkkula, A., Weingartner, E., Weller, R., and Laj, P.: Aerosol decadal trends – Part 1: In-situ optical measurements at GAW and IMPROVE stations, Atmos. Chem. Phys., 13, 869–894, https://doi.org/10.5194/acp-13-869-2013, 2013.

Collaud Coen, M., Andrews, E., Alastuey, A., Arsov, T. P., Backman, J., Brem, B. T., Bukowiecki, N., Couret, C., Eleftheriadis, K., Flentje, H., Fiebig, M., Gysel-Beer, M., Hand, J. L., Hoffer, A., Hooda, R., Hueglin, C., Joubert, W., Keywood, M., Kim, J. E., Kim, S.-W., Labuschagne, C., Lin, N.-H., Lin, Y., Lund Myhre, C., Luoma, K., Lyamani, H., Marinoni, A., Mayol-Bracero, O. L., Mihalopoulos, N., Pandolfi, M., Prats, N., Prenni, A. J., Putaud, J.-P., Ries, L., Reisen, F., Sellegri, K., Sharma, S., Sheridan, P., Sherman, J. P., Sun, J., Titos, G., Torres, E., Tuch, T., Weller, R., Wiedensohler, A., Zieger, P., and Laj, P.: Multidecadal trend analysis of in situ aerosol radiative properties around the world, Atmos. Chem. Phys., 20, 8867–8908, https://doi.org/10.5194/acp-20-8867-2020, 2020.

Dentener, F., Kinne, S., Bond, T., Boucher, O., Cofala, J., Generoso, S., Ginoux, P., Gong, S., Hoelzemann, J. J., Ito, A., Marelli, L., Penner, J. E., Putaud, J.-P., Textor, C., Schulz, M., van der Werf, G. R., and Wilson, J.: Emissions of primary aerosol and precursor gases in the years 2000 and 1750 prescribed data-sets for AeroCom, Atmos. Chem. Phys., 6, 4321–4344, https://doi.org/10.5194/acp-6-4321-2006, 2006.

Durbin, J. and Koopman, S. J.: Time Series Analysis by State Space Methods, Oxford University Press, Oxford, ISBN 978-0-19-964117-8, 2012.

Dusek, U., Frank, G. P., Hildebrandt, L., Curtius, J., Schneider, J., Walter, S., Chand, D., Drewnick, F., Hings, S., Jung, D., Borrmann, S., and Andreae, M. O.: Size matters more than chemistry for cloud-nucleating ability of aerosol particles, Science, 312, 1375–1378, https://doi.org/10.1126/science.1125261, 2006.

Forster, P., Storelvmo, T., Armour, K., Collins, W., Dufresne, J. L., Frame, D., Lunt, D. J., Mauritsen, T., Palmer, M. D., Watanabe, M., Wild, M., and Zhang, H.: The Earth's Energy Budget, Climate Feedbacks, and Climate Sensitivity, in: Climate Change 2021: The Physical Science Basis. Contribution of Working Group I to the Sixth Assessment Report of the Intergovernmental Panel on Climate Change, edited by: Masson-Delmotte, V., Zhai, P., Pirani, A., Connors, S. L., Péan, C., Berger, S., Caud, N., Chen, Y., Goldfarb, L., Gomis, M. I., Huang, H., Leitzell, K., Lonnoy, E., Matthews, J. B. R., Maycock, T. K., Waterfield, T., Yelekçi, O., Yu, R., and Zhou, B., Cambridge University Press, Cambridge, United Kingdom and New York, NY, USA, 923–1054, 2021.

Gantt, B., Meskhidze, N., Facchini, M. C., Rinaldi, M., Ceburnis, D., and O'Dowd, C. D.: Wind speed dependent size-resolved parameterization for the organic mass fraction of sea spray aerosol, Atmos. Chem. Phys., 11, 8777–8790, https://doi.org/10.5194/acp-11-8777-2011, 2011.

Gantt, B., Johnson, M. S., Meskhidze, N., Sciare, J., Ovadnevaite, J., Ceburnis, D., and O'Dowd, C. D.: Model evaluation of marine primary organic aerosol emission schemes, Atmos. Chem. Phys., 12, 8553–8566, https://doi.org/10.5194/acp-12-8553-2012, 2012.

Gliß, J., Mortier, A., Schulz, M., Andrews, E., Balkanski, Y., Bauer, S. E., Benedictow, A. M. K., Bian, H., Checa-Garcia, R., Chin, M., Ginoux, P., Griesfeller, J. J., Heckel, A., Kipling, Z., Kirkevåg, A., Kokkola, H., Laj, P., Le Sager, P., Lund, M. T., Lund Myhre, C., Matsui, H., Myhre, G., Neubauer, D., van Noije, T., North, P., Olivié, D. J. L., Rémy, S., Sogacheva, L., Takemura, T., Tsigaridis, K., and Tsyro, S. G.: AeroCom phase III multi-model evaluation of the aerosol life cycle and optical properties using ground- and space-based remote sensing as well as surface in situ observations, Atmos. Chem. Phys., 21, 87–128, https://doi.org/10.5194/acp-21-87-2021, 2021.

Gong, S. L.: A parameterization of sea-salt aerosol source function for sub- and super-micron particles, Global Biogeochem. Cy., 17, 1097, https://doi.org/10.1029/2003gb002079, 2003.

Guelle, W., Schulz, M., Balkanski, Y., and Dentener, F.: Influence of the source formulation on modeling the atmospheric global distribution of sea salt aerosol, J. Geophys. Res.-Atmos., 106, 27509–27524, https://doi.org/10.1029/2001JD900249, 2001.

Guenther, A., Hewitt, C. N., Erickson, D., Fall, R., Geron, C., Graedel, T., Harley, P., Klinger, L., Lerdau, M., Mckay, W. A., Pierce, T., Scholes, B., Steinbrecher, R., Tallamraju, R., Taylor, J., and Zimmerman, P.: A global model of natural volatile organic compound emissions, J. Geophys. Res., 100, 8873–8892, https://doi.org/10.1029/94JD02950, 1995.

Hamed, A., Joutsensaari, J., Mikkonen, S., Sogacheva, L., Dal Maso, M., Kulmala, M., Cavalli, F., Fuzzi, S., Facchini, M. C., Decesari, S., Mircea, M., Lehtinen, K. E. J., and Laaksonen, A.: Nucleation and growth of new particles in Po Valley, Italy, Atmos. Chem. Phys., 7, 355–376, https://doi.org/10.5194/acp-7-355-2007, 2007.

Hamed, A., Birmili, W., Joutsensaari, J., Mikkonen, S., Asmi, A., Wehner, B., Spindler, G., Jaatinen, A., Wiedensohler, A., Korhonen, H., Lehtinen, K. E. J., and Laaksonen, A.: Changes in the production rate of secondary aerosol particles in Central Europe in view of decreasing SO_2 emissions between 1996 and 2006, Atmos. Chem. Phys., 10, 1071–1091, https://doi.org/10.5194/acp-10-1071-2010, 2010.

Hari, P. and Kulmala, M.: Station for Measuring Ecosystem-Atmosphere Relations (SMEAR II), Boreal Environ. Res., 10, 315–322, 2005.

Heinold, B., Tegen, I., Schepanski, K., and Banks, J. R.: New developments in the representation of Saharan dust sources in the aerosol–climate model ECHAM6-HAM2, Geosci. Model Dev., 9, 765–777, https://doi.org/10.5194/gmd-9-765-2016, 2016.

Hellén, H., Praplan, A. P., Tykkä, T., Ylivinkka, I., Vakkari, V., Bäck, J., Petäjä, T., Kulmala, M., and Hakola, H.: Long-term measurements of volatile organic compounds highlight the importance of sesquiterpenes for the atmospheric chemistry of a boreal forest, Atmos. Chem. Phys., 18, 13839–13863, https://doi.org/10.5194/acp-18-13839-2018, 2018.

Hoesly, R. M., Smith, S. J., Feng, L., Klimont, Z., Janssens-Maenhout, G., Pitkanen, T., Seibert, J. J., Vu, L., Andres, R. J., Bolt, R. M., Bond, T. C., Dawidowski, L., Kholod, N., Kurokawa, J.-I., Li, M., Liu, L., Lu, Z., Moura, M. C. P., O'Rourke, P. R., and Zhang, Q.: Historical (1750–2014) anthropogenic emissions of reactive gases and aerosols from the Community Emissions Data System (CEDS), Geosci. Model Dev., 11, 369–408, https://doi.org/10.5194/gmd-11-369-2018, 2018.

Hussein, T., Dal Maso, M., Petäjä, T., Koponen, I. K., Paatero, P., Aalto, P. P., Hämeri, K., and Kulmala, M.: Evaluation of an automatic algorithm for fitting the particle number size distributions, Boreal Environ. Res., 10, 337–355, 2005.

Hussein, T., Martikainen, J., Junninen, H., Sogacheva, L., Wagner, R., Dal Maso, M., Riipinen, I., Aalto, P. P., and Kulmala, M.: Observation of regional new particle formation in the urban atmosphere, Tellus B, 60, 509–521, https://doi.org/10.1111/j.1600-0889.2008.00365.x, 2008.

Kazil, J., Stier, P., Zhang, K., Quaas, J., Kinne, S., O'Donnell, D., Rast, S., Esch, M., Ferrachat, S., Lohmann, U., and Feichter, J.: Aerosol nucleation and its role for clouds and Earth's radiative forcing in the aerosol-climate model ECHAM5-HAM, Atmos. Chem. Phys., 10, 10733–10752, https://doi.org/10.5194/acp-10-10733-2010, 2010.

Kirkevåg, A., Grini, A., Olivié, D., Seland, Ø., Alterskjær, K., Hummel, M., Karset, I. H. H., Lewinschal, A., Liu, X., Makkonen, R., Bethke, I., Griesfeller, J., Schulz, M., and Iversen, T.: A production-tagged aerosol module for Earth system models, OsloAero5.3 – extensions and updates for CAM5.3-Oslo, Geosci. Model Dev., 11, 3945–3982, https://doi.org/10.5194/gmd-11-3945-2018, 2018.

Kokkola, H., Korhonen, H., Lehtinen, K. E. J., Makkonen, R., Asmi, A., Järvenoja, S., Anttila, T., Partanen, A.-I., Kulmala, M., Järvinen, H., Laaksonen, A., and Kerminen, V.-M.: SALSA – a Sectional Aerosol module for Large Scale Applications, Atmos. Chem. Phys., 8, 2469–2483, https://doi.org/10.5194/acp-8-2469-2008, 2008.

Kokkola, H., Hommel, R., Kazil, J., Niemeier, U., Partanen, A.-I., Feichter, J., and Timmreck, C.: Aerosol microphysics modules in the framework of the ECHAM5 climate model – intercomparison under stratospheric conditions, Geosci. Model Dev., 2, 97–112, https://doi.org/10.5194/gmd-2-97-2009, 2009.

Kokkola, H., Kühn, T., Laakso, A., Bergman, T., Lehtinen, K. E. J., Mielonen, T., Arola, A., Stadtler, S., Korhonen, H., Ferrachat, S., Lohmann, U., Neubauer, D., Tegen, I., Siegenthaler-Le Drian, C., Schultz, M. G., Bey, I., Stier, P., Daskalakis, N., Heald, C. L., and Romakkaniemi, S.: SALSA2.0: The sectional aerosol module of the aerosol–chemistry–climate model ECHAM6.3.0-HAM2.3-MOZ1.0, Geosci. Model Dev., 11, 3833–3863, https://doi.org/10.5194/gmd-11-3833-2018, 2018.

Kuhlbrodt, T., Jones, C. G., Sellar, A., Storkey, D., Blockley, E., Stringer, M., Hill, R., Graham, T., Ridley, J., Blaker, A., Calvert, D., Copsey, D., Ellis, R., Hewitt, H., Hyder, P., Ineson, S., Mulcahy, J., Siahaan, A., and Walton, J.: The Low-Resolution Version of HadGEM3 GC3.1: Development and Evaluation for Global Climate, J. Adv. Model. Earth Sy., 10, 2865–2888, https://doi.org/10.1029/2018MS001370, 2018.

Kunsch, H. R.: The Jackknife and the Bootstrap for General Stationary Observations, Ann. Stat., 17, 1217–1241, https://doi.org/10.1214/aos/1176347265, 1989.

Kyrö, E.-M., Väänänen, R., Kerminen, V.-M., Virkkula, A., Petäjä, T., Asmi, A., Dal Maso, M., Nieminen, T., Juhola, S., Shcherbinin, A., Riipinen, I., Lehtipalo, K., Keronen, P., Aalto, P. P., Hari, P., and Kulmala, M.: Trends in new particle formation in eastern Lapland, Finland: effect of decreasing sulfur emissions from Kola Peninsula, Atmos. Chem. Phys., 14, 4383–4396, https://doi.org/10.5194/acp-14-4383-2014, 2014.

Laine, M.: Introduction to Dynamic Linear Models for Time Series Analysis, in: Geodetic Time Series Analysis in Earth Sciences, edited by: Montillet, M. S. and Bos, J. P., Springer, Cham, 139–156, ISBN: 978-3-030-21718-1, 2020.

Laine, M., Latva-Pukkila, N., and Kyrölä, E.: Analysing time-varying trends in stratospheric ozone time series using the state space approach, Atmos. Chem. Phys., 14, 9707–9725, https://doi.org/10.5194/acp-14-9707-2014, 2014.

Lana, A., Bell, T. G., Simó, R., Vallina, S. M., Ballabrera-Poy, J., Kettle, A. J., Dachs, J., Bopp, L., Saltzman, E. S., Stefels, J., Johnson, J. E., and Liss, P. S.: An updated climatology of surface dimethlysulfide concentrations and emission fluxes in the global ocean, Global Biogeochem. Cy., 25, GB1004, https://doi.org/10.1029/2010GB003850, 2011.

Leskinen, A., Arola, A., Komppula, M., Portin, H., Tiitta, P., Miettinen, P., Romakkaniemi, S., Laaksonen, A., and Lehtinen, K. E. J.: Seasonal cycle and source analyses of aerosol optical properties in a semi-urban environment at Puijo station in Eastern Finland, Atmos. Chem. Phys., 12, 5647–5659, https://doi.org/10.5194/acp-12-5647-2012, 2012.

Liss, P. S. and Merlivat, L.: Air-Sea Gas Exchange Rates: Introduction and Synthesis, in: The Role of Air-Sea Exchange in Geochemical Cycling, Springer Netherlands, 113–127, ISBN: 978-94-009-4738-2, 1986.

Liu, X., Ma, P.-L., Wang, H., Tilmes, S., Singh, B., Easter, R. C., Ghan, S. J., and Rasch, P. J.: Description and evaluation of a new four-mode version of the Modal Aerosol Module (MAM4) within version 5.3 of the Community Atmosphere Model, Geosci. Model Dev., 9, 505–522, https://doi.org/10.5194/gmd-9-505-2016, 2016.

Lohila, A., Penttilä, T., Jortikka, S., Aalto, T., Anttila, P., Asmi, E., Aurela, M., Hatakka, J., Hellén, H., Henttonen, H., Hänninen, P., Kilkki, J., Kyllönen, K., Laurila, T., Lepistö, A., Lihavainen, H., Makkonen, U., Paatero, J., Rask, M., Sutinen, R., Tuovinen, J.-P., Vuorenmaa, J., and Viisanen, Y.: Preface to the special issue on integrated research of atmosphere, ecosystems and environment at Pallas, Boreal Environ. Res., 20, 431–454, 2015.

Makkonen, R., Seland, Ø., Kirkevåg, A., Iversen, T., and Kristjánsson, J. E.: Evaluation of aerosol number concentrations in NorESM with improved nucleation parameterization, Atmos. Chem. Phys., 14, 5127–5152, https://doi.org/10.5194/acp-14-5127-2014, 2014.

Mann, G. W., Carslaw, K. S., Spracklen, D. V., Ridley, D. A., Manktelow, P. T., Chipperfield, M. P., Pickering, S. J., and Johnson, C. E.: Description and evaluation of GLOMAP-mode: a modal global aerosol microphysics model for the UKCA composition-climate model, Geosci. Model Dev., 3, 519–551, https://doi.org/10.5194/gmd-3-519-2010, 2010.

MATLAB: 9.7.0.1296695 (R2019b) Update 4, The MathWorks Inc., Natick, Massachusetts, 2019.

Metzger, S., Dentener, F., Pandis, S., and Lelieveld, J.: Gas/aerosol partitioning: 1. A computationally efficient model, J. Geophys. Res., 107, 4312, https://doi.org/10.1029/2001JD001102, 2002.

Mielonen, T., Portin, H., Komppula, M., Leskinen, A., Tamminen, J., Ialongo, I., Hakkarainen, J., Lehtinen, K. E. J., and Arola, A.: Biomass burning aerosols observed in Eastern Finland during the Russian wildfires in summer 2010 – Part 2: Remote sensing, Atmos. Environ., 47, 279–287, https://doi.org/10.1016/j.atmosenv.2011.07.016, 2012.

Mihalopoulos, N., Stephanou, E., Kanakidou, M., Pilitsidis, S., and Bousquet, P.: Tropospheric aerosol ionic composition in the Eastern Mediterranean region, Tellus B, 49, 314–326, https://doi.org/10.3402/tellusb.v49i3.15970, 1997.

Mikkonen, S., Németh, Z., Varga, V., Weidinger, T., Leinonen, V., Yli-Juuti, T., and Salma, I.: Decennial time trends and diurnal patterns of particle number concentrations in a central European city between 2008 and 2018, Atmos. Chem. Phys., 20, 12247–12263, https://doi.org/10.5194/acp-20-12247-2020, 2020.

Ministry of Education and Culture of Finland and CSC: SmartSMEAR, Fairdata.fi, https://smear.avaa.csc.fi/, last access: 9 October 2019.

Mortier, A., Gliß, J., Schulz, M., Aas, W., Andrews, E., Bian, H., Chin, M., Ginoux, P., Hand, J., Holben, B., Zhang, H., Kipling, Z., Kirkevåg, A., Laj, P., Lurton, T., Myhre, G., Neubauer, D., Olivié, D., von Salzen, K., Skeie, R. B., Takemura, T., and Tilmes, S.: Evaluation of climate model aerosol trends with ground-based observations over the last 2 decades – an AeroCom and CMIP6 analysis, Atmos. Chem. Phys., 20, 13355–13378, https://doi.org/10.5194/acp-20-13355-2020, 2020.

Moseid, K. O., Schulz, M., Storelvmo, T., Julsrud, I. R., Olivié, D., Nabat, P., Wild, M., Cole, J. N. S., Takemura, T., Oshima, N., Bauer, S. E., and Gastineau, G.: Bias in CMIP6 models as compared to observed regional dimming and brightening, Atmos. Chem. Phys., 20, 16023–16040, https://doi.org/10.5194/acp-20-16023-2020, 2020.

Mulcahy, J. P., Johnson, C., Jones, C. G., Povey, A. C., Scott, C. E., Sellar, A., Turnock, S. T., Woodhouse, M. T., Abraham, N. L.,

Andrews, M. B., Bellouin, N., Browse, J., Carslaw, K. S., Dalvi, M., Folberth, G. A., Glover, M., Grosvenor, D. P., Hardacre, C., Hill, R., Johnson, B., Jones, A., Kipling, Z., Mann, G., Mollard, J., O'Connor, F. M., Palmiéri, J., Reddington, C., Rumbold, S. T., Richardson, M., Schutgens, N. A. J., Stier, P., Stringer, M., Tang, Y., Walton, J., Woodward, S., and Yool, A.: Description and evaluation of aerosol in UKESM1 and HadGEM3-GC3.1 CMIP6 historical simulations, Geosci. Model Dev., 13, 6383–6423, https://doi.org/10.5194/gmd-13-6383-2020, 2020.

Myhre, G., Myher, C. E. L., Samset, B. H., and Storelvmo, T.: Aerosols and their Relation to Global Climate and Climate Sensitivity, Nature Education Knowledge, 4, 7, https://www.nature.com/scitable/knowledge/library/aerosols-and-their-relation-to-global-climate-102215345/ (last access: 15 September 2022), 2013.

Neale, R. B., Chen, C.-C., Gettelman, A., Lauritzen, P. H., Park, S., Williamson, D. L., Conley, A. J., Garcia, R., Kinnison, D., Lamarque, J.-F., Marsh, D., Mills, M., Smith, A. K., Tilmes, S., Vitt, F., Morrison, H., Cameron-Smith, P., Collins, W. D., Iacono, M. J., Easter, R. C., Ghan, S. J., Liu, X., Rasch, P. J., and Taylor, M. A.: Description of the NCAR Community Atmosphere Model (CAM 5.0), NCAR TECHNICAL NOTE, NCAR/TN-486+STR, Natl. Cent. for Atmos. Res, Boulder, CO, 289 pp., 2012.

Nguyen, Q. T., Glasius, M., Sørensen, L. L., Jensen, B., Skov, H., Birmili, W., Wiedensohler, A., Kristensson, A., Nøjgaard, J. K., and Massling, A.: Seasonal variation of atmospheric particle number concentrations, new particle formation and atmospheric oxidation capacity at the high Arctic site Villum Research Station, Station Nord, Atmos. Chem. Phys., 16, 11319–11336, https://doi.org/10.5194/acp-16-11319-2016, 2016.

Nieminen, T., Kerminen, V.-M., Petäjä, T., Aalto, P. P., Arshinov, M., Asmi, E., Baltensperger, U., Beddows, D. C. S., Beukes, J. P., Collins, D., Ding, A., Harrison, R. M., Henzing, B., Hooda, R., Hu, M., Hõrrak, U., Kivekäs, N., Komsaare, K., Krejci, R., Kristensson, A., Laakso, L., Laaksonen, A., Leaitch, W. R., Lihavainen, H., Mihalopoulos, N., Németh, Z., Nie, W., O'Dowd, C., Salma, I., Sellegri, K., Svenningsson, B., Swietlicki, E., Tunved, P., Ulevicius, V., Vakkari, V., Vana, M., Wiedensohler, A., Wu, Z., Virtanen, A., and Kulmala, M.: Global analysis of continental boundary layer new particle formation based on long-term measurements, Atmos. Chem. Phys., 18, 14737–14756, https://doi.org/10.5194/acp-18-14737-2018, 2018.

Nightingale, P. D., Malin, G., Law, C. S., Watson, A. J., Liss, P. S., Liddicoat, M. I., Boutin, J., and Upstill-Goddard, R. C.: In situ evaluation of air-sea gas exchange parameterizations using novel conservative and volatile tracers, Global Biogeochem. Cy., 14, 373–387, https://doi.org/10.1029/1999GB900091, 2000.

NILU (Norwegian Institute for Air Research): The ACTRIS Data Centre web portal, NILU, https://actris.nilu.no/, last access: 31 July 2019.

Noe, S. M., Niinemets, Ü., Krasnova, A., Krasnov, D., Motallebi, A., Kängsepp, V., Jõgiste, K., Hõrrak, U., Komsaare, K., Mirme, S., Vana, M., Tammet, H., Bäck, J., Vesala, T., Kulmala, M., Petäjä, T., and Kangur, A.: SMEAR Estonia: Perspectives of a large-scale forest ecosystem – atmosphere research infrastructure, Forestry Studies, 63, 56–84, https://doi.org/10.1515/fsmu-2015-0009, 2015.

O'Connor, T. C., Jennings, S. G., and O'Dowd, C. D.: Highlights of fifty years of atmospheric aerosol research at Mace Head, Atmos. Res., 90, 338–355, https://doi.org/10.1016/j.atmosres.2008.08.014, 2008.

Paasonen, P., Asmi, A., Petäjä, T., Kajos, M. K., Äijälä, M., Junninen, H., Holst, T., Abbatt, J. P. D., Arneth, A., Birmili, W., Van Der Gon, H. D., Hamed, A., Hoffer, A., Laakso, L., Laaksonen, A., Richard Leaitch, W., Plass-Dülmer, C., Pryor, S. C., Räisänen, P., Swietlicki, E., Wiedensohler, A., Worsnop, D. R., Kerminen, V. M., and Kulmala, M.: Warming-induced increase in aerosol number concentration likely to moderate climate change, Nat. Geosci., 6, 438–442, https://doi.org/10.1038/ngeo1800, 2013.

Pacifico, F., Harrison, S. P., Jones, C. D., Arneth, A., Sitch, S., Weedon, G. P., Barkley, M. P., Palmer, P. I., Serça, D., Potosnak, M., Fu, T.-M., Goldstein, A., Bai, J., and Schurgers, G.: Evaluation of a photosynthesis-based biogenic isoprene emission scheme in JULES and simulation of isoprene emissions under present-day climate conditions, Atmos. Chem. Phys., 11, 4371–4389, https://doi.org/10.5194/acp-11-4371-2011, 2011.

Peñuelas, J. and Staudt, M.: BVOCs and global change, Trends Plant Sci., 15, 133–144, https://doi.org/10.1016/j.tplants.2009.12.005, 2010.

Petris, G., Petrone, S., and Campagnoli, P.: Dynamic linear models with R, Springer-Verlag, ISBN: 978-0-387-77238-7, 2009.

R Core Team: R: A Language and Environment for Statistical Computing, https://www.r-project.org/ (last access: 26 August 2022), 2021.

Riccobono, F., Schobesberger, S., Scott, C. E., Dommen, J., Ortega, I. K., Rondo, L., Almeida, J., Amorim, A., Bianchi, F., Breitenlechner, M., David, A., Downard, A., Dunne, E. M., Duplissy, J., Ehrhart, S., Flagan, R. C., Franchin, A., Hansel, A., Junninen, H., Kajos, M., Keskinen, H., Kupc, A., Kürten, A., Kvashin, A. N., Laaksonen, A., Lehtipalo, K., Makhmutov, V., Mathot, S., Nieminen, T., Onnela, A., Petäjä, T., Praplan, A. P., Santos, F. D., Schallhart, S., Seinfeld, J. H., Sipilä, M., Spracklen, D. V., Stozhkov, Y., Stratmann, F., Tomé, A., Tsagkogeorgas, G., Vaattovaara, P., Viisanen, Y., Vrtala, A., Wagner, P. E., Weingartner, E., Wex, H., Wimmer, D., Carslaw, K. S., Curtius, J., Donahue, N. M., Kirkby, J., Kulmala, M., Worsnop, D. R., and Baltensperger, U.: Oxidation products of biogenic emissions contribute to nucleation of atmospheric particles, Science, 344, 717–721, https://doi.org/10.1126/science.1243527, 2014.

Rose, C., Collaud Coen, M., Andrews, E., Lin, Y., Bossert, I., Lund Myhre, C., Tuch, T., Wiedensohler, A., Fiebig, M., Aalto, P., Alastuey, A., Alonso-Blanco, E., Andrade, M., Artíñano, B., Arsov, T., Baltensperger, U., Bastian, S., Bath, O., Beukes, J. P., Brem, B. T., Bukowiecki, N., Casquero-Vera, J. A., Conil, S., Eleftheriadis, K., Favez, O., Flentje, H., Gini, M. I., Gómez-Moreno, F. J., Gysel-Beer, M., Hallar, A. G., Kalapov, I., Kalivitis, N., Kasper-Giebl, A., Keywood, M., Kim, J. E., Kim, S.-W., Kristensson, A., Kulmala, M., Lihavainen, H., Lin, N.-H., Lyamani, H., Marinoni, A., Martins Dos Santos, S., Mayol-Bracero, O. L., Meinhardt, F., Merkel, M., Metzger, J.-M., Mihalopoulos, N., Ondracek, J., Pandolfi, M., Pérez, N., Petäjä, T., Petit, J.-E., Picard, D., Pichon, J.-M., Pont, V., Putaud, J.-P., Reisen, F., Sellegri, K., Sharma, S., Schauer, G., Sheridan, P., Sherman, J. P., Schwerin, A., Sohmer, R., Sorribas, M., Sun, J., Tulet, P., Vakkari, V., van Zyl, P. G., Velarde, F., Villani, P., Vrato-

lis, S., Wagner, Z., Wang, S.-H., Weinhold, K., Weller, R., Yela, M., Zdimal, V., and Laj, P.: Seasonality of the particle number concentration and size distribution: a global analysis retrieved from the network of Global Atmosphere Watch (GAW) near-surface observatories, Atmos. Chem. Phys., 21, 17185–17223, https://doi.org/10.5194/acp-21-17185-2021, 2021.

Salma, I., Németh, Z., Kerminen, V.-M., Aalto, P., Nieminen, T., Weidinger, T., Molnár, Á., Imre, K., and Kulmala, M.: Regional effect on urban atmospheric nucleation, Atmos. Chem. Phys., 16, 8715–8728, https://doi.org/10.5194/acp-16-8715-2016, 2016.

Salter, M. E., Zieger, P., Acosta Navarro, J. C., Grythe, H., Kirkevåg, A., Rosati, B., Riipinen, I., and Nilsson, E. D.: An empirically derived inorganic sea spray source function incorporating sea surface temperature, Atmos. Chem. Phys., 15, 11047–11066, https://doi.org/10.5194/acp-15-11047-2015, 2015.

Schmale, J., Henning, S., Decesari, S., Henzing, B., Keskinen, H., Sellegri, K., Ovadnevaite, J., Pöhlker, M. L., Brito, J., Bougiatioti, A., Kristensson, A., Kalivitis, N., Stavroulas, I., Carbone, S., Jefferson, A., Park, M., Schlag, P., Iwamoto, Y., Aalto, P., Äijälä, M., Bukowiecki, N., Ehn, M., Frank, G., Fröhlich, R., Frumau, A., Herrmann, E., Herrmann, H., Holzinger, R., Kos, G., Kulmala, M., Mihalopoulos, N., Nenes, A., O'Dowd, C., Petäjä, T., Picard, D., Pöhlker, C., Pöschl, U., Poulain, L., Prévôt, A. S. H., Swietlicki, E., Andreae, M. O., Artaxo, P., Wiedensohler, A., Ogren, J., Matsuki, A., Yum, S. S., Stratmann, F., Baltensperger, U., and Gysel, M.: Long-term cloud condensation nuclei number concentration, particle number size distribution and chemical composition measurements at regionally representative observatories, Atmos. Chem. Phys., 18, 2853–2881, https://doi.org/10.5194/acp-18-2853-2018, 2018.

Schmale, J., Sharma, S., Decesari, S., Pernov, J., Massling, A., Hansson, H.-C., von Salzen, K., Skov, H., Andrews, E., Quinn, P. K., Upchurch, L. M., Eleftheriadis, K., Traversi, R., Gilardoni, S., Mazzola, M., Laing, J., and Hopke, P.: Pan-Arctic seasonal cycles and long-term trends of aerosol properties from 10 observatories, Atmos. Chem. Phys., 22, 3067–3096, https://doi.org/10.5194/acp-22-3067-2022, 2022.

Schultz, M. G., Stadtler, S., Schröder, S., Taraborrelli, D., Franco, B., Krefting, J., Henrot, A., Ferrachat, S., Lohmann, U., Neubauer, D., Siegenthaler-Le Drian, C., Wahl, S., Kokkola, H., Kühn, T., Rast, S., Schmidt, H., Stier, P., Kinnison, D., Tyndall, G. S., Orlando, J. J., and Wespes, C.: The chemistry–climate model ECHAM6.3-HAM2.3-MOZ1.0, Geosci. Model Dev., 11, 1695–1723, https://doi.org/10.5194/gmd-11-1695-2018, 2018.

Schutgens, N., Tsyro, S., Gryspeerdt, E., Goto, D., Weigum, N., Schulz, M., and Stier, P.: On the spatio-temporal representativeness of observations, Atmos. Chem. Phys., 17, 9761–9780, https://doi.org/10.5194/acp-17-9761-2017, 2017.

Schutgens, N. A. J., Partridge, D. G., and Stier, P.: The importance of temporal collocation for the evaluation of aerosol models with observations, Atmos. Chem. Phys., 16, 1065–1079, https://doi.org/10.5194/acp-16-1065-2016, 2016.

Sellar, A. A., Jones, C. G., Mulcahy, J. P., Tang, Y., Yool, A., Wiltshire, A., O'Connor, F. M., Stringer, M., Hill, R., Palmieri, J., Woodward, S., de Mora, L., Kuhlbrodt, T., Rumbold, S. T., Kelley, D. I., Ellis, R., Johnson, C. E., Walton, J., Abraham, N. L., Andrews, M. B., Andrews, T., Archibald, A. T., Berthou, S., Burke, E., Blockley, E., Carslaw, K., Dalvi, M., Edwards, J., Folberth, G. A., Gedney, N., Griffiths, P. T., Harper, A. B., Hendry, M. A., Hewitt, A. J., Johnson, B., Jones, A., Jones, C. D., Keeble, J., Liddicoat, S., Morgenstern, O., Parker, R. J., Predoi, V., Robertson, E., Siahaan, A., Smith, R. S., Swaminathan, R., Woodhouse, M. T., Zeng, G., and Zerroukat, M.: UKESM1: Description and Evaluation of the U.K. Earth System Model, J. Adv. Model. Earth Sy., 11, 4513–4558, https://doi.org/10.1029/2019MS001739, 2019.

Sen, P. K.: Estimates of the Regression Coefficient Based on Kendall's Tau, J. Am. Stat. Assoc., 63, 1379–1389, https://doi.org/10.1080/01621459.1968.10480934, 1968.

Sihto, S.-L., Kulmala, M., Kerminen, V.-M., Dal Maso, M., Petäjä, T., Riipinen, I., Korhonen, H., Arnold, F., Janson, R., Boy, M., Laaksonen, A., and Lehtinen, K. E. J.: Atmospheric sulphuric acid and aerosol formation: implications from atmospheric measurements for nucleation and early growth mechanisms, Atmos. Chem. Phys., 6, 4079–4091, https://doi.org/10.5194/acp-6-4079-2006, 2006.

Sindelarova, K., Granier, C., Bouarar, I., Guenther, A., Tilmes, S., Stavrakou, T., Müller, J.-F., Kuhn, U., Stefani, P., and Knorr, W.: Global data set of biogenic VOC emissions calculated by the MEGAN model over the last 30 years, Atmos. Chem. Phys., 14, 9317–9341, https://doi.org/10.5194/acp-14-9317-2014, 2014.

Smith, S. J. and Bond, T. C.: Two hundred fifty years of aerosols and climate: the end of the age of aerosols, Atmos. Chem. Phys., 14, 537–549, https://doi.org/10.5194/acp-14-537-2014, 2014.

Spiro, P. A., Jacob, D. J., and Logan, J. A.: Global inventory of sulfur emissions with $1^\circ \times 1^\circ$ resolution, J. Geophys. Res., 97, 6023–6036, https://doi.org/10.1029/91JD03139, 1992.

Stevens, B., Giorgetta, M., Esch, M., Mauritsen, T., Crueger, T., Rast, S., Salzmann, M., Schmidt, H., Bader, J., Block, K., Brokopf, R., Fast, I., Kinne, S., Kornblueh, L., Lohmann, U., Pincus, R., Reichler, T., and Roeckner, E.: Atmospheric component of the MPI-M Earth System Model: ECHAM6, J. Adv. Model. Earth Sy., 5, 146–172, https://doi.org/10.1002/jame.20015, 2013.

Storelvmo, T., Heede, U. K., Leirvik, T., Phillips, P. C. B., Arndt, P., and Wild, M.: Lethargic Response to Aerosol Emissions in Current Climate Models, Geophys. Res. Lett., 45, 9814–9823, https://doi.org/10.1029/2018GL078298, 2018.

Sun, J., Birmili, W., Hermann, M., Tuch, T., Weinhold, K., Merkel, M., Rasch, F., Müller, T., Schladitz, A., Bastian, S., Löschau, G., Cyrys, J., Gu, J., Flentje, H., Briel, B., Asbach, C., Kaminski, H., Ries, L., Sohmer, R., Gerwig, H., Wirtz, K., Meinhardt, F., Schwerin, A., Bath, O., Ma, N., and Wiedensohler, A.: Decreasing trends of particle number and black carbon mass concentrations at 16 observational sites in Germany from 2009 to 2018, Atmos. Chem. Phys., 20, 7049–7068, https://doi.org/10.5194/acp-20-7049-2020, 2020.

Tegen, I., Harrison, S. P., Kohfeld, K., Prentice, I. C., Coe, M., and Heimann, M.: Impact of vegetation and preferential source areas on global dust aerosol: Results from a model study, J. Geophys. Res.-Atmos., 107, AAC 14-1–AAC 14-27, https://doi.org/10.1029/2001JD000963, 2002.

Tegen, I., Neubauer, D., Ferrachat, S., Siegenthaler-Le Drian, C., Bey, I., Schutgens, N., Stier, P., Watson-Parris, D., Stanelle, T., Schmidt, H., Rast, S., Kokkola, H., Schultz, M., Schroeder, S., Daskalakis, N., Barthel, S., Heinold, B., and Lohmann, U.: The global aerosol–climate model ECHAM6.3–HAM2.3 – Part 1: Aerosol evaluation, Geosci. Model Dev., 12, 1643–1677, https://doi.org/10.5194/gmd-12-1643-2019, 2019.

Theil, H.: A rank-invariant method of linear and polynomial regression analysis, reprinted in 1992 in Henri Theil's contributions to economics and econometrics, Springer, 345–381, https://doi.org/10.1007/978-94-011-2546-8_20, 1950

Tunved, P., Ström, J., and Krejci, R.: Arctic aerosol life cycle: linking aerosol size distributions observed between 2000 and 2010 with air mass transport and precipitation at Zeppelin station, Ny-Ålesund, Svalbard, Atmos. Chem. Phys., 13, 3643–3660, https://doi.org/10.5194/acp-13-3643-2013, 2013.

van Marle, M. J. E., Kloster, S., Magi, B. I., Marlon, J. R., Daniau, A.-L., Field, R. D., Arneth, A., Forrest, M., Hantson, S., Kehrwald, N. M., Knorr, W., Lasslop, G., Li, F., Mangeon, S., Yue, C., Kaiser, J. W., and van der Werf, G. R.: Historic global biomass burning emissions for CMIP6 (BB4CMIP) based on merging satellite observations with proxies and fire models (1750–2015), Geosci. Model Dev., 10, 3329–3357, https://doi.org/10.5194/gmd-10-3329-2017, 2017.

van Noije, T., Bergman, T., Le Sager, P., O'Donnell, D., Makkonen, R., Gonçalves-Ageitos, M., Döscher, R., Fladrich, U., von Hardenberg, J., Keskinen, J.-P., Korhonen, H., Laakso, A., Myriokefalitakis, S., Ollinaho, P., Pérez García-Pando, C., Reerink, T., Schrödner, R., Wyser, K., and Yang, S.: EC-Earth3-AerChem: a global climate model with interactive aerosols and atmospheric chemistry participating in CMIP6 , Geosci. Model Dev., 14, 5637–5668, https://doi.org/10.5194/gmd-14-5637-2021, 2021.

Vehkamäki, H.: An improved parameterization for sulfuric acid–water nucleation rates for tropospheric and stratospheric conditions, J. Geophys. Res., 107, 4622, https://doi.org/10.1029/2002JD002184, 2002.

Vignati, E., Wilson, J., and Stier, P.: M7: An efficient size-resolved aerosol microphysics module for large-scale aerosol transport models, J. Geophys. Res., 109, D22202, https://doi.org/10.1029/2003JD004485, 2004.

Wan, H., Rasch, P. J., Zhang, K., Kazil, J., and Leung, L. R.: Numerical issues associated with compensating and competing processes in climate models: an example from ECHAM-HAM, Geosci. Model Dev., 6, 861–874, https://doi.org/10.5194/gmd-6-861-2013, 2013.

Wanninkhof, R.: Relationship between wind speed and gas exchange over the ocean revisited, Limnol. Oceanogr.-Meth., 12, 351–362, https://doi.org/10.4319/lom.2014.12.351, 2014.

Williams, J., de Reus, M., Krejci, R., Fischer, H., and Ström, J.: Application of the variability-size relationship to atmospheric aerosol studies: estimating aerosol lifetimes and ages, Atmos. Chem. Phys., 2, 133–145, https://doi.org/10.5194/acp-2-133-2002, 2002.

Williams, K. D., Copsey, D., Blockley, E. W., Bodas-Salcedo, A., Calvert, D., Comer, R., Davis, P., Graham, T., Hewitt, H. T., Hill, R., Hyder, P., Ineson, S., Johns, T. C., Keen, A. B., Lee, R. W., Megann, A., Milton, S. F., Rae, J. G. L., Roberts, M. J., Scaife, A. A., Schiemann, R., Storkey, D., Thorpe, L., Watterson, I. G., Walters, D. N., West, A., Wood, R. A., Woollings, T., and Xavier, P. K.: The Met Office Global Coupled Model 3.0 and 3.1 (GC3.0 and GC3.1) Configurations, J. Adv. Model. Earth Sy., 10, 357–380, https://doi.org/10.1002/2017MS001115, 2018.

Woodward, S.: Modeling the atmospheric life cycle and radiative impact of mineral dust in the Hadley Centre climate model, J. Geophys. Res., 106, 18155–18166, https://doi.org/10.1029/2000JD900795, 2001.

Yli-Juuti, T., Mielonen, T., Heikkinen, L., Arola, A., Ehn, M., Isokääntä, S., Keskinen, H.-M., Kulmala, M., Laakso, A., Lipponen, A., Luoma, K., Mikkonen, S., Nieminen, T., Paasonen, P., Petäjä, T., Romakkaniemi, S., Tonttila, J., Kokkola, H., and Virtanen, A.: Significance of the organic aerosol driven climate feedback in the boreal area, Nat. Commun., 12, 5637, https://doi.org/10.1038/s41467-021-25850-7, 2021.

Yool, A., Popova, E. E., and Anderson, T. R.: MEDUSA-2.0: an intermediate complexity biogeochemical model of the marine carbon cycle for climate change and ocean acidification studies, Geosci. Model Dev., 6, 1767–1811, https://doi.org/10.5194/gmd-6-1767-2013, 2013.

Yttri, K. E., Canonaco, F., Eckhardt, S., Evangeliou, N., Fiebig, M., Gundersen, H., Hjellbrekke, A.-G., Lund Myhre, C., Platt, S. M., Prévôt, A. S. H., Simpson, D., Solberg, S., Surratt, J., Tørseth, K., Uggerud, H., Vadset, M., Wan, X., and Aas, W.: Trends, composition, and sources of carbonaceous aerosol at the Birkenes Observatory, northern Europe, 2001–2018, Atmos. Chem. Phys., 21, 7149–7170, https://doi.org/10.5194/acp-21-7149-2021, 2021.

Zender, C. S., Bian, H., and Newman, D.: Mineral Dust Entrainment and Deposition (DEAD) model: Description and 1990s dust climatology, J. Geophys. Res., 108, 4416, https://doi.org/10.1029/2002jd002775, 2003.

Supplement of Atmos. Chem. Phys., 22, 12873–12905, 2022
https://doi.org/10.5194/acp-22-12873-2022-supplement

Atmospheric Chemistry and Physics
Open Access

Supplement of

Comparison of particle number size distribution trends in ground measurements and climate models

Ville Leinonen et al.

Correspondence to: Annele Virtanen (annele.virtanen@uef.fi) and Ville Leinonen (ville.j.leinonen@uef.fi)

S1 Seasonality, SeasC and NIQR

Seasonality of measured and modelled *N* were compared using SeasC for maximum seasonal variation and NIQR for average seasonal variation. In this seasonal comparison, we have concentrated on Aitken and accumulation modes. The results for the nucleation mode are shown in Fig. S18 for maximum variation and in Fig. S21 for average variation. In Figures S19 and S20, maximum variations are shown for Aitken and accumulation mode, respectively. The figures also indicate during which season the minimum and maximum values usually occur.

The maximum variation of medians of measured data values were mostly insensitive to the representation of the data, especially for the accumulation mode, although interquartile ranges did show some variation with varying measurement data representation. Notable exceptions to this general statement were the Aitken mode SeasC values for Zeppelin, K-Puszta, and San Pietro Capofiume. The strong dependence of the Aitken mode SeasC on data representation at Zeppelin is most likely due to the very clean conditions there, which easily leads to large variations in relative changes. At K-Puszta and San Pietro Capofiume, the results from measurement representations appeared to be very sensitive to the assumed upper bound of the Aitken mode, which is 50 nm for the sectional representation and 100 nm for the modal representation. This could result in a shift of particle number between Aitken and accumulation modes and hence could affect the computed SeasC value, especially if the effect was different for different seasons. This becomes apparent when comparing Figs. S19 and S20, where for these two sites the sectional representation had a larger Aitken mode SeasC and a smaller accumulation mode SeasC. The season during which the minimum and maximum values in *N* occur were also mostly independent of data representation, but in some cases shifted to an earlier or later season.

For maximum variation (SeasC) in measured data, there was a clear difference between remote and more polluted sites, with seasonal variations in *N*s being higher in remote sites. Remote sites had generally larger maximum variation due to the more dominating effect of naturally emitted (organic) particles and particle precursors during summer, which was affecting especially the Aitken mode maximum *N* and, hence increasing maximum variation. For measured maximum variation, three sites, Zeppelin (polar), Pallas (remote), and Värriö (remote) had the highest maximum variation, meaning that *N* in summer could be 3-10 times higher than concentrations in winter. For urban and other polluted sites, seasonal variation was much smaller, having maximum variation values of less than 2. Results for measured maximum variation with respect to site classes were consistent with findings of Rose et al. (2021), who presented SeasC results for total *N*s measured in 62 sites globally in 2016 or 2017.

ECHAM-SALSA, NorESM1.2, and UKESM1 had larger maximum variation for polar and remote sites than for urban sites, which was also observed in measurements. However, sometimes the maximum variation was overestimated. ECHAM-SALSA and NorESM1.2 especially seemed to overestimate the Aitken mode maximum variation in many of the sites investigated in this study. For northern sites, Pallas, Värriö, and Zeppelin, higher maximum variation in models was not the only difference, but also the seasonal cycle in these two models was similar to the measured, but different compared to the other three models, as seen for example for Aitken mode in Fig. 14. In addition, compared to the observed modes in Hyytiälä, Melpitz, K-Puszta, Vavihill, Puijo, and Helsinki, NorESM1.2 and ECHAM-SALSA had lower *N*s especially during winter, and this results in higher annual variation.

In Figures S22 and S23, measured average seasonal variation in Aitken and accumulation mode *N* was investigated with NIQR. NIQR had similar patterns as SeasC. This was expected, as both quantities measure seasonal variation, with SeasC focusing more on extreme values. For Aitken mode, the largest average variations were seen in remote sites Zeppelin, Pallas, and Värriö. For accumulation mode, the differences were smaller, remote sites having the largest values, which

were smaller than for Aitken mode. In addition, models seemed to mostly capture average seasonal variation similarly as they captured maximum variation in Aitken and accumulation mode.

In general, models captured average seasonal variation (NIQR) slightly better than maximum variations (SeasC). Variability in the interquartile range was, therefore, better accounted for than the seasonal extremes, which were resulting in higher modelled maximum variation than observations. The reason for higher maximum variation is diverse: for Aitken mode, it is usually due to underestimated lowest interquartile range and especially too small concentrations observed during winter months, whereas for accumulation mode, higher modelled concentrations during summer were usually causing too high maximum variation in models. However, in the big picture, the seasonality variables (NIQR and SeasC) got larger values in remote areas and smaller values in more polluted areas, which was seen in the models even though the magnitude of the seasonality was overestimated or underestimated.

For measured seasonal extremes in the Aitken mode, almost all sites had their minimum concentrations in winter or autumn. Only San Pietro Capofiume had its minimum in Spring. At the other sites, maxima in Aitken mode were either in summer or spring. The seasonal pattern for Aitken mode concentrations was not similar in models compared to measurements, where NorESM1.2 seemed to capture seasonal extremes best, except the magnitude of extremes, which was sometimes overestimated. Aitken mode minimum was more often captured by the models than maximum.

For Accumulation mode, measurements did not show clear differences in average seasonal variation and maximum variation of number concentration between remote and other sites, despite measured maximum variation had on average been slightly larger for remote sites. However, maximum variation of accumulation mode *N* was smaller than maximum variation of Aitken mode in remote sites. Especially NorESM1.2 and also ECHAM-SALSA seemed to overestimate the maximum variation of the Accumulation mode *N* in most of the sites. These overestimates were in almost all cases due to higher modelled *N*s in summer compared to what has been observed.

For seasonal extremes in the accumulation mode, most of the sites had their (observational) minimum concentration either in winter or autumn and maximum in spring or summer. Exceptions were San Pietro Capofiume where the minimum was during spring and maximum in winter, Mace Head where minimum was during summer and maximum during spring, and K-Puszta where the minimum was during summer and maximum in winter. Summer maxima were mostly captured by the models, and in general better than for Aitken mode. For the accumulation mode, the season of maximum number concentration was better captured by the models than the minimum.

The annual cycles of *N*s varied between models, modes, and sites. When calculating the total number of seasonal extremes captured by the models, NorESM1.2 captured most of the seasonal extremes in nucleation, Aitken, and accumulation mode for all sites (33 correct seasons/78 = 6 extremes * 13 sites), followed byECHAM-M7 (31), ECHAM-SALSA (29), UKESM (26) and EC-Earth (22) when model extremes were compared to mode fitting results. Results were varying between different modes, ECHAM-M7 and ECHAM-SALSA had best captured the nucleation mode extremes. NorESM1.2 was best for Aitken mode and UKESM1 showed the best results for accumulation mode.

S2 Additional figures

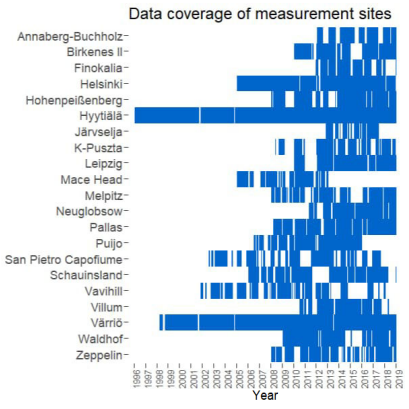

Figure S1 Data coverage of measurement sites. Blue represents the periods where daily averaged data have been calculated, i.e., there is at least 5 measurement points/day. The data coverage of the sites is between 59.6 and 98.4% of the days in the measured period.

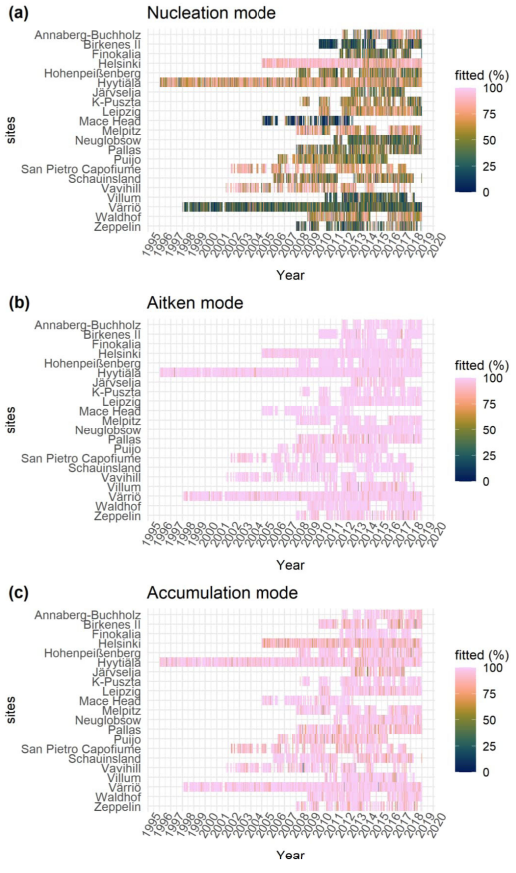

Figure S2 Percentages of fitted nucleation (a), Aitken (b), and accumulation (c) modes at each day and at different sites during the whole measurement time series.

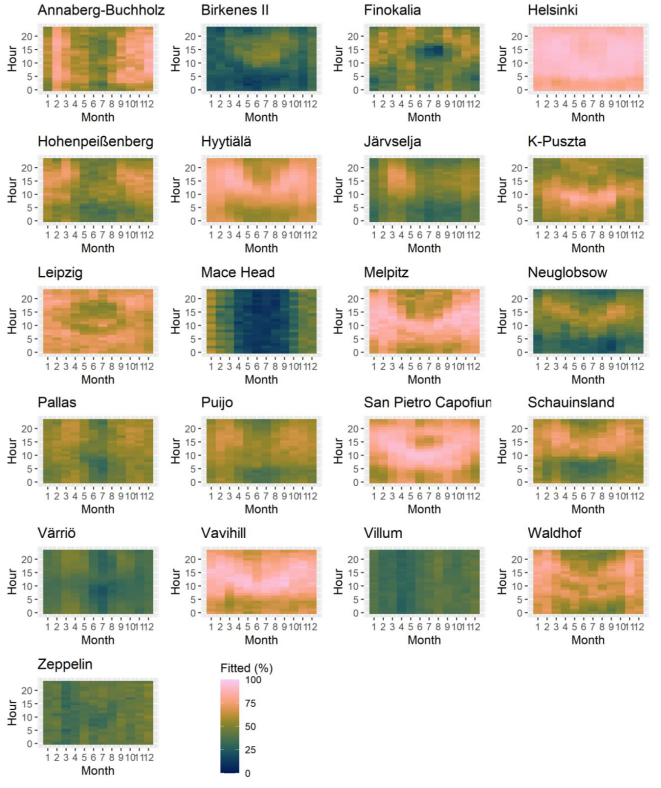

Figure S3 Mean percentages of fitted nucleation modes at each hour and month at different sites during the whole measurement time series.

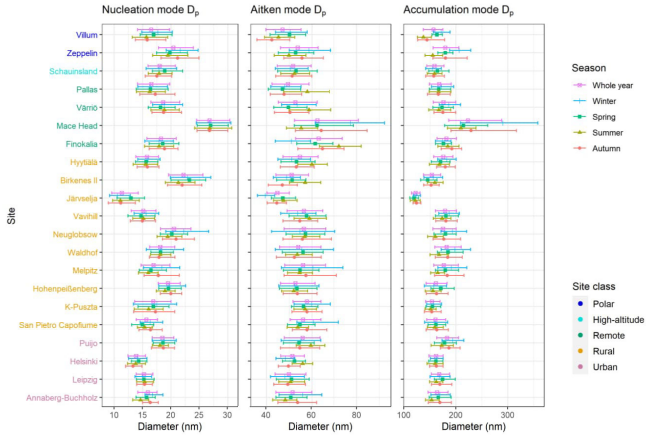

Figure S4 Summary of geometric nucleation, Aitken, and accumulation mode mean diameter D_p for measurement sites and different seasons (winter = Dec, Jan, Feb, spring = Mar, Apr, May, summer = Jun, Jul, Aug, autumn = Sep, Oct, Nov). Medians (dots) and interquartile ranges (25% and 75%, whiskers) for different mode parameters in fitted modes.

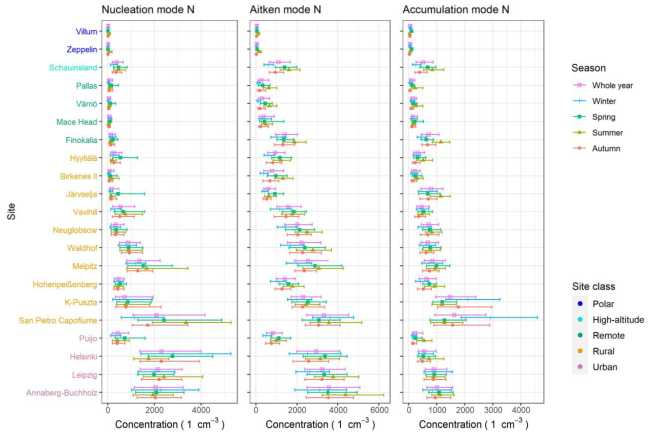

Figure S5 Summary of nucleation, Aitken, and accumulation mode number concentration (N) for measurement sites and different seasons (winter = Dec, Jan, Feb, spring = Mar, Apr, May, summer = Jun, Jul, Aug, autumn = Sep, Oct, Nov). Medians (dots) and interquartile ranges (25% and 75%, whiskers) for different mode parameters in fitted modes.

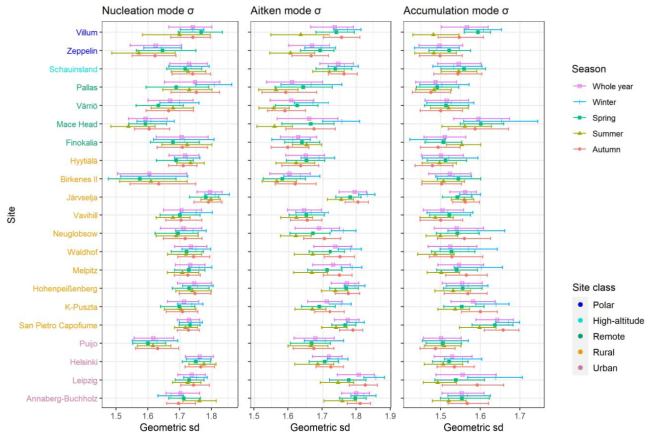

Figure S6 Summary of nucleation, Aitken, and accumulation mode geometric standard deviation σ for measurement sites and different seasons (winter = Dec, Jan, Feb, spring = Mar, Apr, May, summer = Jun, Jul, Aug, autumn = Sep, Oct, Nov). Medians (dots) and interquartile ranges (25% and 75%, whiskers) for different mode parameters in fitted modes.

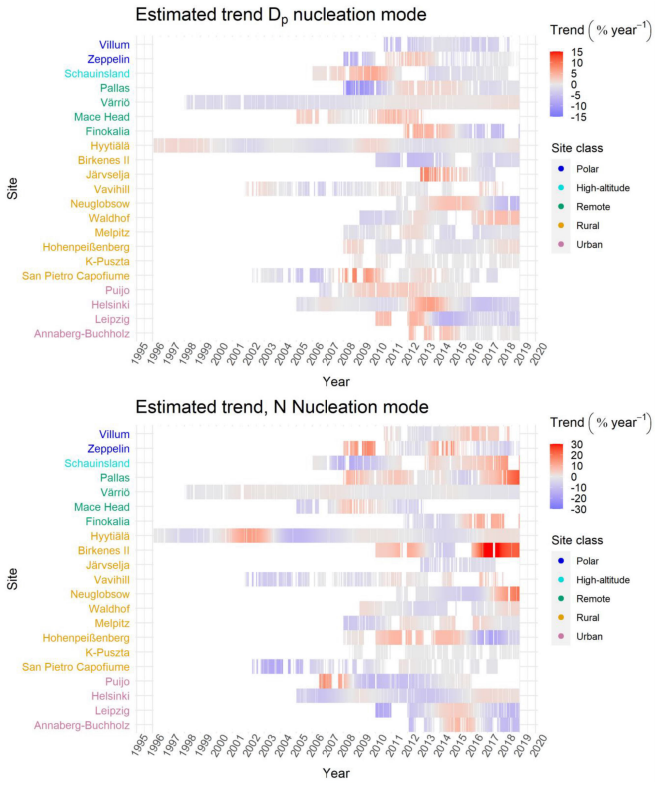

Figure S7 Estimated trends for nucleation mode D_p and N at measurement sites. Trend has been calculated by DLM, see section 2.3.1 for details. The overall trend presented in the figure is comparable with the long-term trend estimates given in section 3.1. To get a DLM trend for one year, the one-day trend given by the model was multiplied by the number of days in a year (365 used for all years) and divided by the mean of the variable over the first observed year. For example, if the trend is showing an increase of 10% / year it means that if the short-term increase would continue for a year, the concentration would be increased by 10% during the year compared to the first year mean.

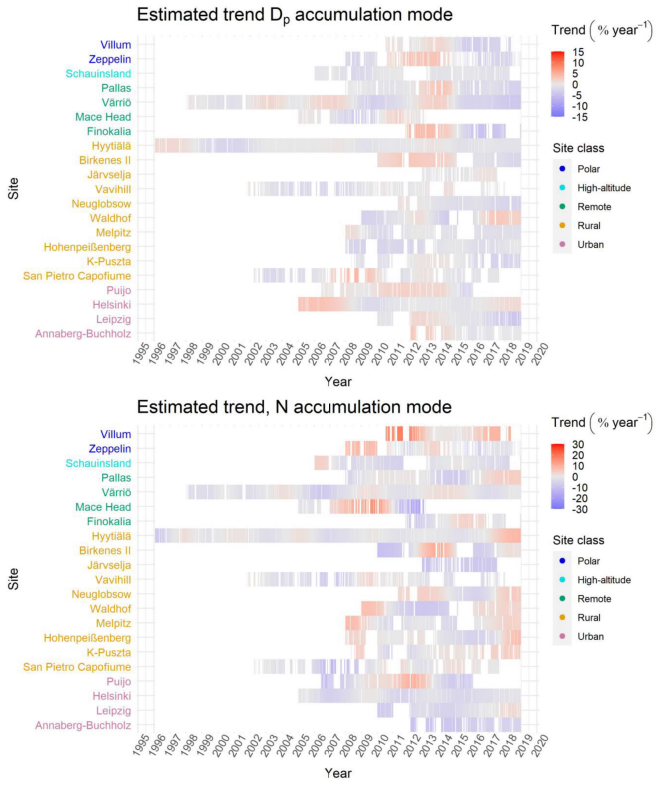

Figure S8 Estimated trends for accumulation mode D_p and N at measurement sites. Trend has been calculated by DLM, see section 2.3.1 for details. The overall trend presented in the figure is comparable with the long-term trend estimates given in section 3.1. To get a DLM trend for one year, the one-day trend given by the model was multiplied by the number of days in a year (365 used for all years) and divided by the mean of the variable over the first observed year. For example, if the trend is showing an increase of 10% / year it means that if the short-term increase would continue for a year, the concentration would be increased by 10% during the year compared to the first year mean.

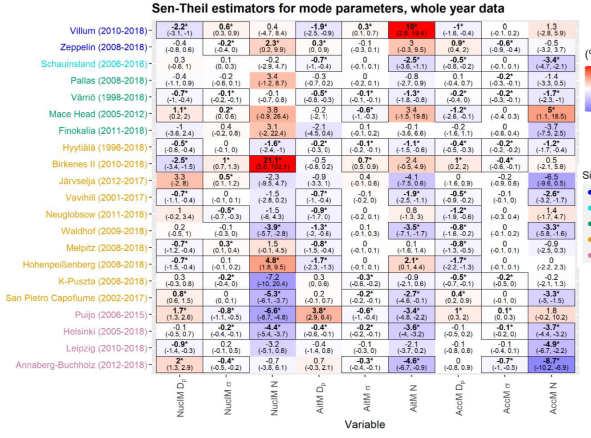

Figure S9 Long-term trend estimators for measured trends of all mode parameters (mean geometric diameter D_p, geometric standard deviation σ, and number concentration N) in nucleation (NuclM), Aitken (AitM), and accumulation mode (AccM). Statistically significant (95% confidence level) trends are bolded, marked with an asterisk, and highlighted with border lines. Trends have been calculated using Sen-Theil estimator and complemented with bootstrap confidence intervals (see section 2.3.2).

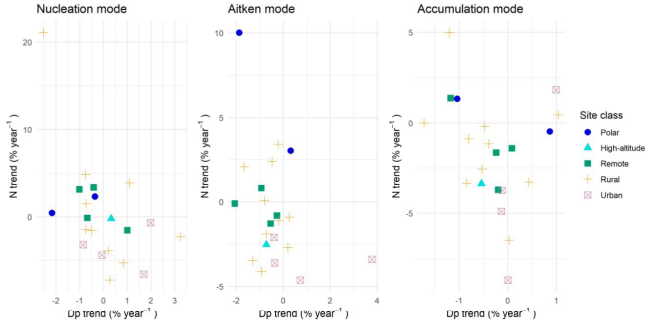

Figure S10 Scatter plot of mean geometric diameter D_p and number concentration N trends for nucleation, Aitken, and accumulation mode (trends are shown also in Fig. S9). Colour of the dots represent the site classification of each site (see Table 1 for environmental site classification).

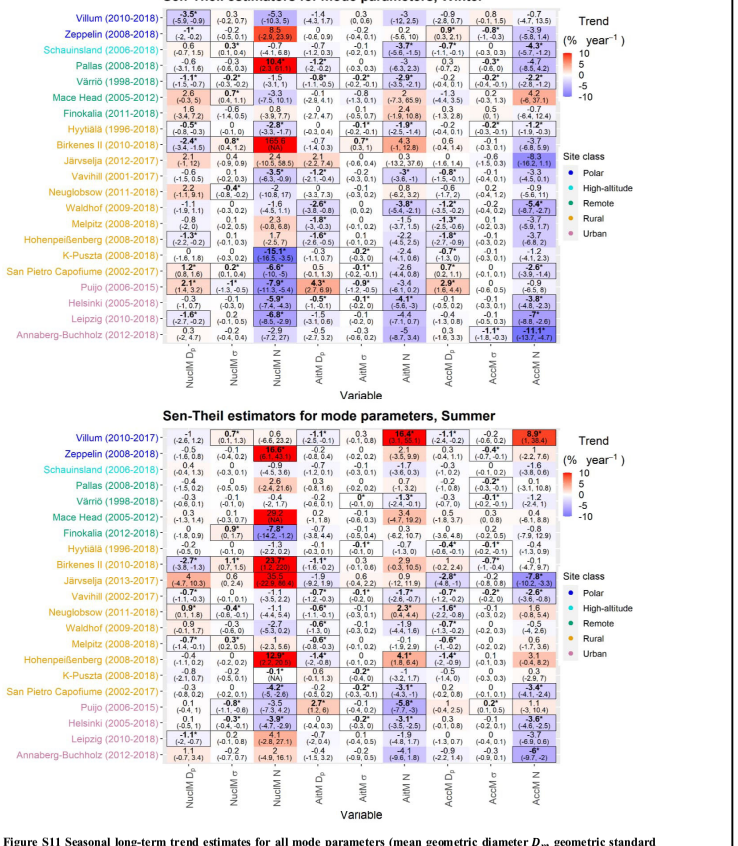

Figure S11 Seasonal long-term trend estimates for all mode parameters (mean geometric diameter D_p, geometric standard deviation σ, and number concentration N in nucleation (NuclM), Aitken (AitM), and accumulation mode (AccM) during winter (January, February, and December) and summer (June, July, and August). Statistically significant (95% confidence level) trends are bolded, marked with an asterisk, and highlighted with border lines. Trends have been calculated using Sen-Theil estimator and complemented with bootstrap confidence intervals (see section 2.3.2). For some cases, function was not able to calculate confidence interval correctly, we have marked those intervals with "(NA)".

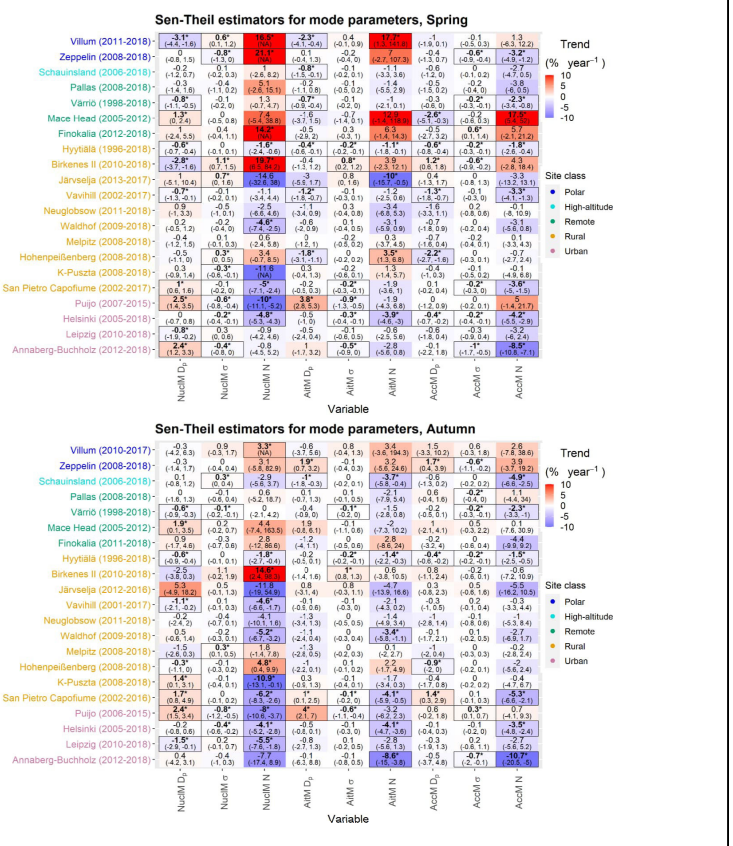

Figure S12 Seasonal long-term trend estimates for all mode parameters (mean geometric diameterD_p, geometric standard deviation σ, and number concentration N in nucleation (NuclM), Aitken (AitM), and accumulation mode (AccM) during spring (March, April, and May) and autumn (September, October, and November). Statistically significant (95% confidence level) trends are bolded, marked with an asterisk, and highlighted with border lines. Trends have been calculated using Sen-Theil estimator and complemented with bootstrap confidence intervals (see section 2.3.2). For some cases, function was not able to calculate confidence interval correctly, we have marked those intervals with "(NA)".

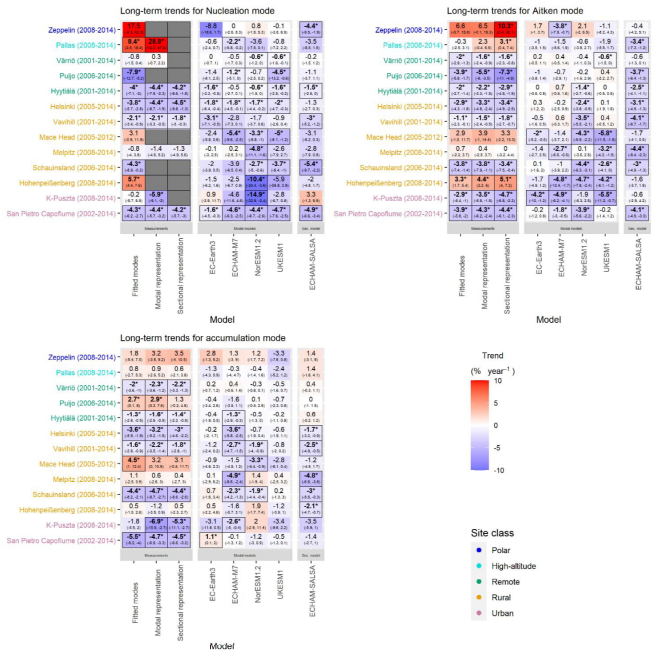

Figure S13 Long-term trend estimates for measured and modelled nucleation, Aitken, and accumulation mode number concentration. The sites (y axis) are arranged by site class and within site class most northerly to most southerly. Statistically significant (95% confidence level) trends are bolded, marked with an asterisk, and surrounded by a black border.

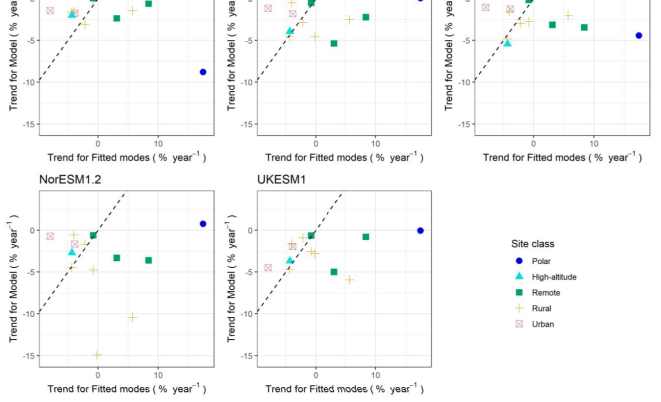

Figure S14 Scatter plots of number concentration (*N*) long-term trend estimates of measurements (Fitted mode) and climate models (model as a subplot title) for nucleation mode based on the data used for model comparison. Colour and shape of dots represent the site classification of each site (see Table 1 for environmental site classification).

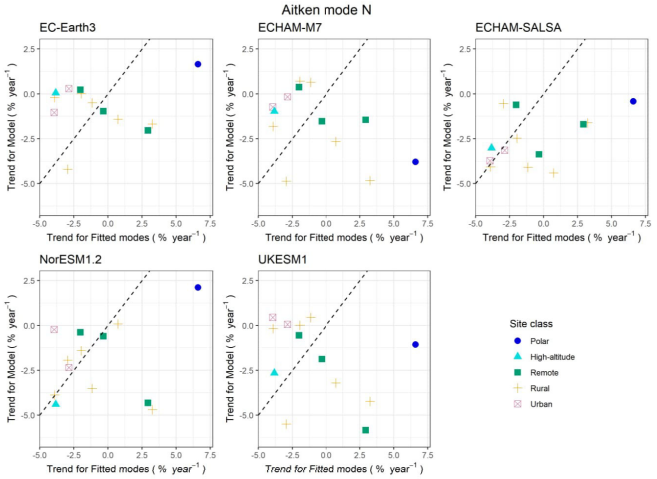

Figure S15 Scatter plots of number concentration (*N*) long-term trend estimates of measurements (Fitted mode) and climate models (model as a subplot title) for Aitken mode based on the data used for model comparison. Colour and shape of dots represent the site classification of each site (see Table 1 for environmental site classification).

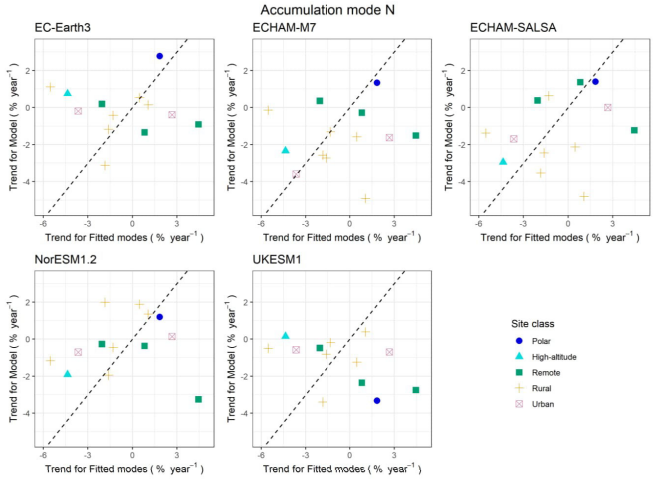

Figure S16 Scatter plots of number concentration (*N*) long-term trend estimates of measurements (Fitted mode) and climate models (model as a subplot title) for accumulation mode based on the data used for model comparison. Colour and shape of dots represent the site classification of each site (see Table 1 for environmental site classification).

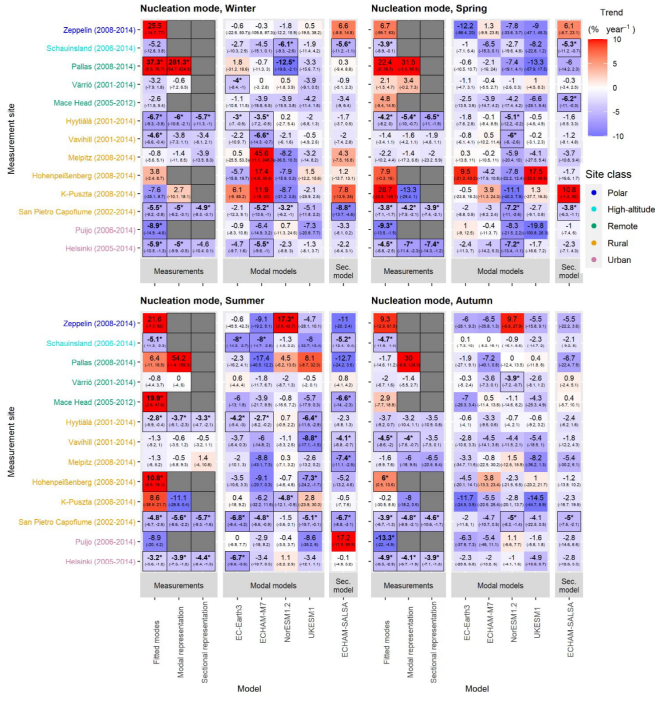

Figure S17 Seasonal trend estimates for nucleation mode number concentration for four seasons: winter (Jan, Feb, Dec), spring (Mar, Apr, May), summer (Jun, Jul, Aug), and autumn (Sep, Oct, Nov). Sites are ordered by site class and within site class from most northerly to most southerly. The bolded number, asterisk, and line border around the estimate indicate that the trend is statistically significant (95% confidence level). Trends have been calculated using Sen-Theil estimator and complemented with bootstrap confidence intervals (see section 2.3.2).

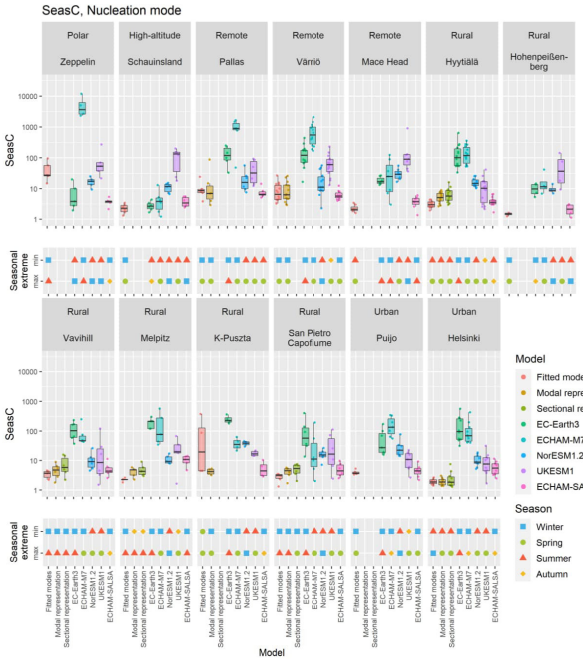

Figure S18 Maximum seasonal variation and seasonal extremes of nucleation mode particles for measurements and climate models. Upper panel: Ratio of maximum and minimum seasonal number concentration (SeasC) for measured and modeled nucleation mode. Points represent SeasC values for single years and box represents the quartiles (1st quartile, median, and 3rd quartile) of SeasC of certain measurement/model in certain site. Whiskers are 1.5*interquartile range. Lower panel: Seasons that most often have had minimum and maximum of number concentrations in measured and modeled nucleation mode.

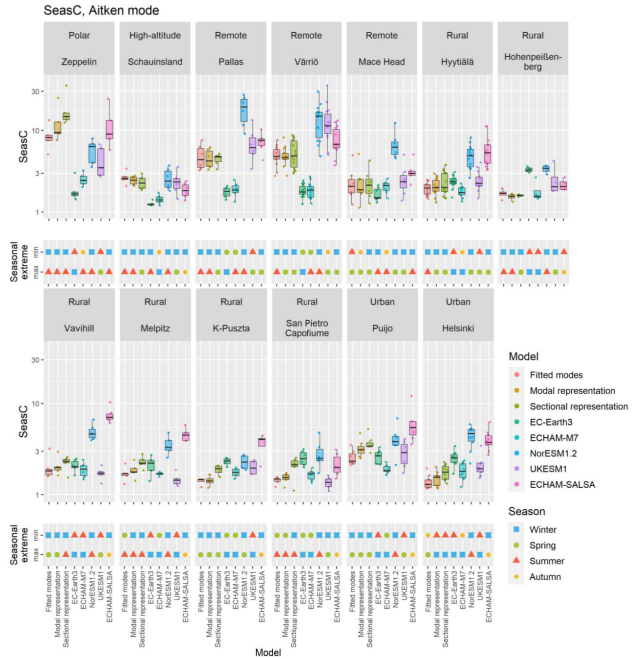

Figure S19. Maximum seasonal variation and seasonal extremes of Aitken mode particles for measurements and climate models. Upper panel: Ratio of maximum and minimum seasonal number concentration (SeasC) for measured and modelled Aitken mode. Points represent SeasC values for single years and box represents the quartiles (1st quartile, median, and 3rd quartile) of SeasC of certain measurement/model in a selected site. Whiskers are 1.5*interquartile range. Lower panel: Seasons that most often have had minimum and maximum number concentrations in measured and modeled Aitken mode.

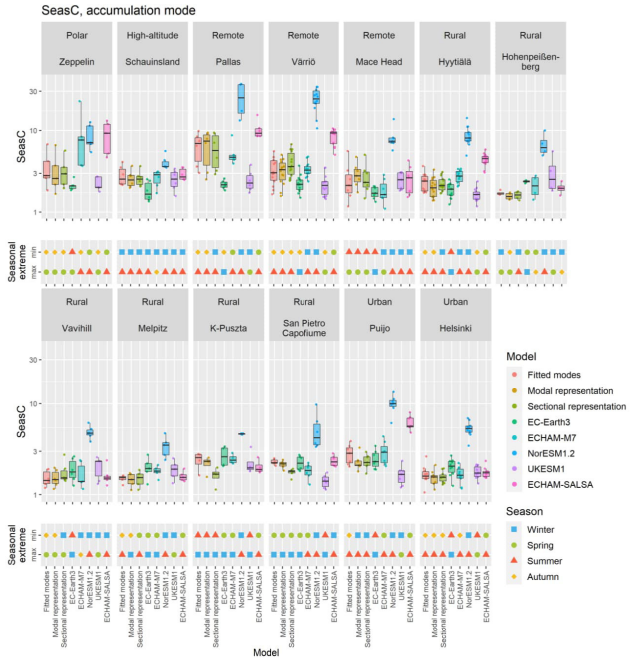

Figure S20. Maximum seasonal variation and seasonal extremes of accumulation mode particles for measurements and climate models. Upper panel: Ratio of maximum and minimum seasonal number concentration (SeasC) for measured and modelled accumulation mode. Points represent SeasC values for single years and box represents the quartiles (1st quartile, median, and 3rd quartile) of SeasC of certain measurement/model in a selected site. Whiskers are 1.5*interquartile range. Lower panel: Seasons that most often have had minimum and maximum number concentrations in measured and modeled accumulation mode.

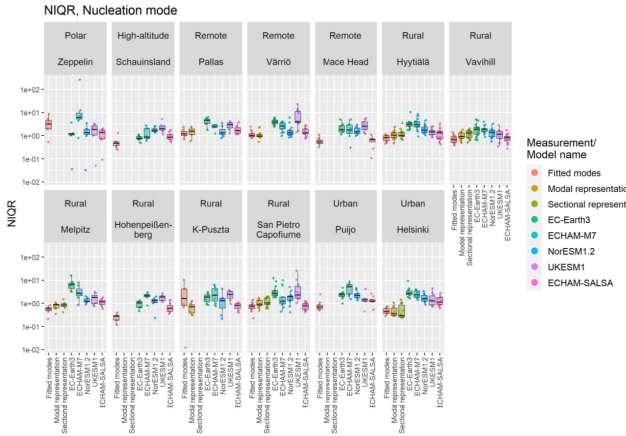

Figure S21 Average seasonal variation and seasonal extremes of nucleation mode particles for measurements and climate models. Normalized Interquartile Range (NIQR) for measured and modeled nucleation mode number concentration in different sites. Points represent NIQR values for single years and box represents the quartiles (1st quartile, median, and 3rd quartile) of NIQR of certain measurement/model in certain site. Whiskers are 1.5*interquartile range.

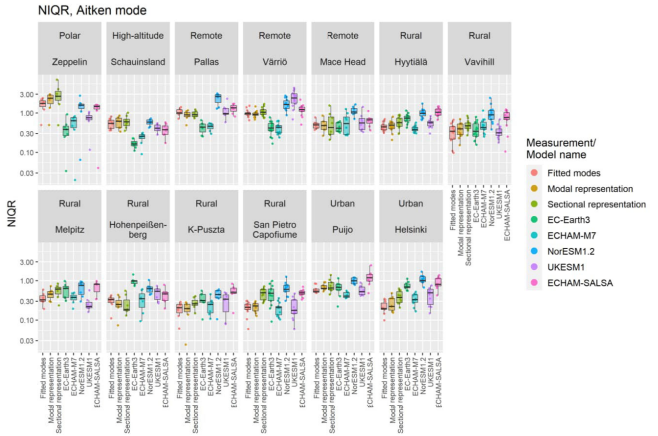

Figure S22 Average seasonal variation and seasonal extremes of Aitken mode particles for measurements and climate models. Normalized Interquartile Range (NIQR) for measured and modeled Aitken mode number concentration in different sites. Points represent NIQR values for single years and box represents the quartiles (1st quartile, median, and 3rd quartile) of NIQR of certain measurement/model in certain site. Whiskers are 1.5*interquartile range.

Figure S23 Average seasonal variation and seasonal extremes of accumulation mode particles for measurements and climate models. Normalized Interquartile Range (NIQR) for measured and modeled accumulation mode number concentration in different sites. Points represent NIQR values for single years and box represents the quartiles (1st quartile, median, and 3rd quartile) of NIQR of certain measurement/model in certain site. Whiskers are 1.5*interquartile range.

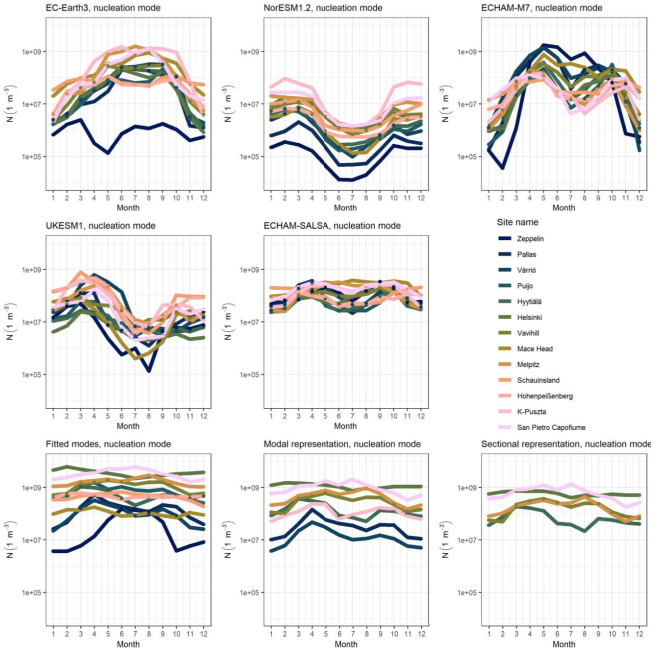

Figure S24 Seasonal cycle of nucleation mode number concentration in measurements and climate models for measurement sites. A subplot represents the seasonal cycle in one model or measurement. Coloured lines represent the median of the monthly means for Aitken mode number concentrations. Sites are ordered from most northerly to most southerly.

References

Rose, C., Collaud Coen, M., Andrews, E., Lin, Y., Bossert, I., Lund Myhre, C., Tuch, T., Wiedensohler, A., Fiebig, M., Aalto, P., Alastuey, A., Alonso-Blanco, E., Andrade, M., Artíñano, B., Arsov, T., Baltensperger, U., Bastian, S., Bath, O., Beukes, J. P., Brem, B. T., Bukowiecki, N., Casquero-Vera, J. A., Conil, S., Eleftheriadis, K., Favez, O., Flentje, H., Gini, M. I., Gómez-Moreno, F. J., Gysel-Beer, M., Hallar, A. G., Kalapov, I., Kalivitis, N., Kasper-Giebl, A., Keywood, M., Kim, J. E., Kim, S.-W., Kristensson, A., Kulmala, M., Lihavainen, H., Lin, N.-H., Lyamani, H., Marinoni, A., Martins Dos Santos, S., Mayol-Bracero, O. L., Meinhardt, F., Merkel, M., Metzger, J.-M., Mihalopoulos, N., Ondracek, J., Pandolfi, M., Pérez, N., Petäjä, T., Petit, J.-E., Picard, D., Pichon, J.-M., Pont, V., Putaud, J.-P., Reisen, F., Sellegri, K.,

Sharma, S., Schauer, G., Sheridan, P., Sherman, J. P., Schwerin, A., Sohmer, R., Sorribas, M., Sun, J., Tulet, P., Vakkari, V., van Zyl, P. G., Velarde, F., Villani, P., Vratolis, S., Wagner, Z., Wang, S.-H., Weinhold, K., Weller, R., Yela, M., Zdimal, V. and Laj, P.: Seasonality of the particle number concentration and size distribution: a global analysis retrieved from the network of Global Atmosphere Watch (GAW) near-surface observatories, Atmos. Chem. Phys., 21(22), 17185–17223, doi:10.5194/acp-21-17185-2021, 2021.

Paper II

Atmos. Chem. Phys., 20, 12247–12263, 2020
https://doi.org/10.5194/acp-20-12247-2020

Atmospheric Chemistry and Physics
Open Access
EGU

Decennial time trends and diurnal patterns of particle number concentrations in a central European city between 2008 and 2018

Santtu Mikkonen[1,2], Zoltán Németh[3], Veronika Varga[3], Tamás Weidinger[4], Ville Leinonen[1], Taina Yli-Juuti[1], and Imre Salma[3]

[1]Department of Applied Physics, University of Eastern Finland, P.O. Box 1627, 70211 Kuopio, Finland
[2]Department of Environmental and Biological Sciences, University of Eastern Finland,
P.O. Box 1627, 70211 Kuopio, Finland
[3]Institute of Chemistry, Eötvös University, P.O. Box 32, 1518 Budapest, Hungary
[4]Department of Meteorology, Eötvös University, P.O. Box 32, 1518 Budapest, Hungary

Correspondence: Imre Salma (salma@chem.elte.hu) and Santtu Mikkonen (santtu.mikkonen@uef.fi)

Received: 30 March 2020 – Discussion started: 7 May 2020
Revised: 25 August 2020 – Accepted: 16 September 2020 – Published: 28 October 2020

Abstract. Multiple atmospheric properties were measured semi-continuously in the Budapest platform for Aerosol Research and Training laboratory, which represents the urban background for the time interval of 2008–2018. Data of 6 full measurement years during a decennial time interval were subjected to statistical time trend analyses by an advanced dynamic linear model and a generalized linear mixed model. The main interest in the analysed data set was on particle number concentrations in the diameter ranges from 6 to 1000 nm (N_{6-1000}), from 6 to 100 nm (N_{6-100}, ultrafine particles), from 25 to 100 nm (N_{25-100}) and from 100 to 1000 nm ($N_{100-1000}$). These data were supported by concentrations of SO_2, CO, NO, NO_x, O_3, PM_{10} mass, as well as air temperature, relative humidity, wind speed, atmospheric pressure, global solar radiation, condensation sink, gas-phase H_2SO_4 proxy, classes of new aerosol particle formation (NPF), and growth events and meteorological macrocirculation patterns. The trend of the particle number concentrations derived as a change in the statistical properties of background state of the data set decreased in all size fractions over the years. Most particle number concentrations showed decreasing decennial statistical trends. The estimated annual mean decline of N_{6-1000} was (4–5) % during the 10-year measurement interval, which corresponds to a mean absolute change of $-590\,cm^{-3}$ in a year. This was interpreted as a consequence of the decreased anthropogenic emissions at least partly from road traffic alongside household heating and industry. Similar trends were not observed for the air pollutant gases. Diurnal statistical patterns of particle number concentrations showed tendentious variations, which were associated with a typical diurnal activity–time pattern of inhabitants in cities, particularly of vehicular road traffic. The trend patterns for NPF event days contained a huge peak from late morning to late afternoon, which is unambiguously caused by NPF and growth processes. These peaks were rather similar to each other in the position, shape and area on workdays and holidays, which implies that the dynamic and timing properties of NPF events are not substantially influenced by anthropogenic activities in central Budapest. The diurnal pattern for N_{25-100} exhibited the largest relative changes, which were related to particle emissions from high-temperature sources. The diurnal pattern for $N_{100-1000}$ – which represents chemically and physically aged particles of larger spatial scale – were different from the diurnal patterns for the other size fractions.

1 Introduction

Atmospheric aerosol can be characterized by various properties. There are several important phenomena and processes in which individual particles play a role. In these cases, particle number concentrations or particle number size distributions are the relevant metrics. Number concentrations of (insoluble) particles produce adverse effects on human health (Oberdörster et al., 2005; Rich et al., 2012; Cassee et al.,

2013; Braakhuis et al., 2014; Ostro et al., 2015; Schmid and Stoeger, 2016; Ohlwein et al., 2019). Individual particles and their properties are also important in cloud formation processes and, therefore, in indirect aerosol climate forcing (Makkonen et al., 2009; Merikanto et al., 2009; Sihto et al., 2011; Kerminen et al., 2012; Carslaw et al., 2013; Gordon et al., 2016). Particle numbers and associated size distributions are relevant properties in several optical interactions in the atmosphere (e.g. Moosmuller et al., 2009) and in various surface-controlled chemical reactions (e.g. Pöschl et al., 2007).

In the global troposphere, it is the new aerosol particle formation (NPF) and consecutive growth process that is the dominant source of particle numbers (Spracklen et al., 2006; Yu et al., 2010; Kulmala et al., 2013; Dunne et al., 2016). This source type occurs in various atmospheric environments around the world and produces secondary particles (Kerminen et al., 2018, and references therein). The major anthropogenic source of (primary) particles is combustion. It includes traffic exhaust mainly from diesel engines, fuel or waste burning in industrial and domestic installations, and residential heating and cooking (Paasonen et al., 2016; Masiol et al., 2018). Nanotechnology and its products can have importance in some limited or occupational environments. In large cities and in longer time intervals, primary particles often prevail over secondary particles (Brines et al., 2015; Salma et al., 2017; Saha et al., 2018).

Ultrafine (UF) particles (with a diameter $d<100$ nm) account for most of the particle number concentrations but have usually negligible contribution to particulate matter (PM) mass. This implies that particle numbers are not covered by legislative regulations on the ambient air quality, which are ordinary based on the PM mass. Particle number concentrations have not been promulgated among the air quality standards yet. There are, however, mitigation policies and control regulations which intend to reduce their ambient levels as part of an overall air-quality improvement strategy since the 1990s. The legislations, for instance in the EU including Hungary, focuses on the particle emissions from diesel engines (Giechaskiel et al., 2018). There were some important changes in the car emissions during the time interval under investigation in this study. These included the introduction of Euro 5 and Euro 6 regulations for light-duty vehicles in January 2011 and Euro VI regulations for heavy-duty vehicles in September 2015 (the number of emitted particles with diameters >23 nm should be $<6\times10^{11}$ km^{-1} for type approval). A prerequisite for the efficient operation of exhaust after treatment devices is having fuel with low sulfur content. The reduction of sulfur in diesel fuel for on-road transport was decreased after several previous phases to <10 ppm in January 2009 (Directive 2009/30/EC, 2009). Sulfur content in fuels for mobile non-road diesel vehicles – including mobile machinery, agricultural and forestry tractors, inland waterway vessels, and recreational crafts – was limited at a level of 1000 ppm from 2008 and at 10 ppm from 2011. Unsuitable and dangerous fuel types for domestic heating are also listed, their emission factors are determined, and the accumulated information is disseminated among potential users. As far as secondary particles are concerned, it is not straightforward to reduce their concentration levels, because the effects of gaseous and aerosol species on NPF are complex and uncertain due to the non-linear relationship and feedbacks in their related processes.

It is relevant to investigate the potential changes, namely overall and diurnal tendencies of particle number concentrations from different sources, on longer timescales because of their role in both health risks and climate change issues. The major source types of particle numbers can be separated by measuring their size distributions. Atmospheric NPF events produce particles of the nucleation mode, which occurs intermittently, and which gradually merges into the larger Aitken mode. High-temperature emission sources ordinarily produce Aitken-mode particles, while transformation processes (physical and chemical ageing) of existing particles in the atmosphere give rise to the accumulation mode. An important property of the nucleation- and Aitken-mode particles is that their residence time is limited to several hours (Raes et al., 2000; Salma et al., 2011, 2016b). This is different from accumulation-mode particles, which reside in the air up to 7 d. This means that the particles of the former two modes are present in the air until their sources are active, and their concentrations can change substantially and rapidly over a day (e.g. Mikkonen et al., 2011a; Salma et al., 2014, 2017; Paasonen et al., 2016). This is advantageous when source types are to be identified or quantified. At the same time, the relatively short residence time is not beneficial when time trends are to be studied and derived. The limited residence time can cause additional, substantial and sudden variability in time with or without time patterns, which can complicate the evaluation.

Particle number concentrations or particle number size distributions in the relevant diameter range (i.e. from a few nanometres to ca. 1 µm) are measured for various purposes. They include fundamental studies on atmospheric nucleation and particle growth phenomena, which usually require semi-continuous long-term measurements. The related experimental data sets have been accumulating gradually (Wehner and Wiedensohler, 2003; Asmi et al., 2013; Kerminen et al., 2018; Nieminen et al., 2018). They can also be exploited for time trend analysis by using appropriate statistical models. At present, however, knowledge on time trends particularly in various size fractions and over several years is largely lacking with few recent exceptions (Masiol et al., 2018; Saha et al., 2018; Sun et al., 2020).

Research activities dedicated to NPF and growth events in Budapest have been going on since November 2008. Measurements for 6 full years were realized in the city centre at a single fixed location. Semi-continuous and critically evaluated data sets consisting of particle number size distributions, concentrations of criteria air pollutants and meteorological data were available for the study. They were combined into

a coherent set, which was utilized in two statistical models developed specifically to determine the time trends for particle number concentrations in several important size fractions from 2008 to 2018. The main objectives of this study are to present and discuss the statistical models, to interpret their results on time trends and diurnal variability, to quantify the change rates, and to relate the temporal tendencies to different atmospheric sources, processes, and environmental circumstances.

2 Methods

2.1 Measurements

Most experimental data in the present study were obtained at a single urban site, namely at the Budapest platform for Aerosol Research and Training (BpART) laboratory (47°28′29.9″ N, 19°3′44.6″ E; 115 m above mean sea level). This location represents a well-mixed average atmospheric environment for the city centre of Budapest due to its geographical and meteorological conditions (Salma et al., 2016a); thus, it can be regarded as an urban background site. The local emissions include diffuse urban traffic exhaust, household or residential emissions, and limited industrial sources together with some off-road transport (diesel rail, shipping and aeroplane emissions). Experimental data for six full-year-long time intervals, i.e. from 3 November 2008 to 2 November 2009, from 13 November 2013 to 12 November 2014, from 13 November 2014 to 12 November 2015, from 13 November 2015 to 12 November 2016, from 28 January 2017 to 27 January 2018 and from 28 January 2018 to 27 January 2019, were available for this single site. A decennial time interval from 3 November 2008 to 2 November 2018 was considered in the statistical analysis. Local time (LT = UTC+1 or daylight-saving time, UTC+2) was chosen as the time base of the data processing, because the ordinary daily activities of inhabitants substantially influence the atmospheric concentrations and several processes in cities (Salma et al., 2014).

The major aerosol measuring system was a flow-switching-type differential mobility particle sizer (DMPS; Aalto et al., 2001). It records particle number concentrations in an electrical mobility diameter range from 6 to 1000 nm in the dry state of particles (with a relative humidity RH $<30\,\%$) in 30 channels (Salma et al., 2011). The measuring system was updated twice: in spring 2013 and winter 2016. However, its major parts including a differential mobility analyser (DMA, Hauke-type analyser with a length of 28 cm) and a condensation particle counter (CPC, TSI model 3775) remained unchanged; they were cleaned and serviced. The diameter resolution of the DMA was also calibrated during the updates. Several data validation or comparative exercises were realized over the years; the most extensive intercomparison was realized in summer 2015 and autumn 2019. First, the measured data by the CPC deployed in the DMPS system were compared to those of an identical stand-alone CPC operated in parallel. The agreement between the instruments was in accordance with the nominal specification of CPCs. As the next step, the integrated concentrations obtained from the size-resolved DMPS data were compared to the concentrations measured directly by the stand-alone CPC. The two instruments were again operated in parallel. The median CPC/DMPS ratio was utilized as correction factor for particle diffusion losses in the DMPS system (Salma et al., 2016a). The time resolution of the DMPS measurements was approximately 10 min in the year 2008–2009, and it was 8 min from 13 November 2013 on. The sampling inlet was installed at a height of 12.5 m above the street level. There was no upper-size cut-off inlet applied to the sampling line, and a rain shield and insect net were only adopted. The measurements were performed according to the international technical standard (Wiedensohler et al., 2012).

Meteorological data for air temperature (T), relative humidity (RH), wind speed (WS), wind direction and atmospheric pressure (p) were obtained from a measurement station of the Hungarian Meteorological Service (HMS), which was operated at a distance of ca. 70 m from the BpART laboratory by standardized methods (Vaisala HMP45D humidity and temperature probe, Vaisala WAV15A anemometer and Vaisala pressure, all from Finland) with a time resolution of 10 min. Global solar radiation (GRad) data were measured by a CMP11 pyranometer (Kipp & Zonen, the Netherlands) at another station of the HMS situated 10 km in the eastern direction with a time resolution of 1 h. Concentrations of pollutants SO_2, CO, NO, NO_x, O_3 and PM_{10} mass were acquired from a measurement station of the National Air Quality Network in Budapest in Széna Square, which is located in the prevailing upwind direction at a distance of 4.5 km from the BpART laboratory. This station ordinarily measures the smallest levels of the criteria air pollutants among the four monitoring stations located in the city centre. It can, therefore, be considered to represent the air pollution in between the urban background and street level or kerbside site. They are measured by UV fluorescence (Ysselbach 43C), IR absorption (Ysselbach 48C), chemiluminescence (Thermo 42C), UV absorption (Ysselbach 49C) and beta-ray attenuation (Thermo 5014I) methods with a time resolution of 1 h.

The availability percentages of the DMPS data over the six 1-year time intervals were 95 %, 99 %, 95 %, 73 %, 99 % and 90 %. The meteorological data were accessible in $>90\,\%$ of the time in each year, while the concentration data for key pollutants were available in $>85\,\%$ of the yearly time intervals.

2.2 Data treatment

Particle number concentrations in the diameter ranges (1) from 6 to 1000 nm (N_{6-1000}), (2) from 6 to 100 nm

(N_{6-100}), (3) from 25 to 100 nm (N_{25-100}) and (4) from 100 to 1000 nm ($N_{100-1000}$) were calculated from the measured and inverted DMPS data. The size ranges were selected to represent (1) the total particles, (2) UF particles, (3) UF particles emitted mainly from incomplete combustion (and partially grown by condensation; this size range is dominated by primary particles in cities most of the time) and (4) physically and chemically aged particles which usually represent a larger spatial extent, respectively (Salma et al., 2014, 2017).

Condensation sink (CS) for vapour molecules onto the surface of existing aerosol particles was calculated for discrete size distributions (Kulmala et al., 2001, 2012; Dal Maso et al., 2002, 2005). Dry particle diameters were considered in the calculations and condensing vapour was assumed to have sulfuric acid properties.

One of the key components for NPF events is the gas-phase H_2SO_4 (Sipilä et al., 2010; Sihto et al., 2011). It is challenging to measure its atmospheric concentration; therefore, the experimental data for long time intervals are rare. The relative effects of gas-phase H_2SO_4 are, however, often estimated by deriving its proxy value. In this study, the H_2SO_4 proxy was calculated according to Mikkonen et al. (2011b), where the best proxy was based on GRad, SO_2 concentration, RH and CS. The proxy is defined for $\mathrm{GRad} > 10\,\mathrm{W\,m^{-2}}$. Another widely used proxy was introduced by Petäjä et al. (2009), but that was created for a clean boreal forest environment. The most recent proxy from Dada et al. (2020) for urban areas was based on global radiation, SO_2 concentration and CS but a somewhat different equation formulation. All experimental data were used with their maximum time resolution.

The influence of large-scale weather types was considered on a daily basis by including codes for macro-circulation patterns (MCPs), which were invented specifically for the Carpathian Basin (Péczely, 1957; Károssy, 2016). The classification is based on the extension and development of cyclones and anticyclones relative to the Carpathian Basin via the daily sea-level pressure maps constructed for 00:00 UTC in the North Atlantic–Europe region. Thus defined MCPs were assigned to the following day in the data. Basic information on the MCPs is summarized in Table 1.

Each data line, containing the date and time, concentrations, CS, H_2SO_4 proxy, meteorological data, and MCP codes, was further labelled by several indices on a daily basis. These labels served to differentiate between various environmental conditions, which can lead to substantial changes in some variables (Salma et al., 2014). The workdays were marked by label WD, while the holidays were denoted by label HD. Varying classes of NPF event days were also labelled differently. The classification was accomplished via the particle number size distribution surface plots (Dal Maso et al., 2005; refined in Németh et al., 2018, for urban sites) on a daily basis. The main classes were NPF event days (marked by label NPF), non-event days (label NE), days with undefined character and days with missing data. The earliest estimated time of the beginning of a nucleation (t_1) was also derived (Németh and Salma, 2014) and was added to the data record as a parameter. Finally, the data lines were labelled according to the actual technical status of the DMPS system. The data obtained from the beginning of the measurements to the first update were labelled as S1, the data derived between the first and second updates were labelled as S2, and the data obtained after the second update were labelled S3.

2.3 Statistical modelling

Atmospheric data are usually not normally distributed; therefore, non-parametric methods are often used to detect their long-term trends (Asmi et al., 2013; Masiol et al., 2018). The coherent data set prepared as described in Sect. 2.2 was analysed in two ways. First, time trends for concentrations of particles and air pollutants were estimated by using a dynamic linear model (DLM) method. Secondly, the factors affecting the changes in particle concentrations were detected with a generalized linear mixed model (GLMM).

2.3.1 Dynamic linear model

Dynamic linear models (Durbin and Koopman, 2012; Petris et al., 2009; Laine, 2020) are state-of-the-art tools for time trend detection. The trend is seen as a statistical change in the properties of the background state of the system. Although changes in aerosol concentrations have previously been approximated with linear trends (e.g. Sun et al., 2020), this is not always the most suitable method since the processes affecting the concentrations are continuously evolving over time. Additionally, time series of atmospheric measurements can include multiple time-dependent cycles (e.g. seasonal and diurnal cycles) which are typically non-stationary – meaning that their distributional properties change over time. The DLM approach effectively decomposes the data series into basic components such as level, trend, seasonality and effect of external forcing by describing statistically the underlying structure of the process that generated the measured data. All these components are defined by Gaussian distributions, and they are allowed to vary in time; the significance and magnitude of this variation can also be modelled and estimated. In the basic setup of the DLM, the sign or the magnitude of the trend is not defined in advance by the model formulation but estimated from the data. The method can detect and quantify trends, but the explanations for the observed changes is provided by the user. Nevertheless, it determines if the observations are consistent with the selected model. We used the DLM to explain variability in the particle concentration time series using the following components: locally linear mean level, trend, seasonal effect, autoregressive component and noise. The autoregressive component is added to the model in order to take account of the autocorrelation in the data, i.e. the correlation between subsequent observations. Here it refers to a first-order autoregressive model (AR(1)).

Table 1. Macro-circulation patterns (MCPs, Péczely codes) and their seasonal and annual occurrences in the Carpathian Basin for years 1958–2010 (Maheras et al., 2018).

MCP no.	Code	Description	Occurrence (%)				
			Winter	Spring	Summer	Autumn	Annual
1	mCc	Cyclone with a cold front over northeastern Europe, northerly wind	7.3	11.3	12.1	8.0	9.7
2	AB	Anticyclone over the British Isles, northerly wind	5.6	7.1	8.6	6.4	6.9
3	CMc	Mediterranean cyclone with a cold front over southern Europe, northerly wind	2.5	3.5	1.8	1.9	2.4
4	mCw	Mediterranean cyclone with a warm front over northeastern Europe, southerly wind	9.2	9.7	5.7	7.2	7.9
5	Ae	Anticyclone over eastern Europe, southerly wind	14.2	11.3	7.3	17.6	12.6
6	CMw	Mediterranean cyclone with a warm front over southern Europe, southerly wind	8.9	8.7	3.7	8.3	7.4
7	zC	Highly developed cyclone over northern Europe, westerly wind	5.0	3.2	2.7	2.9	3.5
8	Aw	Anticyclone over western Europe, westerly wind	13.1	11.2	20.8	12.8	14.6
9	As	Anticyclone over southern Europe, westerly wind	7.0	4.4	2.9	5.6	4.9
10	An	Anticyclone over northern Europe, easterly wind	10.9	12.8	11.3	10.1	11.3
11	AF	Anticyclone over Fennoscandia, easterly wind	2.8	5.2	5.9	3.7	4.4
12	A	Anticyclone over the Carpathian Basin, changing wind direction	11.8	7.3	13.3	13.3	11.4
13	C	Cyclone over the Carpathian Basin, changing wind direction	1.7	4.3	3.9	2.2	3.0

The evolution of the investigated concentrations – after the seasonal and noise components were filtered out – is modelled by using the smoothed mean level. Here, the change in the mean level is the trend of the variable. The statistical model can be described by the following equations (Mikkonen et al., 2015):

$$y_t = \mu_t + \gamma_t + \eta_t + \varepsilon_{\text{obs}}, \varepsilon_{\text{obs}} \sim N(0, \sigma_t^2), \quad (1)$$

$$\mu_t = \mu_{t-1} + \alpha_t + \varepsilon_{\text{level}}, \varepsilon_{\text{level}} \sim N(0, \sigma_{\text{level}}^2), \quad (2)$$

$$\alpha_t = \alpha_{t-1} + \varepsilon_{\text{trend}}, \varepsilon_{\text{trend}} \sim N(0, \sigma_{\text{trend}}^2), \quad (3)$$

$$\eta_t = \rho\eta_{t-1} + \varepsilon_{\text{AR}}, \varepsilon_{\text{AR}} \sim N\left(0, \sigma_{\text{AR}}^2\right), \quad (4)$$

where y_t is the investigated concentration at time t; μ_t is the mean level and α_t is the change in the level from time $t-1$ to time t; γ_t is the seasonal component; η_t is an autoregressive error component; and ρ is the coefficient for autoregressive component (here fixed to $\rho = 0.6$). Here, this latter level is fixed. The Gaussian stochastic ε terms are used for the observation uncertainty and for random dynamics of the level and the trend. The seasonal component γ_t contains dummy variables for each month, so it has a different value for each month with a condition that 12 consecutive months sum to zero. A more detailed description of how the model is written through the state space equation can be found in Mikkonen et al. (2015).

2.3.2 Generalized linear mixed model

Linear mixed models (McCulloch et al., 2008) belong to the family of models that combine several different kinds of models used in multivariate analysis when the data do not fulfil the standard independency and homogeneity assumptions. This is the normal case with measured atmospheric and climatological variables (e.g. Mikkonen et al., 2011a). The main goal of the mixed models is to estimate not only

the mean of the measured response variable but also the variance–covariance structure of the data, which makes the model more valid for complex atmospheric data. In addition, modelling the (co)variances of the variables reduces the bias of the estimates and prevents autocorrelation of the residuals. The model is constructed from a general linear model, written in matrix format as $y = \mathbf{X}\beta + \varepsilon$, by adding a so-called random component (denoted $\mathbf{Z}\boldsymbol{u}$) to the model; thus, the model is given by $y = \mathbf{X}\beta + \mathbf{Z}\boldsymbol{u} + \varepsilon$. Here, if we let n be equal to the number of observations, p be equal to the number of fixed parameters and q be equal to the number of random parameters in the model, then y is the $(n \times 1)$ vector of measurements of the variable of interest, β denotes the unknown $(p \times 1)$ vector of intercept and slope estimates of the model, $\mathbf{X}$ is the $(n \times p)$ matrix of observations from predictor variables, and ε contains the residuals of the model. In the random part, $\mathbf{Z}$ is the $(n \times q)$ design matrix for the $(q \times 1)$ vector of random covariates u with a q-dimensional normal distribution. With adequate choices of the matrix $\mathbf{Z}$, different covariance structures, $\mathrm{Cov}(u) = \mathbf{G}$ and $\mathrm{Cov}(\varepsilon) = \mathbf{R}$, can be defined and fitted. Successful modelling of variances and covariances of the observations provides valid statistical inference for the fixed effects, β, of the mixed model. In contrast to general linear models, the error terms, ε, can be correlated, which makes the modelling more robust. It follows from this that the distribution of observations can be described by a normal distribution with the expectation of $\mathbf{X}\boldsymbol{\beta}$ and covariance matrix $\mathbf{V}$, which is given by $\mathbf{V} = \mathbf{Z}\mathbf{G}\mathbf{Z}' + \mathbf{R}$. With GLMM, it is possible to reliably detect the factors which affect particle number concentrations or which act as indicators for their different sources. The model can be expressed in a mathematical form as in Mikkonen et al. (2011a):

$$\begin{aligned} N_{Di} = {} & \left(\beta_0 + \beta_{\mathrm{setup}} + u_{\mathrm{m}}\right) + \alpha_{\mathrm{d}} + (\beta_{\mathrm{wd}} \cdot \beta_{\mathrm{E}}) \\ & \cdot X_{\mathrm{Ti}} + (\beta_1 + v_{1\,\mathrm{m}}) \cdot \mathrm{SO}_{2,i} + (\beta_2 + v_{2\,\mathrm{m}}) \cdot \mathrm{NO}_{2,i} \\ & + (\beta_3 + v_{3\,\mathrm{m}}) \cdot \mathrm{O}_{3,i} + \beta_4 \cdot \mathrm{GRad}_i + \beta_5 \cdot \mathrm{RH}_i \\ & + \beta_6 \cdot \mathrm{MCP}_i, \end{aligned} \tag{5}$$

where N_{Di} is the number concentration in selected size range in time i; β_0 is a model intercept; β_{setup} is a correction term for changes in the measurement system due to two major upgrades; u_{m} is vector of random intercepts different for each month; α_{d} is average change of N_{Di} per day (i.e. slope of trend); β_{wd} and β_{E} are coefficients for workday and NPF event day, respectively; and X_{Ti} is the corresponding vector showing the type of the day (in both means: WD/HD and E/NE) in time i; β_1 to β_5 are fixed coefficients for SO_2, NO_2, O_3, GRad, and RH, respectively; β_6 is the (13×1) vector of coefficients for different macro-circular patterns (MCPs) indicating the characteristic level of number concentration during each MCP type, which are treated here as categorical variable; and v_{m} represents the random month-specific slopes for SO_2, NO_2, O_3, and GRad. The coefficients of the model can be interpreted in a similar manner as multivariate regression or general linear models: just with an addition of month-specific effects for given variables.

3 Results and discussion

Annual insolation (Q), which expresses the total energy density at a receptor site, was derived from the individual hourly-mean $\mathrm{GRad}_{i,j}$ data, where index i represents the hour of day (from 0 to 23) and index j stands for the day of year (from 1 to 365) as $Q = 3.610^{-6} \sum_{i,j} \mathrm{GRad}_{i,j}$. The units of the individual $\mathrm{GRad}_{i,j}$ data and Q are watt per square metre ($\mathrm{W\,m^{-2}}$) and gigajoule per square metre per year ($\mathrm{GJ\,m^{-2}\,yr^{-1}}$), respectively. The few randomly missing data points were interpolated linearly. Since the major sources of particles in cities include road vehicles and atmospheric nucleation, we added some indicative data on these specific sources as well. The median particle number concentrations are basically in line with many other comparable cities in the world (e.g. Kerminen et al., 2018; Masiol et al., 2018). They indicate a decreasing change (except for $N_{100-1000}$) over the years 2008–2018. At the same time, the annual averages of the other concentrations, meteorological data and auxiliary variables did not change substantially. Annual mean relative occurrence frequency of NPF events stayed almost constant with a mean and SD of $(20 \pm 4)\,\%$, except for the measurement year 2015–2016 when it was unusually small. It is worth adding that NPF increases the existing particle number concentrations in Budapest by a factor of approximately 2 on event days (Salma et al., 2017). The annual medians for the particle formation rate and particle growth rate also stayed constant and seemingly varied only as fluctuations within ca. $\pm 20\,\%$ and $\pm 8\,\%$, respectively. The number of passenger cars that was registered in Budapest remained constant within $\pm 5\,\%$, while the share of the diesel-powered passenger cars increased modestly by a rate of approximately $12\,\%$ from 2008 to 2018 (KSH, 2019). The number (ca. 4000) of buses registered in Budapest and the share ($98\,\%$) of diesel-powered buses in the national bus fleet remained constant.

3.1 Decennial timescale

Overall statistical time trends for particle number concentrations in various size fractions obtained by the DLM are displayed in Fig. 1. The curves confirm that N_{6-1000}, N_{6-100} and N_{25-100} indeed decreased in Budapest between 2008 and 2018, while the change in $N_{100-1000}$ was not significant. The decline mostly took place in a monotonic manner except for perhaps the interval of summer 2016 to spring 2017, when some partial/local increase could be realized for N_{6-1000} and N_{6-100}.

There are several important sources, sinks and atmospheric transformation processes including environmental conditions which can influence the atmospheric concentrations. The major sources include both high-temperature

Table 2. Annual medians of particle number concentrations in the diameter ranges from 6 to 1000 nm (N_{6-1000}), from 6 to 100 nm (N_{6-100}), from 25 to 100 nm (N_{25-100}), and from 100 to 1000 nm ($N_{100-1000}$); concentrations of SO_2, CO, NO, NO_x, O_3, and PM_{10} mass; annual means of air temperature (T), relative humidity (RH), wind speed (WS), atmospheric pressure (P), and annual insolation (Q); annual mean relative occurrence frequency of nucleation (f_{NPF}); annual median formation rate of particles with a diameter of 6 nm (J_6); annual median growth rate of particles with a diameter of 10 nm (GR_{10} – for the rates, see Salma and Németh, 2019); number of passenger cars registered in Budapest (Cars); the mean age of vehicles (Age); and the share of diesel-powered vehicles (Diesel) separately for the 1-year measurement time intervals.

Variable	Unit	2008–2009	2013–2014	2014–2015	2015–2016	2017–2018	2018–2019
N_{6-1000}	$\times 10^3$ cm^{-3}	11.5	9.7	9.3	7.5	8.6	8.3
N_{6-100}	$\times 10^3$ cm^{-3}	9.1	7.2	6.9	5.7	6.8	6.5
N_{25-100}	$\times 10^3$ cm^{-3}	5.1	4.3	4.1	3.3	3.6	3.2
$N_{100-1000}$	$\times 10^3$ cm^{-3}	1.79	2.2	2.0	1.56	1.49	1.53
SO_2	µg m^{-3}	5.0	4.8	4.6	4.8	4.5	5.2
CO	µg m^{-3}	547	488	577	513	534	624
NO	µg m^{-3}	13.3	19.2	23	17.6	20	17.0
NO_x	µg m^{-3}	58	80	89	72	79	73
O_3	µg m^{-3}	23	14.8	19.6	25	20	21
PM_{10}	µg m^{-3}	33	31	39	29	28	36
T	°C	12.0	13.2	13.2	12.9	13.2	13.3
RH	%	64	69	64	69	63	67
WS	m s^{-1}	2.5	2.6	2.8	2.7	2.9	2.5
P	hPa	1001	1003	1005	1004	1004	1004
Q	GJ m^{-2} yr^{-1}	4.45	4.39	4.58	4.52	4.77	4.66
f_{NPF}	%	24	20	23	13.0	23	20
J_6	cm^{-3} s^{-1}	4.2	3.5	4.4	4.6	6.3	4.6
GR_{10}	nm h^{-1}	7.6	6.6	6.5	8.0	7.5	7.0
Cars*	$\times 10^3$	582	573	584	597	634	659
Age*	yr	10.8	13.0	13.4	13.7	14.1	14.2
Diesel*	%	20	24	26	28	29	31

* Status at the end of years 2009, 2013, 2014, 2015, 2017 and 2018, respectively.

emissions and NPF events as discussed in Sect. 1. The latter source is affected by concentrations of precursor and other trace gases, meteorological properties for photochemical reactions, and the interactions among gas-phase chemical species of different origin or type with respect to the formation yield of condensing vapours (Kulmala et al., 2014; McFiggans et al., 2019). The air pollutants listed in Table 2 and gas-phase H_2SO_4 proxy – which are known or expected to affect particle number concentrations – did not exhibit decreasing statistical trends between 2008 and 2018 (Fig. 2). On the one hand, this decoupling suggests that the causes of the decrease in particle number concentrations are not primarily related to meteorological conditions, because they would jointly affect the gas concentrations as well (if their sources are more-or-less constant over a certain time interval). On the other hand, the constant gas concentrations suggest that the decreasing trend in particles does not seem to be related to the major precursors or interacting gaseous chemical species (such as SO_2, H_2SO_4 or NO_2).

As far as the meteorological conditions are concerned, some of them such as WS, atmospheric boundary mixing layer height and T have previously been shown to influence

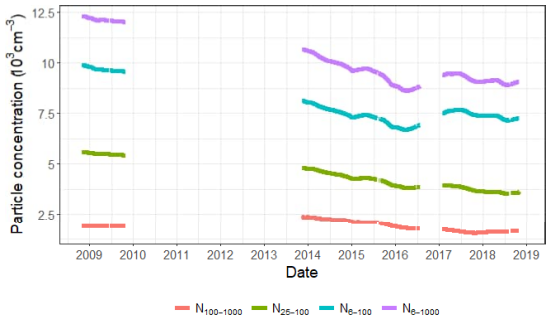

Figure 1. Statistical time trends of particle number concentrations in the diameter ranges from 6 to 1000 nm (N_{6-1000}), from 6 to 100 nm (N_{6-100}), from 25 to 100 nm (N_{25-100}) and from 100 to 1000 nm ($N_{100-1000}$) derived by DLM over a decennial interval.

the temporal variation of aerosol particles (e.g. Birmili et al., 2001; Mikkonen et al., 2011a). The annual means of possibly relevant properties and parameters in Table 2 – except for the particle number concentrations (which are under in-

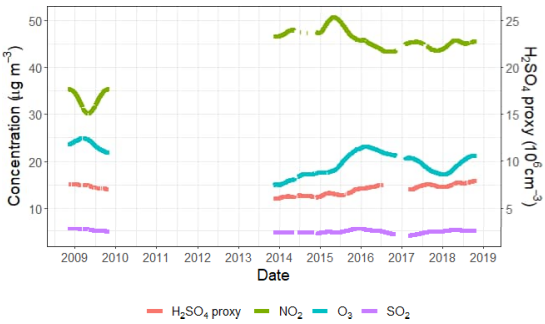

Figure 2. Statistical time trends of gas-phase H_2SO_4 proxy, SO_2, O_3 and NO_2 derived by DLM over the decennial interval.

vestigation) and the fraction of diesel cars – did not show any obvious dependency; they virtually stayed constant over the years of interest. The possible effect of different weather conditions on the concentrations are studied separately by the GLMM and are discussed in Sect. 3.2.2. There were also no substantial or extensive urban constructions in the area (which could influence the urban air flow) nor larger systematic changes in the traffic circulation around the sampling site in the time interval considered. Therefore, the decline in the particle number concentrations can likely be interpreted as a consequence of the decreased anthropogenic particulate emissions in Budapest. The related source sectors can include vehicular road traffic and household heating or cooking. The decline happened at an increasing share of the diesel passenger cars and straitened emission control on (diesel) vehicles; for example, Platt et al. (2017) and Wihersaari et al. (2020) showed that modern diesel engines have lower particle emissions than gasoline engines.

The average decrease rates of particle number concentrations as derived from both the DLM and GLMM statistical approaches are summarized in Table 3. The rates are shown as obtained from the models and scaled for the 10-year measurement interval to ensure the comparability of the slopes. The relative mean changes (in per cent per year) were expressed with respect to the starting value (mean of the first year). There are some differences between the corresponding results of the two models, which were caused by standardizing the concentrations with the predictors in the models and by handling the upgrades of measurement setup differently. The changes in all size fractions were on the same level and only minor differences could be seen. As the estimates always contain some uncertainty, these differences are not considered statistically significant. The largest difference between the two models was observed for $N_{100-1000}$ (which had the lowest absolute concentrations). One possible cause for this might be that GLMM standardizes the results for variables indicating anthropogenic emissions; thus, the size fraction that is the most sensitive for the emissions has the strongest effect. Considering all these, the rates from the two statistical models agree well. Furthermore, the rates for N_{6-1000} and N_{6-100} were identical. This is explained by the fact that these two size fractions are strongly connected; the typical N_{6-100}/N_{6-1000} mean ratio in central Budapest is 75 %–80 % (Salma and Németh, 2019). A small difference was also seen for N_{25-100}. In urban areas, this size fraction is mainly composed of particles from high-temperature emission sources. The source types responsible for the observed decline are further discussed in Sect. 3.2.1.

Our results concerning the decennial change rates (and our conclusions with regard to their causes mainly discussed in Sect. 3.2.1) are comparable and are in line with some other very recent studies. Sun et al. (2020) investigated the statistical concentration trends in particle numbers (and equivalent black carbon mass) at multiple urban, rural or background sites within the German Ultrafine Aerosol Network. Decreasing annual slopes of (−7.0 to −1.7) % were obtained for several size fractions (which are different from our intervals), and the most likely factors for the decreasing trends were assigned to declining anthropogenic emissions due to emission mitigation policies of the EU. Masiol et al. (2018) evaluated statistical time trends of particle number concentrations in various size fractions (which are different again from the previous and present studies) in Rochester, NY, USA, and obtained a typical decline rate of $-4.6\,\%\,\mathrm{yr}^{-1}$ for total particles. These outcomes and our data as well seem to be different from the results obtained by Saha et al. (2018) in the urban Pittsburgh, PA, USA, by comparing two intervals of 2001–2002 and 2016–2017. It should be mentioned that in the latter research, the experimental setup for measuring particle number size distributions had a lower diameter limit of detection at 11 nm; some methodological approaches (e.g. classification of events) were different from ours, and the time trend was not derived by statistical modelling. The authors concluded that both the frequency of NPF events and their dynamic properties were reduced by (40–50) % over the past 15 years, resulting in ca. 48 % reduction of UF concentrations. The changes were attributed to dramatic reductions in SO_2 emissions in the larger region.

3.2 Diurnal timescale

Diurnal statistical patterns of the particle number concentrations in different size fractions were predicted by the GLMM considering the following variables: GRad; RH; concentrations of SO_2, NO_2, and O_3; and labels for workdays and holidays, NPF event days and non-event days, and for MCP codes. The initial screening for possible prediction variables was done in earlier papers. Studies such as Hyvönen et al. (2005), Mikkonen et al. (2006) and Nieminen et al. (2014) suggested that meteorological and trace gas variables affect NPF. Furthermore, Mikkonen et al. (2011a), Guo et al. (2012) and Zaidan et al. (2018) studied the factors which influence the growth of freshly formed particles as

Table 3. Decrease rates of particle number concentrations in the diameter ranges from 6 to 1000 nm, from 6 to 100 nm, from 25 to 100 nm and from 100 to 1000 nm obtained by the dynamic linear model and generalized linear mixed model as a mean absolute change per year during the 10-year measurement interval and as a relative mean change per year with respect to the mean value of the first year.

	Dynamic linear model		Generalized linear mixed model	
Size fraction (nm)	Mean change per year (cm^{-3})	Relative mean change (% yr^{-1})	Mean change per year (cm^{-3})	Relative mean change (% yr^{-1})
6–1000	−510	−4	−660	−5
6–100	−400	−4	−480	−5
25–100	−310	−6	−360	−5
100–1000	−50	−3	−180	−8

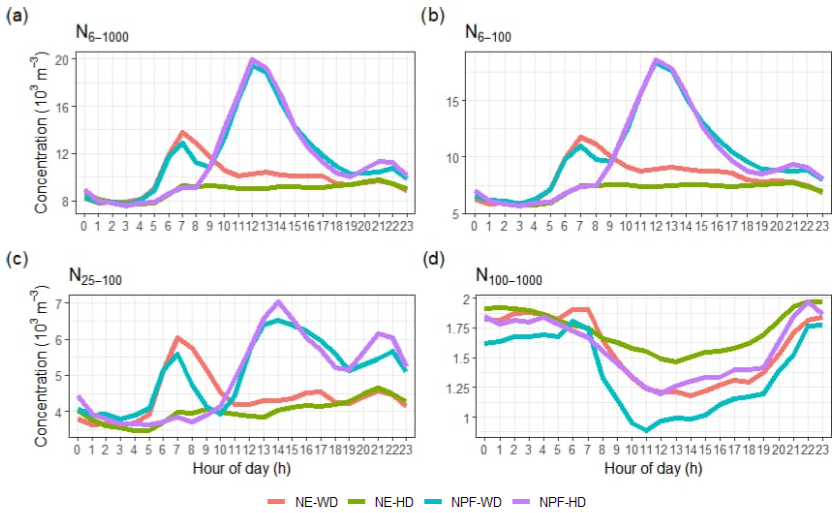

Figure 3. Diurnal patterns of particle number concentrations in the diameter ranges from 6 to 1000 nm (N_{6-1000}), from 6 to 100 nm (N_{6-100}), from 25 to 100 nm (N_{25-100}) and from 100 to 1000 nm ($N_{100-1000}$) (with factor and unit of $\times 10^3$ cm^{-3}). Red: non-event on workdays, green: non-event on holidays, cyan: event on workdays, purple: event on holidays.

well as the concentrations of particles in larger size fractions and specified the possible predictors. All variables found in these screenings and measured at our site were tested one-by-one in the GLMM model in a stepwise manner. In each step, the significance of the added or removed variable was investigated by a likelihood ratio test (e.g. Pinheiro and Bates, 2000) until the final model shown in Eq. (4) was formed. The effect of the H_2SO_4 proxy was also tested, and the results for the daytime concentrations were similar to those obtained with the selection of variables above. However, the modelling results for night-time were biased since the proxy is defined for GRad >10 W m^{-2}; therefore, we decided not to include the proxy in the final model.

3.2.1 Diurnal statistical patterns

Modelled diurnal pattern of particle number concentrations for event days on workdays, event days on holidays, non-event days on workdays and non-event days on holidays separately for different size fractions are shown in Fig. 3. The curves in Fig. 3a–c resemble tendentious variations, which can be associated with typical diurnal activity–time patterns of inhabitants in cities, particularly with road traffic. They are also perfectly in line with the mean diurnal tendencies of experimentally determined concentrations in central Budapest (Salma et al., 2014, 2017) and are consistent with the time variations in many other European cities (Hussein et al., 2004; Aalto et al., 2005; Moore et al., 2007; Avino et al., 2011; Dall'Osto et al., 2013).

In the statistical diurnal patterns of UF particles (Fig. 3b), there is a huge peak from late morning to late afternoon on event days. This is unambiguously caused by NPF and growth processes. The peaks on workdays and holidays are rather similar to each other in the position, shape and magnitude (area), which means that the dynamics and timing of

NPF events in general are not substantially influenced by anthropogenic activities, which are more intensive on workdays than on holidays. It is worth mentioning that the overall contribution of NPF to particle number concentrations is less than what is seemingly indicated by the diurnal patterns alone since NPF events occur on approximately 20 % of days (Table 2). Emissions from vehicular road traffic are represented by a notable peak during the morning rush hours (between 05:30 and 08:30 LT) on workdays. It is noted that the boundary layer mixing height is usually increased during this interval because of the increasing solar radiation intensity and mixing intensity. Another peak occurred around 21:00 LT and thus later than the afternoon rush, which usually happens between 16:30 and 18:30 LT. Under strong anticyclonic conditions, the evolution of the boundary layer mixing height and mixing intensity can decrease the concentration levels in the afternoons until sunset, and this can compensate the increased intensity of emissions. This all means that the afternoon peak is realized in a fuzzy manner since it is more influenced by local meteorology than by vehicular emissions. The effect of residential heating and combustion activities during evenings can also play a role. It is worth noting that the early-morning rush-hour peak on event days was smaller than on non-event days, which agrees with our earlier observation derived directly from experimental data (Salma et al., 2017) and is in line with the overall picture on urban NPF events (Zhang et al., 2015; Kulmala et al., 2017). On holidays, the modelled diurnal variation for non-event days contained an increasing part in the morning to a modest concentration level, which remains fairly constant over the daytime. This is explained by the differences in daily activities of citizens on workdays and holidays as far as both their intensity and timing are concerned.

The statistical diurnal patterns of N_{6-1000} trends (Fig. 3a) were very similar or analogous to those of N_{6-100}. These two size fractions are strongly connected with each other as explained in Sect. 3.1. The diurnal curves for N_{25-100} (Fig. 3c) were also similar to the previous corresponding curves as far as the character and shape are concerned, while there were also evident differences between their relative structures. The peaks for the early-morning and late-afternoon rush hours were relatively larger than in the trends of 6–100 or 6–1000 nm size fractions due to the higher contribution of primary particles from high-temperature sources in this size fraction. New particle formation generally occurs on days when N_{25-100} particles are smaller before the event onset (between 08:00 and 11:00 LT). The maximum of the peaks associated with NPF events in Fig. 3a and b – which is between 12:00 and 13:00 LT – was also shifted to later, i.e. to ca. 14:00 LT in Fig. 3c. This can be explained by the time needed for freshly nucleated particles to reach the diameter range >25 nm.

The statistical diurnal patterns for $N_{100-1000}$ seem very different from the smaller size ranges. First, their time variations were rather small in comparison to the other size fractions. On workdays, they only showed a modest elevation from 06:00 to 08:00 LT (morning rush hours), which is mainly caused by resuspension of road or surface dust particles by moving vehicles or by emissions of coarse particles from material wear. This morning peak was even missing on holidays, but another small and broad elevation showed up from 21:00 to 22:00 LT. This and the overall changes during the daylight time are primarily related to the daily cycling of local meteorological conditions, in particular boundary layer mixing height under stable anticyclonic weather conditions, which were outlined above.

3.2.2 Effects of variables

Monthly-mean coefficients (mean v_m slopes in Eq. 4) of NO_2, O_3 and SO_2 derived by GLMM, which express their partial effects on particle number concentrations, are shown in Fig. 4 for different size fractions.

The coefficients of SO_2 and NO_2 are positive, while O_3 seems to have a decreasing effect on particle number concentrations. The coefficients all have seasonal patterns, which means that the magnitude of their effect on particle concentrations are of different magnitude in different months. This means, for example, that $1\,\mu g\,m^{-3}$ increase in NO_2 concentration increases N_{6-1000} concentration in January by $154\,m^{-3}$ but in June by $50\,m^{-3}$. This could, however, be partly caused by annual changes in boundary layer mixing height or some other variable affecting particle concentrations (and correlating with these) but not measured at the site. The boundary layer mixing height tends to be smaller in Budapest in winter than in the other seasons (Salma et al., 2011), which ordinarily results in higher atmospheric concentrations at steady-state absolute amounts of chemical species. The coefficients of NO_2 on N_{6-1000}, N_{6-100} and N_{25-100} were higher in winter. This may indicate that large fractions of particles in these three size fractions originate from residential heating, and NO_2 acts as an indicator for this source. Another major source of NO_2 and primary particles is the road traffic, but this does not show seasonal variation in Budapest. The seasonal effect of NO_2 on chemically aged regional-type particles ($N_{100-1000}$) may not be significant.

The partial effect of O_3 on N_{6-1000}, N_{6-100} and N_{25-100} was weaker in summer, late spring and early autumn. These time intervals coincide with relatively large O_3 concentrations in the area. Ozone has a strong seasonal variation (as shown in Fig. S1 in the Supplement). The negative correlation between O_3 concentration and its effect on particle concentrations needs further clarification since O_3 participates in a large variety of complex atmospheric processes and also serves as a marker for photochemical processes which influence secondary particle formation. The influence of O_3 on $N_{100-1000}$ was virtually negligible, likely due to the regional character of these particles (which are usually chemically aged and often represent a larger spatial scale due to their longer atmospheric residence time) similarly to NO_2. In ad-

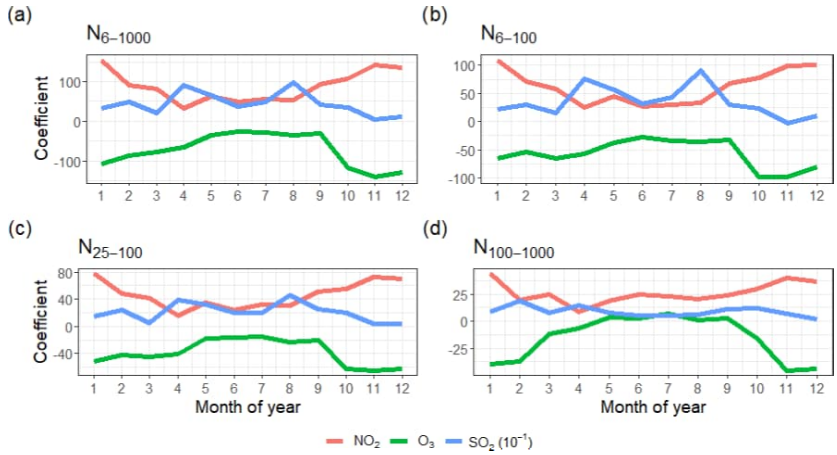

Figure 4. Distribution of monthly-mean coefficients (which are proportional to the partial effects) for NO_2, O_3 and SO_2 on particle number concentrations separately in the diameter ranges from 6 to 1000 nm (N_{6-1000}), from 6 to 100 nm (N_{6-100}), from 25 to 100 nm (N_{25-100}) and from 100 to 1000 nm ($N_{100-1000}$).

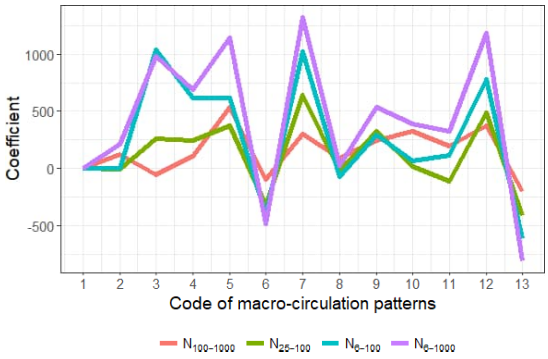

Figure 5. Distribution of monthly-mean coefficients (which are proportional to the partial effects) for macro-circulation patterns (Péczely codes) on particle number concentrations separately in the diameter ranges from 100 to 1000 nm ($N_{100-1000}$), from 25 to 100 nm (N_{25-100}), from 6 to 100 nm (N_{6-100}) and from 6 to 1000 nm (N_{6-1000}).

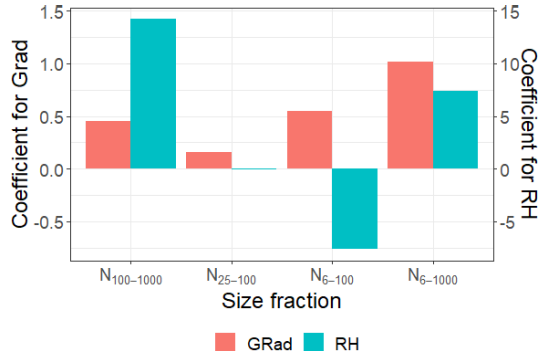

Figure 6. Coefficients (which are proportional to the partial effects) for global radiation (GRad) and relative humidity (RH) separately in the diameter ranges from 100 to 1000 nm ($N_{100-1000}$), from 25 to 100 nm (N_{25-100}), from 6 to 100 nm (N_{6-100}) and from 6 to 1000 nm (N_{6-1000}).

dition, O_3 might act as an indicator of particulate pollution from traffic, power plants and other anthropogenic sources. Then, more ozone would indicate higher numbers of larger particles and, due to coagulation, fewer smaller particles.

The partial effects of SO_2 on the particle number concentrations were the largest of the three gases considered. In N_{6-1000}, N_{6-100} and N_{25-100}, two peaks appeared: one in spring and another one in late summer. This shape is in line with the average distribution of the monthly-mean relative NPF occurrence frequency in Budapest (Salma and Németh, 2019). The latter distribution consists of absolute and local minima in January (with a monthly-mean occurrence frequency of 5.9 %) and August (17.0 %), respectively, and absolute and local maxima in April (41 %) and September (26 %), respectively. The distribution of the SO_2 coefficient suggests and confirms that SO_2, via NPF events, contributes (to a substantial extent) to the particle number concentrations in cities. The influence of SO_2 on $N_{100-1000}$ was virtually negligible, likely due to the regional character of these particles similarly to the other two gases included in the model.

Figure 5 summarizes the effect of macro-circulation patterns on particle number concentrations in the different size

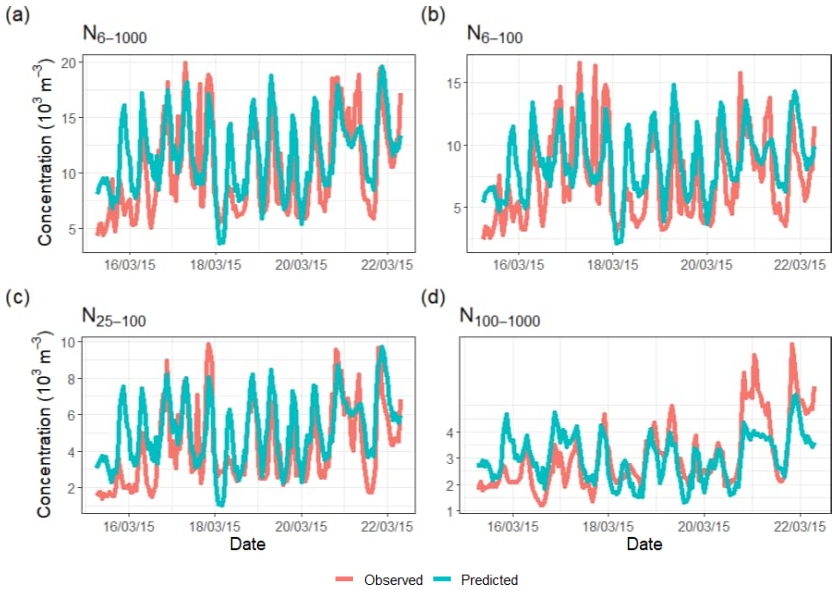

Figure 7. Observed (red line) and predicted (cyan line) time series for an illustrative example period separately in the size fractions of 6–1000, 6–100, 25–100 and 100–1000 nm.

fractions. It is seen that the larger regional-type particles are less affected by the MCPs than the smaller particles. The weather conditions favouring NPF events can be identified from the curves by looking at the largest coefficients for the size fraction of 6–100 nm.

It seems that the MCP nos. 3 (Mediterranean cyclone with a cold front over southern Europe, northerly wind), 7 (highly developed cyclone over northern Europe, westerly wind) and 12 (anticyclone over the Carpathian Basin, changing wind direction) can represent favourable conditions for NPF events than the other MCPs. Under these conditions, the weather in the area is typically windy, with average solar radiation (expect for MCP no. 3 in summer when it shows low daily values), with strong planetary bounding layer evolution; consequently, the pollutants concentrations are below the average (expect for the winter inversions in MCP no. 12). The air pollution situations are better separated by MCP codes in summer than in winter. The weather type classified as no. 6 (Mediterranean cyclone with a warm front over southern Europe, southerly wind) does not favour the events. Under these conditions, the weather is typically cloudy and rainy with lower-than-average solar radiation. This situation is often associated with polluted air in Budapest. Proportions for NPF days for different MCP codes, which are shown Table S1 in the Supplement, also confirm these conclusions. In order to see if the decreasing concentrations are due to changes in meteorological patterns, we investigated separately the occurrence of the MCP patterns during the measurement period. We found no significant changes in the occurrence of the patterns and thus the decreasing particle concentrations are due to something else than the meteorological patterns.

The coefficients for GRad and RH for different size fractions are shown in Fig. 6. It was found that these variables do not have seasonal dependency; i.e. they contribute with equal strength to particle concentrations throughout the year. Effect of GRad is positive for all size fractions, but it is weaker for larger (regional-type or already chemically aged or processed) particles. The latter contribution could be related to the bias in meteorological properties as well. The RH has a negligible effect on the size fraction of 25–100 nm. It strongly and positively affects the largest particles, which means that the particles are larger within higher humidity. This might be related to local meteorology, as higher RH probably means more clouds and more clouds probably means less radiation and lower boundary layer, and this could cause higher particle concentration. In contrast, the effect of RH on the smallest particles was negative, which is probably caused by high RH values, which limit NPF (e.g. Hamed et al., 2011).

3.2.3 Goodness-of-fit evaluation for GLMM

In order to estimate the uncertainty of the models for different size fractions, we calculated the mean absolute errors relative to the dependent variable mean, given by Willmott et

Table 4. Goodness-of-fit estimates for GLMM as expressed by the mean absolute error relative to the dependent variable mean and by Spearman's rank correlation coefficient separately in the size fractions of 6–1000, 6–100, 25–100 and 100–1000 nm.

Size fraction	Error	Correlation
6–1000	0.30	0.73
6–100	0.32	0.72
25–100	0.34	0.71
100–1000	0.34	0.73

al. (2009):

$$\mathrm{Err} = \left(n^{-1}\sum_{i=1}^{n}\left|y_i - \hat{y}_i\right|\right)\cdot\overline{y}^{-1}, \quad (6)$$

where n is the number of observations, y_i represents the observed particle number concentrations, $\hat{y}_i$ represents the predicted values given by the GLMM and $\overline{y}$ is the mean of the observed values. In addition, we calculated Spearman's rank correlation coefficients between the observed and predicted values for all size fractions. Both goodness-of-fit estimates are shown in Table 4. As the relative errors for different size fractions are within a range of 0.30–0.34 and the correlations are higher than 0.70, it can be concluded that the model fitted the data with this size and measurement uncertainty well.

Figure 7 illustrates how well the GLMM model predicts the observations in all size fractions within a randomly selected period of 1 week in March 2015. The figure shows that the predicted values follow the observations fairly well in all size fractions. Overall, the statistical model finds the peaks of the concentration, but it slightly underestimates the highest peaks and fastest fluctuations and, in some cases, overestimates the lowest concentrations.

4 Conclusions

In the present study, we determined decennial statistical time trends and diurnal statistical patterns of atmospheric particle number concentrations in various relevant size fractions in the city centre of Budapest in an interval of 2008–2018. The decennial statistical trends showed a decreasing character in all applied size fractions of particle concentrations. The mean overall decrease rate was approximately −5 % when scaled for the 10-year measurement interval. One of the likely explanations of the decline is due to the decreased anthropogenic emissions in the city. The diurnal statistical patterns suggested that reduced traffic emissions were most likely an important factor in causing the observed changes. It is expected that traffic intensity changed in a modest manner in the city centre during the time interval of interest, so our results indicate that the reductions are most likely related to lower emission factors. This appears to follow some changes of sulfur content in fuels and control measures on emissions for on-road heavy-duty diesel vehicles. Introduction of better particle filters in diesel cars, cleaner fuel and more sophisticated diesel engines could also contribute. Modernized technologies in residential and household heating could also contribute. The magnitude of the traffic emission reduction cannot be completely conclusive in all aspects for the moment, and further investigations are planned on the basis of the present results. The changes appear to have responded to both the policy on urban air quality and the influence of economic circumstances of inhabitants. Excitingly, the mean ages of passenger cars and busses in Hungary increased during the years under investigation. The exact explanation and confirmation of the decrease require continuation of the related measurements with independent experimental systems and further dedicated studies. The present results can be also used for evaluating the effectiveness of present and prospective mitigation policies.

The diurnal statistical patterns can be also utilized in interpreting some properties of NPF events in urban environments and in explaining time evolution of particle number concentration. As a result of the GLMM, we could, for instance, give a parametrization for predicting particle concentrations in different size fractions. Models similar to those developed in the present study could be used for other particle sizes or locations as well. The same parameterization could be used at least in areas with similar concentration levels of particles and pollutants, while the extrapolation of the results to cleaner or more polluted environments needs to be confirmed before use. Conjugate or linked parameterizations to be developed for varying environments can be implemented as a part of atmospheric models to predict the concentrations of climatically active particles in order to reduce their extensive computational times. In addition, this could also contribute to solving some current uncertain issues in the theoretical description of NPF and growth processes, particularly when predicting cloud condensation nuclei concentrations.

Data availability. The observational data used in this paper are available on request from the corresponding author Imre Salma (salma@chem.elte.hu).

Supplement. The supplement related to this article is available online at: https://doi.org/10.5194/acp-20-12247-2020-supplement.

Author contributions. IS and SM formulated the original concept; ZN, VV, TW and IS collected and processed the experimental data; SM, VL and TY were responsible for the statistical data analyses and their physical basis; SM and IS interpreted the results; IS and SM wrote the article with contributions from all co-authors.

Competing interests. The authors declare that they have no conflict of interest.

Financial support. The research was supported by the National Research, Development and Innovation Office, Hungary (contracts K116788, PD124283 and K132254), by the János Bolyai Research Scholarship of the Hungarian Academy of Sciences (ZN), by the European Regional Development Fund and the Hungarian government (GINOP-2.3.2-15-2016-00028), by the Nessling Foundation, by the Academy of Finland Centre of Excellence (grant no. 307331), and by the Academy of Finland competitive funding to strengthen university research profiles (PROFI) for the University of Eastern Finland (grant no. 325022) and Academy of Finland project (grant no. 299544).

Review statement. This paper was edited by Andreas Petzold and reviewed by two anonymous referees.

References

Aalto, P., Hämeri, K., Becker, E., Weber, R., Salm, J., Mäkelä, J., Hoell, C., O'Dowd, C., Karlsson, H., Väkevä, M., Koponen, I. K., Buzorius, G., and Kulmala, M.: Physical characterization of aerosol particles during nucleation events, Tellus B, 53, 344–358, 2001.

Aalto, P., Hämeri, K., Paatero, P., Kulmala, M., Bellander, T., Berglind, N., Bouso, L., Castaño-Vinyals, G., Sunyer, J., Cattani, G., Marconi, A., Cyrys, J., von Klot, S., Peters, A., Zetzsche, K., Lanki, T., Pekkanen, J., Nyberg, F., Sjövall, B., and Forastiere, F.: Aerosol particle number concentration measurements in five European cities using TSI-3022 condensation particle counter over a three-year period during health effects of air pollution on susceptible subpopulations, J. Air Waste Manage. Assoc., 55, 1064–1076, 2005.

Asmi, A., Collaud Coen, M., Ogren, J. A., Andrews, E., Sheridan, P., Jefferson, A., Weingartner, E., Baltensperger, U., Bukowiecki, N., Lihavainen, H., Kivekäs, N., Asmi, E., Aalto, P. P., Kulmala, M., Wiedensohler, A., Birmili, W., Hamed, A., O'Dowd, C., G Jennings, S., Weller, R., Flentje, H., Fjaeraa, A. M., Fiebig, M., Myhre, C. L., Hallar, A. G., Swietlicki, E., Kristensson, A., and Laj, P.: Aerosol decadal trends – Part 2: In-situ aerosol particle number concentrations at GAW and ACTRIS stations, Atmos. Chem. Phys., 13, 895–916, https://doi.org/10.5194/acp-13-895-2013, 2013.

Avino, P., Casciardi, S., Fanizza, C., and Manigrasso, M.: Deep investigation of ultrafine particles in urban air, Aerosol Air Qual. Res., 11, 654–663, 2011.

Birmili, W., Wiedensohler, A., Heintzenberg, J., and Lehmann, K.: Atmospheric particle number size distribution in central Europe: Statistical relations to air masses and meteorology, J. Geophys. Res.-Atmos., 106, 32005-18, 2001.

Braakhuis, H. M., Park, M. V., Gosens, I., De Jong, W. H., and Cassee, F. R.: Physicochemical characteristics of nanomaterials that affect pulmonary inflammation, Part. Fibre Toxicol., 11, 18, https://doi.org/10.1186/1743-8977-11-18, 2014.

Brines, M., Dall'Osto, M., Beddows, D. C. S., Harrison, R. M., Gómez-Moreno, F., Núñez, L., Artíñano, B., Costabile, F., Gobbi, G. P., Salimi, F., Morawska, L., Sioutas, C., and Querol, X.: Traffic and nucleation events as main sources of ultrafine particles in high-insolation developed world cities, Atmos. Chem. Phys., 15, 5929–5945, https://doi.org/10.5194/acp-15-5929-2015, 2015.

Cassee, F. R., Héroux, M.-E., Gerlofs-Nijland, M. E., and Kelly, F. J.: Particulate matter beyond mass: recent health evidence on the role of fractions, chemical constituents and sources of emission, Inhal. Toxicol. 25, 802–812, 2013.

Carslaw, K. S., Lee, L. A., Reddington, C. L., Pringle, K. J., Rap, A., Forster, P. M., Mann, G. W., Spracklen, D. V., Woodhouse, M. T., Regayre, L. A., and Pierce, J. R: Large contribution of natural aerosols to uncertainty in indirect forcing, Nature, 503, 67–71, 2013.

Dada, L., Ylivinkka, I., Baalbaki, R., Li, C., Guo, Y., Yan, C., Yao, L., Sarnela, N., Jokinen, T., Daellenbach, K. R., Yin, R., Deng, C., Chu, B., Nieminen, T., Wang, Y., Lin, Z., Thakur, R. C., Kontkanen, J., Stolzenburg, D., Sipilä, M., Hussein, T., Paasonen, P., Bianchi, F., Salma, I., Weidinger, T., Pikridas, M., Sciare, J., Jiang, J., Liu, Y., Petäjä, T., Kerminen, V.-M., and Kulmala, M.: Sources and sinks driving sulfuric acid concentrations in contrasting environments: implications on proxy calculations, Atmos. Chem. Phys., 20, 11747–11766, https://doi.org/10.5194/acp-20-11747-2020, 2020.

Dal Maso, M., Kulmala, M., Lehtinen, K. E. J., Mäkelä, J. M., Aalto, P. P., and O'Dowd, C.: Condensation and coagulation sinks and formation of nucleation mode particles in coastal and boreal forest boundary layers, J. Geophys. Res., 107, 8097, https://doi.org/10.1029/2001jd001053, 2002.

Dal Maso, M., Kulmala, M., Riipinen, I., Wagner, R., Hussein, T., Aalto, P. P., and Lehtinen, K. E. J.: Formation and growth of fresh atmospheric aerosols: eight years of aerosol size distribution data from SMEAR II, Hyytiälä, Finland, Boreal Environ. Res., 10, 323–336, 2005.

Dall'Osto, M., Querol, X., Alastuey, A., O'Dowd, C., Harrison, R. M., Wenger, J., and Gómez-Moreno, F. J.: On the spatial distribution and evolution of ultrafine particles in Barcelona, Atmos. Chem. Phys., 13, 741–759, https://doi.org/10.5194/acp-13-741-2013, 2013.

Directive 2009/30/EC: Official Journal of the European Union, L 140, EN, 88–113, 2009.

Dunne, E. M., Gordon, H., Kürten, A., Almeida, J., Duplissy, J., Williamson, C., Ortega, I. K., Pringle, K. J., Adamov, A., Baltensperger, U., Barmet, P., Benduhn, F., Bianchi, F., Breitenlechner, M., Clarke, A., Curtius, J., Dommen, J., Donahue, N. M., Ehrhart, S., Flagan, R. C., Franchin, A., Guida, R., Hakala, J., Hansel, A., Heinritzi, M., Jokinen, T., Kangasluoma, J., Kirkby, J., Kulmala, M., Kupc, A., Lawler, M. J., Lehtipalo, K., Makhmutov, V., Mann, G., Mathot, S., Merikanto, J., Miettinen, P., Nenes, A., Onnela, A., Rap, A., Reddington, C. L. S., Riccobono, F., Richards, N. A. D., Rissanen, M. P., Rondo, L., Sarnela, N., Schobesberger, S., Sengupta, K., Simon, M., Sipilä, M., Smith, J. N., Stozkhov, Y., Tomé, A., Tröstl, J., Wagner, P. E., Wimmer, D., Winkler, P. M., Worsnop, D. R., and Carslaw, K. S.: Global atmospheric particle formation from CERN CLOUD measurements, Science, 354, 1119–1124, 2016.

Durbin, J. and Koopman, S. J.: Time series analysis by state space methods, Oxford University Press, Oxford, 2012.

Giechaskiel, B., Lahde, T., Suarez-Bertoa, R., Clairotte, M., Grigoratos, T., Zardini, A., Perujo, A., and Martini, G.: Particle number measurements in the European legislation and future JRC activities, Combustion Engines, 174, 3–16, 2018.

Gordon, H., Sengupta, K., Rap, A., Duplissy, J., Frege, C., Williamson, C., Heinritzi, M., Simon, M., Yan, C., Almeida, J., Tröstl, J., Nieminen, T., Ortega, I. K., Wagner, R., Dunne, E. M., Adamov, A., Amorim, A., Bernhammer, A. K., Bianchi, F., Breitenlechner, M., Brilke, S., Chen, X., Craven, J. S., Dias, A., Ehrhart, S., Fischer, L., Flagan, R. C., Franchin, A., Fuchs, C., Guida, R., Hakala, J., Hoyle, C. R., Jokinen, T., Junninen, H., Kangasluoma, J., Kim, J., Kirkby, J., Krapf, M., Kürten, A., Laaksonen, A., Lehtipalo, K., Makhmutov, V., Mathot, S., Molteni, U., Monks, S. A., Onnela, A., Peräkylä, O., Piel, F., Petäjä, T., Praplan, A. P., Pringle, K. J., Richards, N. A. D., Rissanen, M. P., Rondo, L., Sarnela, N., Schobesberger, S., Scott, C. E., Seinfeld, J. H., Sharma, S., Sipilä, M., Steiner, G., Stozhkov, Y., Stratmann, F., Tomé, A., Virtanen, A., Vogel, A. L., Wagner, A. C., Wagner, P. E., Weingartner, E., Wimmer, D., Winkler, P. M., Ye, P., Zhang, X., Hansel, A., Dommen, J., Donahue, N. M., Worsnop, D. R., Baltensperger, U., Kulmala, M., Curtius, J., and Carslaw, K. S.: Reduced anthropogenic aerosol radiative forcing caused by biogenic new particle formation, P. Natl. Acad. Sci. USA, 113, 12053–12058, 2016.

Guo, H., Wang, D. W., Cheung, K., Ling, Z. H., Chan, C. K., and Yao, X. H.: Observation of aerosol size distribution and new particle formation at a mountain site in subtropical Hong Kong, Atmos. Chem. Phys., 12, 9923–9939, https://doi.org/10.5194/acp-12-9923-2012, 2012.

Hamed, A., Korhonen, H., Sihto, S.-L., Joutsensaari, J., Järvinen, H., Petäjä, T., Arnold, F., Nieminen, T., Kulmala, M., Smith, J. N., Lehtinen, K. E. J., and Laaksonen, A.: The role of relative humidity in continental new particle formation, J. Geophys. Res., 116, D03202, https://doi.org/10.1029/2010JD014186, 2011.

Hussein, T., Puustinen, A., Aalto, P. P., Mäkelä, J. M., Hämeri, K., and Kulmala, M.: Urban aerosol number size distributions, Atmos. Chem. Phys., 4, 391–411, https://doi.org/10.5194/acp-4-391-2004, 2004.

Hyvönen, S., Junninen, H., Laakso, L., Dal Maso, M., Grönholm, T., Bonn, B., Keronen, P., Aalto, P., Hiltunen, V., Pohja, T., Launiainen, S., Hari, P., Mannila, H., and Kulmala, M.: A look at aerosol formation using data mining techniques, Atmos. Chem. Phys., 5, 3345–3356, https://doi.org/10.5194/acp-5-3345-2005, 2005.

Károssy, C.: A Kárpát-medence Péczely-féle makroszinoptikus időjárási helyzeteinek katalógusa 1881–2015 (Catalogue of the Péczely macrosynoptic weather types for the Carpathian Basin 1881–2015, in Hungarian), OSKAR Kiadó, Budapest, 2016.

Kerminen, V.-M., Paramonov, M., Anttila, T., Riipinen, I., Fountoukis, C., Korhonen, H., Asmi, E., Laakso, L., Lihavainen, H., Swietlicki, E., Svenningsson, B., Asmi, A., Pandis, S. N., Kulmala, M., and Petäjä, T.: Cloud condensation nuclei production associated with atmospheric nucleation: a synthesis based on existing literature and new results, Atmos. Chem. Phys., 12, 12037–12059, https://doi.org/10.5194/acp-12-12037-2012, 2012.

Kerminen, V.-M., Chen, X., Vakkari, V., Petäjä, T., Kulmala, M., and Bianchi, F.: Atmospheric new particle formation and growth: review of field observations, Environ. Res. Lett., 13, 103003, https://doi.org/10.1088/1748-9326/aadf3c, 2018.

KSH: National register of road vehicles (in Hungarian), Hungarian Central Statistical Office, Budapest, 2019.

Kulmala, M., Dal Maso, M., Mäkelä, J. M., Pirjola, L., Väkevä, M., Aalto, P., Miikkulainen, P., Hämeri, K., and O'Dowd, C. D.: On the formation, growth and composition of nucleation mode particles, Tellus B, 53, 479–490, 2001.

Kulmala, M., Petäjä, T., Nieminen, T., Sipilä, M., Manninen, H. E., Lehtipalo, K., Dal Maso, M., Aalto, P. P., Junninen, H., Paasonen, P., Riipinen, I., Lehtinen, K. E. J., Laaksonen, A., and Kerminen, V.-M.: Measurement of the nucleation of atmospheric aerosol particles, Nat. Protoc., 7, 1651–1667, https://doi.org/10.1038/nprot.2012.091, 2012.

Kulmala, M., Kontkanen, J., Junninen, H., Lehtipalo, K., Manninen, H. E., Nieminen, T., Petäjä, T., Sipilä, M., Schobesberger, S., Rantala, P., Franchin, A., Jokinen, T., Järvinen, E., Äijälä, M., Kangasluoma, J., Hakala, J., Aalto, P. P., Paasonen, P., Mikkilä, J., Vanhanen, J., Aalto, J., Hakola, H., Makkonen, U., Ruuskanen, T., Mauldin, R. L. III, Duplissy, J., Vehkamäki, H., Bäck, J., Kortelainen, A., Riipinen, I., Kurtén, T., Johnston, M. V., Smith, J. N., Ehn, M., Mentel, T. F., Lehtinen, K. E. J., Laaksonen, A., Kerminen, V.-M., and Worsnop, D. R.: Direct observations of atmospheric aerosol nucleation, Science, 339, 943–946, 2013.

Kulmala, M., Petäjä, T., Ehn, M., Thornton, J., Sipilä, M., Worsnop, D. R., and Kerminen, V.-M.: Chemistry of atmospheric nucleation: On the recent advances on precursor characterization and atmospheric cluster composition in connection with atmospheric new particle formation, Annu. Rev. Phys. Chem., 65, 21–37, 2014.

Kulmala, M., Kerminen, V. M., Petäjä, T., Ding, A. J., and Wang, L.: Atmospheric gas-to-particle conversion: why NPF events are observed in megacities, Faraday Discuss., 200, 271–288, https://doi.org/10.1039/C6FD00257A, 2017.

Laine, M.: Introduction to Dynamic Linear Models for Time Series Analysis, in: Geodetic Time Series Analysis in Earth Sciences, edirted by: Montillet, J. P. and Bos, M., Springer, 139–156, 2020.

Maheras, P., Tolika, K., Tegoulias, I., Anagnostopoulou, Ch., Szpirosz, K. Károssy, Cs., and Makra, L.: Comparison of an automated classification system with an empirical classification of circulation patterns over the Pannonian basin, Central Europe, Meteorol. Atmos. Phys., 131, 739–751, https://doi.org/10.1007/s00703-018-0601-x, 2018.

Makkonen, R., Asmi, A., Korhonen, H., Kokkola, H., Järvenoja, S., Räisänen, P., Lehtinen, K. E. J., Laaksonen, A., Kerminen, V.-M., Järvinen, H., Lohmann, U., Bennartz, R., Feichter, J., and Kulmala, M.: Sensitivity of aerosol concentrations and cloud properties to nucleation and secondary organic distribution in ECHAM5-HAM global circulation model, Atmos. Chem. Phys., 9, 1747–1766, https://doi.org/10.5194/acp-9-1747-2009, 2009.

Masiol, M., Squizzato, S., Chalupa, D., Utell, M. J., Rich, D. Q., and Hopke, P. K.: Long-term trends in submicron particle concentrations in a metropolitan area of the northeastern United States, Sci. Total Environ., 633, 59–70, 2018.

McCulloch, C. E., Searle, S. R., and Neuhaus, J. M.: Generalized, linear, and mixed models, 2nd ed., Wiley, New York, 2008.

McFiggans, G., Mentel, T. F., Wildt, J., Pullinen, I., Kang, S., Kleist, E., Schmitt, S., Springer, M., Tillmann, R., Wu, C., Zhao, D., Hallquist, M., Faxon, C., Le Breton, M., Hallquist, A. M., Simpson, D., Bergstroem, R., Jenkin, M. E., Ehn, M., Thornton, J. A., Alfarra, M. R., Bannan, T. J., Percival, C. J., Priestley, M., Topping, D., and Kiendler-Scharr, A.: Secondary organic aerosol reduced by mixture of atmospheric vapours, Nature, 565, 587–593, 2019.

Merikanto, J., Spracklen, D. V., Mann, G. W., Pickering, S. J., and Carslaw, K. S.: Impact of nucleation on global CCN, Atmos. Chem. Phys., 9, 8601–8616, https://doi.org/10.5194/acp-9-8601-2009, 2009.

Mikkonen, S., Lehtinen, K. E. J., Hamed, A., Joutsensaari, J., Facchini, M. C., and Laaksonen, A.: Using discriminant analysis as a nucleation event classification method, Atmos. Chem. Phys., 6, 5549–5557, https://doi.org/10.5194/acp-6-5549-2006, 2006.

Mikkonen, S., Korhonen, H., Romakkaniemi, S., Smith, J. N., Joutsensaari, J., Lehtinen, K. E. J., Hamed, A., Breider, T. J., Birmili, W., Spindler, G., Plass-Duelmer, C., Facchini, M. C., and Laaksonen, A.: Meteorological and trace gas factors affecting the number concentration of atmospheric Aitken ($D_p = 50$ nm) particles in the continental boundary layer: parameterization using a multivariate mixed effects model, Geosci. Model Dev., 4, 1–13, https://doi.org/10.5194/gmd-4-1-2011, 2011a.

Mikkonen, S., Romakkaniemi, S., Smith, J. N., Korhonen, H., Petäjä, T., Plass-Duelmer, C., Boy, M., McMurry, P. H., Lehtinen, K. E. J., Joutsensaari, J., Hamed, A., Mauldin III, R. L., Birmili, W., Spindler, G., Arnold, F., Kulmala, M., and Laaksonen, A.: A statistical proxy for sulphuric acid concentration, Atmos. Chem. Phys., 11 11319–11334, https://doi.org/10.5194/acp-11-11319-2011, 2011b.

Mikkonen, S., Laine, M., Mäkelä, H. M., Gregow, H., Tuomenvirta, H., Lahtinen, M., and Laaksonen, A.: Trends in the average temperature in Finland, 1847-2013, Stoch. Environ. Res. Risk Ass., 29, 1521–1529, 2015.

Moore, K. F., Ning, Z., Ntziachristos, L., Schauer, J. J., and Sioutas, C.: Daily variation in the properties of urban ultrafine aerosol – Part I: Physical characterization and volatility, Atmos. Environ., 41, 8633–8646, 2007.

Moosmuller, H., Chakrabarty, R. K., and Arnott, W: Aerosol light absorption and its measurement: A review, J. Quant. Sp. Radiat. Transf., 110, 844–878, 2009.

Németh, Z. and Salma, I.: Spatial extension of nucleating air masses in the Carpathian Basin, Atmos. Chem. Phys., 14, 8841–8848, https://doi.org/10.5194/acp-14-8841-2014, 2014.

Németh, Z., Rosati, B., Zíková, N., Salma, I., Bozó, L., Dameto de España, C., Schwarz, J., Ždímal, V., and Wonaschütz, A.: Comparison of atmospheric new particle formation and growth events in three Central European cities, Atmos. Environ., 178, 191–197, 2018.

Nieminen, T., Asmi, A., Dal Maso, M., P. Aalto, P., Keronen, P., Petäjä, T., Kulmala, M., and Kerminen, V.-M.: Trends in atmospheric new-particle formation: 16 years of observations in a boreal-forest environment, Boreal Env. Res., 19, 191–214, 2014.

Nieminen, T., Kerminen, V.-M., Petäjä, T., Aalto, P. P., Arshinov, M., Asmi, E., Baltensperger, U., Beddows, D. C. S., Beukes, J. P., Collins, D., Ding, A., Harrison, R. M., Henzing, B., Hooda, R., Hu, M., Hõrrak, U., Kivekäs, N., Komsaare, K., Krejci, R., Kristensson, A., Laakso, L., Laaksonen, A., Leaitch, W. R., Lihavainen, H., Mihalopoulos, N., Németh, Z., Nie, W., O'Dowd, C., Salma, I., Sellegri, K., Svenningsson, B., Swietlicki, E., Tunved, P., Ulevicius, V., Vakkari, V., Vana, M., Wiedensohler, A., Wu, Z., Virtanen, A., and Kulmala, M.: Global analysis of continental boundary layer new particle formation based on long-term measurements, Atmos. Chem. Phys., 18, 14737–14756, https://doi.org/10.5194/acp-18-14737-2018, 2018.

Oberdörster, G., Oberdörster, E., and Oberdörster, J.: Nanotoxicology: an emerging discipline evolving from studies of ultrafine particles, Environ. Health Perspect., 113, 823–839, 2005.

Ohlwein, S., Kappeler, R., Joss, M. K., Künzli, N., and Hoffmann, B.: Health effects of ultrafine particles: a systematic literature review update of epidemiological evidence, Int. J. Public Health, 685, 547–559, 2019.

Ostro, B., Hu, J., Goldberg, D., Reynolds, P., Hertz, A., Bernstein, L., and Kleeman, M. J.: Associations of mortality with long-term exposures to fine and ultrafine particles, species and sources: results from the California teachers study cohort, Environ. Health Perspect., 123, 549–556, 2015.

Paasonen, P., Kupiainen, K., Klimont, Z., Visschedijk, A., Denier van der Gon, H. A. C., and Amann, M.: Continental anthropogenic primary particle number emissions, Atmos. Chem. Phys., 16, 6823–6840, https://doi.org/10.5194/acp-16-6823-2016, 2016.

Péczely, G.: Grosswetterlagen in Ungarn (Large-scale weather situations in Hungary, in German), Publication of the Hungarian Meteorological Institute, 30, Budapest, 86, pp., 1957.

Petäjä, T., Mauldin, III, R. L., Kosciuch, E., McGrath, J., Nieminen, T., Paasonen, P., Boy, M., Adamov, A., Kotiaho, T., and Kulmala, M.: Sulfuric acid and OH concentrations in a boreal forest site, Atmos. Chem. Phys., 9, 7435–7448, https://doi.org/10.5194/acp-9-7435-2009, 2009.

Petris, G., Petrone, S., and Campagnoli, P.: Dynamic linear models, Springer, New York, 2009.

Pinheiro, J. C. and Bates, D. M.: Mixed-Effects Models in S and S-PLUS, Springer, 2000.

Platt, S. M., El Haddad, I., Pieber, S. M., Zardini, A. A., Suarez-Bertoa, R., Clairotte, M., Daellenbach, K. R., Huang, R.-J., Slowik, J. G., Hellebust, S., Temime-Roussel, B., Marchand, N., de Gouw, J., Jimenez, J. L., Hayes, P. L., Robinson, A. L., Baltensperger, U., Astorga, C., and Prévôt, A. S. H.: Gasoline cars produce more carbonaceous particulate matter than modern filter-equipped diesel cars, Sci. Rep., 7, 4926, https://doi.org/10.1038/s41598-017-03714-9, 2017.

Pöschl, U., Rudich, Y., and Ammann, M.: Kinetic model framework for aerosol and cloud surface chemistry and gas-particle interactions – Part 1: General equations, parameters, and terminology, Atmos. Chem. Phys., 7, 5989–6023, https://doi.org/10.5194/acp-7-5989-2007, 2007.

Raes, F., Van Dingenen, R., Vignati, E., Wilson, J., Putaud, J. P., Seinfeld, J. H., and Adams, P.: Formation and cycling of aerosol in the global troposphere, Atmos. Environ., 34, 4215–4240, 2000.

Rich, D. Q., Zareba, W., Beckett, W., Hopke, P. K., Oakes, D., Frampton, M. W., Bisognano, J., Chalupa, D., Bausch, J., O'Shea, K., Wang, Y., and Utell, M. J.: Are ambient ultrafine, accumulation mode, and fine particles associatedwith adverse cardiac responses in patients undergoing cardiac rehabilitation?, Environ. Health Perspect., 120, 1162–1169, 2012.

Saha, P. K., Robinson, E. S., Shah, R. U., Zimmerman, N., Apte, J. S., Robinson, A. L., and Presto, A. A.: Reduced ultrafine particle concentration in urban air: changes in nucleation and anthropogenic emissions, Environ. Sci. Technol., 52, 6798–6806, 2018.

Salma, I., Borsós, T., Weidinger, T., Aalto, P., Hussein, T., Dal Maso, M., and Kulmala, M.: Production, growth and properties of ultrafine atmospheric aerosol particles in an

urban environment, Atmos. Chem. Phys., 11, 1339–1353, https://doi.org/10.5194/acp-11-1339-2011, 2011.

Salma, I., Borsós, T., Németh, Z., Weidinger, T., Aalto, T., and Kulmala, M.: Comparative study of ultrafine atmospheric aerosol within a city, Atmos. Environ., 92, 154–161, 2014.

Salma, I., Németh, Z., Weidinger, T., Kovács, B., and Kristóf, G.: Measurement, growth types and shrinkage of newly formed aerosol particles at an urban research platform, Atmos. Chem. Phys., 16, 7837–7851, https://doi.org/10.5194/acp-16-7837-2016, 2016a.

Salma, I., Németh, Z., Kerminen, V.-M., Aalto, P., Nieminen, T., Weidinger, T., Molnár, Á., Imre, K., and Kulmala, M.: Regional effect on urban atmospheric nucleation, Atmos. Chem. Phys., 16, 8715–8728, https://doi.org/10.5194/acp-16-8715-2016, 2016b.

Salma, I., Varga, V., and Németh, Z.: Quantification of an atmospheric nucleation and growth process as a single source of aerosol particles in a city, Atmos. Chem. Phys., 17, 15007–15017, https://doi.org/10.5194/acp-17-15007-2017, 2017.

Salma, I. and Németh, Z.: Dynamic and timing properties of new aerosol particle formation and consecutive growth events, Atmos. Chem. Phys., 19, 5835–5852, https://doi.org/10.5194/acp-19-5835-2019, 2019.

Schmid, O. and Stoeger, T.: Surface area is the biologically most effective dose metric for acute nanoparticle toxicity in the lung, J. Aerosol Sci., 99, 133–143, 2016.

Sihto, S.-L., Mikkilä, J., Vanhanen, J., Ehn, M., Liao, L., Lehtipalo, K., Aalto, P. P., Duplissy, J., Petäjä, T., Kerminen, V.-M., Boy, M., and Kulmala, M.: Seasonal variation of CCN concentrations and aerosol activation properties in boreal forest, Atmos. Chem. Phys., 11, 13269–13285, https://doi.org/10.5194/acp-11-13269-2011, 2011.

Sipilä, M., Berndt, T., Petäjä, T., Brus, D., Vanhanen, J., Stratmann, F., Patokoski, J., Mauldin, R. L., Hyvärinen, A. P., Lihavainen, H., and Kulmala, M.: The role of sulfuric acid in atmospheric nucleation, Science, 327, 1243, https://doi.org/10.1126/science.1180315, 2010.

Spracklen, D. V., Carslaw, K. S., Kulmala, M., Kerminen, V.-M., Mann, G. W., and Sihto, S.-L.: The contribution of boundary layer nucleation events to total particle concentrations on regional and global scales, Atmos. Chem. Phys., 6, 5631–5648, https://doi.org/10.5194/acp-6-5631-2006, 2006.

Sun, J., Birmili, W., Hermann, M., Tuch, T., Weinhold, K., Merkel, M., Rasch, F., Müller, T., Schladitz, A., Bastian, S., Löschau, G., Cyrys, J., Gu, J., Flentje, H., Briel, B., Asbach, C., Kaminski, H., Ries, L., Sohmer, R., Gerwig, H., Wirtz, K., Meinhardt, F., Schwerin, A., Bath, O., Ma, N., and Wiedensohler, A.: Decreasing trends of particle number and black carbon mass concentrations at 16 observational sites in Germany from 2009 to 2018, Atmos. Chem. Phys., 20, 7049–7068, https://doi.org/10.5194/acp-20-7049-2020, 2020.

Wehner, B. and Wiedensohler, A.: Long term measurements of submicrometer urban aerosols: statistical analysis for correlations with meteorological conditions and trace gases, Atmos. Chem. Phys., 3, 867–879, https://doi.org/10.5194/acp-3-867-2003, 2003.

Wihersaari, H., Pirjola, L., Karjalainen, P., Saukko, E., Kuuluvainen, H., Kulmala, K., Keskinen, J., and Rönkkö, T.: Particulate emissions of a modern diesel passenger car under laboratory and real-world transient driving conditions, Environ. Pollut., 265, 114948, https://doi.org/10.1016/j.envpol.2020.114948, 2020.

Wiedensohler, A., Birmili, W., Nowak, A., Sonntag, A., Weinhold, K., Merkel, M., Wehner, B., Tuch, T., Pfeifer, S., Fiebig, M., Fjäraa, A. M., Asmi, E., Sellegri, K., Depuy, R., Venzac, H., Villani, P., Laj, P., Aalto, P., Ogren, J. A., Swietlicki, E., Williams, P., Roldin, P., Quincey, P., Hüglin, C., Fierz-Schmidhauser, R., Gysel, M., Weingartner, E., Riccobono, F., Santos, S., Grüning, C., Faloon, K., Beddows, D., Harrison, R., Monahan, C., Jennings, S. G., O'Dowd, C. D., Marinoni, A., Horn, H.-G., Keck, L., Jiang, J., Scheckman, J., McMurry, P. H., Deng, Z., Zhao, C. S., Moerman, M., Henzing, B., de Leeuw, G., Löschau, G., and Bastian, S.: Mobility particle size spectrometers: harmonization of technical standards and data structure to facilitate high quality long-term observations of atmospheric particle number size distributions, Atmos. Meas. Tech., 5, 657–685, https://doi.org/10.5194/amt-5-657-2012, 2012.

Willmott, C. J., Matsuura, K., and Robeson, S. M.: Ambiguities inherent in sums-of-squares-based error statistics, Atmos. Environ., 43, 749–752, https://doi.org/10.1016/j.atmosenv.2008.10.005, 2009.

Yu, F., Luo, G., Bates, T. S., Anderson, B., Clarke, A., Kapustin, V., Yantosca, R. M., Wang, Y., and Wu, S.: Spatial distributions of particle number concentrations in the global troposphere: simulations, observations, and implications for nucleation mechanisms, J. Geophys. Res., 115, D17205, https://doi.org/10.1029/2009JD013473, 2010.

Zaidan, M. A., Haapasilta, V., Relan, R., Paasonen, P., Kerminen, V.-M., Junninen, H., Kulmala, M., and Foster, A. S.: Exploring non-linear associations between atmospheric new-particle formation and ambient variables: a mutual information approach, Atmos. Chem. Phys., 18, 12699–12714, https://doi.org/10.5194/acp-18-12699-2018, 2018.

Zhang, R., Wang, G., Guo, S., Zamora, M. L., Ying, Q., Lin, Y., Wang, W., Hu, M., and Wang, Y.: Formation of urban fine particulate matter, Chem. Rev., 115, 3803–3855, 2015.

Supplement of Atmos. Chem. Phys., 20, 12247–12263, 2020
https://doi.org/10.5194/acp-20-12247-2020-supplement

Atmospheric Chemistry and Physics Open Access EGU

Supplement of

Decennial time trends and diurnal patterns of particle number concentrations in a central European city between 2008 and 2018

Santtu Mikkonen et al.

Correspondence to: Imre Salma (salma@chem.elte.hu) and Santtu Mikkonen (santtu.mikkonen@uef.fi)

Table S1. Proportions of NPF event days and non-event days for different macro-circulation patterns (MCP).

MCP code	Non-event days	Event days
1	0.88	0.12
2	0.82	0.18
3	0.80	0.20
4	0.90	0.10
5	0.78	0.22
6	0.93	0.07
7	0.82	0.18
8	0.86	0.14
9	0.91	0.09
10	0.80	0.20
11	0.89	0.11
12	0.83	0.17
13	0.87	0.13

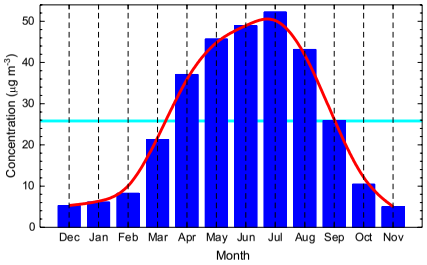

Figure S1. Overall distribution of monthly median O_3 concentrations averaged over the whole measurement interval. The horizontal line in cyan indicates the overall annual mean concentration of 26 μg m^{-3}, and the smooth curve in red serves to guide the eye.

Paper III

https://doi.org/10.5194/amt-2023-77
Preprint. Discussion started: 25 May 2023

Atmospheric Measurement Techniques Discussions

Challenges and solutions in determining dilution ratios and emission factors from chase measurements of passenger vehicles

Ville Leinonen[1], Miska Olin[2], Sampsa Martikainen[2], Panu Karjalainen[2], and Santtu Mikkonen[1,3]

[1]Department of Technical Physics, University of Eastern Finland, Kuopio, Finland.
[2]Aerosol Physics Laboratory, Tampere University, Tampere, Finland.
[3]Department of Environmental and Biological Sciences, University of Eastern Finland, Kuopio, Finland.

Correspondence to: Ville Leinonen (ville.j.leinonen@uef.fi)

Abstract. Vehicle chase measurements used for studying real-world emissions apply various methods for calculating emission factors. Currently available methods are typically based on the dilution of emitted carbon dioxide (CO_2) and the assumption that other emitted pollutants dilute similarly. A problem with the current methods arises when the studied vehicle is not producing CO_2, e.g., during engine motoring events, such as on downhills. This problem is also encountered when studying non-exhaust emissions, e.g., from electric vehicles. In this study, we compare multiple methods previously applied for determining the dilution ratios. Additionally, we present a method applying Multivariate Adaptive Regression Splines and a new method called Near-Wake Dilution. We show that emission factors calculated with both methods are in line with the current methods with vehicles producing CO_2. In downhill sections, the new methods were more robust to low CO_2 concentrations than some of the current methods. The methods introduced in this study can hence be applied in chase measurements with changing driving conditions and be possibly extended to estimate non-exhaust emissions in the future.

1 Introduction

Anthropogenically emitted gaseous compounds and particulate matter have effects on both climate and human health (Forster et al., 2021; Lelieveld et al., 2015). Vehicle emissions contribute to a significant proportion of those emissions, especially in urban environments. Vehicle emissions are regulated in legislation but the regulation even for new vehicles is still under development and the new regulations do not completely cover the existing fleet. Fulfilling the regulation requirements is controlled in periodical technical inspection (PTI) of vehicles but the inspection protocol is limited to a few parameters, and, for example, the particle number (PN) is accounted only in some forerunner countries. Additionally, regarding particle emission regulations, only a fraction of the total emission is regulated. The limits for PN only consider nonvolatile particles, and the particle mass (PM) formed from the precursor gases via nucleation and condensation as the exhaust gas dilutes and cools upon exiting the tailpipe is mostly neglected. The amount of particle matter (both in terms of PN and PM) formed this way can be considerable (Karjalainen et al., 2014b; Keskinen and Rönkkö, 2010; Kittelson, 1998; Giechaskiel et al., 2007).

https://doi.org/10.5194/amt-2023-77
Preprint. Discussion started: 25 May 2023

A variety of measurement methodologies exist for studying emissions: official type-approval tests (that depend on the local legislation) are typically conducted by driving a predetermined driving cycle on a chassis dynamometer. In Europe, Portable Emission Measurement System (PEMS) protocol is also included for in-use compliance testing since 2016 (European Commission, 2016) including NOx, PN, and CO emissions in real drive. NOx emissions must be measured on all Euro 6 vehicles—passenger cars and light-commercial vehicles. On-road PN emissions are to be measured on all Euro 6 vehicles which have a PN limit set (diesel and GDI). CO emissions also must be measured and recorded on all Euro 6 vehicles. RDE emission limits (Emission Standards: Europe: Cars and Light Trucks: RDE Testing, 2023) are defined by multiplying the respective emission limit by a conformity factor (CF) for a given emission.

Remote sensing methods, such as snapshot measurements in fixed locations, or chasing vehicles with a mobile measurement unit sampling the diluted exhaust aerosol, are used for academic purposes (Karjalainen et al., 2014a; Simonen et al., 2019; Wang et al., 2010; Ježek et al., 2015b; Herndon et al., 2005; Shorter et al., 2005; Wang et al., 2017; Park et al., 2011; Pirjola et al., 2004). These methods have potential for elaborate use and could also be applied in monitoring vehicles fulfilling the regulation requirements.

The chase method has the considerable advantage of subjecting the exhaust aerosol to a real atmospheric dilution. The advantage of chase method is that the measured aerosol corresponds to the actual emission of the vehicle and not only a fraction (e.g., primary emissions only); however, the prevailing ambient conditions can strongly affect the particle formation, which is simultaneously an asset but also a drawback. On one side, this is the real particle population that is formed at a given time causing the immediate air quality effects, but on the other side, the method is hence not very repeatable between different testing conditions with respect to semi-volatile particle number and size. Additionally, the chase method is fast, and the individual measurement of vehicle's emission factor could be carried out in a minute time scales (Olin et al., 2023).

There exist several methods for calculating an emission factor (EF) from chase measurements (Hansen and Rosen, 1990; Zavala et al., 2006; Wihersaari et al., 2020; Ježek et al., 2015a). These methods are based on the CO_2 produced by the engine and on the assumption that all emitted components dilute similarly to CO_2. Downhill is problematic since engines do not generally inject fuel there because of no need for providing mechanical power (called engine motoring), and hence do not emit CO_2. However, previous studies (Rönkkö et al., 2014; Karjalainen et al., 2014a, 2016) suggest that engine motoring events can emit nanoparticles, originating from the lubricating oil. The chase vehicle observes these elevated concentrations in the plume, but it is difficult to assess the EF of the vehicle under measurement since the dilution ratio (DR) calculated with CO_2 is not available. In addition, most of the current methods have been used for a longer time interval, whereas short time interval EFs of accelerating and braking might be more interesting for studying. Also, a specific need to calculate EFs without CO_2emissions is when studying non-exhaust emissions (e.g., particulate emissions from tires and brakes). In the future, when the fraction of

https://doi.org/10.5194/amt-2023-77
Preprint. Discussion started: 25 May 2023

electric passenger vehicles is increasing, the research interest might shift towards non-exhaust emission. The new methods introduced in this study could be useful for estimating non-exhaust emission factors as well.

In this study, we will compare different calculation methods for EFs of vehicles based on chase measurements: particle number concentration (N) to CO_2 concentration ratio -based methods (Hansen and Rosen, 1990; Zavala et al., 2006; Olin et al., 2023), a method that calculates the raw particle number concentration, N_{raw}, based on DR (Wihersaari et al., 2020), and two new methods to be introduced in this paper, based on Near-Wake Dilution and Multivariate Adaptive Regression Splines for DR in a remote-sensing-type chase measurement setting. Most of the methods used in this study can also be applied for snapshot-type measurements where DR needs to be defined. Our aim is to improve EF calculation, especially for short time intervals with variable DR, by achieving better understanding about the variables that affect DR. The new methods are both based on the DR-modelling approach: using the DR calculation of the CO_2-based methods for the time periods when they work properly. We then extend the models to the whole measurement period by either using physical method (Near-Wake Dilution) or statistical method (Multivariate Adaptive Regression Splines) to estimate the DR for all measurement time points. We then compare the results from the new methods to the current methods for longer time intervals and separately for downhill sections. We also calculate DR and EF using only data from remote sensing measurements, without additional information on the measured vehicle, such as on-board diagnostics (OBD) data (i.e., from the chase measurements). Development of this kind of methods are crucial if remote sensing measurements are applied on on-road monitoring of vehicle emissions, as suggested by, e.g., the European H2020-project CARES (https://cares-project.eu/).

2 Methods

2.1 Experiments

Particle number concentrations and CO_2 concentrations in exhaust plumes of six passenger vehicles (three diesel and three gasoline) were measured with the chase method during wintertime, in February in Siilinjärvi, Finland (Figure 1). The time and the location were selected because the main purpose of the measurement campaign was in studying wintertime real-world vehicle emissions, which is in the scope of future studies, applying methods introduced in this publication. The measurement instruments were installed inside the mobile laboratory of Tampere University (Aerosol and Trace gas Mobile Laboratory, ATMo-Lab, Simonen et al. (2019); Rönkkö et al, (2017)). Data from the OBD and GPS from the test vehicles were saved at a 1 second time resolution (Figure 2). The chase route 1) was 13.8 km long including uphill and downhill driving, stops, accelerations and steady drive, also artificial short stops to simulate traffic lights. The route selection was based on bearing two major principles in mind. On one hand, there was a fuel station as a starting point with enough space for parking the test vehicles overnight, connection to electric grid to be used with electrical preheaters, and spaces were regularly cleared of snow. On the other hand, the station was located close to roads ideal for tests: they were in good condition and were maintained well

https://doi.org/10.5194/amt-2023-77
Preprint. Discussion started: 25 May 2023

during winter, and the traffic rates were very low implying that the background exhaust plumes are negligible. The route was also well suited for this study, because it included steep and long downhill sections.

The test protocol included a short period of engine idling at the beginning, driving the route, two predetermined stops and finishing the route at the start location. The time stamps of passing vehicles and other possible external emission sources were recorded during the drives.

Information about the vehicles, individual drives and outside temperatures are shown in Table 1. During the test period of four days, the outside temperature varied between -9 and -28 °C. The fleet included three (Euro 5-6) diesel vehicles (two passenger cars and one van) and three (Euro 6) gasoline vehicles (passenger cars). The number of measured drives totaled 33; in addition, there was a drive for every measurement day for measuring ambient background concentrations along the route. 11 drives were dedicated to subfreezing–cold start (cold start in subfreezing temperatures) measurements, 12 to preheated–cold start measurements (using electric preheaters or fuel-combusting auxiliary heaters), and 10 to hot start measurements (the engine had been heated to its normal operating temperature by driving).

Figure 1. Driving route consisting of low-traffic small roads in Siilinjärvi, Finland. The colored line indicates an example drive with the speed profile (color). Start and stop locations were the same position on a parking lot of a local fuel station. Two artificial short

https://doi.org/10.5194/amt-2023-77
Preprint. Discussion started: 25 May 2023

stops were introduced along the test route to simulate traffic lights. Downhills that are used in the results section are indicated by white lines on the side of the route marking. Source: Earthstar Geographics.

2.2 Measurement setup

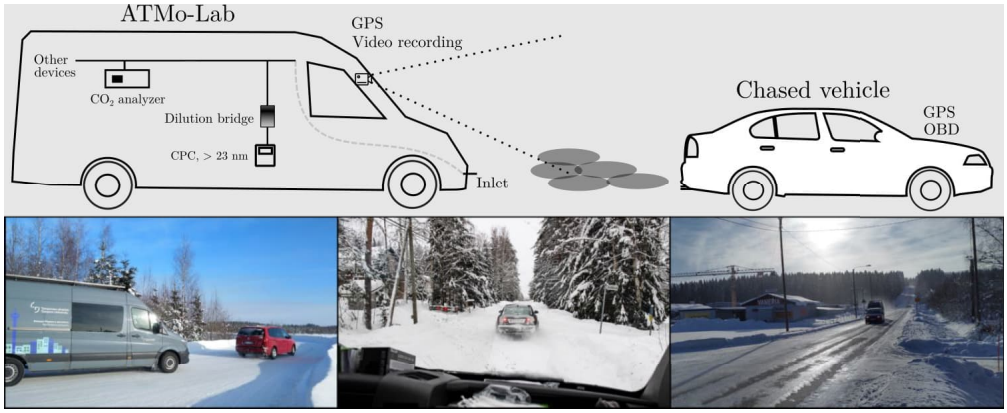

Figure 2. Schematic view of the measurement setup used in this study and example photos from the chasing route for illustration of the chasing measurements. In addition, other devices were installed but their data were not used in this study.

The measurement setup, including only the devices of which data are involved in this study, is presented in Figure 2. The number concentration of particles larger than 23 nanometers in diameter (N) was measured with an Airmodus model A23 condensation particle counter (CPC) and the CO_2 concentration with a LI-COR LI-840A analyzer. The exhaust sample was drawn to the instruments through a sampling inlet installed on the front bumper of the vehicle. Before the CPC, the sample was diluted with a set of bifurcated flow diluters (DR=158±14). The drives were also recorded with a video camera installed on the windshield and the location of the ATMo-Lab was recorded using GPS. OBD data from the chased vehicle were collected using OBDLink LX Bluetooth device (OBDLink® LX - Top-Notch Scan Tool Compatible With Motoscan, 2023). All the devices were recording data with one second time resolution, which was averaged to the time resolution five second. Averaging makes the data more robust to small (1-2 sec) time differences between measurements from the vehicle (OBD) and variables measured with ATMo-Lab.

Table 1: Information on the studied vehicles.

Vehicle	Fuel	Registration year	Engine displacement (l)	Emission class	Odometer reading (km)	Number of drives

https://doi.org/10.5194/amt-2023-77
Preprint. Discussion started: 25 May 2023

Audi A6	Diesel	2008	3.0	Euro 5	236,000	6
Seat Alhambra	Diesel	2012	2.0	Euro 5	169,000	6
VW Transporter	Diesel	2019	2.0	Euro 6	36,000	4
Ford Focus	Gasoline	2018	1.0	Euro 6	78,000	5
Skoda Octavia 1.0	Gasoline (MHEV)	2020	1.0	Euro 6	1,000	6
Skoda Octavia 2.0	Gasoline	2019	2.0	Euro 6	21,000	6

2.3 Methods for calculating EF

The methods we use are mostly modeling DR and observed differences between measured and background concentrations and based on those calculating the EF of a vehicle. Used methods (introduced more in detail in the following subsections) for calculating EF can be divided into four categories based on whether the OBD data is used in the method and whether the method needs some additional (hereafter learning) data from other vehicles to evaluate the effect of some variables (e.g., speed change) to the emissions. Table 2 shows all the methods used in this study. All methods are introduced in the following subsections 2.3.1-2.3.7. Table 3 summarizes the main differences of the methods described in subsections 2.3.1-2.3.7 and shows the formulas used to calculate the EF in each of the methods.

The dataset used in this study was limited to considering only times when the chased vehicle was moving, i.e., its speed was positive. Also, the effect of chase distance, i.e., the distance between the chased vehicle and ATMo-Lab, was assumed to be constant, not affecting the dilution ratio of emission.

Table 2: Division of the methods for calculating EF of a vehicle. OBD data means the data collected from the chased vehicle (see also Figure 2) and learning data means the data collected from other drives of the same vehicle and from other vehicles (including data from ATMo-Lab and, also from OBD if its data is used). Methods are introduced in more detail in subsections 2.3.1-2.3.7.

		Uses learning data: yes	Uses learning data: no
Uses OBD data	yes	MARS-OBD, NWD	N/CO_2 integral, N/CO_2 linear, N/CO_2 RRPA, N_{raw}

https://doi.org/10.5194/amt-2023-77
Preprint. Discussion started: 25 May 2023

no	MARS-chase	N/CO_2 Traficom

Methods that require data to be fitted before applying into DR estimation or EF calculation were fitted using DR calculated from N_{raw} method as a response variable. Only the data from the times with exhaust mass flow rates (Q) exceeding $0.3\ g\ s^{-1}$ and fuel flow rates exceeding $0.02\ g\ s^{-1}$ were used in forming models, which were then used for the whole data also including the times with the flow rates below those limits.

Other methods of modeling DR (NWD and MARS-methods, described below) are based on the observed linear or non-linear dependencies between DR and explanatory variable(s). These methods assume that the factors affecting DR measured in the situations where the measured vehicle is not in the engine motoring mode can be extrapolated also to situations with the motoring mode. Hence, for the downhill sections, the following methods do not calculate the DR based on the measured CO_2; instead, they use other parameters not based on CO_2 (some examples include vehicle speed v_t, exhaust flow rate Q and the vehicle rear shape) to estimate the DR.

For calculating EF and its uncertainty, bootstrap sampling (Efron, 1979) has been used to estimate the uncertainty in EF calculations. A bootstrap sample is a random sample of observations (observation = time point) with replacement, i.e., one observation can occur multiple times in a bootstrap sample. The analysis, e.g., fitting the model and calculating the EF is performed for this bootstrap sample. Multiple bootstrap samples are usually taken, here 100 is the number of samples.

Bootstrap helps to estimate the whole uncertainty, in this case the uncertainty related to e.g., differences in vehicle driving profile, possible uncertainties in time allocation, and uncertainty in model fitting. Bootstrap is useful when estimating complex estimators or their uncertainty, without (here) explicitly estimating uncertainties of single sources of uncertainty and covariance structure of uncertainties.

Table 3: Summary of the methods used in this study. Formulas to calculate EF, main differences to other methods, and references to the literature describing the method. Methods are introduced in more detail in subsections 2.3.1-2.3.7.

https://doi.org/10.5194/amt-2023-77
Preprint. Discussion started: 25 May 2023

Atmospheric Measurement Techniques Discussions

Method	Formula to calculate EF	Differences to other methods	Reference
Methods using fraction of N and CO2			
N/CO_2 integral (subsection 2.3.1)	$\frac{\int_t[N_t^{meas} - N^{bg}]dt}{\int_t[CO_{2,t}^{meas} - CO_2^{bg}]dt} * \frac{a_{\frac{g}{cm^3}}^{ppm} * a_{g_{fuel}}^{gCO_2} * m_{fuel}}{s_{drive}}$	m_{fuel} is taken from OBD measurements of the vehicle. For other terms of the formula, see subsection 2.3.1.	Hansen and Rosen (1990)
N/CO_2 Traficom (2.3.2)	$\frac{\int_t[N_t^{meas} - N^{bg}]dt}{\int_t[CO_{2,t}^{meas} - CO_2^{bg}]dt} * \frac{a_{\frac{g}{cm^3}}^{ppm} * a_{g_{fuel}}^{gCO_2} * m_{fuel}}{s_{drive}}$	m_{fuel} is taken from Finnish national database for vehicles (Traficom), otherwise as N/CO_2 integral.	This study
N/CO_2 linear (2.3.3)	$\frac{\Delta N}{\Delta CO_{2_{linear}}} * \frac{a_{\frac{g}{cm^3}}^{ppm} * a_{g_{fuel}}^{gCO_2} * m_{fuel}}{s_{drive}}$	Ratio of N and CO_2 ($\frac{\Delta N}{\Delta CO_{2_{linear}}}$) is estimated using the linear model to the background corrected values of N and CO_2. Otherwise as N/CO2 integral.	Zavala et al. (2006)
N/CO_2 RRPA (2.3.4)	$\frac{\Delta N}{\Delta CO_{2_{RRPA}}} * \frac{a_{\frac{g}{cm^3}}^{ppm} * a_{g_{fuel}}^{gCO_2} * m_{fuel}}{s_{drive}}$	Ratio of N and CO_2 ($\frac{\Delta N}{\Delta CO_{2_{RRPA}}}$) is estimated using the robust linear model to the measured values of N and CO_2 without background correction. Otherwise as N/CO_2 integral.	Olin et al. (2023)
Methods using dilution ratio			
N_{raw} (2.3.5)	$\frac{\int_t[(N_t^{meas} - N^{bg}) * DR_{N_{raw},t} * Q_t]dt}{\rho_{exh} * \int_t v_t\, dt}$	Dilution ratio ($DR_{N_{raw},t}$) is calculated based on measured dilution of CO_2. For other terms of the formula and details, see subsection 2.3.5.	Wihersaari et al. (2020)

https://doi.org/10.5194/amt-2023-77
Preprint. Discussion started: 25 May 2023

Atmospheric Measurement Techniques Discussions

Near-Wake Dilution (NWD, 2.3.6)	$\frac{\int_t[(N_t^{meas} - N^{bg}) * DR_{NWD,t} * Q_t]dt}{\rho_{exh} * \int_t v_t\, dt}$	Dilution ratio $DR_{NWD,t}$ is calculated based on a linear function of the ratio of the vehicle speed v_t and the mass exhaust flow rate Q_t. See subsection 2.3.6 and Supplement for more details. Otherwise as N_{raw}.	This study
MARS-OBD (2.3.7)	$\frac{\int_t[(N_t^{meas} - N^{bg}) * DR_{MARS-OBD,t} * Q_t]dt}{\rho_{exh} * \int_t v_t\, dt}$	Dilution ratio $DR_{MARS-OBD,t}$ is calculated based on Multivariate Adaptive Regression Spline (MARS) model for DR. See subsections 2.3.7 and 3.2 for more details. Otherwise as N_{raw}.	This study
MARS-chase (2.3.7)	$\frac{\int_t[(N_t^{meas} - N^{bg}) * DR_{MARS-chase,t} * Q_{MARS-chase,t}]dt}{\rho_{exh} * \int_t v_t\, dt}$	Dilution ratio $DR_{MARS-chase,t}$ is calculated based on Multivariate Adaptive Regression Spline (MARS) model for DR. Variables available from ATMo-Lab (i.e., no OBD data) are used. Also, the exhaust flow rate ($Q_{MARS-chase,t}$) is estimated using splines. See subsections 2.3.7 and 3.2 for more details. Otherwise as N_{raw}.	This study

2.3.1 N/CO_2 integral

The simplest method to calculate EF is based on N/CO_2 measured from the diluted exhaust. The method was introduced by Hansen and Rosen (1990) and has been widely used thereafter. It is based on the relation of the excess CO_2 ($\Delta CO_2 = CO_{2,t}^{meas} - CO_2^{bg}$) and particle concentration ($\Delta N = N_t^{meas} - N^{bg}$). Here the superscripts meas and bg denote measured and background concentrations, respectively. Here *t* denotes that the measured concentrations have been measured specifically at time *t*, whereas the background concentrations have been defined as a median of the background measurement measured at the same route on the same day. However, the method by Hansen and Rosen, (1990) uses the following integral form (over a longer measurement period than, e.g., one second) to diminish possible uncertainties caused by imperfect time synchronizations of the devices measuring CO_2 and the studied pollutant:

https://doi.org/10.5194/amt-2023-77
Preprint. Discussion started: 25 May 2023

$$EF_{\Delta N/\Delta CO_2} = \frac{\int_t [N_t^{meas} - N^{bg}]dt}{\int_t [CO_{2,t}^{meas} - CO_2^{bg}]dt} * \frac{a_{\frac{g}{cm^3}}^{ppm} * a_{g_{fuel}}^{gCO_2} * m_{fuel}}{s_{drive}} \quad (1)$$

where CO_2 concentrations are in ppm and particle concentrations in 1 cm^{-3}. a_{g/cm^3}^{ppm} is the conversion factor for CO_2 from ppm to g cm^{-3} ($10^6/0.0018 = 5.55*10^8$, where 10^6 is a number of molecules and 0.0018 is the approximate density of CO_2 [g cm^{-3}] at 20 °C), $a_{g_{fuel}}^{gCO_2}$ is the conversion factor for g_{CO_2} to g_{fuel} (2392/750 = 3.189 for gasoline and 2640/835 = 3.162 for diesel, where the 2392 and 2640 are the approximate masses of CO2 produced [g] per liter of fuel for gasoline and diesel respectively (Conversion Guidelines-Greenhouse gas emissions, 2023) and 750 and 835 are the approximate densities [g] of a fuel [$g\ l^{-1}$) for gasoline and diesel, respectively. Those densities are within the ranges of densities provided by one major fuel supplier in Finland (Neste Futura 95E10 Technical Data Sheet, 2023; Neste Futura Diesel -29/-38 Technical Data Sheet, 2023)). Variable m_{fuel} is the mass of the used fuel (in g, from OBD data) and s_{drive} is the length of the drive (in km). In this study, EF is calculated over the whole measurement period and EF is expressed in 1 km^{-1}. This method (and all other N/CO_2 method versions) is based on the assumptions that CO_2 and the pollutant dilute equally in an exhaust plume and that the amount of emitted CO_2 is directly related to the fuel consumption. Whereas the N/CO_2 integral method is robust to imperfect time synchronizations and to the engine motoring events (because the integral in the denominator never becomes very small, unlike in cases with, e.g., one-second resolution), the method, however, assumes also that EF is constant during the integration time period in chase measurements (Olin et al., 2023).

2.3.2 N/CO_2 Traficom

The N/CO_2 Traficom method is calculated similarly to N/CO_2 integral method, over the whole measurement period, but the fuel consumption m_{fuel} is estimated from the national vehicle database (Traficom) instead of using actual consumption from OBD. Using the fuel consumption estimation from the register plates makes the method independent from OBD-data, i.e., the method can be calculated directly based on the measurement data from ATMo-Lab. This kind of a method, that is not using OBD-data, is suitable, e.g., for real-world emission monitoring approaches for private vehicles driving on public roads. We have used constant fuel consumptions reported for combined driving (combining urban and extra-urban driving) that are between 4.6 (Ford) and 7.6 (VW) liters of fuel per 100 km.

2.3.3 N/CO_2 linear

The N/CO_2 linear method used, e.g., by Zavala et al. (2006) was also tested in this study. The method estimates N/CO_2 by fitting a line for ΔN and ΔCO_2. The slope of that line is used to replace the first fraction term in Eq. (1) when calculating EF. The used linear model has an assumption that the line passes the origin, i.e., with no emitted CO_2, no particles are emitted. Therefore, non-exhaust particles are not counted. This method also assumes that EF is constant during the time period used

https://doi.org/10.5194/amt-2023-77
Preprint. Discussion started: 25 May 2023

for fitting. However, as the drives cannot be assumed to have constant EF due to multiple different sections of driving, the linear model is fitted separately to one-minute time periods, in which the vehicle can be assumed to have more constant EF throughout the period. For the periods when the slope is estimated to be negative, the EF is set to zero.

2.3.4 N/CO_2 RRPA

The RRPA (Robust Regression Plume Analysis) method presented in (Olin et al., 2023) is based on the N/CO_2 linear method but without no need to determinethe background concentrations of N and CO_2 Similarly to N/CO_2 linear method, the slope is used to replace the first fraction term in Eq. (1) when calculating EF.

Contrary to the N/CO_2 linear method, this method uses robust linear model (in this study using *rlm*-function in R environment (R Core Team, 2022)) for fitting the line. We used robust linear regression instead of ordinary least squares approach because the data contains varying number of datapoints which can be considered as outliers, in statistical point of view, and those could bias the fit for the slope in ordinary least squares estimation (Mikkonen et al., 2019). The robust regression automatically downweighs the possible outliers by giving less weight to the data points that are not close to the estimated line. Hence, momentary disturbances (such as from other pollutant sources near the measurement location) should not disturb the estimation of the slope. As for the N/CO_2 linear method, the N/CO_2 RRPA method assumes constant EF for the fitted period and is also fitted to a one-minute time periods. For the periods when the slope is estimated to be negative, the EF is set to zero.

2.3.5 N_{raw}

A bit more advanced method (based on the method by Wihersaari et al. (2020)) to calculate DR and EF is using the measured and raw concentrations of CO_2 and using the exhaust mass flow rate (Q):

$$DR_{N_{raw},t} = \frac{CO_{2,t}^{raw} - CO_2^{bg}}{CO_{2,t}^{meas} - CO_2^{bg}} \quad (2)$$

$$EF_{N_{raw}} = \frac{\int_t [(N_t^{meas} - N^{bg}) * DR_{N_{raw},t} * Q_t] dt}{\rho_{exh} * \int_t v_t dt} \quad (3)$$

where $N_t^{meas}$is the measured particle number concentration, N^{bg} is the estimated background particle number concentration, $CO_{2,t}^{raw}$ is the concentration of CO_2 in the raw exhaust (calculated from the OBD data), ρ_{exh} is the exhaust density (air density at the standard temperature of 20 °C used here), and v_t is the vehicle speed. We denote the method as N_{raw} method from here onwards. This method can be thought of as the best performing model in a real-world chasing situation with varying EF and DR. However, this method requires well-synchronized data. Five second time resolution was used, as it is not so prone to errors caused, e.g., by engine motoring events.

https://doi.org/10.5194/amt-2023-77
Preprint. Discussion started: 25 May 2023

225 **2.3.6 Near-Wake Dilution (NWD)**

In the NWD method, we are building a robust linear model for DR as a linear function of the ratio of the vehicle speed v_t and the mass exhaust flow rate Q , taking also into account the shape of the vehicle's rear and the fuel used. The method is based on the assumption that the outdoor air passing by the vehicle's rear while driving dilutes the exhaust plume and that the dilution is proportional to the ratio of the mass flows passing the rear and exhausted from the tailpipe (Chang et al., 2012) . The method
230 minimizes the weighted linear model (iterated reweighted least squares robust regression):

$$DR_{NWD,t} = \gamma + \kappa \frac{v_t}{Q_t} \quad (4)$$

where dilution ratio at time t (DR_t) used to fit the model is calculated from the OBD chase measurement data as in the N_{raw} method (Eq. (2)). Parameters γ and κ are coefficients fitted for every vehicle measured in this study. More detailed derivation of the formula and detailed discussion about the possible variables that are related to the parameters γ and κ are presented in
235 the Supplement. The NWD model is fitted separately for each vehicle, except when the data from the studied vehicle is not used to fit a model (Fig. 6). In that case, the rear shape has been used as a categorical variable for the five-vehicle data to fit the NWD model. Categorical variables b_1 and b_2 estimate the effect of different rear types on DR: $DR_{NWD,t} = \gamma + b_1 + (\kappa + b_2)\frac{v_t}{Q_t}$.

As the model is only dependent on the speed and exhaust flow, the model assumes that the distance from the vehicle remains
240 constant and is independent of the speed (the effect of the distance is incorporated into the kappa and gamma parameters). Constant driving distances were tried to maintain during these chase measurements. DR is calculated for all datapoints using the modeled dependency (presented later in Fig. 3).

EFs with the NWD method were then calculated similarly to the N_{raw} method in formula (3), with different method to calculate the dilution ratio being the only difference between methods. The NWD method is robust to engine motoring events because
245 the CO_2 concentration is not involved in the equation used to calculate EF (after fitting the kappa and gamma parameters). In addition, the method can possibly be used to determine non-exhaust emissions as well.

2.3.7 Multivariate Adaptive Regression Splines (MARS)

We used Multivariate Adaptive Regression Splines (MARS: Friedman, 1991; Hastie et al., 2009) to model the dependency of DR on certain variables that could affect the dilution of exhaust, I.e. vehicle exhaust flow rate, speed, speed change
250 (acceleration), altitude change, and direction of wind.. Besides variables that are fitted with splines, two categorial variables describing the rear shape and fuel type used in the vehicle were used. Those categorical variables affect only the level, not the shape of the spline (see Fig. 4).

https://doi.org/10.5194/amt-2023-77
Preprint. Discussion started: 25 May 2023

To avoid overfitting, i.e., that the model fits well to the learning data but is not generalizable to any new dataset, we used 5-fold cross-validation (Hastie et al., 2009). In 5-fold cross validation, the dataset is divided into five distinct subsets of the same size. Then four of those subsets are used to train the model (training dataset) and one is used to test the fit of the model to new dataset (testing dataset). This is repeated five times, so that each subset is once used as a testing dataset.

We built two methods based on MARS: one is based on all variables (OBD-data and the data from chase measurement; a method called MARS-OBD), and the other one is based on the measured data consisting only variables that are available with remote sensing methods (a method called MARS-chase).

EFs from the MARS methods were calculated similarly to the N_{raw} method (formula (3)), with the only difference to N_{raw} in how the DR is calculated. As for NWD, DR is calculated for all datapoints using the modeled dependency (presented later in Fig. 4). MARS models are also robust for engine motoring events or even for non-exhaust emissions, like the NWD model, because the CO_2 concentration is not used (after the model construction). In addition, the MARS-chase model can be used in real-world emission monitoring approaches.

3 Results and discussion

3.1 Fitting the NWD model parameters

Our results indicate that DR can be approximated with linear function of the ratio of v_t and Q; hence, it was used as one method to estimate DR. Figure 3 shows the robust linear regression fits between DR and $\frac{v_t}{Q}$.

According to the results, in addition to $\frac{v_t}{Q}$, we suppose that modelled DR is mostly affected by the rear shape of the vehicle (included in the parameter κ). Generally, the values of $\frac{v_t}{Q}$ are higher for the gasoline vehicles compared to the diesel vehicles, due to lean burn combustion used in diesel engines. This results also in higher values of DR (determined with Eq. (2)) for the gasoline vehicles.

https://doi.org/10.5194/amt-2023-77
Preprint. Discussion started: 25 May 2023

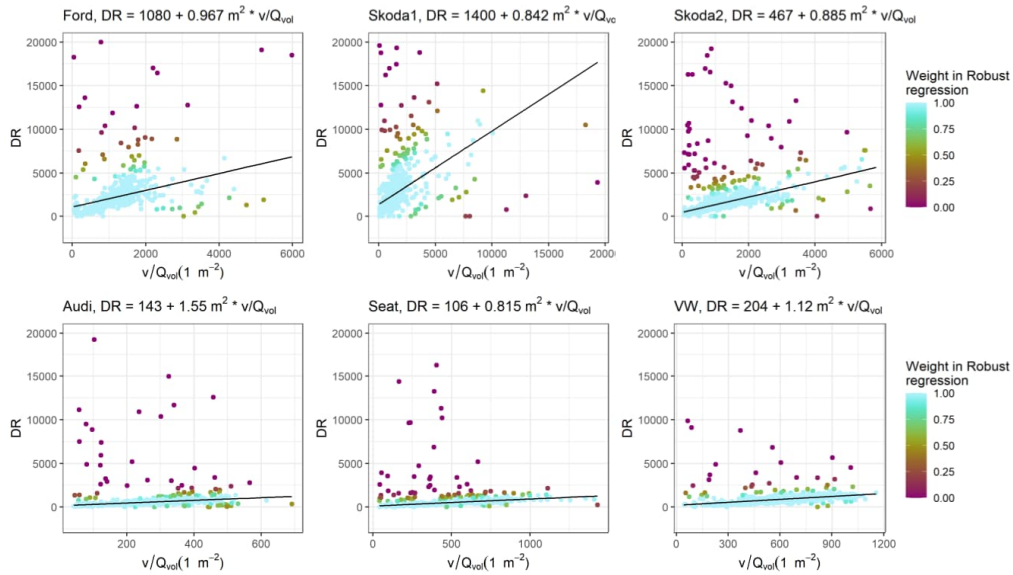

Figure 3. Robust linear regression fits for DR for each vehicle used in NWD method. The color represents the weight of the observation in the final robust linear fit. The equations of the linear fits are shown in the titles of each subplot. Volumetric exhaust flow rate $Q_{vol} = \frac{Q}{3.6 \cdot \rho_{fuel}}$ has been used in this figure instead of the mass flow rate used elsewhere, because the NWD model is based on the volumetric flows.

3.2 Constructing the MARS models

Figure 4 shows the behaviour of the splines in the measured data between DR and the predictor variables used in the MARS models. The shape of the splines is the same for all vehicles, as it is defined from the full dataset, but the level varies due to different properties of the vehicles, such as fuel and presumably the rear shapes.

The variables used in the models shown in Fig. 4 are organized so that the variables in the upper row are for the method using also the OBD-data from the chased vehicle (MARS-OBD) and the variables in the lower row are for the method using only variables from ATMo-Lab (MARS-chase). With the MARS-OBD method, changes in Q explain most of the changes observed in DR, and the dependency of Q on DR is as expected from the concept behind the NWD model. In addition to Q, wind component calculated abeam of the vehicle was seen to affect the DR, but the effect is very minor. Unlike in the MARS-chase method, variables such as speed change and altitude change were not needed (based on their effect on the model fit, measured

https://doi.org/10.5194/amt-2023-77
Preprint. Discussion started: 25 May 2023

Atmospheric Measurement Techniques Discussions
Open Access
EGU

with R^2 values) in the MARS-OBD method, which indicates that the changes in Q (and slightly in the lateral wind speed) sufficiently explain most of the changes in DR.

For the MARS-chase method, the effect of Q was replaced by using several variables that could explain the power generated by an engine – and thus Q. The result seems to be in line with theory, the most evident changes to DR being caused by changes in driving speed (e.g., when accelerating) and altitude (e.g., when driving uphill), and the absolute speed of a vehicle (due to air drag). Observed dependencies of those variables with DR were described with piecewise linear splines with one or two threshold values (knots). The effect of changes in speed and altitude were close to linear. The effect of v_t was not linear, as the DR had its minimum after threshold speed slightly higher than 10 m/s.

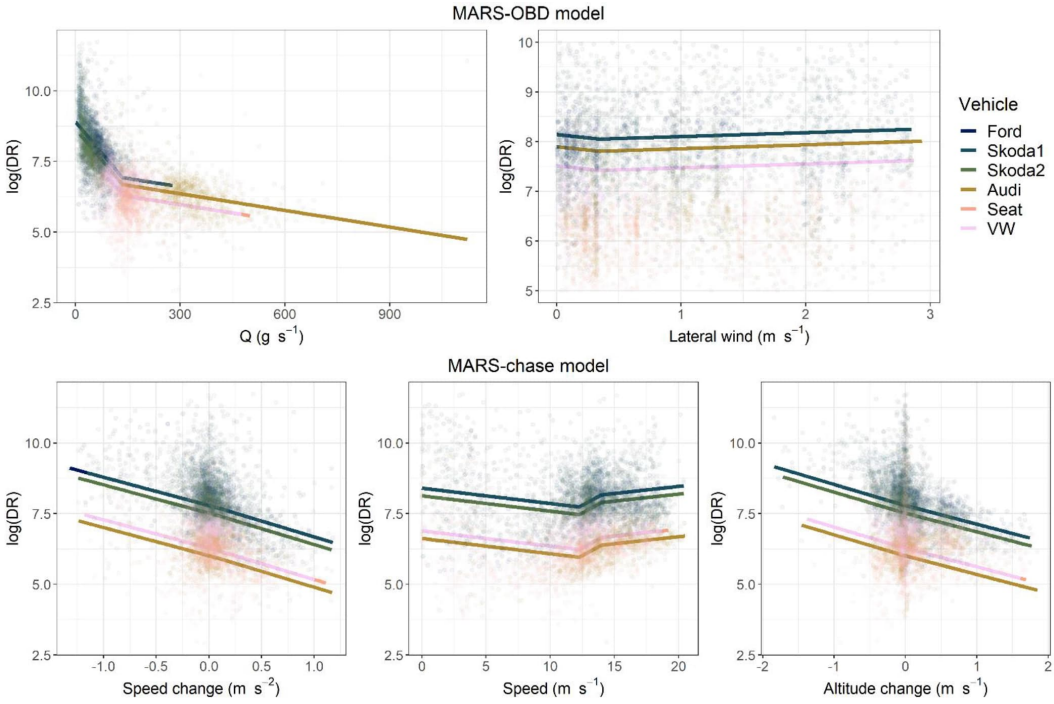

Figure 4. Multiple adaptive regression spline fits for logarithm (natural) of DR shown for each variable used in MARS-OBD (upper row) and in MARS-chase (lower row). Measurement points are colored based on the vehicle used. Different colored lines show the regression splines for each vehicle (see also categorical variables in the method description section 2.3.7), with some splines overlapping with each other.

https://doi.org/10.5194/amt-2023-77
Preprint. Discussion started: 25 May 2023

3.3 Comparison of the EF calculation methods for the whole drive

When the calculated DR estimates were applied on the EF calculation for the whole drive, it was seen that the results are mostly similar with all methods. Figure 5 illustrates how the calculated EF varies with different methods when applied on two different vehicles, one with gasoline and one with diesel engine, on two different drives with varying outside temperature.

The results in Figure 5 give confidence on EF calculation with varying information in use, as the methods with different background information end up mostly to within an order of magnitude. This is specifically good news for monitoring-type measurements, to be performed on-road, having limited information on the monitored vehicle. However, there can still be some notable differences between the methods, for example the difference of a factor of 2-3 between the N_{raw} and other methods for Skoda2 –24 °C. The clearest anomalies from the consensus of EF are N/CO_2 RRPA for the Skoda2 –26 °C drive being 25 to 45 % of the EFs given by other methods than N_{raw} and N/CO_2 linear, and N_{raw} method for both Skoda2 drives showing 2 to 4.2 times higher EFs than most of the methods (other than N/CO_2 linear and N/CO_2 RRPA). For RRPA some of the one-minute interval EFs were estimated to be zero, which probably explains the lower EFs calculated for that method. For N_{raw} method, the difference comes from the time points where dilution ratio is estimated to be larger, e.g., in NWD and MARS-models, i.e., points clearly above modeled lines in Figs 3 and 4. If measured concentration of particles above background $N_t^{meas} - N^{bg}$ is high enough for those points, it results also high EF for that point.

https://doi.org/10.5194/amt-2023-77
Preprint. Discussion started: 25 May 2023

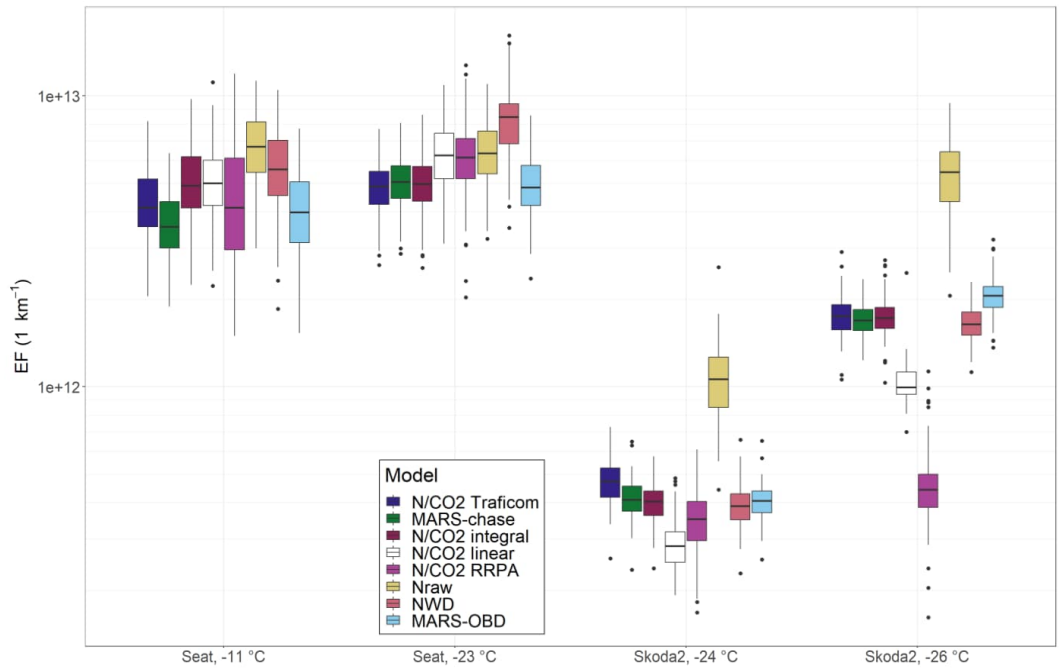

Figure 5. Emission factor examples of > 23 nm particles for Seat and Skoda 2, hot starts, except Seat –11 C that is with the subfreezing–cold start, and Skoda –26 C that is with the preheated–cold start. Results are calculated from 100 bootstrap samples (see Sect. 2.3 for the description of bootstrap sampling).

The methods that use learning data (the MARS methods and the NWD method, see Table 2) were validated with leave-one-out type cross-validation by omitting one of the vehicles from the model fitting and then by applying the fitted coefficients to predict the EFs for the omitted vehicle. The results are shown in Fig. 6, which confirms the findings in Fig. 5, that the constructed methods can calculate the EFs also for the vehicle omitted from the model construction. For the methods that don't use learning data (all N/CO_2 methods and the N_{raw} method), i.e., data from the other drives to form a model, the results are almost the same (bootstrap sampling can change the calculated EFs slightly) as in Fig. 5. For Skoda2, the MARS-chase method shows higher EF values than the other methods in Fig. 6. This is probably because the data measured with Audi (being the only vehicle having a similar rear shape to Skoda2) has been used in the MARS-chase model to estimate the effect of the rear shape on the DR (see Sect. 2.3.7 for categorical variables and Fig. 3 for the fits). However, using the data from a diesel vehicle

https://doi.org/10.5194/amt-2023-77
Preprint. Discussion started: 25 May 2023

in modelling DR for a gasoline vehicle may not work properly due to different dilution mechanics (as is also observed from the different fitting parameters obtained with using the NWD model)) even though the fuel type parameter for Skoda2 is different than for Audi. In addition, Audi is the only vehicle in this study having two exhaust pipes on both sides of the vehicle rear; therefore, the dilution mechanics may differ notably from the other vehicles. Thus, the rear shape parameter (constant categorial variable used to estimate the effect of the rear shape on DR) might have increased the estimated DR for Skoda2, and hence also the estimated EF. One solution for this issue would be to increase the sample size of the vehicles, probably leading to a better estimate for the rear shape of Skoda2 in the MARS-chase method. For Seat, the MARS-chase method gives similar results to the other methods; however, the NWD method gives slightly higher EFs than the other methods. This is due to imperfect modeling of dilution ratio of Seat based on the model from other five vehicles. This indicates that EFs could be calculated in-situ based on the measurements from ATMo-Lab and OBD, if the OBD data is required in the method. The increase in the number of vehicles in the learning data would probably increase the accuracy of the methods that require learning data, including the MARS-chase method as well.

https://doi.org/10.5194/amt-2023-77
Preprint. Discussion started: 25 May 2023

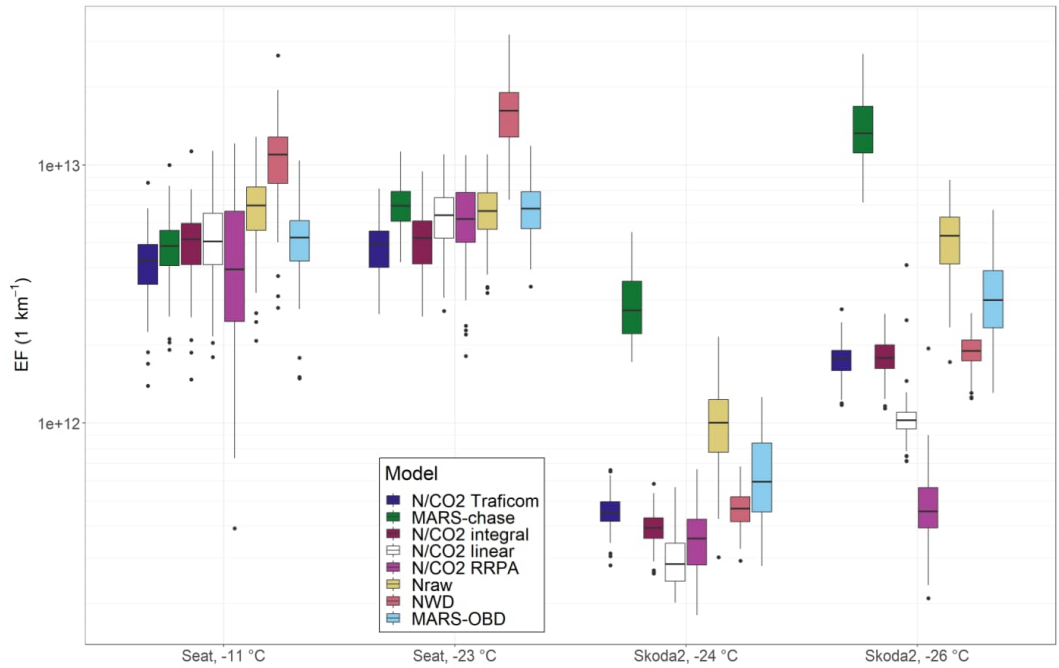

Figure 6. Emission factors for the drives of which data are omitted (details in Sect. 3.3) from the model construction (MARS-chase, NWD, MARS-OBD) for Seat and Skoda2, hot starts, except Seat –11 C that is with the subfreezing–cold start, and Skoda –26 C that is with the preheated–cold start. Results are calculated from 100 bootstrap samples (see Sect. 2.3 for the description of bootstrap sampling).

3.4 Comparison of the EF calculation methods for the downhill section

When examining how the different methods perform in different driving conditions, such as the change in the altitude, Fig. 7 shows that, overall, the methods agree quite well for Seat, but there are a lot of discrepancies for Skoda2. It is obvious why the N/CO_2 Traficom method overestimates the EFs during the downhill section: because the used fuel consumption refers to the combined driving fuel consumption data, i.e., to a much higher consumption than really occurs in downhills. In addition, the N_{raw} method gives relatively high estimates for EFs, especially for Skoda2. This is due to relatively low CO_2 values observed at the times with high particle emissions, resulting in higher DRs with the N_{raw} method compared to the other methods. N/CO_2 linear shows clearly lower EF values for Skoda2, similarly to, but less pronounced, in Figs. 5 and 6. For RRPA method, many of the EF estimates for bootstrap samples (89 out of 100 for Skoda2, -24 °C and 39 for Skoda2, -26 °C) are zero, i.e. for every minute interval (2 or 3 intervals in each bootstrap sample), the estimated linear dependency between N and CO_2 concentrations

https://doi.org/10.5194/amt-2023-77
Preprint. Discussion started: 25 May 2023

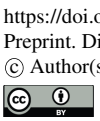

Atmospheric Measurement Techniques Discussions

is negative, and hence the EF is estimated to be zero. The assumption of constant EF is not valid in downhill sections, and the concentrations of N and CO_2, and exhaust flow rate are mostly lower than average of the whole round, whereas the DR, that is used in many other methods, is mostly higher than average of the whole round. We believe that those are the reasons why RRPA is giving EFs so different than other methods for downhill sections.

Other methods (MARS-chase, N/CO_2 integral, NWD, and MARS-OBD) give similar values for EF. This is kind of expected as the methods are fitted using data from the full drives (as in the case in Figs. 5 and 7). Therefore, the N/CO_2 is estimated mostly from the data with above-zero fuel consumption; hence, the number of particles emitted per extra CO_2 emitted should be estimated well. The other methods are also based on data with above-zero fuel consumption; thus, the dilution ratio for the downhills can also be estimated.

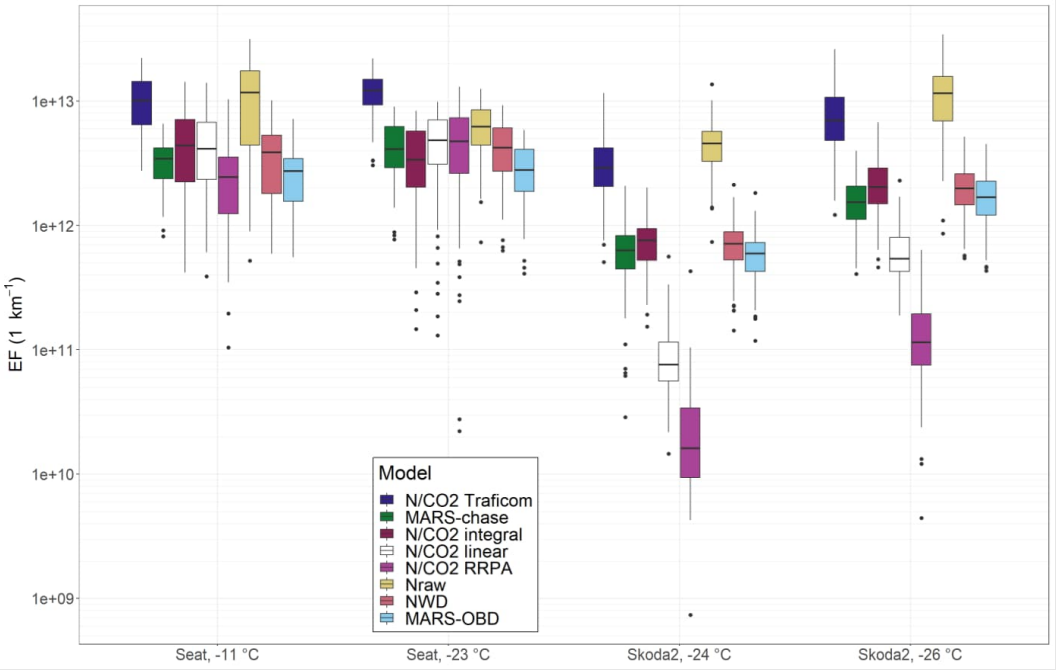

Figure 7. Emission factors of > 23 nm particles for downhill sections and for Seat and Skoda 2, hot starts, except Seat –11 C that is with the subfreezing–cold start, and Skoda –26 C that is with the preheated–cold start. Results are calculated from 100 bootstrap samples (see Sect. 2.3 for the description of bootstrap sampling). For Skoda2, some EFs (89 for Skoda2, -24 °C and 39 for Skoda2, -26 °C) are zero. Only EFs above zero are shown in this figure.

https://doi.org/10.5194/amt-2023-77
Preprint. Discussion started: 25 May 2023

4 Conclusions

There are methods to define DRs and EFs that do require OBD data from the vehicle under tests and methods that do not require. We conclude that most of the N/CO_2-methods are not suitable for transient driving, where EF is constantly changing during the drive, which is indicated by results that differ from the ones obtained with the other methods.

For those time points where the measured CO_2 is close to its background value, the new methods (the NWD and the MARS methods) work better than the old ones. Among these, the NWD method is physically more realistic and hence easier to interpret. We believe both the NWD, and the MARS methods introduced are extendable also to non-exhaust emissions. Both methods would require some prescribed database to characterize the effect of vehicle's shape on DR. The number of required vehicles for the database can be from one (if the interest is only emissions of a specific vehicle) to some hundreds of vehicles (monitoring of emissions from random vehicles from the fleet).

The MARS methods are based on the dependencies of the measured variables on DR from the N_{raw} method. It fixes the problems of the N_{raw} method at the time points where DR is estimated to be very high with the N_{raw} method. On the other hand, the MARS methods do not have as clear physical interpretation as the NWD method. The MARS methods are; however, very adaptive methods and DR could be modeled using variables other than the ones used in this paper, which might increase the physical interpretability of the methods.

If the MARS-methods were used with other variables, for their generalizability, it would be beneficial to use such variables that are generally measured in the chase measurements. Positive sides of the MARS methods also include that in the MARS-chase method, no variables measured directly from the vehicle diagnostics are not needed. This enables the observation in the middle of traffic, also in driving situations where EF and DR cannot be assumed constant.

The weakness of these methods is that the time points with the vehicle speed of zero, have been omitted in this study. This limits the usability of the method in e.g., urban conditions where the vehicle is stationary a significant part of the time. In this study we wanted to focus especially on times when the vehicle is moving, including downhills, and the fuel flow rate is zero or close to zero. The times when the vehicle is stationary could be added to the methods (MARS and NWD) by separately considering the speeds of zero. In the first place, it could be implemented by using e.g., the N_{raw}-method for those times.

Vehicle chase studies in the future are not only limited to determination of the exhaust originated species, since the NWD method could be used to define the non-exhaust particle emission originating, e.g., from the brakes and tires of the vehicle under the test. In addition to being an important tool in emission research especially in real-world emission factor determination including the semi-volatile particles, the chase method has potential to be a monitoring tool for vehicle fleets in official purposes: high emitting vehicles could be identified while driving with simultaneous particle and CO_2 sensor signals and

processed for further detailed measurements according to e.g., the new PTI protocol where particle number concentrations are measured on low idle.

Code and data availability

Data will be opened at the time of final publication. Until the publication of the article, data can be requested from the corresponding author.

Author contribution

Ville Leinonen: Conceptualization, Data curation, Formal analysis, Investigation, Methodology, Writing – original draft preparation, Writing – review & editing

Miska Olin: Conceptualization, Data curation, Formal analysis, Investigation, Methodology, Project administration, Resources, Supervision, Writing – original draft preparation, Writing – review & editing

Sampsa Martikainen: Investigation, Writing – review & editing

Panu Karjalainen: Conceptualization, Funding acquisition, Investigation, Methodology, Project administration, Resources, Supervision, Writing – review & editing

Santtu Mikkonen: Conceptualization, Funding acquisition, Methodology, Project administration, Supervision, Writing – review & editing

Competing interests

The authors declare that they have no conflict of interest.

Acknowledgements

This research is a campaign of the "AHMA" project funded by the Jane and Aatos Erkko's Foundation, supported by the Academy of Finland project "EFFi" (grant no. 322120). P.K. acknowledges funding from Tampere Institute for Advanced Study (Tampere IAS). S.Mi. is supported by the Academy of Finland competitive funding to strengthen university research profiles (PROFI) for the University of Eastern Finland (grant no. 325022). S.Ma acknowledges the funding from Kone Foundation. This research has received support from the Academy of Finland Flagship Programme "ACCC" (grant nos.

Atmospheric Measurement Techniques Discussions

337550 and 337551). Tampere University's measurement van, ATMo-Lab, contributes to the INAR RI and ACTRIS infrastructures.

References

Chang, V. W. C., Hildemann, L. M., and Chang, C. H.: Dilution Rates for Tailpipe Emissions: Effects of Vehicle Shape, Tailpipe Position, and Exhaust Velocity, http://dx.doi.org/10.3155/1047-3289.59.6.715, 59, 715–724, https://doi.org/10.3155/1047-3289.59.6.715, 2012.

Emission Standards: Europe: Cars and Light Trucks: RDE Testing: https://dieselnet.com/standards/eu/ld_rde.php#limits, last access: 11 April 2023.

Efron, B.: Bootstrap Methods: Another Look at the Jackknife, Ann. Stat., 7, 1–26, https://doi.org/10.1214/aos/1176344552, 1979.

European Commission: Commission Regulation (EU) 2016/427, 2016.

Forster, P. M., Storelvmo, T., Armour, K., Collins, W., Dufresne, J. L., Frame, D., Lunt, D. J., Mauritsen, T., Palmer, M. D., Watanabe, M., Wild, M., and Zhang, H.: Chapter 7: The Earth's Energy Budget, Climate Feedbacks, and Climate Sensitivity, in: Climate Change 2021: The Physical Science Basis. Contribution of Working Group I to the Sixth Assessment Report of the Intergovernmental Panel on Climate Change, edited by: Masson-Delmotte, V., Zhai, P., Pirani, A., Connors, S. L., Péan, C., Berger, S., Caud, N., Chen, Y., Goldfarb, L., Gomis, M. I., Huang, M., Leitzell, K., Lonnoy, E., Matthews, J. B. R., Maycock, T. K., Waterfield, T., Yelekçi, O., Yu, R., and Zhou, B., Cambridge University Press. In Press, 2021.

Friedman, J. H.: Multivariate Adaptive Regression Splines, Ann. Stat., 19, 1–67, https://doi.org/10.1214/aos/1176347963, 1991.

Giechaskiel, B., Ntziachristos, L., Samaras, Z., Casati, R., Scheer, V., and Vogt, R.: Effect of speed and speed-transition on the formation of nucleation mode particles from a light duty diesel vehicle, in: SAE Technical Papers, https://doi.org/10.4271/2007-01-1110, 2007.

Hansen, A. D. A. and Rosen, H.: Individual measurements of the emission factor of aerosol black carbon in automobile plumes, J. Air Waste Manag. Assoc., 40, 1654–1657, https://doi.org/10.1080/10473289.1990.10466812, 1990.

Hastie, T., Tibshirani, R., and Friedman, J.: The Elements of Statistical Learning, Springer New York, New York, NY,

https://doi.org/10.1007/978-0-387-84858-7, 2009.

Herndon, S. C., Shorter, J. H., Zahniser, M. S., Wormhoudt, J., Nelson, D. D., Demerjian, K. L., and Kolb, C. E.: Real-time measurements of SO2, H2CO, and CH 4 emissions from in-use curbside passenger buses in New York City using a chase vehicle, Environ. Sci. Technol., 39, 7984–7990, https://doi.org/10.1021/es0482942, 2005.

Innovation Norway: Conversion Guidelines-Greenhouse gas emissions: https://www.eeagrants.gov.pt/media/2776/conversion-guidelines.pdfv, last access: 22 May 2023.

Ježek, I., Katrašnik, T., Westerdahl, D., and Mocnik, G.: Black carbon, particle number concentration and nitrogen oxide emission factors of random in-use vehicles measured with the on-road chasing method, Atmos. Chem. Phys., 15, 11011–11026, https://doi.org/10.5194/acp-15-11011-2015, 2015a.

Ježek, I., Drinovec, L., Ferrero, L., Carriero, M., and Močnik, G.: Determination of car on-road black carbon and particle number emission factors and comparison between mobile and stationary measurements, Atmos. Meas. Tech., 8, 43–55, https://doi.org/10.5194/amt-8-43-2015, 2015b.

Karjalainen, P., Pirjola, L., Heikkilä, J., Lähde, T., Tzamkiozis, T., Ntziachristos, L., Keskinen, J., and Rönkkö, T.: Exhaust particles of modern gasoline vehicles: A laboratory and an on-road study, Atmos. Environ., 97, 262–270, https://doi.org/10.1016/j.atmosenv.2014.08.025, 2014a.

Karjalainen, P., Rönkkö, T., Pirjola, L., Heikkilä, J., Happonen, M., Arnold, F., Rothe, D., Bielaczyc, P., and Keskinen, J.: Sulfur driven nucleation mode formation in diesel exhaust under transient driving conditions, Environ. Sci. Technol., 48, 2336–2343, https://doi.org/10.1021/es405009g, 2014b.

Karjalainen, P., Ntziachristos, L., Murtonen, T., Wihersaari, H., Simonen, P., Mylläri, F., Nylund, N.-O., Keskinen, J., and Rönkkö, T.: Heavy Duty Diesel Exhaust Particles during Engine Motoring Formed by Lube Oil Consumption, https://doi.org/10.1021/ACS.EST.6B03284, 2016.

Keskinen, J. and Rönkkö, T.: Can real-world diesel exhaust particle size distribution be reproduced in the laboratory? A critical review, https://doi.org/10.3155/1047-3289.60.10.1245, 2010.

Kittelson, D. B.: Engines and nanoparticles: A review, https://doi.org/10.1016/S0021-8502(97)10037-4, 1 June 1998.

Lelieveld, J., Evans, J. S., Fnais, M., Giannadaki, D., and Pozzer, A.: The contribution of outdoor air pollution sources to premature mortality on a global scale, Nature, 525, 367–371, https://doi.org/10.1038/nature15371, 2015.

Mikkonen, S., Pitkänen, M. R. A., Nieminen, T., Lipponen, A., Isokääntä, S., Arola, A., and Lehtinen, K. E. J.: Technical note: Effects of uncertainties and number of data points on line fitting-a case study on new particle formation, Atmos. Chem. Phys., 19, 12531–12543, https://doi.org/10.5194/acp-19-12531-2019, 2019.

Neste: Neste Futura Diesel -29/-38 Technical Data Sheet: https://www.neste.fi/static/datasheet_pdf/150445_en.pdf, last access: 22 May 2023.

Neste: Neste Futura 95E10 Technical Data Sheet: https://www.neste.fi/static/datasheet_pdf/130177_en.pdf, last access: 22 May 2023.

OBDLink® LX - Top-Notch Scan Tool Compatible With Motoscan: https://www.obdlink.com/products/OBDlink-lx/, last access: 11 April 2023.

Olin, M., Oikarinen, H., Marjanen, P., Mikkonen, S., and Karjalainen, P.: High Particle Number Emissions Determined with Robust Regression Plume Analysis (RRPA) from Hundreds of Vehicle Chases, Submitted, 2023.

Park, S. S., Kozawa, K., Fruin, S., Mara, S., Hsu, Y. K., Jakober, C., Winer, A., and Herner, J.: Emission Factors for High-Emitting Vehicles Based on On-Road Measurements of Individual Vehicle Exhaust with a Mobile Measurement Platform, https://doi.org/10.1080/10473289.2011.595981, 61, 1046–1056, https://doi.org/10.1080/10473289.2011.595981, 2011.

Pirjola, L., Parviainen, H., Hussein, T., Valli, A., Hämeri, K., Aaalto, P., Virtanen, A., Keskinen, J., Pakkanen, T. A., Mäkelä, T., and Hillamo, R. E.: "Sniffer"—a novel tool for chasing vehicles and measuring traffic pollutants, Atmos. Environ., 38, 3625–3635, https://doi.org/10.1016/J.ATMOSENV.2004.03.047, 2004.

R Core Team: R: A Language and Environment for Statistical Computing, https://www.r-project.org/, 2022.

Rönkkö, T., Pirjola, L., Ntziachristos, L., Heikkilä, J., Karjalainen, P., Hillamo, R., and Keskinen, J.: Vehicle engines produce exhaust nanoparticles even when not fueled, Environ. Sci. Technol., 48, 2043–2050, https://doi.org/10.1021/es405687m, 2014.

Rönkkö, T., Kuuluvainen, H., Karjalainen, P., Keskinen, J., Hillamo, R., Niemi, J. V., Pirjola, L., Timonen, H. J., Saarikoski, S., Saukko, E., Järvinen, A., Silvennoinen, H., Rostedt, A., Olin, M., Yli-Ojanperä, J., Nousiainen, P., Kousa, A., and Dal Maso, M.: Traffic is a major source of atmospheric nanocluster aerosol, Proc. Natl. Acad. Sci. U. S. A., 114, 7549–7554, https://doi.org/10.1073/pnas.1700830114, 2017.

Shorter, J. H., Herndon, S., Zahniser, M. S., Nelson, D. D., Wormhoudt, J., Demerjian, K. L., and Kolb, C. E.: Real-time measurements of nitrogen oxide emissions from in-use New York City transit buses using a chase vehicle, Environ. Sci.

Technol., 39, 7991–8000, https://doi.org/10.1021/es048295u, 2005.

Simonen, P., Kalliokoski, J., Karjalainen, P., Rönkkö, T., Timonen, H., Saarikoski, S., Aurela, M., Bloss, M., Triantafyllopoulos, G., Kontses, A., Amanatidis, S., Dimaratos, A., Samaras, Z., Keskinen, J., Dal Maso, M., and Ntziachristos, L.: Characterization of laboratory and real driving emissions of individual Euro 6 light-duty vehicles – Fresh particles and secondary aerosol formation, Environ. Pollut., 255, 113175, https://doi.org/10.1016/j.envpol.2019.113175, 2019.

Wang, F., Ketzel, M., Ellermann, T., Wåhlin, P., Jensen, S. S., Fang, D., and Massling, A.: Particle number, particle mass and NOx emission factors at a highway and an urban street in Copenhagen, Atmos. Chem. Phys., 10, 2745–2764, https://doi.org/10.5194/acp-10-2745-2010, 2010.

Wang, J. M., Jeong, C. H., Zimmerman, N., Healy, R. M., Hilker, N., and Evans, G. J.: Real-World Emission of Particles from Vehicles: Volatility and the Effects of Ambient Temperature, Environ. Sci. Technol., 51, 4081–4090, https://doi.org/10.1021/ACS.EST.6B05328/SUPPL_FILE/ES6B05328_SI_001.PDF, 2017.

Wihersaari, H., Pirjola, L., Karjalainen, P., Saukko, E., Kuuluvainen, H., Kulmala, K., Keskinen, J., and Rönkkö, T.: Particulate emissions of a modern diesel passenger car under laboratory and real-world transient driving conditions, Environ. Pollut., 265, 114948, https://doi.org/10.1016/j.envpol.2020.114948, 2020.

Zavala, M., Herndon, S. C., Slott, R. S., Dunlea, E. J., Marr, L. C., Shorter, J. H., Zahniser, M., Knighton, W. B., Rogers, T. M., Kolb, C. E., Molina, L. T., and Molina, M. J.: Characterization of on-road vehicle emissions in the Mexico City Metropolitan Area using a mobile laboratory in chase and fleet average measurement modes during the MCMA-2003 field campaign, Atmos. Chem. Phys., 6, 5129–5142, https://doi.org/10.5194/acp-6-5129-2006, 2006.

S1 Concept of the Near-Wake Dilution (NWD) model

The model is based on a concept that there is a near-wake region right behind a moving vehicle and a far-wake region further behind (Fig. S1). A similar model has previously been presented by Chang et al. (2009) for the purpose of wind tunnel experiments. However, here we modify the model slightly to be used with chase experiments. The vehicle exhaust is thought to mix with the surrounding air, i.e., to dilute, within the near-wake region. This dilution caused by the vehicle movement is thought to be in its full extent in the transition region (at the distance of x_{tr} from the tailpipe). Dilution in the far-wake region is much slower because the air parcel to be diluted is the exhaust already mixed with the surrounding area within the near-wake region, instead of the raw exhaust only.

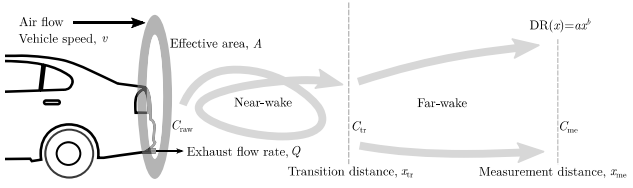

Figure S1. Schematics of the Near-Wake Dilution (NWD) model.

In the near-wake region, the eddies caused by the rear of the vehicle during driving are large and efficient to mix the exhaust with the surrounding air rapidly. The air flow is thought to pass an imaginary surface, having the effective area of A, with the speed equal to the vehicle speed (v). The volumetric flow rate of this diluting air then becomes vA, and the volumetric flow rate of the exhaust (in equal temperature to the outdoor air) is Q. The dilution ratio for a pollutant of interest is

$$\mathrm{DR} = \frac{C_{\mathrm{raw}}}{C} \tag{S1}$$

where C_{raw} is the concentration of the pollutant in the raw exhaust and C the concentration in the diluted air. Analogous to a simple flow-controlled diluter, DR at the distance of x_{tr} is

$$\mathrm{DR}(x_{\mathrm{tr}}) = \frac{vA}{Q} + \epsilon \tag{S2}$$

where ϵ is included to account any nonidealities in this concept, e.g., because DR cannot be 0 when the vehicle is stationary ($v = 0$) or because the transition region is not infinitesimally short in reality.

Many vehicle exhaust chase studies (e.g., Morawska et al. (2007)) have shown that DR typically depends on the chase distance (x in meters) with the function

$$\mathrm{DR}(x) = ax^b \tag{S3}$$

where a and b are parameters depending on vehicle category and study and are roughly the following: $a = 10...100$ and $b = 1.0...1.5$ (Keskinen and Rönkkö, 2010). Equation S3 is, however, valid only in the far-wake region (Olin, 2013), i.e., when $x > x_{\mathrm{tr}}$. Parameter b seems to not depend on v (Morawska et al., 2007), suggesting that dilution occurring in the far-wake region are driven by the dynamics of the outdoor air, such as by crosswind, rather than the vehicle speed-dependent air flow that dilutes the exhaust in the near-wake region. However, because increasing v decreases the time between releasing the exhaust from the studied vehicle and the measurement with the chase vehicle, dilution should yet be vehicle speed-dependent

also in the far-wake region (lower b with higher v). Possibly higher turbulence levels with higher v induced by the moving vehicle, however, enhance the dilution rate also in the far-wake region (higher b with higher v) and thus almost cancels the effect of v out, leading to an almost vehicle speed-independent b.

Combining eqs S2 and S3, we obtain

$$\mathrm{DR}(x_{\mathrm{tr}}) = \frac{vA}{Q} + \epsilon = ax_{\mathrm{tr}}^b \tag{S4}$$

and the parameter a can be solved:

$$a = \frac{vA}{Qx_{\mathrm{tr}}^b} + \frac{\epsilon}{x_{\mathrm{tr}}^b}. \tag{S5}$$

Considering the measurement distance in a chase experiment, x_{m}, we further obtain (using eqs S3 and S5)

$$\mathrm{DR}(x_{\mathrm{me}}) = ax_{\mathrm{me}}^b = \frac{vAx_{\mathrm{me}}^b}{Qx_{\mathrm{tr}}^b} + \frac{\epsilon x_{\mathrm{me}}^b}{x_{\mathrm{tr}}^b}. \tag{S6}$$

The absolute values for parameters A, x_{me}, x_{tr}, b, and ϵ remains unknown. Nevertheless, when chasing a specific vehicle with a constant x_{me}, we can assume that all these parameters are constant. A is thought to depend on the rear shape of the vehicle, as well as is the case of x_{tr} but v may also affect x_{tr} slightly due to altered shapes of the eddies behind the vehicle. Because dilution in the far-wake region is assumed to not depend on v, the value of b presumably depends mainly on the dynamics in the outdoor air but maybe on the rear shape as well. Additionally, although the temperature of the raw exhaust is assumed to not affect the dilution dynamics, since using mass flow rates rather than volumetric flow rates in calculations typically cancels temperature out, it may still have an effect on the dilution dynamics depending on whether cooling and simultaneous expansion occurs in the near-wake or far-wake region. These uncertainties involved in this model can presumably be also accounted by the inclusion of parameter ϵ in eq S2.

Equation S6 can be further arranged to

$$\mathrm{DR}(x_{\mathrm{me}}) = \frac{v}{Q}\frac{Ax_{\mathrm{me}}^b}{x_{\mathrm{tr}}^b} + \frac{\epsilon x_{\mathrm{me}}^b}{x_{\mathrm{tr}}^b} = \frac{v}{Q}\kappa + \gamma \tag{S7}$$

where the number of free parameters has been reduced from five to two (κ and γ). Using information on the measured concentration, C_{me}, and on C_{raw}, e.g., from CO_2 measurements and its known concentration in the raw exhaust when the engine is combusting fuel, $\mathrm{DR}(x_{\mathrm{me}})$ and further the parameters κ and γ can be obtained. This can be done by plotting the obtained $\mathrm{DR}(x_{\mathrm{me}})$ data as a function of v/Q (recorded via OBD). When the dilution dynamics satisfies the theory behind this model, the data points are scattered so that linear behavior is seen. Thus, linear regression can be performed on the data points originated from the times when the engine was combusting fuel and the rest of the data points (from the times when the engine was in a motoring state) are outliers.

Whereas the study by Chang et al. (2009) uses the multiplication of the real height and width of a vehicle as the imaginary surface which the diluting air passes through, we think consider it a free parameter here instead. That is because the rear surface of a vehicle is actually the surface that does not pass any flow through but the areas around it do; therefore, A may be connected more to the perimeter of the rear rather than its surface area. In addition, the placing of the exhaust pipe or pipes on the rear of the vehicle can also affect dilution mechanics. E.g., in a case of double exhaust pipes on the both sides of the rear of a vehicle can lead to stronger dilution in reality, resulting in higher value for A when it is fitted with available data. Because the chase settings for every studied vehicle in this study are similar, we can consider κ being mostly dependent on the rear shape of a vehicle. Since γ, the parameter involving nonidealities in the NWD model, seems to be clearly higher with the gasoline vehicles of this study compared to the diesel vehicles, we consider it being mostly dependent on the used fuel in this study.

References

Chang, V. W.-C., Hildemann, L. M., and hisn Chang, C.: Dilution Rates for Tailpipe Emissions: Effects of Vehicle Shape, Tailpipe Position, and Exhaust Velocity, J. Air Waste Manage., 59, 715–724, https://doi.org/10.3155/1047-3289.59.6.715, 2009.

Keskinen, J. and Rönkkö, T.: Can real-world diesel exhaust particle size distribution be reproduced in the laboratory? A critical review, J. Air Waste Manage., 60, 1245–1255, https://doi.org/10.3155/1047-3289.60.10.1245, 2010.

Morawska, L., Ristovski, Johnson, Jayaratne, and Mengersen, K.: Novel Method for On-Road Emission Factor Measurements Using a Plume Capture Trailer, Environ. Sci. Technol., 41, 574–579, https://doi.org/10.1021/es060179z, 2007.

Olin, M.: Dieselpakokaasun hiukkaspäästöjen muodostumisprosessin simulointi, M.Sc. thesis, Tampere University of Technology, Tampere, Finland, http://urn.fi/URN:NBN:fi:tty-201312191517, 2013.

Paper IV

Environmental Science: Atmospheres

ROYAL SOCIETY OF CHEMISTRY

PAPER

View Article Online
View Journal | View Issue

Cite this: *Environ. Sci.: Atmos.*, 2022, **2**, 1551

Modeling atmospheric aging of small-scale wood combustion emissions: distinguishing causal effects from non-causal associations†

Ville Leinonen, *[a] Petri Tiitta,‡[b] Olli Sippula,[bc] Hendryk Czech, §[b] Ari Leskinen,[ad] Sini Isokääntä,[a] Juha Karvanen[e] and Santtu Mikkonen [ab]

Received 2nd May 2022
Accepted 6th October 2022

DOI: 10.1039/d2ea00048b

rsc.li/esatmospheres

Small-scale wood combustion is a significant source of particulate emissions. Atmospheric transformation of wood combustion emissions is a complex process involving multiple compounds interacting simultaneously. Thus, an advanced methodology is needed to study the process in order to gain a deeper understanding of the emissions. In this study, we are introducing a methodology for simplifying this complex process by detecting dependencies of observed compounds based on a measured dataset. A statistical model was fitted to describe the evolution of combustion emissions with a system of differential equations derived from the measured data. The performance of the model was evaluated using simulated and measured data showing the transformation process of small-scale wood combustion emissions. The model was able to reproduce the temporal evolution of the variables in reasonable agreement with both simulated and measured data. However, as measured emission data are complex due to multiple simultaneous interacting processes, it was not possible to conclude if all detected relationships between the variables were causal or if the variables were merely co-variant. This study provides a step toward a comprehensive, but simple, model describing the evolution of the total emissions during atmospheric aging in both gas and particle phases.

Environmental significance

Residential wood combustion in stoves is known as a substantial primary source of particulate matter in Europe with significant potential for secondary organic aerosol (SOA) formation during atmospheric aging. Despite numerous laboratory studies with combustion-related SOA precursors under different oxidation conditions, interactions between those conditions and aerosol constituents over the course of ageing have not been understood yet. In this study we formed a stochastic model that, based on the obtained structure of the variables and coefficients of 'reactions' from the measured dataset, was able to reproduce the evolution of emission in a smog chamber. Our model raises evidence for interactive processes not taken into account before with possible implications for air pollution forecasts and at-source reduction of secondary pollutant formation.

1 Introduction

Small-scale wood combustion is a common method for residential heating and has been identified as a substantial contributor to ambient levels of particulate matter in several European areas.[1–5] Wood combustion-derived aerosol, in particular from manually-fired logwood stoves, contains substantial quantities of several air pollutants, such as black carbon, polycyclic aromatic hydrocarbons (PAH), volatile organic compounds (VOC) and CO,[6,7] with consequences for Earth's radiative forcing,[8] cloud formation,[9] and human health.[10] After their release into the atmosphere, wood combustion emissions are immediately transformed in a complex process known as "atmospheric aging" involving multiphase chemistry, leading to the oxidation and functionalization of particulate and gaseous pollutants[11,12] and the consequent formation of secondary organic and inorganic aerosol (SOA and SIA, respectively). The formation of SOA has been reported to enhance the organic aerosol concentration by a factor of two to three times the concentration of the particulate organic aerosol emitted by wood combustion, after less

[a]*Department of Applied Physics, University of Eastern Finland, Kuopio, Finland. E-mail: ville.j.leinonen@uef.fi*

[b]*Department of Environmental and Biological Sciences, University of Eastern Finland, Kuopio, Finland*

[c]*Department of Chemistry, University of Eastern Finland, P. O. Box 111, 80101 Joensuu, Finland*

[d]*Finnish Meteorological Institute, Kuopio, Finland*

[e]*Department of Mathematics and Statistics, University of Jyvaskyla, Jyvaskyla, Finland*

† Electronic supplementary information (ESI) available. See DOI: **https://doi.org/10.1039/d2ea00048b**

‡ Now at: Finnish Meteorol. Inst., Atmospher. Res. Ctr Eastern Finland, Kuopio FI-70211, Finland.

§ Now at: Cooperation group "Comprehensive Molecular Analytics (CMA)", Helmholtz Zentrum München, 81379 München, Germany.

than 1.5 days of photochemical aging.[13–15] In addition, atmospheric aging of wood combustion emissions at nighttime has been identified as a substantial enhancer of aerosol particle concentrations.[13,16] Consequently, it has been found that atmospheric aging alters the toxicological properties of wood combustion aerosols[17,18] in addition to changing the optical properties,[19,20] with implications for the climate and human health.

Smog chambers or environmental chambers have been used to study the atmospheric transformation of single VOC or combustion emissions for several decades, offering a controlled environment and conditions similar to the atmosphere, to study the effects of, for example, the photochemical age, relative humidity, NO_x, addition of seed aerosol, oxidizing agents, *etc.* on emission transformation.[13,21–24] Despite several known reaction pathways from smog chamber experiments for single emission constituents or compound classes, such as PAHs,[25] interactions between all constituents of a real-world combustion aerosol complicate the prediction of secondary aerosol formation and its physicochemical properties.

Radicals, such as hydroxyl (OH), ozone (O_3), and nitrate (NO_3), are known to play an important role in SOA chemistry.[11] OH is the most important radical during photochemical aging, whereas NO_3 and O_3 are more important during dark aging.[13,26] SOA formed from photochemical and dark aging differ by chemical composition. However, both aging mechanisms are important and must be taken into account when evaluating the whole-climate implications of aging processes.[27] Nitrate radical chemistry is an efficient SOA formation mechanism and also an important pathway for the production of organic nitrates, serving as a NO_x sink in the atmosphere.[28]

A few studies have been made to capture the atmospheric evolution of wood combustion emissions in both the gaseous and particulate phases.[29–32,86]

Models of SOA formation and the evolution of the compounds leading to SOA can be divided into at least two groups. One group of modelling, such as the volatility basis set, aims to describe one or several features of the emission. In the volatility basis set (VBS) approach,[33,34] the evolution of the constituent phases are modeled based on the volatilities of the compounds, considering the equilibrium concentrations of different compounds in gas and particle phases and how different factors, such as chemical and physical reactions, affect the equilibrium state. This approach with the observational data from smog chamber experiments has been commonly used to estimate the SOA mass produced from combustion emission[35–40] and to estimate the proportional contributions of different SOA precursors to formed SOA.[41] The VBS scheme has been also applied to model biomass-burning organic aerosol in regional chemical transport models.[42,43]

The second approach to model SOA, and in particular its precursors in the gas phase, is the family of explicit chemical modeling. There exist several chemical models such as the Master Chemical Mechanism (MCM)[44,45] and GECKO-A,[46] which combine large numbers of chemical reactions and predetermined reaction coefficients to replicate the evolution of the system. The MCM has recently been applied to wood-burning emissions by running the model with the most important primary emission species to model the evolution of gas-phase species using a smaller selection of reactions from the entire system.[47] These can be used to parametrize SOA production. The Statistical Oxidation Model (SOM) offers an approach somewhere between one-quality models and explicit chemical models. The SOM uses several qualities of compounds (such as their volatility and numbers of constituent carbon and oxygen atoms) to predict the SOA mass and atomic O : C ratio.[48] The SOM has been used to simulate the formation and composition of biomass burning SOA in an environmental chamber.[49]

All approaches—volatility-based, SOM, and explicit chemical modeling—are based on differential equations. These equations describe the evolution of some quantity that we are interested in modeling and can be transformed into the final product of the model. For the volatility approach, this is the volatility distribution of particles; in chemical modeling, it defines the quantities of substances in the system.

In the approaches mentioned above, the changes of gas concentrations and numbers of particles in time can be considered consequences of reactions occurring in the system. Reactions are caused by the initial compounds and certain properties of these compounds. The reaction coefficients and concentrations of initial compounds determine the rate of reactions occurring in time. Compounds can be considered causally related as those are related to each other through chemical reactions. If a reaction is favorable, initial compounds lead to an increase in products while their own concentrations decrease.

In this study, we described the connections between primary emissions and aging conditions using a causal model.[50] Models aiming to study causality are slowly being introduced to studies in atmospheric sciences, but this is the first attempt to build a causality-based model for combustion emissions. In the field of atmospheric science, causal discovery has been applied in different subfields to both test the usability of the method for a certain kind of dataset, but also to understand the causal pathways of a certain phenomenon. Examples of studies includes exploring causal networks in biosphere–atmosphere interactions,[51] discovering causality in spatio-temporal datasets of surface pressures in oceans,[52,53] discovering causal pathways among atmospheric disturbances of different spatial scales in geopotential height data,[54] and testing causal discovery in synthetic atmospheric datasets of advection and diffusion.[55]

The aim of this study was to evaluate whether it is possible to learn the causal relationships of variables from the system of atmospheric aging without having explicit prior information about these relations. On that account, we created a model for the complex interactions between aerosol constituents in both gaseous and particulate phases.[13,30] Here, we present the first version of our model that is able to represent dependencies between observed variables in the chamber studies in Tiitta *et al.* (2016)[13] and Hartikainen *et al.* (2018).[30] In addition, we discuss the issues in data processing related to the modeling of wood combustion aging, and more generally, emission aging

data sets by applying the model to artificial, simulated data sets and evaluating its accuracy.

2 Data and methods

Chamber experiments for studying the atmospheric transformation of residential wood combustion emissions were conducted in the ILMARI environmental chamber[56] at the University of Eastern Finland, as described by Tiitta *et al.* (2016).[13] The particulate emissions of the dataset have been studied by Tiitta *et al.* (2016)[13] and volatile emissions by Hartikainen *et al.* (2018).[30]

Briefly, five chamber experiments were conducted in total using a modern heat-storing masonry heater[57] as the emission source. The masonry heater was operated with spruce logs, using both fast ignition and slow ignition for initiating the combustion experiment (detailed procedure described in Tiitta *et al.*, 2016)[13] to adjust the VOC-to-NO_x ratio. In each experiment, a sample of the combustion exhaust was diluted and fed into the chamber for 35 min, including the ignition, flaming combustion and residual char-burning phases of the combustion.[58] This was followed by stabilization (*i.e.* the period when organic compounds should reach an equilibrium state in the chamber) of the sample, after which the oxidative aging of the sample was initiated by feeding ozone into the chamber. The end of the stabilization period is treated as the starting point in our analysis. Both dark and UV-light aging experiments were conducted, representing evolution at nighttime and daytime in the atmosphere, respectively.

To investigate the daytime ambient conditions, in which OH radicals dominate the oxidative aging of emissions, we used two experiments (experiments 4B and 5B, Tiitta *et al.*, 2016).[13] In those, UV lights (blacklight lamps, 350 nm) were switched on immediately after feeding ozone into the chamber, and the wood combustion emission was photochemically aged for four hours. The estimated photochemical age of the sample at the end of the experiment was 0.6–0.8 days, based on the measured OH radical exposure. Two experiments were also used to investigate the nighttime evolution (experiments 2B and 3B, Tiitta *et al.*, 2016).[13] In those, the aging was conducted first without the UV radiation; after 4 hours of dark aging, the UV lights were switched on. The dark aging period represents nighttime ambient conditions, in which ozone and nitrate radicals dominate the oxidative aging of emissions.[13,59] The conditions in the chamber simulate polluted atmospheric boundary-layer conditions with an OH concentration of (0.5–5) $\times 10^6$ molecule per cm^3, ozone concentrations of 20–90 ppb and NO_x concentrations of 40–120 ppb[13] with a lower VOC-to-NO_x ratio (fast ignition: ratio $\approx$ 3) yielding smaller total emissions including SOA than the slow ignition cases (ratio $\approx$ 5).

The evolution of gases and particles in the chamber was measured by comprehensive online measurements. Gas-phase organic and inorganic compounds were measured using single gas analyzers (NO, NO_2, and O_3) and a Proton-Transfer-Reactor Time-of-Flight Mass Spectrometer (PTR-TOF-MS 8000, Ionicon Analytik, Innsbruck, Austria). The PTR-MS data set has been described in detail by Hartikainen *et al.* (2018).[30] The submicron particle size distribution was measured using a Scanning Mobility Particle Sizer (SMPS, CPC 3022, TSI) and the chemical composition and mass concentration of the particles using a Soot Particle Aerosol Mass Spectrometer (SP-HR-TOF-AMS).[60] The AMS was used to characterize the chemical signatures of particulate chemical species (organic, NO_3, SO_4, NH_4, and Chl), of which NO_3 and organic species (hereafter referred to as OA) were used as Positive Matrix Factorization (PMF) factors (POA1–2, SOA1–3, details below) in this study.

Dark and UV-induced aging were treated separately in further data analysis because the intense UV radiation affects the transformation of emissions due to photochemical reactions and further influences the dependencies between the variables. Furthermore, we had two experiments with different ignition techniques, one with fast ignition and one with slow ignition for both dark (2B and 3B) and UV light-induced aging (4B and 5B). Both experiments with the same aging type were combined into a single data set for the model.

The ignition type, which determines how fast the logwood ignites, influences the emission factors of POA and VOC emission from wood combustion, particularly those of carbonyls, aromatic hydrocarbons, and furanoic and phenolic compounds.[13,30] Hartikainen *et al.* (2018)[30] showed that during aging, furanoic and phenolic compounds decreased, while nitrogen-containing organic compounds were produced in both gaseous and particulate phases. In addition, photochemical aging especially increased the concentrations of certain gaseous carbonyls, particularly acid anhydrides.[30] As we combined the results of both experiments with different ignition types into a single data set, we assumed that the reactions in the chamber were similar in both data sets and that only the concentrations of the compounds differed.

2.1 Data processing

For modeling purposes, the data are needed to be harmonized and transformed into an applicable form. The SMPS provided detailed measurements of size distributions, each consisting of over 100 bins by the particle (mobility) diameter, ranging from 14.1–14.6 nm to 710.5–736.5 nm. For this study, we used a simpler representation of the size distribution, size binning of wall-loss corrected (see Section 2.3 in Tiitta *et al.*, 2016)[13] SMPS time series which were grouped into four larger size classes. These four classes roughly represent atmospherically relevant particle modes: under 25 nm (nucleation mode, hereafter NuclM), 25 to 100 nm (Aitken mode, AitM), 100 to 300 nm (accumulation mode, AccM), and over 300 nm (coarse mode, CoarM). Measured size bins were summed to form number concentrations of particles in four classes.

As OH radicals are one of the main oxidants in the atmospheric transformation of emission during photochemical aging, we applied OH concentration level estimation formulas (1–3) from Barmet *et al.* (2012)[61] to calculate the OH concentration time series. The estimation was based on the d9-butanol tracer method, and the slope was determined separately for each time point from 20 observations (time period of 30 min) around the time at which the OH concentration was estimated.

The reason for using only a 30-minute interval for estimating the OH at the time was that the decline of d9-butanol (hence the concentration of OH) was highly varying during the experiment. The decline in d9-butanol levels was highest right after UV lights were turned on. The slope estimation (see formula (3) in Barmet *et al.*[61]) using whole time series could have given too small estimates for the OH level right after UV lights have been turned on. Concentrations of OH that were estimated to be negative were set to zero. However, negative values were only estimated for dark aging experiments, where, according to our initial assumption, OH was not allowed to affect other variables in the model.

The applied instruments measured concentrations and size distributions with different time resolutions. PTR-MS measured every 2 seconds, whereas the SMPS scan time and sample analysis took a total of 5 minutes to conduct a single measurement. To combine variables measured by multiple measurement devices into one data set, it is important to transform data appropriately to express variables to the same time resolution. We applied simple cubic spline interpolation to interpolate SMPS data to the same time resolution as AMS data, which was 2 minutes. Data from PTR-MS and other gas analyzers were averaged over a 2 minute period.

2.1.1 Dimension reduction of PTR-MS and AMS data sets. The particle and gas phase data provided by AMS and PTR-MS, respectively, consist of mass spectra of many chemical compounds and their fragments (hereafter referred as tracers). To formulate a model that could provide a simple representation of the evolution of the emissions, we need to compress the information provided by a large number of single tracers. Thus, we aim to describe the evolution of spectra by combining tracers into a smaller number of factors with dimension reduction techniques for both gas- and particle-phase measurement (from PTR and AMS) data sets. Tracers share some properties and the underlying dependencies in the data set.

However, it is not necessarily self-evident which dimension reduction method should be applied to the data set of interest. Isokääntä *et al.* (2020)[62] studied the importance of selecting the appropriate dimension reduction method to the data set in atmospheric studies. Specifically, they investigated mass spectrometer data sets acquired from chamber studies. They found that fragmentation of compounds and rapid changes in chemical composition (such as that caused by turning on UV lights) should be considered when selecting the dimension reduction technique. They suggest that for data sets in which fragmentation is usually not problematic, exploratory factor analysis (EFA) or principal component analysis (PCA) might extract those rapid changes from the data more efficiently than PMF.

We aimed to compare multiple experiments in further data analysis, and thus we applied dimension reduction techniques to the PTR-MS data sets, using all the data to form the factors instead of applying a dimension reduction method separately. For PTR-MS data, both EFA and PCA were tested, but only EFA was selected for further analysis as it provided interpretable factors. EFA was applied using the function *fa* from package *psych*[63] in the R environment.[64] The minimum residual technique was used for EFA and oblique Oblimin-rotation was used to enhance the separation of the tracers in each factor. In addition, tracers that had no significant contribution (*i.e.*, loading) on any of the factors were removed from analysis, and factorization was performed again only to the remaining tracers. These removed tracers were mainly instrumental backgrounds or compounds with very small concentrations without any clear structure as a time series. Time series for the factors were calculated by the sum score method, wherein the original data are multiplied directly with the loading values from EFA, possibly with some threshold limit.[65] We selected an absolute value of 0.3 as a threshold for the loadings, meaning any loading values smaller than that were suppressed to zero before the multiplication.[66] PTR factor 2 was scaled to be positive by adding the minimum value to all the time points. Negative values were caused by the baseline correction of PTR-MS data and factorization. Factors (see Fig. 1) were identified based on their temporal evolution and identified tracers as well as their average carbon oxidation state (OS_C) contributing to each factor. For PTR-MS data, three factors were found: (1) primary VOCs, (2) photochemical aging products, and (3) dark aging products.

PTR-MS data sets adequately identified the representative compounds (*i.e.*, tracers that were identifiable) as a time series. It must be noted that detailed interpretation of factors would require identification for most of the compounds in the chamber, including highly oxygenated organic molecules, which was not possible with the current measurement setup.[67–70] Accurate optimization of factors is outside the scope of this study.

Factorization of the AMS data by PMF has been described in Tiitta *et al.* (2016)[13] so we only summarize it here. PMF[71,72] was applied to classify the OA into five subgroups. Two factors

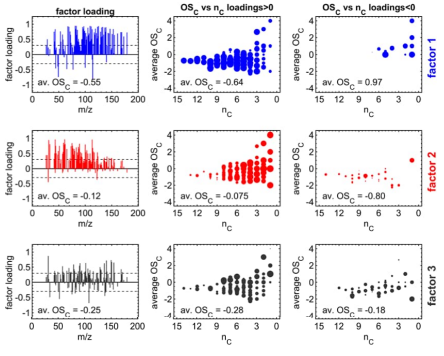

Fig. 1 Illustration of the three factor loadings (in rows) from exploratory factor analysis (EFA) including the average carbon oxidation state (OS_C) for PTR-MS factors. Subplots in the left column contain the coefficients of the factor loadings and the limit of ±0.3 (dashed line), separating relevant from redundant variables. Subplots in the center (for *m*/*z* with positive factor loadings) and the right column (for *m*/*z* with negative factor loadings) visualize the OS_C dependent on the carbon number (n_C) of the detected sum formula.[73]

describe the primary organic aerosol particles (POA): (1) biomass-burning OA and (2) hydrocarbon-like OA. Three factors represent the major oxidants in the formation processes of SOA: (1) formation by ozonolysis, (2) formation by nitrate/peroxy radicals, and (3) formation by OH radicals. PMF was performed using the PMF Evaluation Tool v.2.08.[72]

2.1.2 Filtering time series. Measurements can be thought of as discrete observations from the continuous process of emission transformation. They contain measurement uncertainty, which arises from limitations of the measurement regarding the representativeness, accuracy or other factors affecting the measurement event or applied instruments. The uncertainties, referred to in the model as measurement errors, are estimated and taken into account in the filtering procedure (detailed motivation for filtering in ESI S1†).

Multiple statistical methods can be applied to estimate the state α_t of the time series from data. Instead of using all observations from the time series (smoothing), we used only observations before the estimated state (filtering). The reason for using filtering instead of smoothing was that if the model would be used to predict the evolution of the system after the end of the measurement, the information is only available until the last observation.

The filtering method was similar to locally estimated scatterplot smoothing,[74] in which observations are weighted according to the proximity of the measurement $y_{k,t0}$ from the measurement y_{k,t_0} which state is estimated.

$$\alpha_{k,t_0} = \sum_{t=1}^{t_0} w\left(\frac{t-t_0}{h}\right)\left(y_{k,t} - \beta_0 - \beta_1(t-t_0)\right) \quad (1)$$

$$w(x) = \{(1-|x|^3)^3\}, \text{ when } |x| < 1,\ 0, \text{ when } |x| \geq 1 \quad (2)$$

We applied the method separately to every time series. The number of previous measurements used (h = time window) to estimate the current state α_{k,t_0} was determined in each individual time series by calculating a weighted linear regression (with coefficients β_0 and β_1 and weights $w(x)$) to the time series and choosing a window such that the filtered time series was representative to time series. The time series had different ratios of noise to total variation due to different measurement instruments and time resolutions. Fig. 2 shows the effect of filtering for one variable during experiment 2B.

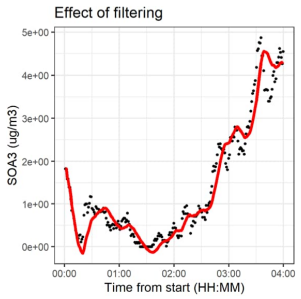

Fig. 2 Effect of filtering for one variable during the dark aging period of experiment 2B. The dots represent the original measurements, and the line represents the filtered values.

2.2 Creating the model

We present a simple four-step procedure describing how the model was applied to the processed version of the emission data set. Sections 2.2.1–2.2.4 provide more detailed descriptions of selected steps in the model creation.

(1) Applying the causal discovery algorithm[75] for finding the potential causal relationships between measured variables and measured changes ($\Delta(x)$:s) in time. The algorithm returns possible causes for each measured change.

(2) Forming all possible interaction variables from measured variables such that both variables in the interaction should be potential causes suggested by the causal discovery algorithm. In addition, prior assumptions are taken into account, and thus variables with the given limitations are restricted from being considered interaction variables.

(3) Using the least absolute shrinkage and selection operator (LASSO)[76] to select predictor variables amongst interaction variables (and possible single variables suggested by the algorithm). Simultaneously, estimating the coefficients of each selected predictor using a linear model.

(4) Calculating the modeled evolution using the ordinary differential equation (ODE) system *deSolve*,[77] using estimated coefficients as reaction coefficients, the first observation from the experiment as the initial state and with multiple values of two parameters which the user needs to define. Select values of those parameters based on the smallest RMSE for the calculated evolution.

Sections 2.2.1–2.2.4 provide more detailed descriptions of selected steps in the model creation.

As the output of the procedure, we learn linear differential equations for each variable of interest $x_j, j = 1, \ldots, n$, eqn (3):

$$\Delta(x_{j,t}) = x_{j,t+1} - x_{j,t} = \beta_0 + \beta_1 x_{1,t} + \beta_2 x_{2,t} + \ldots + \beta_{ik} x_{i,t} x_{k,t} + \ldots (3)$$

These differential equations describe how the difference of the variable value between subsequent time points is determined by values of measured variables (x_i:s describe the variables used as itself and $x_i x_k$ variables used as interaction variables) immediately before the time interval.

2.2.1 Using a causal discovery algorithm. A causal discovery algorithm[78] attempts to find the causal structure of variables in a studied system. The causal structure refers to qualitative knowledge on the causal relations. For instance, the algorithm may indicate that X causes Y but gives no information on the strength of the effect. Fig. 3 illustrates causal graphs where one-headed arrows, called edges, tell the direction of the causality.

Causal discovery methods can be divided into constraint-based and score-based approaches.[78,79] We applied the PC-algorithm[78] which is a constraint-based method implemented in the R package *r-causal*.[75] In constraint-based methods, a series of tests for (conditional) independence between the variables are carried out. Based on these tests, conclusions on

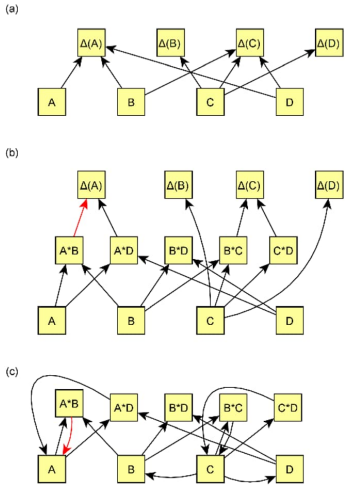

Fig. 3 Examples of causal graphs and how interaction variables are formed. (a) Variables are linked to other variables by affecting $\Delta(x)$ (denoted as $\Delta(A)$ for variable A). The causal discovery algorithm searches, for each $\Delta(x)$, for the most probable variables that could have an effect. (b) The interaction variables are linked to the edges using the causal discovery algorithm. All possible interaction variables are formed based on edges in graph (a). For example, because A, B, and D all affect $\Delta(A)$, interaction variables A × B, A × D, and B × D are formed, and those are possible to affect $\Delta(A)$. In this graph, we assume that some of the interaction edges (*e.g.*, B × D → $\Delta(A)$) are not selected in least absolute shrinkage and selection operator (LASSO). (c) Alternative way figure (b) can be drawn as a cyclic graph. Edge from, *e.g.*, A × B → $\Delta(A)$ in figure (b) is substituted by an edge A × B → A in figure (c). We have used (c) to represent the edges in the results section. The color of the edge is related to the direction of the effect: black indicates a positive effect and red denotes a negative effect.

the causal structure can be made. For instance, if X and Y are dependent, Z and Y are dependent, but X and Z are independent when conditioned on Y, it can be concluded that the causal graph has a V-structure $X \rightarrow Y \leftarrow Z$. However, without auxiliary information it is possible to construct the causal graph only up to an equivalence class,[78] which in practice means the direction of some arrows may remain unknown.

The implementation of the PC-algorithm[75] has two parameters which the user needs to define, "depth" and "alpha" which are hereafter referred to as tuning parameters. Wongchokprasitti (2019)[75] explains that the depth determines "a number of nodes conditioned on in the search". Depth values used in the algorithm were two, three, and infinite, meaning that every node can be further conditioned in the search. Alpha, which is set between zero and one, indicates the statistical significance of the dependency between searched variables. However, significance was used here as a tuning parameter to allow the number of edges to rise with larger alpha values. Alpha values of 0.01, 0.05, 0.2, and 0.3 have been used for wood combustion data sets. For simulated data sets (see Sections 3.1 and S2†) alpha values of 0.05, 0.2, and 0.3 were used. For depth, values of 3 and −1 (describing unlimited depth) were used.

The PC-algorithm was used to search for potential cause variables (sources or sinks) for each measured compound (AMS: NO_3, POA1–2, SOA1–3, SMPS: NuclM, AitM, AccM, CoarM, PTR: factors PTR1–3, gas phase: NO, NO_2, O_3, OH). A crucial part of the causal discovery algorithm is the implementation of prior knowledge. We used prior information to restrict presumably impossible or negligible dependencies. The apparent *a priori* difference in prior information between the two aging types is that in dark aging, OH is not allowed to affect any of the variables; however, in photochemical aging, OH can affect other variables excluding those derived from the particle size distribution. OH was also forced to affect SOA3, which was characterized as OH radical formation products in a previous study.[13] Furthermore, the effects from size distribution variables on any other variables, POA on SOA, AMS variables on gas-phase variables, and negligible variables (those with small concentrations) on any other variable were not permitted. As the applied causal discovery algorithm is based on correlations, variables that have negligible effects on absolute concentrations could have been found to have large effects in this correlation-based search due to randomness. Allowed dependencies for causal discovery algorithm have been listed in Table 1.

Table 1 Allowed predictors for each response variable given for a causal discovery algorithm

Allowed dependencies	
Response variable $\Delta(x)$	Predictor variable
Dark aging	
Size variables (NuclM, AitM, AccM, CoarseM)	Size variables (NuclM, AitM, AccM, CoarseM)
SOA1–3	SOA1–3, NO_3, PTR1–3, gas-phase variables (NO, NO_2, O_3)
POA1–2, NO_3	POA1–2, SOA1–3, NO_3, PTR1–3, gas-phase variables (NO, NO_2, O_3)
PTR1-3, gas-phase variables (NO, NO_2, O_3)	PTR1-3, gas-phase variables (NO, NO_2, O_3)
Photochemical aging	
Size variables (NuclM, AitM, AccM CoarseM)	Size variables (NuclM, AitM, AccM, CoarseM)
SOA1–3	SOA1–3, NO_3, PTR1–3, gas-phase variables (NO, NO_2, O_3, OH)
POA1–2, NO_3	POA1–2, SOA1–3, NO_3, PTR1–3, gas-phase variables (NO, NO_2, O_3, OH)
PTR1–3, gas-phase variables (NO, NO_2, O_3, OH)	PTR1–3, gas-phase variables (NO, NO_2, O_3, OH)

2.2.2 Forming interaction variables. The causal discovery algorithm suggested several potential edges (*i.e.*, directed connections) between variables which were turned into interaction variables. We used the suggestion from the discovery algorithm as a starting point to form a final structure to be used in the model. For each variable Y, the algorithm provided a list of variables X that could cause Y, $X \rightarrow Y$. We used those variables X to form interaction variables for explaining Y.

Interaction variables predicting Y were formed by pairing potential causes of Y. Both paired variables needed to be suggested by the causal discovery algorithm. The only limitation for variables was that variable interactions were not allowed to violate prior assumptions, as explained in Section 2.2.1. For example, if it is known that Z cannot cause Y, it cannot be included in a list of interaction variables that could cause Y. In this step, we formed a list of potential interaction variables for each variable Y. Fig. 3b shows an example of the formation of interaction variables.

In addition to interaction variables, we also allowed some single variables to act as predictors. The evolution of the physical properties of particles and many chemical reactions typically involves more than, for example, just one compound or phase state, but there are exceptions. As an example, particles of the same size can coagulate during evolution and form larger particles.

Similar solutions appear in the literature. In chemical kinetics theory,[80] one or more variables react to form other compound(s). The changes in time of the produced compound's concentration can then be represented as a product of concentrations of reacting compounds multiplied by the rate coefficient and time t. Interaction variables and some single variables found by the algorithm were used to select suitable explanatory variables for the effects of variables to the response variable $\Delta(x)$.

The calculation of interaction variables may be performed directly by using all possible variables in the data set and then selecting suitable explanatory variables for each response variable from amongst all interaction variables. This can be performed by a causal discovery algorithm or some other method. However, if the number of initial (single) variables is n, then the number of possible two-variable interactions is $\binom{n}{2} = \frac{n!}{2!(n-2)!}$, which is large even for relatively small n. Therefore, a preselection of most potential variables to form these interaction variables reduces the number of interaction variables formed remarkably. The preselection is also justified because then we do not have clearly incorrect interaction variables in the next step (LASSO). We found out that the interaction variables can be highly correlated, therefore some clearly incorrect interaction variables could be selected, if all variables will be used for forming interaction variables.

2.2.3 Accounting for multicollinearity with LASSO. Interaction variables also give rise to some challenges for the selection of variables. Interaction variables are often highly correlated, as two interaction variables may share one common variable. Highly correlated variables can lead to multicollinearity in coefficient estimation. When data have a multicollinearity problem, coefficients of interaction variables might suffer from biases, and small changes in the model can lead to large changes in its output. Therefore, it is important to note the possibility of multicollinearity in predictors.

When interaction variables have been formed, there are usually many correlated variables that can explain each response variable $\Delta(x)$. We used LASSO regression (Bayesian approach[81] based on Park & Casella, 2008 (ref. 82)) to reduce the number of variables and multicollinearity in the set of explanatory variables. LASSO shrinks the coefficients of some redundant variables to be almost or equal to zero, and thus reduces the number of effective variables. Variables with coefficients close to zero were consequently excluded from the structure. Variables that had non-zero coefficients in the LASSO fit were used as predictor variables for $\Delta(x)$s. Coefficients of these variables were used as coefficients in the final model. Fig. 3b shows an example of the exclusion of some interaction variables after using LASSO.

Negative coefficients are only permitted when the measured value of a predicted variable is decreased due to the process, which is shown in the model as the interaction variable including the variable that is predicted itself. Without this limitation, the modeled value of a variable can fall below zero during a calculation, which is not physically realistic. If a variable with a negative coefficient does not have a predicted variable in the response variable, the model attempts to fix that by changing the predictor to one with a positive coefficient (usually negatively correlated with the original predictor) or to some interaction variable that includes the predicted variable.

2.2.4 Finding the best model and calculating the evolution based on the fit. We evaluated the model fit by calculating the evolution of the system based on the model's structure and estimated coefficients. We used the R package *deSolve*[77] to calculate the evolution of the modeled linear ordinary differential equation system. Selection of the best model was then performed based on that evolution. We calculated the Root Mean Squared Error (RMSE) for each variation of the tuning parameters (see Section 2.2.1 for description) and selected the model based on the smallest RMSE for the calculated evolution.

As we had only two data sets for both dark and light induced aging, we did not want to use separate data sets for training and evaluating the model fit. As the ignition type also affects, for example, the chemical composition of the emission,[13] evolution between the data sets might not be directly comparable. Therefore, we used both ignition types for searching for the structure and estimating the coefficients of the model.

2.3 Simulation studies

In order to validate our model, we fitted it first to simulated data mimicking combustion emissions and then to real measured data from wood combustion experiments. Details about data generation and experiments can be found in ESI S2, Tables 2 and S1.† For the case where the dependencies between variables are not completely known, causal discovery algorithms offer a solution to find missing causal pathways, noncausal dependencies, and covariances. As a causal discovery algorithm

Table 2 Datasets used in this study. Wood combustion datasets are measured datasets from the ILMARI environment (Tiitta *et al.*, 2016). Simulated datasets are completely artificial datasets representing the evolution of differential equation systems

	Dataset	How evolution is formed
Wood combustion datasets	2B and 3B	Dark aging experiments of wood combustion emission
	4B and 5B	Photochemical aging experiments of wood combustion emission
Simulated datasets	Small	Differential equation system using mass action kinetics
	Large	Differential equation system. Independent linear differential equations for each variable. System does not follow mass action kinetics

attempts to search for dependencies based on data, there might be incorrect dependencies in the structure formed by an algorithm. These can be due to, for example, uncertainties in the measured concentrations of variables, which can result in an observed dependence that is weak and therefore not selected for the model.

The atmospheric aging process of wood combustion emissions is one such case in which we have limited prior knowledge. For the reliability of the obtained results from our experimental data sets, it is important to know how the causal discovery algorithm combined with our model would function, if we had the information regarding the correct structure resulting from the aging process (see Table S1†). Thus, we simulated a data set representing our observations with known structures and connections in order to test and validate our model for combustion measurement-type data. The details of the simulations are provided in the ESI S2.†

3 Results

As the evolution of emission is known to be different in the dark and under UV aging conditions, experiments were separated based on the aging type. In addition, prior information was defined separately for dark and UV aging experiments (see Section 2.2.1).

The causal discovery algorithm was used for both dark aging experiments (the dark aging parts of 2B and 3B) using the data from the experiments as the input for the model. Similarly, the UV aging parts of 4B and 5B were used to search the structure for UV aging. Thus, both experiments with the same aging type have the same dependence structure between variables, and the coefficients for the experiments of the same aging type were the same. After estimating the coefficients, modeled evolution of the system was then calculated and compared to the measured evolution of the experiment. The best model based on tuning parameters (alpha and depth, details in Section 2.2) was then selected. The time point zero in each experiment represents the start of the aging period. As the full graph of the model holds so many connections, it is impossible to interpret. Thus, we show here only subsets of the full graph. Magnitudes of each effect are given in Table S8† for dark aging experiments and Table S9† for photochemical aging experiments.

For dark aging experiments, the sub-graph of the model showing dependencies for SOA variables is shown in Fig. 4. Coefficients for the edges are provided in the ESI.† For SOA, most of the edges connected seem to be possible causes.

For SOA1, the main increase of the concentration is due to the reaction with ozone ($O_3 \times SOA1 \rightarrow SOA1$). The benefit of this type of model is that the variables in the model can be act at the same time as outcomes and predictor variables for some other variable. More specifically, the current level of a variable can be the predictor for the level at the next time point. *e.g.* in the example of $O_3 \times SOA1$, reactions of existing SOA1 with O_3 decrease the level of SOA1. If, in turn, SOA1 reacts with NO_3, it increases the level of SOA1.

In SOA2, organic nitrates are present which were formed through oxidation of organic emission constituents by nitrate radicals ($NO_2 \times SOA2 \rightarrow SOA2$). For SOA3, the change in concentration is minor compared to that of SOA2 during dark aging. According to the model, some increase in SOA2 and SOA3 occurs due to ozone reactions ($O_3 \times SOA2 \rightarrow SOA2$ and $O_3 \times SOA3 \rightarrow SOA3$). Based on Tiitta *et al.* (2016),[13] SOA1 is formed by

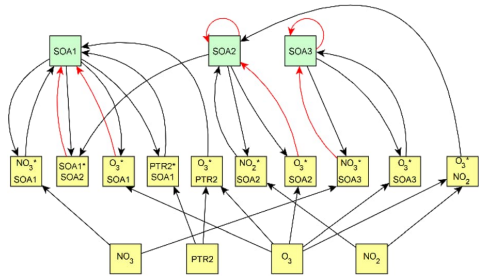

Fig. 4 Secondary organic aerosol (SOA)-related part of the causal graph for dark aging experiments. SOA variables are highlighted in green. O_3 and NO_2 are measured from the gas phase, PTR2 is formed from Proton-Transfer-Reactor Time-of-Flight Mass Spectrometer (PTR-ToF-MS) measurements, and NO_3 signatured aerosol and SOA1–3 are given by particle-phase measurements with an Aerosol Mass Spectrometer (AMS). PTR2 represents photochemical aging products and SOA factors represents (1) formation by ozonolysis, (2) formation by nitrate/peroxy radicals, and (3) formation by OH radicals. The color of the arrow represents the sign of the effect, black arrows have positive coefficient and red arrows have negative.

ozonolysis, SOA2 is formed by NO_3 and RO_3 radicals, and SOA3 is formed by OH radicals. SOA3 is mostly formed during the UV aging period; hence the edges related to SOA3 during the dark aging period are not very important.

Fig. 5 shows that the evolution based on the model for both experiments follow the measured evolution well for SOA2, but for SOA1 the model was not able to accurately describe the evolution. In general, some factors (SOA1, SOA3, and PTR2) have minor differences between the measured and modeled evolutions in one or both experiments. Differences between the evolution calculated based on the Lasso approach and Jackknife resampling with OLS in *e.g.* Fig. 5 are most likely due to the differences in estimation methods which causes differences in estimated coefficients and hence, the modeled evolution. All coefficients for the dark aging model and figures for other variables can be found in the ESI file (Table S8 and Fig. S2–S4).†

Fig. 6 shows the subgraph of the dependences for particle-size variables. Most of the coefficients are as expected: variables affecting themselves have negative coefficients, thus possibly relating to the coagulation of particles of the same size and hence decreasing the number concentration of the size class. In addition, there are usually negative coefficient for reactions of

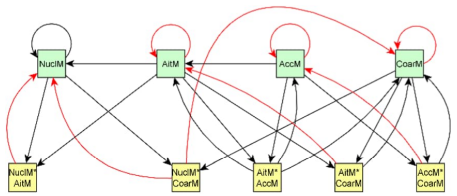

Fig. 6 Particle size related part of the causal graph for dark aging experiments. Particle-size related variables (nucleation mode (NuclM, <25 nm), Aitken mode (AitM, 25–100 nm), accumulation mode (AccM, 100–300 nm), and coarse mode (CoarseM, >300 nm)), are highlighted in green and yellow squares represent interaction variables. All variables are measured using a Scanning Mobility Particle Sizer (SMPS). The color of the arrow represents the sign of the effect; black arrows represent the positive coefficient and red arrows the negative coefficient.

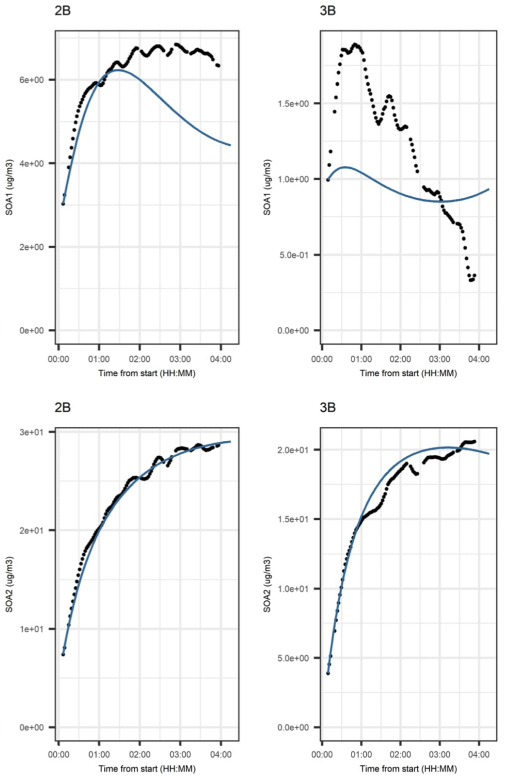

Fig. 5 Evolution of secondary organic aerosol (SOA) factors 1 and 2 from Aerosol Mass Spectrometer (AMS) particle-phase measurements in dark aging experiments. SOA factors represent (1) formation by ozonolysis, and (2) formation by nitrate/peroxy radicals. Black points represent the filtered version of variable and the blue line shows the modeled evolution.

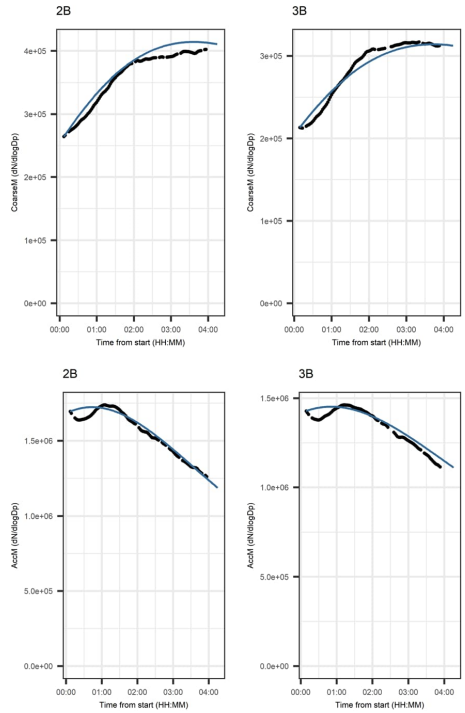

Fig. 7 Evolution of the number concentration of coarse (CoarseM, >300 nm) and accumulation mode (AccM, 100–300 nm) particles in dark aging experiments. Black points represent the filtered version of variables and the blue line shows the modeled evolution. For photochemical aging experiments, the difference between the measured and modeled evolution is slightly larger than for dark aging experiments. The largest differences between measured and modeled evolutions were in variables NO and NO_2 on both experiments.

a variable with a larger size mode, e.g. NuclM × CoarM → NuclM possibly due to coagulation of nucleation mode particles with coarse mode particles. Positive coefficients are mostly related to reactions with smaller sized particles, possibly due to the coagulation of particles resulting in larger particles (*e.g.* AitM × CoarM → CoarM and AccM × CoarM → CoarM). However, there are some dependencies that do not follow the expectations listed above. As seen in Fig. 7, the modeled evolution is in agreement with the measured one in both experiments. Fig. 8 shows the graph for SOA variables in photochemical aging experiments. For SOA3, which has the most significant increase during the experiments, reactions of O_3 with PTR1 and PTR1 (primary VOCs) and OH reacting with SOA3 are the most important sources. Formation by OH is suggested in Tiitta *et al.* (2016).[13] SOA1 is also related to OH and O_3 during photochemical aging, whereas SOA2 is mostly related to reactions with gas-phase products of PTR2 (nitrate/peroxy radicals). Edges O_3 → SOA1 and PTR2 → SOA2 are in line with Tiitta *et al.* (2016),[13] whereas OH → SOA1 is not suggested there. Fig. 9 shows the evolution of PTR3 and SOA3. All coefficients for the photochemical aging model and figures for other variables not shown here can be found in the ESI file (ESI S4, Table S9 and Fig. S5–S7).†

Fig. 10 shows the subgraph of the dependencies for particle-size variables in photochemical aging experiments. As also seen in dark aging experiments (Fig. 6), most of the estimated coefficients follow the same expectations as listed in a paragraph discussing particle-size variables during dark aging experiments. However, there are also some coefficients that do not conform to expectations. As in the dark aging experiments,

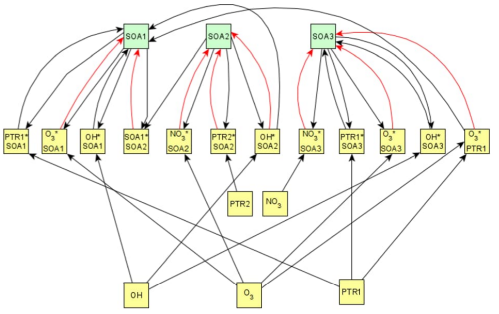

Fig. 8 Secondary organic aerosol (SOA)-related part of the causal graph for photochemical aging experiments. SOA factors 1–3 whose evolution is described by other variables are highlighted in green. O_3 is measured from the gas phase, factors PTR1–2 are formed from Proton-Transfer-Reactor Time-of-Flight Mass Spectrometer (PTR-ToF-MS) measurements, the hydroxyl radical (OH) is derived from d9-butanol concentrations, and NO_3 signatured aerosol and SOA1–3 are given by particle-phase measurements with an Aerosol Mass Spectrometer (AMS). PTR factors represent (1) primary VOCs and (2) photochemical aging products and SOA factors represent (1) formation by ozonolysis, (2) formation by nitrate/peroxy radicals, and (3) formation by OH radicals. The color of the arrow represents the sign of the effect, black arrows represent the positive coefficient and red arrows the negative coefficient.

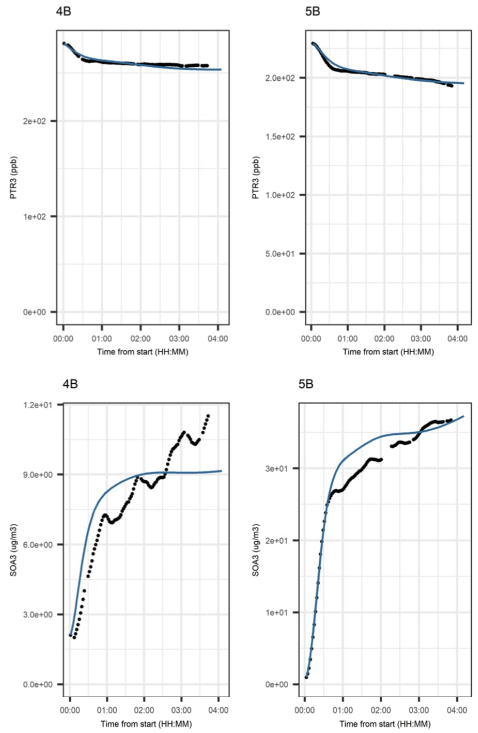

Fig. 9 Evolution of PTR3 and SOA3 factors in photochemical aging experiments. PTR3 is a factor derived from Proton-Transfer-Reactor Time-of-Flight Mass Spectrometer (PTR-ToF-MS) measurements and represents dark aging products; SOA3 is a secondary organic aerosol (SOA) factor derived from Aerosol Mass Spectrometer (AMS) particle-phase measurements and represents compounds that are formed by hydroxyl (OH) radicals. PTR3 represents dark aging products and SOA3 represents formation by OH radicals. Black points represent the filtered version of variable and the blue line shows the modeled evolution.

there are some positive coefficients between a single variable and a smaller size class (here CoarM → NuclM, CoarM → AccM, and AitM → NuclM) that should be negative due to coagulation. Some interactions between smaller size classes should not physically have a large effect on larger size class number concentration, *e.g.* NuclM × AitM → CoarM. In addition, in photochemical experiments, the evolution of larger particles is well captured by the model (Fig. 11).

Simulated data mimicking the combustion emissions was used to validate model performance. The aim was to test how the method (causal discovery algorithm + interaction variables + LASSO, see Section 2.2.1) would perform in a situation in which we know the system, in terms of both causal connections between the variables and how the system has evolved during the observation time.

Detailed results from the simulation studies are presented in ESI S3.† In general, we found that most of the dependencies that the algorithm found were correct, or the predictor variables

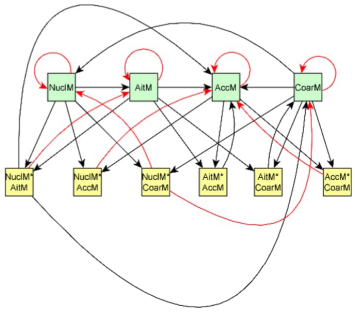

Fig. 10 Particle-size related part of the causal graph for photochemical aging experiments. Particle-size related variables (nucleation mode (NuclM, <25 nm), Aitken mode (AitM, 25–100 nm), accumulation mode (AccM, 100–300 nm), and coarse mode (CoarseM, >300 nm)) are highlighted in green; yellow squares represent interaction variables. All variables are measured using a Scanning Mobility Particle Sizer (SMPS). The color of the arrow represents the sign of the effect; black arrows represent positive coefficient and red arrows the negative coefficient.

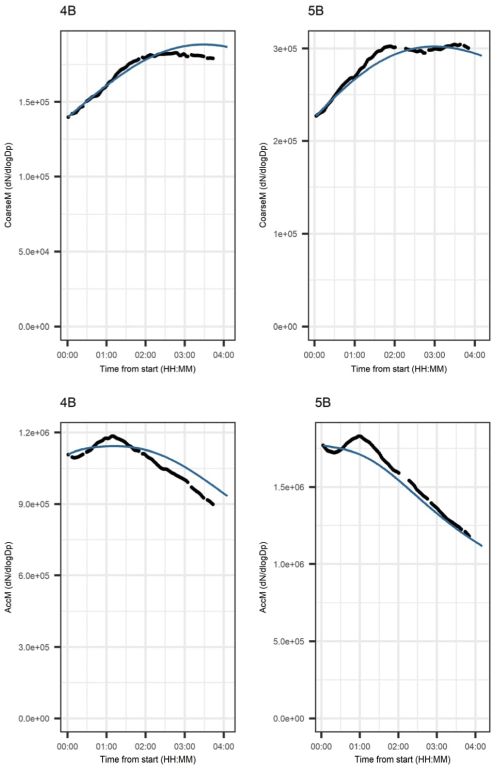

Fig. 11 Evolution of the number concentration of coarse (CoarseM, >300 nm) and accumulation mode (AccM, 100–300 nm) particles in photochemical aging experiments. Black points represent the filtered version of the variable and the blue line shows the modeled evolution.

that were suggested to cause a change in the variable $\Delta(x)$ had a high correlation with the correct cause. We also found that correct prior information could increase the fraction of exactly correct edges.

We also tested whether it was necessary to use a filtering method for "measured" (simulated + the error mimicking measurement uncertainty) time series before applying a causal discovery algorithm. We found that the filtering method we used for time series reduced the error in the fit when the uncertainty related to the variable was high (Fig. S1†). Also, filtering improved the accuracy of the suggested causal structure if the observed noise in measurements was relatively high.

4 Summary and conclusions

In this study, we showed that a statistical model created for aging of small-scale wood combustion data was able to describe the complex evolution of combustion emissions. Dependencies between the observed time series were studied using a causal discovery algorithm, which provides information on the measured data in two levels of detail. It offers a method to detect the dependencies between variables in measured data and find potential causes for the observed dependencies in the data set. The model was first fitted on simulated data in order to test the accuracy of the fit, the prediction ability of the model, and how the dependency structure is formed for data with known properties. Following that test, the model was fitted on a small-scale wood combustion data set to examine how it performs with real observations. Predictive accuracy of the model can be considered a reasonable measure for many possible applications, where an explicit causal understanding of the system is not needed. Model creation is described step-by-step in Section 2.2 and the solving of the model is based on differential equations (for which the relevant coefficients can be found in Tables S7 and S8†).

As atmospheric measurement data contain large uncertainties, and our measurements of combustion emissions and their aging are no exception, we studied how these uncertainties affect our model by using simulated data sets (see ESI S2, Tables S4 and S5†). Based on the simulations, we filtered the initial time series before applying the model and could reduce the error related to the measurement process, thus making the model and the obtained structure more accurate (see ESI S2 and Fig. S1†). We recommend considering the errors in similar future studies by filtering the data.

With carefully planned chamber experiments in a state-of-the-art facility, we were able to study the dependencies between all measured variables and differentiating correct predictors to explain the variables of interest from variables just covarying with them. This was achieved by controlling the number of compounds such that only a limited number of the possible explaining variables were able to affect the variable of interest. It was then possible to measure whether the supposed interaction between compounds/variables was present or not. It is evident that the modeling of the complete structure and correct causal paths of the evolution of combustion emissions require more initial knowledge about the dependencies

between the different gaseous and particulate matter. Additionally, increasing the number of experiments in the model validation would likely lead to a better result, as some of the dependencies detected in some experiments can be neglected in other experiments if those are not causal.

For wood combustion emission experiments, the modeled evolution successfully mimicked the evolution measured in the chamber. Some varying practices in the experiments, such as the ignition type and the resulting changes in combustion efficiency, can affect the composition of the PTR-MS and AMS factors. This might result in varying coefficients in different experiments. Taking this into account, the model described the evolution in the experiments well. Recently, there have been multiple studies applying various dimension reduction techniques on oxidation chamber data sets illustrating that the selection of the technique can have a large impact on the interpretation of the results.[62,83–85] For this type of study (aging of the emission by oxidation), an ideal factorization would include the oxidation products from the same generation in one factor. However, more detailed investigation of the most suitable dimension reduction technique is beyond the scope of this work. In future development of the model, however, the choice of dimension reduction technique should be investigated in more detail.

The presented model used temporal evolution of the compounds in (1) factors calculated for particle- and gas-phase mass spectrometer data and (2) forming a structure for dependencies between compound groups and some specific compounds. It must be acknowledged that our model is not based on the explicit details of the chemical formulae of the compounds nor on the number of carbon and oxygen of the species as is, for example, SOM. In the case of complex systems such as wood combustion, which contains hundreds to thousands of different emission species, explicit knowledge is not available. Thus, the data-based model introduced here can provide important information for further studies on the detailed chemistry of the combustion process.

Based on the simulated experiments, the model captures the evolution well. Most of the dependencies between the variables without causal attribution in the simulated model are co-varying with at least some of the dependencies assumed as causal by the researchers. Due to complex chemistry behind the measured data and a great number of compounds and phenomena not measured in our study, the results of the model cannot directly be interpreted as the causal evolution of the combustion emissions in the atmospheric chamber. However, it can still be taken as a good description of the process. In addition, based on the simulations (see ESI, Tables S6 and S7†), the model could process prior information more efficiently, which is a topic for further development of the model.

The model introduced here provides a step towards a more complete understanding of variable interactions in laboratory experiments considering atmospheric aging. With the introduced model, the dependencies between variables can be detected with lower computational cost than the detailed chemistry models would require. The results of the model give new insight on the data itself and give prior information for more detailed chemical analyses. More research and different observational data sets are still needed for more precise quantification of the dependence structure between the studied variables.

Code and data availability

Codes and data related to this manuscript have been published in Zenodo (DOI: 10.5281/zenodo.7220521).

Author contributions

SM and JK developed the idea of the study. PT, HC, OS, and AL carried out wood combustion experiments. VL, SM and JK developed the model with substance input from HC, PT and OS. VL and SI performed the data analysis. VL prepared the manuscript with contributions from all co-authors.

Conflicts of interest

The authors declare that they have no conflict of interest.

Acknowledgements

This work was supported by the Academy of Finland Centre of Excellence (grant no. 307331), Academy of Finland Flagship funding (grant no. 337550), the Academy of Finland Competitive funding to strengthen university research profiles (PROFI) for the University of Eastern Finland (grant no. 325022) and for the University of Jyväskylä (grant no. 311877) and the Nessling foundation. Data collection for this study has been partly funded by the European Union's 10 Horizon 2020 Research and Innovation Programme through the EUROCHAMP-2020 Infrastructure Activity (grant no. 730997). Funding sources have no involvement in study design, data analysis, or preparation of the manuscript.

References

1 R. L. Cordell, M. Mazet, C. Dechoux, S. M. L. Hama, J. Staelens, J. Hofman, C. Stroobants, E. Roekens, G. P. A. Kos, E. P. Weijers, K. F. A. Frumau, P. Panteliadis, T. Delaunay, K. P. Wyche and P. S. Monks, Evaluation of biomass burning across North West Europe and its impact on air quality, *Atmos. Environ.*, 2016, **141**, 276–286.

2 M. Glasius, A. M. K. Hansen, M. Claeys, J. S. Henzing, A. D. Jedynska, A. Kasper-Giebl, M. Kistler, K. Kristensen, J. Martinsson, W. Maenhaut, J. K. Nøjgaard, G. Spindler, K. E. Stenström, E. Swietlicki, S. Szidat, D. Simpson and K. E. Yttri, Composition and sources of carbonaceous aerosols in Northern Europe during winter, *Atmos. Environ.*, 2018, **173**, 127–141.

3 R. M. Qadir, J. Schnelle-Kreis, G. Abbaszade, J. M. Arteaga-Salas, J. Diemer and R. Zimmermann, Spatial and temporal variability of source contributions to ambient PM10 during winter in Augsburg, Germany using organic and inorganic tracers, *Chemosphere*, 2014, **103**, 263–273.

4 J. Hovorka, P. Pokorná, P. K. Hopke, K. Křůmal, P. Mikuška and M. Píšová, Wood combustion, a dominant source of winter aerosol in residential district in proximity to a large automobile factory in Central Europe, *Atmos. Environ.*, 2015, **113**, 98–107.

5 C. Reche, M. Viana, F. Amato, A. Alastuey, T. Moreno, R. Hillamo, K. Teinilä, K. Saarnio, R. Seco, J. Peñuelas, C. Mohr, A. S. H. Prévôt and X. Querol, Biomass burning contributions to urban aerosols in a coastal Mediterranean City, *Sci. Total Environ.*, 2012, **427–428**, 175–190.

6 J. Orasche, T. Seidel, H. Hartmann, J. Schnelle-Kreis, J. C. Chow, H. Ruppert and R. Zimmermann, Comparison of Emissions from Wood Combustion. Part 1: Emission Factors and Characteristics from Different Small-Scale Residential Heating Appliances Considering Particulate Matter and Polycyclic Aromatic Hydrocarbon (PAH)-Related Toxicological Potential of Particle-Bound Organic Species, *Energy Fuels*, 2012, **26**, 6695–6704.

7 J. Tissari, O. Sippula, J. Kouki, K. Vuorio and J. Jokiniemi, Fine Particle and Gas Emissions from the Combustion of Agricultural Fuels Fired in a 20 kW Burner, *Energy Fuels*, 2008, **22**, 2033–2042.

8 A. K. Frey, K. Saarnio, H. Lamberg, F. Mylläri, P. Karjalainen, K. Teinilä, S. Carbone, J. Tissari, V. Niemelä, A. Häyrinen, J. Rautiainen, J. Kytömäki, P. Artaxo, A. Virkkula, L. Pirjola, T. Rönkkö, J. Keskinen, J. Jokiniemi and R. Hillamo, Optical and Chemical Characterization of Aerosols Emitted from Coal, Heavy and Light Fuel Oil, and Small-Scale Wood Combustion, *Environ. Sci. Technol.*, 2014, **48**, 827–836.

9 U. Dusek, G. P. Frank, A. Massling, K. Zeromskiene, Y. Iinuma, O. Schmid, G. Helas, T. Hennig, A. Wiedensohler and M. O. Andreae, Water uptake by biomass burning aerosol at sub- and supersaturated conditions: closure studies and implications for the role of organics, *Atmos. Chem. Phys.*, 2011, **11**, 9519–9532.

10 A. Kocbach Bølling, J. Pagels, K. Yttri, L. Barregard, G. Sallsten, P. E. Schwarze and C. Boman, Health effects of residential wood smoke particles: the importance of combustion conditions and physicochemical particle properties, *Part. Fibre Toxicol.*, 2009, **6**, 29.

11 M. Hallquist, J. C. Wenger, U. Baltensperger, Y. Rudich, D. Simpson, M. Claeys, J. Dommen, N. M. Donahue, C. George, A. H. Goldstein, J. F. Hamilton, H. Herrmann, T. Hoffmann, Y. Iinuma, M. Jang, M. E. Jenkin, J. L. Jimenez, A. Kiendler-Scharr, W. Maenhaut, G. McFiggans, T. F. Mentel, A. Monod, A. S. H. Prévôt, J. H. Seinfeld, J. D. Surratt, R. Szmigielski and J. Wildt, The formation, properties and impact of secondary organic aerosol: current and emerging issues, *Atmos. Chem. Phys.*, 2009, **9**, 5155–5236.

12 U. Pöschl, Atmospheric Aerosols: Composition, Transformation, Climate and Health Effects, *Angew. Chem., Int. Ed.*, 2005, **44**, 7520–7540.

13 P. Tiitta, A. Leskinen, L. Hao, P. Yli-Pirilä, M. Kortelainen, J. Grigonyte, J. Tissari, H. Lamberg, A. Hartikainen, K. Kuuspalo, A.-M. Kortelainen, A. Virtanen, K. E. J. Lehtinen, M. Komppula, S. Pieber, A. S. H. Prévôt, T. B. Onasch, D. R. Worsnop, H. Czech, R. Zimmermann, J. Jokiniemi and O. Sippula, Transformation of logwood combustion emissions in a smog chamber: formation of secondary organic aerosol and changes in the primary organic aerosol upon daytime and nighttime aging, *Atmos. Chem. Phys.*, 2016, **16**, 13251–13269.

14 A. Bertrand, G. Stefenelli, E. A. Bruns, S. M. Pieber, B. Temime-Roussel, J. G. Slowik, A. S. H. Prévôt, H. Wortham, I. El Haddad and N. Marchand, Primary emissions and secondary aerosol production potential from woodstoves for residential heating: influence of the stove technology and combustion efficiency, *Atmos. Environ.*, 2017, **169**, 65–79.

15 E. A. Bruns, M. Krapf, J. Orasche, Y. Huang, R. Zimmermann, L. Drinovec, G. Močnik, I. El-Haddad, J. G. Slowik, J. Dommen, U. Baltensperger and A. S. H. Prévôt, Characterization of primary and secondary wood combustion products generated under different burner loads, *Atmos. Chem. Phys.*, 2015, **15**, 2825–2841.

16 J. K. Kodros, D. K. Papanastasiou, M. Paglione, M. Masiol, S. Squizzato, K. Florou, K. Skyllakou, C. Kaltsonoudis, A. Nenes and S. N. Pandis, Rapid dark aging of biomass burning as an overlooked source of oxidized organic aerosol, *Proc. Natl. Acad. Sci. U. S. A.*, 2021, **117**, 33028–33033.

17 E. Z. Nordin, O. Uski, R. Nyström, P. Jalava, A. C. Eriksson, J. Genberg, P. Roldin, C. Bergvall, R. Westerholm, J. Jokiniemi, J. H. Pagels, C. Boman and M.-R. Hirvonen, Influence of ozone initiated processing on the toxicity of aerosol particles from small scale wood combustion, *Atmos. Environ.*, 2015, **102**, 282–289.

18 L. Künzi, P. Mertes, S. Schneider, N. Jeannet, C. Menzi, J. Dommen, U. Baltensperger, A. S. H. Prévôt, M. Salathe, M. Kalberer and M. Geiser, Responses of lung cells to realistic exposure of primary and aged carbonaceous aerosols, *Atmos. Environ.*, 2013, **68**, 143–150.

19 J. Martinsson, A. C. Eriksson, I. E. Nielsen, V. B. Malmborg, E. Ahlberg, C. Andersen, R. Lindgren, R. Nyström, E. Z. Nordin, W. H. Brune, B. Svenningsson, E. Swietlicki, C. Boman and J. H. Pagels, Impacts of Combustion Conditions and Photochemical Processing on the Light Absorption of Biomass Combustion Aerosol, *Environ. Sci. Technol.*, 2015, **49**, 14663–14671.

20 N. K. Kumar, J. C. Corbin, E. A. Bruns, D. Massabó, J. G. Slowik, L. Drinovec, G. Močnik, P. Prati, A. Vlachou, U. Baltensperger, M. Gysel, I. El-Haddad and A. S. H. Prévôt, Production of particulate brown carbon during atmospheric aging of residential wood-burning emissions, *Atmos. Chem. Phys.*, 2018, **18**, 17843–17861.

21 M. L. Hinks, J. Montoya-Aguilera, L. Ellison, P. Lin, A. Laskin, J. Laskin, M. Shiraiwa, D. Dabdub and S. A. Nizkorodov, Effect of relative humidity on the composition of secondary organic aerosol from the oxidation of toluene, *Atmos. Chem. Phys.*, 2018, **18**, 1643–1652.

22 Y. Li, U. Pöschl and M. Shiraiwa, Molecular corridors and parameterizations of volatility in the chemical evolution of organic aerosols, *Atmos. Chem. Phys.*, 2016, **16**, 3327–3344.

23 S. M. Platt, I. El Haddad, A. A. Zardini, M. Clairotte, C. Astorga, R. Wolf, J. G. Slowik, B. Temime-Roussel, N. Marchand, I. Ježek, L. Drinovec, G. Močnik, O. Möhler, R. Richter, P. Barmet, F. Bianchi, U. Baltensperger and A. S. H. Prévôt, Secondary organic aerosol formation from gasoline vehicle emissions in a new mobile environmental reaction chamber, *Atmos. Chem. Phys.*, 2013, **13**, 9141–9158.

24 A. T. Lambe, P. S. Chhabra, T. B. Onasch, W. H. Brune, J. F. Hunter, J. H. Kroll, M. J. Cummings, J. F. Brogan, Y. Parmar, D. R. Worsnop, C. E. Kolb and P. Davidovits, Effect of oxidant concentration, exposure time, and seed particles on secondary organic aerosol chemical composition and yield, *Atmos. Chem. Phys.*, 2015, **15**, 3063–3075.

25 I. J. Keyte, R. M. Harrison and G. Lammel, Chemical reactivity and long-range transport potential of polycyclic aromatic hydrocarbons – a review, *Chem. Soc. Rev.*, 2013, **42**, 9333.

26 R. Atkinson, Atmospheric chemistry of VOCs and NO(x), *Atmos. Environ.*, 2000, **34**, 2063–2101.

27 V. Vakkari, V.-M. Kerminen, J. P. Beukes, P. Tiitta, P. G. van Zyl, M. Josipovic, A. D. Venter, K. Jaars, D. R. Worsnop, M. Kulmala and L. Laakso, Rapid changes in biomass burning aerosols by atmospheric oxidation, *Geophys. Res. Lett.*, 2014, **41**, 2644–2651.

28 A. Kiendler-Scharr, A. A. Mensah, E. Friese, D. Topping, E. Nemitz, A. S. H. Prevot, M. Äijälä, J. Allan, F. Canonaco, M. Canagaratna, S. Carbone, M. Crippa, M. Dall Osto, D. A. Day, P. De Carlo, C. F. Di Marco, H. Elbern, A. Eriksson, E. Freney, L. Hao, H. Herrmann, L. Hildebrandt, R. Hillamo, J. L. Jimenez, A. Laaksonen, G. McFiggans, C. Mohr, C. O'Dowd, R. Otjes, J. Ovadnevaite, S. N. Pandis, L. Poulain, P. Schlag, K. Sellegri, E. Swietlicki, P. Tiitta, A. Vermeulen, A. Wahner, D. Worsnop and H.-C. Wu, Ubiquity of organic nitrates from nighttime chemistry in the European submicron aerosol, *Geophys. Res. Lett.*, 2016, **43**, 7735–7744.

29 G. Isaacman-Vanwertz, P. Massoli, R. O'Brien, C. Lim, J. P. Franklin, J. A. Moss, J. F. Hunter, J. B. Nowak, M. R. Canagaratna, P. K. Misztal, C. Arata, J. R. Roscioli, S. T. Herndon, T. B. Onasch, A. T. Lambe, J. T. Jayne, L. Su, D. A. Knopf, A. H. Goldstein, D. R. Worsnop and J. H. Kroll, Chemical evolution of atmospheric organic carbon over multiple generations of oxidation, *Nat. Chem.*, 2018, **10**, 462–468.

30 A. Hartikainen, P. Yli-Pirilä, P. Tiitta, A. Leskinen, M. Kortelainen, J. Orasche, J. Schnelle-Kreis, K. E. J. Lehtinen, R. Zimmermann, J. Jokiniemi and O. Sippula, Volatile Organic Compounds from Logwood Combustion: Emissions and Transformation under Dark and Photochemical Aging Conditions in a Smog Chamber, *Environ. Sci. Technol.*, 2018, **52**, 4979–4988.

31 A. Hartikainen, P. Tiitta, M. Ihalainen, P. Yli-Pirilä, J. Orasche, H. Czech, M. Kortelainen, H. Lamberg, H. Suhonen, H. Koponen, L. Hao, R. Zimmermann, J. Jokiniemi, J. Tissari and O. Sippula, Photochemical transformation of residential wood combustion emissions: dependence of organic aerosol composition on OH exposure, *Atmos. Chem. Phys.*, 2020, **20**, 6357–6378.

32 D. S. Tkacik, E. S. Robinson, A. Ahern, R. Saleh, C. Stockwell, P. Veres, I. J. Simpson, S. Meinardi, D. R. Blake, R. J. Yokelson, A. A. Presto, R. C. Sullivan, N. M. Donahue and A. L. Robinson, A dual-chamber method for quantifying the effects of atmospheric perturbations on secondary organic aerosol formation from biomass burning emissions, *J. Geophys. Res. Atmos.*, 2017, **122**, 6043–6058.

33 N. M. Donahue, A. L. Robinson, C. O. Stanier and S. N. Pandis, Coupled partitioning, dilution, and chemical aging of semivolatile organics, *Environ. Sci. Technol.*, 2006, **40**, 2635–2643.

34 N. M. Donahue, S. A. Epstein, S. N. Pandis and A. L. Robinson, A two-dimensional volatility basis set: 1. organic-aerosol mixing thermodynamics, *Atmos. Chem. Phys.*, 2011, **11**, 3303–3318.

35 G. Ciarelli, I. El Haddad, E. Bruns, S. Aksoyoglu, O. Möhler, U. Baltensperger and A. S. H. Prévôt, Constraining a hybrid volatility basis-set model for aging of wood-burning emissions using smog chamber experiments: a box-model study based on the VBS scheme of the CAMx model (v5.40), *Geosci. Model Dev.*, 2017, **10**, 2303–2320.

36 E. A. Bruns, I. El Haddad, J. G. Slowik, D. Kilic, F. Klein, U. Baltensperger and A. S. H. Prévôt, Identification of significant precursor gases of secondary organic aerosols from residential wood combustion, *Sci. Rep.*, 2016, **6**, 1–9.

37 A. L. Robinson, N. M. Donahue, M. K. Shrivastava, E. A. Weitkamp, A. M. Sage, A. P. Grieshop, T. E. Lane, J. R. Pierce and S. N. Pandis, Rethinking Organic Aerosols: Semivolatile Emissions and Photochemical Aging, *Science*, 2007, **315**, 1259–1262.

38 B. Zhao, S. Wang, N. M. Donahue, W. Chuang, L. H. Ruiz, N. L. Ng, Y. Wang and J. Hao, Evaluation of one-dimensional and two-dimensional volatility basis sets in simulating the aging of secondary organic aerosol with smog-chamber experiments, *Environ. Sci. Technol.*, 2015, **49**, 2245–2254.

39 S. H. Jathar, T. D. Gordona, C. J. Hennigan, H. O. T. Pye, G. Pouliot, P. J. Adams, N. M. Donahue and A. L. Robinson, Unspeciated organic emissions from combustion sources and their influence on the secondary organic aerosol budget in the United States, *Proc. Natl. Acad. Sci. U. S. A.*, 2014, **111**, 10473–10478.

40 S. H. Jathar, N. M. Donahue, P. J. Adams and A. L. Robinson, Testing secondary organic aerosol models using smog chamber data for complex precursor mixtures: influence of precursor volatility and molecular structure, *Atmos. Chem. Phys.*, 2014, **14**, 5771–5780.

41 G. Stefenelli, J. Jiang, A. Bertrand, E. A. Bruns, S. M. Pieber, U. Baltensperger, N. Marchand, S. Aksoyoglu, A. S. H. Prévôt, J. G. Slowik and I. El Haddad, Secondary organic aerosol formation from smoldering and flaming combustion of biomass: a box model parametrization based on volatility basis set, *Atmos. Chem. Phys.*, 2019, **19**, 11461–11484.

42 G. Ciarelli, S. Aksoyoglu, I. El Haddad, E. A. Bruns, M. Crippa, L. Poulain, M. Äijälä, S. Carbone, E. Freney, C. O'Dowd, U. Baltensperger and A. S. H. Prévôt, Modelling winter organic aerosol at the European scale with CAMx: evaluation and source apportionment with a VBS parameterization based on novel wood burning smog chamber experiments, *Atmos. Chem. Phys.*, 2017, **17**, 7653–7669.

43 G. Ciarelli, S. Aksoyoglu, M. Crippa, J. L. Jimenez, E. Nemitz, K. Sellegri, M. Äijälä, S. Carbone, C. Mohr, C. O'dowd, L. Poulain, U. Baltensperger and A. S. H. Prévôt, Evaluation of European air quality modelled by CAMx including the volatility basis set scheme, *Atmos. Chem. Phys.*, 2016, **16**, 10313–10332.

44 S. M. Saunders, M. E. Jenkin, R. G. Derwent and M. J. Pilling, Protocol for the development of the Master Chemical Mechanism, MCM v3 (Part A): tropospheric degradation of non-aromatic volatile organic compounds, *Atmos. Chem. Phys.*, 2003, **3**, 161–180.

45 M. E. Jenkin, S. M. Saunders and M. J. Pilling, The tropospheric degradation of volatile organic compounds: a protocol for mechanism development, *Atmos. Environ.*, 1997, **31**, 81–104.

46 B. Aumont, S. Szopa and S. Madronich, Modelling the evolution of organic carbon during its gas-phase tropospheric oxidation: development of an explicit model based on a self generating approach, *Atmos. Chem. Phys.*, 2005, **5**, 2497–2517.

47 M. M. Coggon, C. Y. Lim, A. R. Koss, K. Sekimoto, B. Yuan, J. B. Gilman, D. H. Hagan, V. Selimovic, K. J. Zarzana, S. S. Brown, J. M. Roberts, M. Müller, R. Yokelson, A. Wisthaler, J. E. Krechmer, J. L. Jimenez, C. Cappa, J. H. Kroll, J. de Gouw and C. Warneke, OH chemistry of non-methane organic gases (NMOGs) emitted from laboratory and ambient biomass burning smoke: evaluating the influence of furans and oxygenated aromatics on ozone and secondary NMOG formation, *Atmos. Chem. Phys.*, 2019, **19**, 14875–14899.

48 C. D. Cappa and K. R. Wilson, Multi-generation gas-phase oxidation, equilibrium partitioning, and the formation and evolution of secondary organic aerosol, *Atmos. Chem. Phys.*, 2012, **12**, 9505–9528.

49 A. Akherati, Y. He, M. M. Coggon, A. R. Koss, A. L. Hodshire, K. Sekimoto, C. Warneke, J. De Gouw, L. Yee, J. H. Seinfeld, T. B. Onasch, S. C. Herndon, W. B. Knighton, C. D. Cappa, M. J. Kleeman, C. Y. Lim, J. H. Kroll, J. R. Pierce and S. H. Jathar, Oxygenated Aromatic Compounds are Important Precursors of Secondary Organic Aerosol in Biomass-Burning Emissions, *Environ. Sci. Technol.*, 2020, **54**, 8568–8579.

50 J. Pearl, *Causality: Models, Reasoning and Inference*, Cambridge University Press, 2009.

51 C. Krich, J. Runge, D. G. Miralles, M. Migliavacca, O. Perez-Priego, T. El-Madany, A. Carrara and M. D. Mahecha, Estimating causal networks in biosphere-atmosphere interaction with the PCMCI approach, *Biogeosciences*, 2020, **17**, 1033–1061.

52 J. Runge, P. Nowack, M. Kretschmer, S. Flaxman and D. Sejdinovic, Detecting and quantifying causal associations in large nonlinear time series datasets, *Sci. Adv.*, 2019, **5**, DOI: **10.1126/sciadv.aau4996**.

53 J. Runge, V. Petoukhov, J. F. Donges, J. Hlinka, N. Jajcay, M. Vejmelka, D. Hartman, N. Marwan, M. Paluš and J. Kurths, Identifying causal gateways and mediators in complex spatio-temporal systems, *Nat. Commun.*, 2015, **6**, 8502.

54 S. M. Samarasinghe, Y. Deng and I. Ebert-Uphoff, *J. Atmos. Sci.*, 2020, **77**, 925–941.

55 I. Ebert-Uphoff and Y. Deng, Causal discovery in the geosciences—using synthetic data to learn how to interpret results, *Comput. Geosci.*, 2017, **99**, 50–60.

56 A. Leskinen, P. Yli-Pirilä, K. Kuuspalo, O. Sippula, P. Jalava, M.-R. Hirvonen, J. Jokiniemi, A. Virtanen, M. Komppula and K. E. J. Lehtinen, Characterization and testing of a new environmental chamber, *Atmos. Meas. Tech.*, 2015, **8**, 2267–2278.

57 A. A. Reda, H. Czech, J. Schnelle-Kreis, O. Sippula, J. Orasche, B. Weggler, G. Abbaszade, J. M. Arteaga-Salas, M. Kortelainen, J. Tissari, J. Jokiniemi, T. Streibel and R. Zimmermann, Analysis of Gas-Phase Carbonyl Compounds in Emissions from Modern Wood Combustion Appliances: Influence of Wood Type and Combustion Appliance, *Energy Fuels*, 2015, **29**, 3897–3907.

58 H. Czech, O. Sippula, M. Kortelainen, J. Tissari, C. Radischat, J. Passig, T. Streibel, J. Jokiniemi and R. Zimmermann, On-line analysis of organic emissions from residential wood combustion with single-photon ionisation time-of-flight mass spectrometry (SPI-TOFMS), *Fuel*, 2016, **177**, 334–342.

59 S. S. Brown and J. Stutz, Nighttime radical observations and chemistry, *Chem. Soc. Rev.*, 2012, **41**, 6405.

60 T. B. Onasch, A. Trimborn, E. C. Fortner, J. T. Jayne, G. L. Kok, L. R. Williams, P. Davidovits and D. R. Worsnop, Soot Particle Aerosol Mass Spectrometer: Development, Validation, and Initial Application, *Aerosol Sci. Technol.*, 2012, **46**, 804–817.

61 P. Barmet, J. Dommen, P. F. DeCarlo, T. Tritscher, A. P. Praplan, S. M. Platt, A. S. H. Prévôt, N. M. Donahue and U. Baltensperger, OH clock determination by proton transfer reaction mass spectrometry at an environmental chamber, *Atmos. Meas. Tech.*, 2012, **5**, 647–656.

62 S. Isokääntä, E. Kari, A. Buchholz, L. Hao, S. Schobesberger, A. Virtanen and S. Mikkonen, Comparison of dimension reduction techniques in the analysis of mass spectrometry data, *Atmos. Meas. Tech.*, 2020, **13**, 2995–3022.

63 W. Revelle, *psych: Procedures for Psychological, Psychometric, and Personality Research*, Evanston, Illinois, 2018.

64 R Core Team, *R: A Language and Environment for Statistical Computing*, Vienna, Austria, 2019.

65 A. L. Comrey, *A First Course in Factor Analysis*, Academic Press, 1973.

66 A. G. Yong and S. Pearce, A Beginner's Guide to Factor Analysis: Focusing on Exploratory Factor Analysis, *Tutor. Quant. Methods Psychol.*, 2013, **9**, 79–94.

67 M. R. Canagaratna, J. T. Jayne, J. L. Jimenez, J. D. Allan, M. R. Alfarra, Q. Zhang, T. B. Onasch, F. Drewnick, H. Coe, A. Middlebrook, A. Delia, L. R. Williams, A. M. Trimborn, M. J. Northway, P. F. DeCarlo, C. E. Kolb, P. Davidovits and D. R. Worsnop, Chemical and microphysical characterization of ambient aerosols with the aerodyne aerosol mass spectrometer, *Mass Spectrom. Rev.*, 2007, **26**, 185–222.

68 J. de Gouw and C. Warneke, Measurements of volatile organic compounds in the earth's atmosphere using proton-transfer-reaction mass spectrometry, *Mass Spectrom. Rev.*, 2007, **26**, 223–257.

69 L. E. Hatch, R. J. Yokelson, C. E. Stockwell, P. R. Veres, I. J. Simpson, D. R. Blake, J. J. Orlando and K. C. Barsanti, Multi-instrument comparison and compilation of non-methane organic gas emissions from biomass burning and implications for smoke-derived secondary organic aerosol precursors, *Atmos. Chem. Phys.*, 2017, **17**, 1471–1489.

70 B. Yuan, A. R. Koss, C. Warneke, M. Coggon, K. Sekimoto and J. A. de Gouw, Proton-Transfer-Reaction Mass Spectrometry: Applications in Atmospheric Sciences, *Chem. Rev.*, 2017, **117**, 13187–13229.

71 P. Paatero, Least squares formulation of robust non-negative factor analysis, *Chemom. Intell. Lab. Syst.*, 1997, **37**, 23–35.

72 I. M. Ulbrich, M. R. Canagaratna, Q. Zhang, D. R. Worsnop and J. L. Jimenez, Interpretation of organic components from Positive Matrix Factorization of aerosol mass spectrometric data, *Atmos. Chem. Phys.*, 2009, **9**, 2891–2918.

73 J. H. Kroll, N. M. Donahue, J. L. Jimenez, S. H. Kessler, M. R. Canagaratna, K. R. Wilson, K. E. Altieri, L. R. Mazzoleni, A. S. Wozniak, H. Bluhm, E. R. Mysak, J. D. Smith, C. E. Kolb and D. R. Worsnop, Carbon oxidation state as a metric for describing the chemistry of atmospheric organic aerosol, *Nat. Chem.*, 2011, **3**, 133–139.

74 W. S. Cleveland, Robust Locally Weighted Regression and Smoothing Scatterplots, *J. Am. Stat. Assoc.*, 1979, **74**, 829.

75 C. Wongchokprasitti, *rcausal: R-Causal Library*, 2019.

76 R. Tibshirani, Regression Shrinkage and Selection via the Lasso, *J. R. Stat. Soc., B: Stat. Methodol.*, 1996, **58**, 267–288.

77 K. Soetaert, T. Petzoldt and R. W. Setzer, Solving Differential Equations in R: Package deSolve, *J. Stat. Softw.*, 2010, **33**, 1–25.

78 P. Spirtes, C. N. Glymour and R. Scheines, *Causation, Prediction, and Search*, MIT Press, 2000.

79 X. Shen, S. Ma, P. Vemuri, G. Simon, M. W. Weiner, P. Aisen, R. Petersen, C. R. Jack, A. J. Saykin, W. Jagust, J. Q. Trojanowki, A. W. Toga, L. Beckett, R. C. Green, J. Morris, L. M. Shaw, Z. Khachaturian, G. Sorensen, M. Carrillo, L. Kuller, M. Raichle, S. Paul, P. Davies, H. Fillit, F. Hefti, D. Holtzman, M. M. Mesulam, W. Potter, P. Snyder, A. Schwartz, T. Montine, R. G. Thomas, M. Donohue, S. Walter, D. Gessert, T. Sather, G. Jiminez, A. B. Balasubramanian, J. Mason, I. Sim, D. Harvey, M. Bernstein, N. Fox, P. Thompson, N. Schuff, C. DeCArli, B. Borowski, J. Gunter, M. Senjem, D. Jones, K. Kantarci, C. Ward, R. A. Koeppe, N. Foster, E. M. Reiman, K. Chen, C. Mathis, S. Landau, N. J. Cairns, E. Franklin, L. Taylor-Reinwald, V. Lee, M. Korecka, M. Figurski, K. Crawford, S. Neu, T. M. Foroud, S. Potkin, K. Faber, S. Kim, K. Nho, L. Thal, N. Buckholtz, M. Albert, R. Frank, J. Hsiao, J. Kaye, J. Quinn, L. Silbert, B. Lind, R. Carter, S. Dolen, L. S. Schneider, S. Pawluczyk, M. Beccera, L. Teodoro, B. M. Spann, J. Brewer, H. Vanderswag, A. Fleisher, J. L. Heidebrink, J. L. Lord, S. S. Mason, C. S. Albers, D. Knopman, K. Johnson, R. S. Doody, J. Villanueva-Meyer, V. Pavlik, V. Shibley, M. Chowdhury, S. Rountree, M. Dang, Y. Stern, L. S. Honig, K. L. Bell, B. Ances, M. Carroll, M. L. Creech, M. A. Mintun, S. Schneider, A. Oliver, D. Marson, D. Geldmacher, M. N. Love, R. Griffith, D. Clark, J. Brockington, E. Roberson, H. Grossman, E. Mitsis, R. C. Shah, L. deToledo-Morrell, R. Duara, M. T. Greig-Custo, W. Barker, C. Onyike, D. D'Agostino, S. Kielb, M. Sadowski, M. O. Sheikh, A. Ulysse, M. Gaikwad, P. M. Doraiswamy, J. R. Petrella, S. Borges-Neto, T. Z. Wong, E. Coleman, S. E. Arnold, J. H. Karlawish, D. A. Wolk, C. M. Clark, C. D. Smith, G. Jicha, P. Hardy, P. Sinha, E. Oates, G. Conrad, O. L. Lopez, M. A. Oakley, D. M. Simpson, A. P. Porsteinsson, B. S. Goldstein, K. Martin, K. M. Makino, M. S. Ismail, C. Brand, A. Preda, D. Nguyen, K. Womack, D. Mathews, M. Quiceno, A. I. Levey, J. J. Lah, J. S. Cellar, J. M. Burns, R. H. Swerdlow, W. M. Brooks, L. Apostolova, K. Tingus, E. Woo, D. H. S. Silverman, P. H. Lu, G. Bartzokis, N. R. Graff-Radford, F. Parfitt, K. Poki-Walker, M. R. Farlow, A. M. Hake, B. R. Matthews, J. R. Brosch, S. Herring, C. H. van Dyck, R. E. Carson, M. G. MacAvoy, P. Varma, H. Chertkow, H. Bergman, C. Hosein, S. Black, B. Stefanovic, C. Caldwell, G.-Y. R. Hsiung, B. Mudge, V. Sossi, H. Feldman, M. Assaly, E. Finger, S. Pasternack, I. Rachisky, J. Rogers, D. Trost, A. Kertesz, C. Bernick, D. Munic, E. Rogalski, K. Lipowski, S. Weintraub, B. Bonakdarpour, D. Kerwin, C.-K. Wu, N. Johnson, C. Sadowsky, T. Villena, R. S. Turner, K. Johnson, B. Reynolds, R. A. Sperling, K. A. Johnson, G. Marshall, J. Yesavage, J. L. Taylor, B. Lane, A. Rosen, J. Tinklenberg, M. N. Sabbagh, C. M. Belden, S. A. Jacobson, S. A. Sirrel, N. Kowall, R. Killiany, A. E. Budson, A. Norbash, P. L. Johnson, T. O. Obisesan, S. Wolday, J. Allard, A. Lerner, P. Ogrocki, C. Tatsuoka, P. Fatica, E. Fletcher, P. Maillard, J. Olichney, O. Carmichael, S. Kittur, M. Borrie, T.-Y. Lee, R. Bartha, S. Johnson, S. Asthana, C. M. Carlsson, P. Tariot, A. Burke, A. M. Milliken, N. Trncic, S. Reeder, V. Bates, H. Capote, M. Rainka, D. W. Scharre, M. Kataki, B. Kelly, E. A. Zimmerman, D. Celmins, A. D. Brown, G. D. Pearlson, K. Blank, K. Anderson, L. A. Flashman, M. Seltzer, M. L. Hynes, R. B. Santulli, K. M. Sink, L. Gordineer, J. D. Williamson, P. Garg, F. Watkins, B. R. Ott, G. Tremont, L. A. Daiello, S. Salloway, P. Malloy, S. Correia, H. J. Rosen, B. L. Miller, D. Perry, J. Mintzer, K. Spicer, D. Bachman, N. Pomara, R. Hernando, A. Sarrael, S. K. Schultz, K. E. Smith, H. Koleva and The Alzheimer's Disease Neuroimaging Initiative, Challenges and Opportunities with Causal Discovery Algorithms:

Application to Alzheimer's Pathophysiology, *Sci. Rep.*, 2020, **10**, 2975.

80 J. H. Seinfeld and S. N. Pandis, *Atmospheric Chemistry and Physics*, Wiley, 2016.

81 P. Wang, *Gibbs Sampler for Bayesian Lasso*, **https://cs.gmu.edu/~pwang7/gibbsBLasso.html**, accessed, 13 December 2019.

82 T. Park and G. Casella, The Bayesian Lasso, *J. Am. Stat. Assoc.*, 2008, **103**, 681–686.

83 A. Buchholz, A. Ylisirniö, W. Huang, C. Mohr, M. Canagaratna, D. R. Worsnop, S. Schobesberger and A. Virtanen, Deconvolution of FIGAERO–CIMS thermal desorption profiles using positive matrix factorisation to identify chemical and physical processes during particle evaporation, *Atmos. Chem. Phys.*, 2020, **20**, 7693–7716.

84 A. R. Koss, M. R. Canagaratna, A. Zaytsev, J. E. Krechmer, M. Breitenlechner, K. J. Nihill, C. Y. Lim, J. C. Rowe, J. R. Roscioli, F. N. Keutsch and J. H. Kroll, Dimensionality-reduction techniques for complex mass spectrometric datasets: application to laboratory atmospheric organic oxidation experiments, *Atmos. Chem. Phys.*, 2020, **20**, 1021–1041.

85 B. Rosati, R. Teiwes, K. Kristensen, R. Bossi, H. Skov, M. Glasius, H. B. Pedersen and M. Bilde, Factor analysis of chemical ionization experiments: numerical simulations and an experimental case study of the ozonolysis of α-pinene using a PTR-ToF-MS, *Atmos. Environ.*, 2019, **199**, 15–31.

86 A. T. Ahern, E. S. Robinson, D. S. Tkacik, R. Saleh, L. E. Hatch, K. C. Barsanti, C. E. Stockwell, R. J. Yokelson, A. A. Presto, A. L. Robinson, R. C. Sullivan and N. M. Donahue, Production of Secondary Organic Aerosol During Aging of Biomass Burning Smoke From Fresh Fuels and Its Relationship to VOC Precursors, *J. Geophys. Res. Atmos.*, 2019, **124**(6), 3583–3606.

Electronic Supplementary Material (ESI) for Environmental Science: Atmospheres.

Supplement to the manuscript 'Modeling atmospheric aging of small-scale wood combustion emissions: distinguishing causal effects from non-causal associations'

Ville Leinonen, Petri Tiitta, Olli Sippula, Hendryk Czech, Ari Leskinen, Sini Isokääntä, Juha Karvanen, and Santtu Mikkonen

Table of contents

Figures

Tables

S1 Motivation for time series filtering

The measurement $y_{k,t}$ at time t for time series y_k is the sum of the true value $\alpha_{k,t}$ and the measurement error $\varepsilon_{k,t}$. These measurement errors comprise sampling from the chamber ($\varepsilon_{k_{sampling},t}$), error related to the estimation of particles and gases losses to chamber walls ($\varepsilon_{k_{wall-loss},t}$), and error related to processing of measurement instrument data from raw data into more useful form ($\varepsilon_{k_{processing},t}$).

Measurements $y_{k,t}$ were presented as

$y_{k,t} = \alpha_{k,t} + \varepsilon_{k,t}$ (A.1)

$\varepsilon_{k,t} = \varepsilon_{k_{sampling},t} + \varepsilon_{k_{wall-loss},t} + \varepsilon_{k_{processing},t}$ $(A.2)$

where the error term $\varepsilon_{k,t}$ is independent in time and follows a specified distribution presenting all uncertainties. The state $\alpha_{k,t}$ describes the estimate of the real state of the variable in the chamber and the error term $\varepsilon_{k,t}$ represents the error related to the estimation of the state.

Understanding the evolution of the state $\alpha_{k,t}$ of the variable is the question of interest. We would like to understand the factors affecting the change of state during the aging of emissions. Therefore, we estimated the state $\alpha_{k,t}$ from measurements $y_{k,t}$ for each variable.

S2 Methods for simulation studies

Two simulated data sets (see Table 1 in the main text) were formed to study how model would perform in a situation where we know the correct evolution and structure. Both data sets were formed using R-package deSolve (Soetaert et al., 2010). Data sets describe the evolution of Ordinary Differential Equation (ODE) system which length is 100. The difference between data sets is the way how differential equations of variables are linked to each other. In smaller data sets, differential equations are following the Laws of Mass Action, applied in R-package

episode (Mikkelsen, 2017; Seinfeld and Pandis, 2016, see Table S1 for coefficients used in the system). In larger data set, equations have been formed independently for each variable, using pre-defined causal structure for variables (see Table S2 for coefficients used in the system. We called these data sets as simulated data sets throughout the text.

Table S1 Coefficients for smaller simulated dataset.

$\Delta(x)$	Predictor	Coefficient
V2	V1+V3	0.021
V1	V2	0.0225
V4	V2	0.0225
V1	V2+V4	0.015
V5	V2+V3	0.02
V2	V5	0.01
V4	V5	0.01
V6	V2+V5	0.02
V2	V6	0.03
V5	V6	0.03
V7	V6	0.015
V7	V2+V8	0.02
V2	V7	0.03
V8	V7	0.03
V3	V4	0.015

Table S2 Coefficients for larger simulated dataset.

Gases			Particle chemical composition		
$\Delta(x)$	Predictor	Coefficient	$\Delta(x)$	Predictor	Coefficient
NO2	NO2*NuclM	-2.30E-08	NO3	NO3*O3	8.15E-04
O3	PTR3	1.59E-03	NO3	NO3*AitM	-1.33E-07
O3	O3*PTR1	4.19E-04	NO3	NO3*NuclM	-4.67E-08
O3	O3*NuclM	-7.85E-07	NO3	NO3*CoarseM	-4.21E-08
O3	O3*CoarseM	-1.22E-07	NO3	AitM*O3	1.52E-08
O3	NuclM*PTR3	1.06E-07	NO3	AitM	1.37E-10
O3	PTR1*CoarseM	4.90E-08	NO3	AitM*CoarseM	1.19E-12

OH	PTR2*OH	-2.44E-02
PTR1	PTR1	-6.59E-03
PTR1	PTR3*PTR1	3.00E-05
PTR1	PTR1*NuclM	-1.08E-07
PTR1	NuclM	1.42E-08
PTR1	CoarseM*PTR1	-6.58E-09
PTR1	PTR3*NuclM	1.31E-09
PTR1	NuclM*CoarseM	2.45E-12
PTR2	PTR2	5.86E-03
PTR2	AitM*PTR2	-1.17E-08
PTR3	PTR3	-1.22E-03
PTR3	PTR3*PTR2	6.09E-05
PTR3	PTR3*CoarseM	2.05E-09

Particle size

Δ(x)	Predictor	Coefficient
AccM	AccM*PTR3	-1.03E-05
AccM	NuclM*CoarseM	9.83E-07
AccM	NuclM*AccM	-1.26E-07
AccM	AccM*CoarseM	-1.03E-08
AitM	AitM	4.39E-02
AitM	PTR3*AitM	-2.23E-04
AitM	AitM*AccM	6.12E-09
CoarseM	AccM*NO2	8.82E-06
CoarseM	NuclM*CoarseM	-7.89E-08
CoarseM	AitM*CoarseM	-5.05E-08
CoarseM	AitM*AccM	1.36E-08
NuclM	NuclM	-2.02E-03
NuclM	NuclM*CoarseM	1.77E-07
NuclM	AccM*NuclM	-5.19E-08
POA1	AitM*POA1	-1.58E-08
POA2	POA2	9.55E-02
POA2	PTR1*POA2	-1.20E-02
POA2	POA2*O3	1.34E-03
POA2	AitM	5.99E-07
POA2	AitM*POA2	-5.06E-08
SOA1	O3*SOA1	-7.46E-05
SOA1	NuclM*SOA1	1.25E-07
SOA2	O3	2.81E-02
SOA2	POA2*SOA2	-1.57E-03
SOA2	SOA2*O3	-8.86E-04
SOA2	SOA2	3.40E-04
SOA2	NuclM*SOA2	-7.10E-08
SOA3	SOA2*POA2	6.42E-04
SOA3	SOA2*SOA1	4.16E-04
SOA3	SOA3	-1.49E-04
SOA3	SOA3*SOA2	1.26E-05
SOA3	NuclM*SOA3	-1.76E-07

Several questions of interest existed related to the properties of input data set and data pretreatment (Table S3). Firstly, we were interested to study how the precision of the measurements by analytical instrumentation is related to the model fit, which is assessed by

using different proportions of random noise mimicking the measurement error and the number of measurements made in time. To mimic the measurement error, normally distributed random noise was added to the variables. The standard deviation of the added random noise have been proportional to the standard deviation of the simulated variables due to evolution process. The proportion of the standard deviation of the random noise have been called fraction of added uncertainty. The number of measurements during the same evolution length (100) was altered to be between 26 and 401.

Secondly, we were interested to know whether the methods we applied to increase the quality of data are increasing the quality of the fit, i.e. accuracy of fit and obtained causal structure. Does filtering or smoothing of time series improve the fit and accuracy of prediction and is there an optimal time resolution to which data should be averaged?

Thirdly, the amount of necessary prior information was the question of interest. We were interested to study the importance of prior information given to a causal discovery algorithm to the modeled structure. Does addition of prior information improve the accuracy of modeled structure and how much prior information is necessary to get a reasonably good fit for the model.

The question about necessity of the prior information is also related to the dependence of model fit and the correctness of the structure. Intuitively, one might think that the correct structure would produce the best fit for the evolution. As many of the variables are highly dependent, it is probable that we will fail to obtain the exactly correct structure between variables. In addition to the differences between obtained and real structure in the model, we are interested about the predictive value of the obtained model compared to the simulated evolution. If dependent variables which we use in the model to explain the evolution are correlated with real causes in the data set, the model might still be able to predict the evolution of emission in the chamber.

Table S3 Simulated experiments to study the model performance. Aim of simulation studies is to investigate how different parameters affect model capability to return correct structure and goodness of fit.

	How test was performed	Purpose of the test
Measurement frequency (Table S4 and S5)	Reducing or increasing number of simulated 'measurement' points in given time (100). Frequency of 1/4,1/2,1,2,4 time points was used. This means dataset has 401, 201, 101, 51 and 26 measurement points during time simulation time 0-100.	To see whether increasing or decreasing measurement frequency would help making model better. Increasing of points with same measurement noise would lead to lower signal/noise ratio?
Measurement uncertainty (Table S4 and S5)	Adding normally distributed random noise to the simulated evolution. This random noise was representing the possible measurement uncertainty.	Purpose was to see if the measurement uncertainty reduces both structural accuracy and fit accuracy.
Filtering and smoothing (Figure S1)	Applied filtering and smoothing to original variables of simulated dataset.	How filtering or smoothing would improve the fit and structure of the model? Is it reasonable to use filtering or smoothing of dataset before making a model?
Prior Information (Table S6 and S7)	Using prior information about the edges possible in the model. Using both correct and incorrect prior information. Fraction of information from all correct prior information was used as a measure of information.	Does addition of prior information help model to get correct structure and good fit?

Accuracy tests for causal discovery algorithms have been performed earlier (Scheines and Ramsey, 2016; Singh et al., 2017). However, those tests are dependent on the used data set. In our case, variables that explain the evolution of some variable do not originate directly from the discovery algorithm. Our situation differs from the tests performed earlier as the variables from the algorithm are used to form possible interaction variables, not directly to explain the evolution.

We measured the performance of the model in simulated data set by two ways. First is the accuracy of the model fit to the simulated data set: how well the model can capture simulated evolution and how well the model can predict the simulated evolution after fitted data set. Second can be called as structural accuracy: how well the underlying causal structure of variables can be returned by the model.

For measuring accuracy of the model fit, we compared the evolution obtained from the model to measurements. Evolution was then compared to true evolution, not including the error added to the simulations, using Root Mean Squared Error (RMSE) for each time series. To equally weight each time series when calculating RMSE, each time series were scaled by dividing those with its standard deviation before calculating RMSE. In further text, we refer to this scaled version as RMSE.

In addition to the accuracy of the model, we also evaluated the predictive accuracy of the model. We used the obtained coefficients from the model to predict further time steps of the evolution of the system. Then we compared the prediction to the same time steps from the real system and evaluate the accuracy of model prediction using RMSE. Prediction length was 30% of the simulated data set used to fit a model.

For measuring structural accuracy, we used adjacency precision (AP), adjacency recall (AR) (Scheines and Ramsey, 2016) and F-score (Singh et al., 2017). AP was defined as a fraction of correct edges in the model of all proposed edges. AR was defined as a fraction of correct edges in the model of all correct edges. F-score was defined based on AP and AR as

$F_{score} = 2 * \frac{AP * AR}{AP + AR}$.

In addition to F-score, we wanted to study whether incorrect predictors for variables were close to correct causes and whether the model could find a good replacement for each correct predictor that was not chosen for modeled structure. Correlation was used to measure closeness here. For each correct predictor we calculated correlation between it and each predictor in the model (for same$\Delta(x)$). The maximum of these correlations was taken as the value for that

predictor. This results that if the correct predictor was in the model, correlation was 1. In the results section we have calculated the mean value of correlations for all the predictors.

S3 Results of simulation studies

As expected, the model fit to the data was better when the error assigned on it was lower. The effect of measurement error is reported for simulated data sets (Tables S4 and S5). The effect of uncertainty was small for F-score and correlation between the correct edges and edges in the model. This was expected, as the error makes the data set noisier. Furthermore, as the simulations also studied the effect of time resolution in measurements, in both data sets the optimal number of measurements during one experiment was related to the amount of error applied (Tables S4 and S5). For lower error, higher time resolution leads to better results when the real change between subsequent time points was dominating the change observed and if many observations about the evolution process were available. In case of high error, fewer observations from the phenomenon were preferred, as the signal to noise ratio was low and increasing the number of observations would make it even lower. However, the dependence between sample size and fraction of error was weak. This is still opposite of what is expected and could be due to a small sample size.

We found that in some cases, there were unstabilities in computations. These can be seen as large numbers of RMSE in the tables S4 and S5. These are resulted by some variable that gets large values in the differential equation system, resulting the system to be unstable. We haven't been studied the exact reason for the unstability. This could be due to the inaccurate estimation of the structure, i.e. some incorrect edge in the model results a dependence that is having "large" coefficient, and that differential equation would result system to be unstable. Other option is that the estimate itself is overestimated, i.e., due to low number of points or inaccuracies in the measured differences that are modeled.

Table S4 Effect of measurement frequency and fraction of error to goodness of fit parameters of the model for larger simulated dataset. Variable 'Fraction of added uncertainty' is a standard deviation of random noise added to simulation data (sd of each time series is adjusted to 1). Number of edges is the number of edges in the model, RMSE is Root Mean Squared Error, F-score is a measure of structural accuracy, based on a number of correct and incorrect edges, see S1 for more information. Mean correlation is mean correlation between proposed and correct predictor variable. For each row, number of replications is 10. For number of observations = 401, and fraction of added uncertainty = 0.5, there is 2/10 cases, when some unstabilities result large values for RMSE.

Number of observations	Fraction of added uncertainty	Mean number of edges in the model	Mean of RMSE	Mean of RMSE for prediction	Mean of Fscore	Mean correlation of correct predictor and selected predictor
26	0.01	35.9	17.07	12.86	0.22	0.88
51	0.01	46.2	17.47	16.2	0.22	0.88
101	0.01	41.1	19.43	18.13	0.22	0.87
201	0.01	39.1	23	20.63	0.2	0.86
401	0.01	28	24.46	17.85	0.21	0.83
26	0.05	30	19.97	16.51	0.19	0.82
51	0.05	29.9	19.77	20.07	0.17	0.84
101	0.05	29.5	17.05	19.03	0.19	0.89
201	0.05	27.4	19.84	22.21	0.19	0.92
401	0.05	24.5	23.61	20.71	0.18	0.93
26	0.1	25.9	19.96	15.68	0.17	0.86
51	0.1	28.9	18.91	19.51	0.2	0.93
101	0.1	28	21.24	21.56	0.19	0.93
201	0.1	22.4	28.06	35.83	0.18	0.92
401	0.1	19.8	33.86	22.49	0.18	0.91
26	0.5	33.7	31.17	25.76	0.19	0.93
51	0.5	28.3	47.12	31.35	0.19	0.92
101	0.5	41.1	1757.27	38.03	0.22	0.94
201	0.5	44.3	344.31	42.27	0.23	0.94
401	0.5	46.1	2.19841E+18	71.84	0.23	0.93

Table S5 Effect of number of observations and fraction added uncertainty to goodness of fit parameters of the model in smaller simulated dataset. Variable 'Fraction of added uncertainty' is a standard deviation of random noise added to simulation data (sd of each time series is adjusted to 1). Number of edges is the number of edges in the model, RMSE is Root Mean Squared Error, F-score is a measure of structural accuracy, based on a number of correct and incorrect edges, see S1 for more information. Mean correlation is mean correlation between proposed and correct predictor variable. For each row, number of replications is 10. For number of observations = 401, and fraction of added uncertainty = 0.5, there is 1/10 cases, when some unstabilities result large values for RMSE.

Number of observations	Fraction of added uncertainty	Mean number of edges in the model	Mean of RMSE	Mean of RMSE for prediction	Mean of Fscore	Mean correlation of correct predictor and selected predictor
26	0.01	15.3	7.76	4.5	0.22	0.85
51	0.01	17.7	5.88	4.16	0.23	0.87
101	0.01	22.5	4.64	3.67	0.21	0.81
201	0.01	22.5	4.02	3.71	0.21	0.75
401	0.01	18.4	6.68	4.07	0.26	0.81
26	0.05	12.6	8.79	4.71	0.13	0.75
51	0.05	14.1	8.93	3.89	0.2	0.79
101	0.05	16.8	7.89	3.33	0.25	0.81
201	0.05	13.8	10.83	2.85	0.19	0.8
401	0.05	11.5	17.93	3.9	0.24	0.8
26	0.1	10.1	9.91	3.59	0.17	0.77
51	0.1	10.6	10.99	2.92	0.24	0.78
101	0.1	11.3	15.23	4.35	0.24	0.79
201	0.1	9.8	22.61	8.1	0.31	0.68
401	0.1	7.4	32.08	11.81	0.32	0.63
26	0.5	5.6	31.64	12.85	0.23	0.61
51	0.5	5	40.16	21.21	0.23	0.59
101	0.5	6	47.46	29.68	0.22	0.63
201	0.5	6.4	51.29	36.34	0.23	0.65
401	0.5	8.2	2.49773E+17	795977.48	0.26	0.76

Filtering or smoothing of the time series representing measurements reduces the error, especially when measurement uncertainty was high (Figure S1). These methods were also improving the accuracy of model prediction. To understand importance of applying smoothing or filtering method in a real data set, we need to understand whether the error in the real data set is large enough that applying filtering or smoothing method is reasonable. We assume the error related to the time series as the difference between these data sets. The standard deviation of the error was then compared to the standard deviation of the filtered data set to estimate the fraction of the error of the whole standard deviation in the time series.

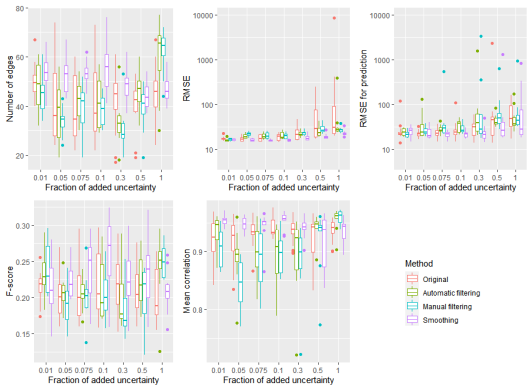

Figure S1 Effect of filtering and smoothing to the goodness of fit parameters. Method 'Original' means that time series is used without filtering or smoothing. In automatic and manual filtering, filter have been applied by selecting length of the filtering window by cross-validation (automatic) or by manual selection. Window length in smoothing have been chosen by cross-validation. Variable 'Fraction of added uncertainty' is a standard

deviation of random noise added to simulation data (standard deviation of each time series is adjusted to 1), see S1 for more information. Number of edges is the number of edges in the model, RMSE is Root Mean Squared Error, F-score is a measure of structural accuracy, based on number of correct and incorrect edges, see S1 for more information. Mean correlation is mean correlation between proposed and correct predictor variable. There is some additional points that are outside of the figure and are due to some unstabilities in the fit. For RMSE, there is one larger value for smoothing, two larger values for manual filtering and two for original time series, all with fraction of added uncertainty of 1. For predicted RMSE, there is one larger value for smoothed, uncertainty 0.1, three for manually filtered, with uncertainties 0.3, 0.3, and 1, and one for automatically filtered, with uncertainty 0.5.

In Aerosol Mass Spectrometer (AMS) and Proton-Transfer-Reactor Time-of-Flight Mass Spectrometer (PTR-ToF-MS) data sets and in coarse size bin (>300nm) of Scanning Mobility Particle Sizer (SMPS) measurements, the fraction of standard deviation of error was around 10-20% of the whole standard deviation. Variables measured by gas analyzers contained the least amount of error, approximately 1-5% of the standard deviation of filtered time series. However, because the fraction of error of some variables is high, applying of the filtering methods to real data set was reasonable.

Reasons why applying the filtering methods to the data set is not improving the fit before the error is relatively high could be assessed further but is not on the scope of this study. In addition to the fraction of error, the sample size is probably related to the necessity of the filtering method. These simulations for the larger data set were performed using the sample size of 100, which is the same sample size that was used in the shortest experiment.

Fourthly, prior information was closely related especially to the correctness of the obtained dependence structure between variables in the data set. In some situations, there might be large amounts of prior information from previous studies available, which might help to construct the structure based on prior knowledge. This means that the correctness of the structure is high, and the causal inference based on the structure and the observed data set has higher quality.

From wood combustion emission experiments, we do not have much prior knowledge about the phenomenon. Even though there has been and currently is a vast amount of research about the oxidative aging of combustion emissions, the number of possible reactions occurring during experiments is very high and the reaction coefficients are therefore hard to estimate. Thus, the construction of the complete causal structure between variables might be out of reach based on low amount of prior information.

One question of interest is that how the incorrect edges in the structure are related to the missing or present correct edges. Based on the nature of the causal discovery algorithm one might think that the algorithm is not able to separate between causal and non-causal associations. Therefore, it might be that in the model the real cause is replaced with an indicative one. This decreases the accuracy of the structure, but not necessarily affect the fit or accuracy of prediction of the model. Especially if the dependence between a real and an indicative cause is strong. Decreased accuracy in the structure may produce incorrect interpretations of the causal effects.

We found that there is a small difference in both goodness of fit and structure accuracy parameters when the number of correct and incorrect edges in prior information is varied in the smaller, artificial data set. Larger amount of correct prior information led to slightly lower RMSE for the model and prediction (Table S6). Addition of correct prior information led to lower RMSE and higher F-score. For prediction, the information had not much effect. Incorrect prior information didn't affect the prediction accuracy, nor the F-score as would have been expected. F-score was even higher when there was more incorrect information available (Table S7). This indicates that the prior information is not optimally used in the current version of the model and should be handled better in the future.

Table S6 Effect of correct prior information for the goodness of fit parameters of the model in smaller simulated dataset. Fractions of correct and incorrect information about dependencies are X -> Y dependencies given as a prior information for causal discovery algorithm. Variable 'Fraction of added uncertainty' is a standard deviation of random noise added to simulation data (standard deviation of each time series is adjusted to 1). Number of edges is the number of edges in the model, RMSE is Root Mean Squared Error, F-score is a measure of structural accuracy, based on a number of correct and incorrect edges, see S1 for more information. Mean correlation is mean correlation between proposed and correct predictor variable. For each row, number of replications is 10, number of observations is 101, and fraction of added uncertainty is 0.5.

Fraction of correct information about dependencies	Fraction of correct info about non-dependencies	Fraction of incorrect info about dependencies	Fraction of incorrect info about non-dependencies	Mean number of edges in the model	Mean of RMSE	Mean of RMSE for prediction	Mean of Fscore	Mean correlation of correct predictor and selected predictor
0.05	0.05	0	0	10.4	15.85	4.98	0.2	0.79
0.3	0.05	0	0	22.1	8.99	4.85	0.36	0.87
0.5	0.05	0	0	31.2	7.62	4.74	0.44	0.9
0.05	0.3	0	0	11	15.36	4.95	0.23	0.8
0.3	0.3	0	0	20.7	12.31	4.83	0.36	0.83
0.5	0.3	0	0	30.9	7.07	4.54	0.43	0.9
0.05	0.5	0	0	10.8	14.55	4.93	0.23	0.8
0.3	0.5	0	0	22	6.73	5.2	0.38	0.88
0.5	0.5	0	0	32.3	5.19	5.33	0.48	0.93

Table S7 Effect of incorrect prior information for the goodness of fit parameters of the model in smaller simulated dataset. Fractions of correct and incorrect information about dependencies are X -> Y dependencies given as a prior information for causal discovery algorithm. Variable 'Fraction of added uncertainty' is a standard deviation of random noise added to simulation data (standard deviation of each time series is adjusted to 1). Number of edges is the number of edges in the model, RMSE is Root Mean Squared Error, F-score is a measure of structural accuracy, based on a number of correct and incorrect edges, see S1 for more information. Mean correlation is mean correlation between proposed and correct predictor variable. For each row, number of replications is 10, number of observations is 101, and fraction of added uncertainty is 0.5.

Fraction of correct information about dependencies	Fraction of correct info about non-dependencies	Fraction of incorrect info about dependencies	Fraction of incorrect info about non-dependencies	Mean number of edges in the model	Mean of RMSE	Mean of RMSE for prediction	Mean of Fscore	Mean correlation of correct predictor and selected predictor
0.3	0.3	0	0	20.7	12.31	4.83	0.36	0.83
0.3	0.3	0.3	0	32.5	6.2	5.07	0.45	0.9
0.3	0.3	0.5	0	41.9	2.23	5.15	0.51	0.95
0.3	0.3	0	0.3	21.1	9.14	4.59	0.38	0.87
0.3	0.3	0.3	0.3	33	5.51	5.61	0.49	0.91
0.3	0.3	0.5	0.3	44.6	3.16	5.96	0.5	0.95
0.3	0.3	0	0.5	22	10.5	4.62	0.4	0.86
0.3	0.3	0.3	0.5	32.7	5.34	5.09	0.48	0.92
0.3	0.3	0.5	0.5	44.2	2.43	4.6	0.51	0.95

S4 Additional information about the models for wood combustion experiments

Related to wood combustion experiments, evolution of variables that are not represented in the main text are represented in Figures S2-S7. Figures S2-S4 show the evolution in dark aging experiments and Figures S5-S7 in photochemical aging experiments. Tables S8 and S9 provide estimated coefficients used to describe evolution in dark and photochemical aging experiments.

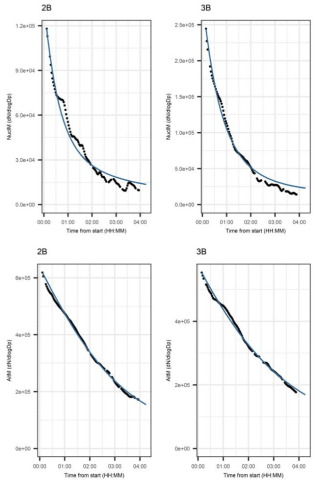

Figure S2 Evolution of size distribution variables in dark aging experiments. Size distribution (Nucleation mode (NuclM, < 25 nm) and Aitken mode (AitM, 25-100 nm)) are from

Scanning Mobility Particle Sizer (SMPS) measurements. Black points represent the filtered version of variable and the blue line shows the modeled evolution.

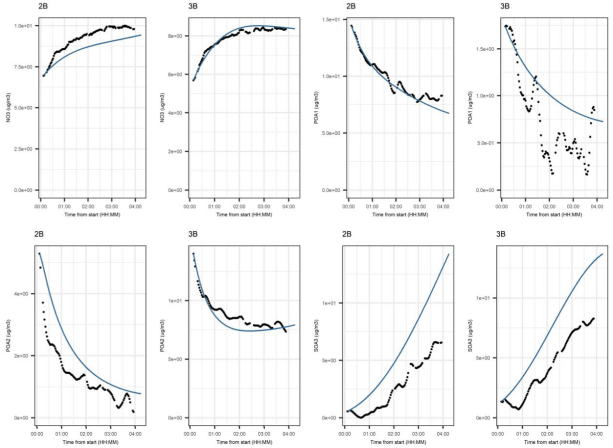

Figure S3 Evolution of nitrate (NO_3) signatured aerosol, primary organic aerosol (POA) factors 1-2, and secondary organic aerosol (SOA) factor 3 in dark aging experiments. All variables are from Aerosol Mass Spectrometer (AMS) measurements. POA factors are representing 1) biomass-burning OA and 2) hydrocarbon-like OA and SOA3 is representing formation by OH radicals. Black points represent the filtered version of variable

and the blue line shows the modeled evolution.

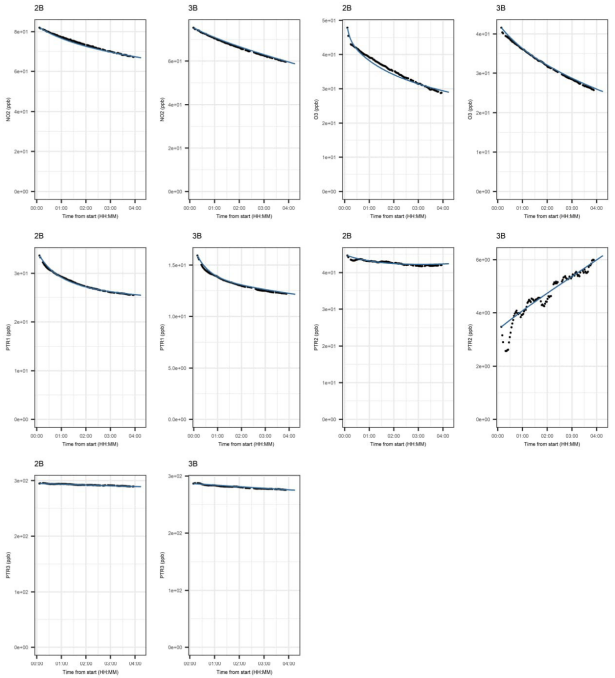

Figure S4 Evolution of gas variables (NO_2, O_3, and PTR factors 1-3) in dark aging experiments. NO_2 and O_3 are from gas analyzers and PTR factors are from Proton-Transfer-Reactor Time-of-Flight Mass Spectrometer (PTR-ToF-MS). PTR factors are representing 1) primary VOCs, 2) photochemical aging products, and 3) dark aging products. Black points represent the filtered version of variable and the blue line shows the modeled evolution.

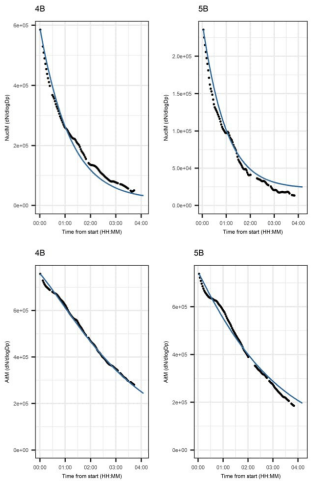

Figure S5 Evolution of size distribution variables in photochemical aging experiments. Size distribution (Nucleation mode (NuclM, < 25 nm) and Aitken mode (AitM, 25-100

nm)) are from Scanning Mobility Particle Sizer (SMPS) measurements. Black points represent the filtered version of variable and the blue line shows the modeled evolution.

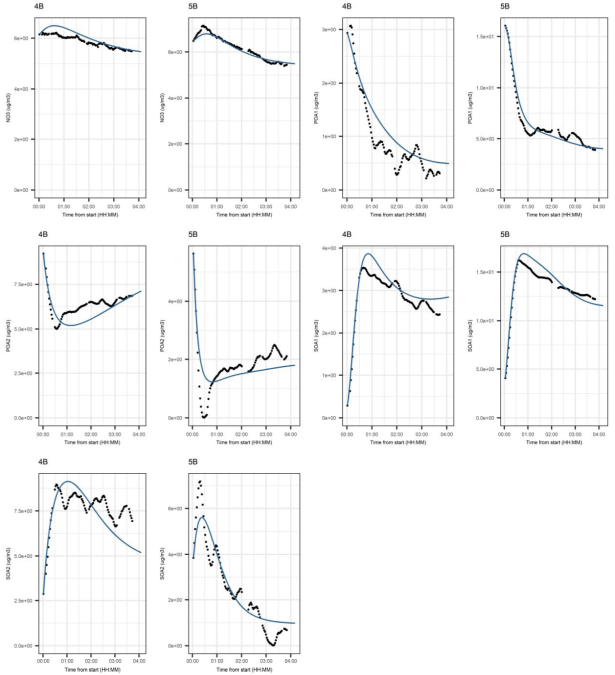

Figure S6 Evolution of nitrate (NO3) signatured aerosol, primary organic aerosol (POA) factors 1-2, and secondary organic aerosol (SOA) factors 1-2 in photochemical aging experiments. All variables are from Aerosol Mass Spectrometer (AMS) measurements. POA factors are representing 1) biomass-burning OA and 2) hydrocarbon-like OA and SOA factors are representing 1) formation by ozonolysis and 2) formation by nitrate/peroxy radicals. Black points represent the filtered version of variable and the blue line shows

the modeled evolution.

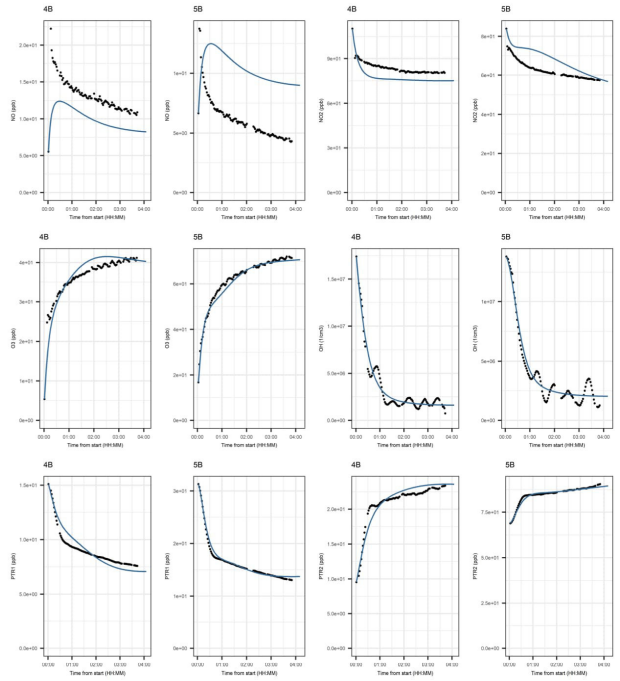

Figure S7 Evolution of gas variables (NO, NO_2, O_3, OH, PTR1, and PTR2) in photochemical aging experiments. NO, NO2 and O_3 are from gas analyzers. OH (derived from d9-butanol measurements), PTR1, and PTR2 are from Proton-Transfer-Reactor Time-of-Flight Mass Spectrometer (PTR-ToF-MS). PTR factors are representing 1) primary VOCs and 2) photochemical aging products. Black points represent the filtered version of variable and the blue line shows the modeled evolution.

Table S8 Coefficients for dark aging experiments. $\Delta(x)$ is the variable which its predictors are affecting. Estimate is the coefficient for the linear differential equation (1) in the main text. Gases (NO, NO2, O3) are measured by gas analyzers and PTR factors (PTR1-3) are from Proton-Transfer-Reactor Time-of-Flight Mass Spectrometer (PTR-ToF-MS) measurements. Particle chemical composition, nitrate (NO3) signatured aerosol and primary and secondary organic aerosol factors (POA1-2, SOA1-3) are derived from Aerosol Mass Spectrometer (AMS) measurements. Particle size distribution variables are representing typical aerosol modes, nucleation (NuclM, < 25 nm), Aitken (AitM, 25-100 nm), accumulation (AccM, 100-300 nm), and coarse (CoarseM, > 300 nm). Size distribution variables are derived from Scanning Mobility Particle Sizer (SMPS) measurements.

Gases

$\Delta(x)$	Predictor	Estimate	$\Delta(x)$	Predictor	Estimate
NO2	NO2	-0.0515	PTR1	PTR1*PTR2	0.000213
NO2	O3*NO2	-0.00078	PTR1	PTR3*PTR1	-7.7E-05
NO2	PTR3*O3	0.00026	PTR1	PTR3*O3	7.22E-05
NO2	PTR3*NO2	0.00014	PTR1	PTR1	-6.7E-06
O3	O3	0.00664	PTR2	PTR2	0.00387
O3	NO2*O3	0.00541	PTR2	O3	0.000744
O3	O3*PTR3	-0.00249	PTR2	O3*PTR2	-0.00013
O3	O3*PTR2	-0.00066	PTR2	PTR1*PTR2	-1.7E-05
O3	NO2*PTR3	0.000569	PTR3	PTR2	0.0126
PTR1	PTR1*O3	-0.00111	PTR3	PTR3	-0.00037
PTR1	PTR2*O3	0.000436	PTR3	PTR3*PTR2	-3.8E-05

Particle chemical composition

$\Delta(x)$	Predictor	Estimate	$\Delta(x)$	Predictor	Estimate
NO3	NO3	0.0656	POA2	NO2*POA2	-0.00515

NO3	POA2	0.0231	SOA1	SOA1	0.0352
NO3	POA2*NO3	-0.00673	SOA1	NO3*SOA1	0.00939
NO3	SOA2	0.00465	SOA1	SOA2*SOA1	-0.00405
NO3	SOA2*NO3	-0.00226	SOA1	O3*SOA1	-0.00164
NO3	NO3*POA1	-0.00212	SOA1	PTR2*SOA1	0.000556
NO3	POA1	0.000713	SOA1	O3*PTR2	5.62E-05
NO3	POA1*SOA2	0.000185	SOA2	SOA2	-0.0618
NO3	POA2*SOA2	-4.2E-07	SOA2	SOA2*O3	-0.0035
POA1	POA1	0.0327	SOA2	NO2*SOA2	0.00215
POA1	SOA1*POA1	0.00114	SOA2	NO2*O3	0.000308
POA1	NO2*POA1	-0.00062	SOA3	SOA3	-0.0497
POA2	POA2	0.0577	SOA3	SOA3*O3	0.00216
POA2	NO3*POA2	0.0128	SOA3	NO3	0.00145
POA2	O3*POA2	0.00553	SOA3	NO3*SOA3	-0.00029

Particle size

$\Delta(x)$	Predictor	Estimate	$\Delta(x)$	Predictor	Estimate
AccM	AccM	-0.0027	CoarseM	AitM*AccM	2.99E-09
AccM	AccM*AitM	1.26E-08	CoarseM	AccM*CoarseM	2.94E-09
AccM	AccM*CoarseM	-1.2E-08	CoarseM	NuclM*CoarseM	-2E-09
AitM	AitM	-0.0124	CoarseM	AitM*CoarseM	3.71E-10
AitM	AccM	0.00142	NuclM	NuclM	0.0197
AitM	CoarseM*AitM	-4.1E-08	NuclM	AitM	0.00214
AitM	AitM*AccM	5.8E-09	NuclM	NuclM*CoarseM	-9.6E-08
CoarseM	CoarseM	-0.00573	NuclM	AitM*NuclM	-7.6E-08

Table S9 Coefficients for photochemical aging experiments. is the variable which its predictors are affecting. Estimate is the coefficient for the linear differen-tial equation (1) in the main text. Gases (NO, NO2, O3) are measured by gas analyzers and PTR factors (PTR1-3) are from Proton-Transfer-Reactor Time-of-Flight Mass Spectrometer (PTR-ToF-MS) measurements. Particle chemical composition, nitrate (NO3) signatured aerosol and primary and secondary organic aerosol factors (POA1-2, SOA1-3) are derived from Aerosol Mass Spectrometer (AMS) measurements. Particle size distribution variables are representing typical aerosol modes, nucleation (NuclM, < 25 nm), Aitken (AitM, 25-100 nm), accumulation (AccM, 100-300 nm), and coarse (CoarseM, > 300 nm). Size distribution variables are derived from Scanning Mobility Particle Sizer (SMPS) measurements.

Gases

$\Delta(x)$	Predictor	Estimate	$\Delta(x)$	Predictor	Estimate
NO	NO	-0.0199	OH	PTR3*OH	-0.00055
NO	OH	2.26E-07	PTR1	PTR1	0.0533
NO	NO*OH	-1.6E-08	PTR1	PTR1*O3	-0.00189
NO2	NO2	0.0156	PTR1	PTR2*PTR1	0.000357
NO2	O3*NO2	-0.00036	PTR1	PTR2*O3	0.000121
NO2	OH*O3	6.25E-09	PTR1	PTR2	-8E-05
NO2	OH*NO2	-4E-09	PTR1	OH	3.43E-08
O3	PTR1	0.0969	PTR1	PTR1*OH	-6E-09
O3	O3	-0.0149	PTR2	PTR2	-0.0185
O3	PTR1*O3	0.000421	PTR2	O3	0.00312
O3	OH	1.08E-07	PTR2	O3*PTR2	0.000178
O3	OH*O3	-7.5E-09	PTR2	OH	2.64E-08
O3	OH*PTR1	6.92E-09	PTR2	OH*PTR2	9.9E-10
OH	PTR3	349	PTR2	OH*O3	9.25E-10
OH	PTR3*PTR1	28.9	PTR3	O3	0.0869
OH	PTR3*PTR2	4.11	PTR3	PTR3	0.0107
OH	OH	0.0303	PTR3	O3*PTR3	-0.00058
OH	PTR1*OH	0.00388	PTR3	PTR3*OH	-7.3E-10
OH	PTR2*OH	-0.00094			

Particle chemical composition

$\Delta(x)$	Predictor	Estimate	$\Delta(x)$	Predictor	Estimate

NO3	O3	0.00231	SOA1	PTR1*SOA1	0.0034
NO3	NO3	-0.00155	SOA1	O3*SOA1	-0.00149
NO3	O3*NO3	-0.00044	SOA1	O3*PTR1	0.000707
NO3	OH*NO3	4.23E-10	SOA1	SOA1*OH	2.9E-09
NO3	OH*O3	5.68E-11	SOA1	SOA2*OH	7.59E-10
POA1	POA1*NO3	-0.0148	SOA2	SOA2	0.054
POA1	POA1*PTR1	0.00705	SOA2	O3*SOA2	-0.00138
POA1	POA1	-0.00475	SOA2	PTR2*SOA2	-0.00042
POA1	OH*POA1	-1.4E-08	SOA2	OH	4.18E-08
POA1	OH*PTR1	2.47E-09	SOA2	SOA2*OH	-3.3E-09
POA2	NO3	0.0137	SOA3	NO3*SOA3	-0.0358
POA2	POA2	-0.0091	SOA3	O3	0.0275
POA2	POA2*POA1	-0.0091	SOA3	PTR1*SOA3	0.0118
POA2	NO3*POA2	0.00171	SOA3	O3*SOA3	-0.00026
POA2	POA2*OH	-2E-09	SOA3	PTR1*O3	-3.2E-05
SOA1	SOA2*SOA1	-0.0078	SOA3	SOA3*OH	2.31E-09

Particle size

$\Delta(x)$	Predictor	Estimate	$\Delta(x)$	Predictor	Estimate
AccM	CoarseM	0.216	AitM	AitM*NuclM	-5.3E-09
AccM	AccM	-0.0477	CoarseM	CoarseM	-0.00544
AccM	AitM	5.48E-05	CoarseM	AitM*CoarseM	2.06E-08
AccM	NuclM*AitM	2.29E-07	CoarseM	NuclM*CoarseM	-1.8E-08
AccM	NuclM*AccM	-2.1E-07	CoarseM	NuclM*AitM	1.87E-09
AccM	CoarseM*AccM	-9.4E-08	NuclM	NuclM	-0.0194
AccM	AitM*AccM	9.21E-08	NuclM	CoarseM	0.00284
AitM	AitM	-0.0124	NuclM	CoarseM*NuclM	-6.2E-08
AitM	NuclM	0.0123			

References for Supplement

Mikkelsen, F. V.: episode: Estimation with Penalisation in Systems of Ordinary Differential Equations, [online] Available from: https://cran.r-project.org/package=episode, 2017.

Scheines, R. and Ramsey, J.: Measurement Error and Causal Discovery., CEUR Workshop Proc., 1792, 1–7 [online] Available from: http://www.ncbi.nlm.nih.gov/pubmed/28280453 (Accessed 20 February 2019), 2016.

Seinfeld, J. H. and Pandis, S. N.: Atmospheric Chemistry and Physics, edited by J. H. Seinfeld and S. N. Pandis, Wiley., 2016.

Singh, K., Gupta, G., Tewari, V. and Shroff, G.: Comparative Benchmarking of Causal Discovery Techniques, [online] Available from: http://arxiv.org/abs/1708.06246 (Accessed 28 May 2019), 2017.

Soetaert, K., Petzoldt, T. and Setzer, R. W.: Solving Differential Equations in R: Package deSolve, J. Stat. Softw., 33(9), 1–25, doi:10.18637/jss.v033.i09, 2010.